

Diese Dissertation wurde begutachtet von:

Univ.Prof. Dipl.-Ing. Dr.techn. Robert Liska

Univ.Prof. Dipl.-Ing. Dr. mont. Jürgen Stampfl

Univ.Prof. Dipl.-Ing. Dr. Heinz Redl



**TECHNISCHE
UNIVERSITÄT
WIEN**

PhD Thesis

Dissertation

Novel Biocompatible Initiators for Direct Cell Encapsulation *via* Two-Photon Induced Photopolymerization

ausgeführt zum Zwecke der Erlangung des akademischen Grades eines

Doktors der technischen Wissenschaften

unter der Leitung von

Univ.Prof. Dipl.-Ing. Dr.techn. Robert Liska

E163

Institut für Angewandte Synthesechemie

eingereicht an der Technischen Universität Wien

Fakultät für Technische Chemie

von

Dipl.-Ing. Maximilian Tromayer

00525241

Schönbrunner Straße 96/2/18, 1050 Wien

Wien, 07.08.2018

Dipl.-Ing. Maximilian Tromayer

"The more I know, the more I know that I don't know."

- Socrates

Abstract

Two-photon induced polymerization (2PP) uses femtosecond-pulsed lasers to enable true 3D printing with high spatial control and resolutions in the sub-micrometer range. This allows fabrication of parts with ultra-small features such as photonic crystals, optical waveguides, microelectronic components and scaffolds for tissue engineering. 2PP-fabricated scaffolds have been used to microengineer 3D cell cultures, with the ultimate aim of studying stimulus - cellular response relationships, or testing of pharmaceutical compounds. In comparison to the approach of seeding cells onto pre-fabricated scaffolds, direct cell encapsulation into hydrogels supports higher initial cell loading, uniformity of cell distribution and a more intimate cell-matrix contact. Commercial initiators used in UV-encapsulation have proven inadequate for 2PP cell encapsulation strategies due to their low two-photon absorption, and the success of recently developed water-soluble two-photon initiators (2PIs), such as P2CK, has so far been limited because of their relatively high cyto- and phototoxicity.

This aim of this thesis was to design novel highly effective 2PIs that enable a biocompatible 2PP cell encapsulation process. To hinder 2PI transmembrane migration and prevent the intracellular formation of free radicals and reactive oxygen species (ROS) upon laser excitation, a macromolecular hyaluronan-based initiator HAPI was developed. Laser scanning microscopy imaging of 2PI autofluorescence demonstrated that in contrast to small molecule references, HAPI does not accumulate inside cells. While the cyto- and phototoxicity of HAPI were lower in comparison to P2CK, some cell damage was still observed after 2PP encapsulation.

A second strategy aimed at reducing the formation of ROS, which result from side reactions competing with the slow bimolecular electron transfer mechanism that is assumed to govern radical generation of conventional 2PIs. Thus, photocleavable compounds - which form radicals in a mechanism similar to biocompatible commercial UV-initiators - were studied as 2PIs. The cleavable trichloromethyl-triazine based system 2BC acted as efficient 2PI, but was impractical to use due to a tendency to cause overpolymerization as well as excessive visible light sensitivity. Investigation of cleavable diazosulfonates resulted in the development of AS7, which exhibits excellent biocompatibility and is highly effective as 2PI at fast writing speeds up to 1 m/s. ASC/TERT1 stem cells 2PP encapsulated in methacrylated gelatin hydrogels with AS7 showed no signs of photodamage, and were spreading and proliferating in the gel during a 5 day observation period after structuring.

Kurzfassung

Zwei-Photonen induzierte Polymerisation (2PP) nutzt Femtosekunden-gepulste Laser für 3D Druck mit hoher räumlicher Kontrolle und Auflösungen bis in den sub-Mikrometer-Bereich. Dies ermöglicht die Herstellung von Bauteilen mit ultrakleinen strukturellen Merkmalen wie photonische Kristalle, optische Wellenleiter, mikroelektronische Komponenten oder Gerüste für Gewebezüchtung. 2PP-produzierte Gerüste werden zur Mikromanipulation von 3D-Zellkulturen eingesetzt, mit dem letztendlichen Ziel der Untersuchung von zellulären Reiz-Reaktions-Zusammenhängen oder Pharmaforschung. Im Vergleich zur oberflächlichen Zellaussaat auf vorgefertigten Gerüsten bietet die direkte Zellverkapselung in Hydrogele höhere initiale Zelldichten, gleichmäßigere Zellverteilung und innigeren Zell-Matrix-Kontakt. Kommerzielle Initiatoren die in der UV-Verkapselung eingesetzt werden haben sich durch ihre niedrige Zwei-Photonen-Absorption als ungeeignet für 2PP-Zellverkapselung erwiesen, und der Erfolg kürzlich entwickelter wasserlöslicher Zwei-Photonen-Initiatoren (2PIs) wie P2CK war bislang durch deren relativ hohe Cyto- und Phototoxizität begrenzt.

Das Ziel dieser Arbeit war die Konzeption neuer hocheffizienter 2PIs, die eine biokompatible 2PP-Zellverkapselung ermöglichen. Um die 2PI-Membrangängigkeit zu senken und die intrazelluläre Bildung freier Radikale und reaktiver Sauerstoffspezies (ROS) nach Laseranregung zu verhindern, wurde ein makromolekularer Hyaluronan-basierter Initiator HAPI entwickelt. Konfokalmikroskopie-Aufnahmen der 2PI-Autofluoreszenz zeigen, dass HAPI sich im Gegensatz zu niedermolekularen Referenz-2PIs nicht im Zellinneren anreichert. Obwohl HAPI im Vergleich zu P2CK eine geringere Cyto- und Phototoxizität aufweist, wurden nach 2PP-Verkapselungstests immer noch Zellschäden beobachtet. Eine zweite Strategie sollte die Bildung von ROS reduzieren, die in Nebenreaktionen entstehen welche mit dem langsamen, bimolekularen Elektronentransfer-Mechanismus konkurrieren, der für die Radikalbildung konventioneller 2PIs angenommen wird. Daher wurden photosplaltbare Verbindungen als 2PIs untersucht, die Radikale durch einen Mechanismus bilden, der dem biokompatibler kommerzieller UV-Initiatoren ähnelt. Das splaltbare Trichlormethyl-Triazin-basierte System 2BC agierte als effizienter 2PI, wurde jedoch aufgrund der Neigung zu unkontrollierbarer Polymerisation und übermäßiger Lichtempfindlichkeit nicht weiterentwickelt. Die Untersuchung splaltbarer Diazosulfonate führte zur Entwicklung von AS7, das exzellente Biokompatibilität aufweist und bei höchsten Schreibgeschwindigkeiten bis 1 m/s als effizienter 2PI wirkt. ASC/TERT1-Stammzellen die mit AS7 in methacrylierte Gelatine-Hydrogele 2PP-verkapselt wurden zeigten keine Anzeichen von Photoschäden und breiteten sich während einer 5-tägigen Beobachtungsperiode nach dem Strukturieren im Gel aus.

Danksagung

An dieser Stelle möchte ich mich herzlich bei allen bedanken, die ein Gelingen dieser Arbeit ermöglicht haben.

Mein besonderer Dank gilt Prof. Robert Liska für seine engagierte Betreuung und den Freiraum, den er mir sowohl beim Herangehen an die interessanten Aufgabenstellungen dieser Arbeit als auch bei der Mitarbeit an weiteren Forschungsprojekten gewährt hat.

Für die Erstellung der externen Gutachten danke ich Prof. Jürgen Stampfl vom Institut für Werkstoffwissenschaft und Werkstofftechnologie und Prof. Heinz Redl, Direktor des Ludwig Boltzmann Instituts für klinische und experimentelle Traumatologie.

Für die fruchtbare Zusammenarbeit bedanke ich mich bei meinen Bachelorstudenten Christina Schmidleithner und Zacharias Thiel, bei Peter Gruber, Marica Markovic, Agnes Dobos, Wolfgang Steiger und Prof. Aleksandr Ovsianikov vom Institut für Werkstoffwissenschaft und Werkstofftechnologie, bei Prof. Aliasghar Ajami von der Semnan Universität, bei Sergej Naumov und Prof. Tom Scherzer vom Leibniz-Institut für Oberflächenmodifizierung, bei Arnulf Rosspeintner und Prof. Eric Vauthey von der Universität Genf, bei Prof. Roman Dedic von der Karls-Universität sowie bei Anna Eibel und Prof. Georg Gescheidt-Demner von der TU Graz.

Weiters möchte ich mich bei all meinen Laborkollegen sowie dem nicht-wissenschaftlichen Personal des Instituts für Angewandte Synthesechemie bedanken, für ihre Hilfsbereitschaft, die angenehme und produktive Arbeitsatmosphäre, die angeregten Diskussionen sowohl chemischer als auch diverser anderer Sachverhalte, gemeinsame Konferenzbesuche und natürlich Freizeitaktivitäten, wo auch der Spaß nie zu kurz kam.

Größter Dank geht an meine Eltern Inge und Erich, und an Manuel, ohne deren geduldige und liebevolle Unterstützung über die vielen Jahre des Studiums hinweg mir dessen erfolgreicher Abschluss wohl kaum möglich gewesen wäre.

Ich danke Euch allen ganz herzlich!

Table of Contents

EXP

INTRODUCTION	1	
OBJECTIVE	21	
STATE OF THE ART	23	
RESULTS & DISCUSSION	29	
1. Macromolecular 2PI with hindered transmembrane migration	29	
1.1. Synthesis of precursor compounds	33	
1.1.1. Side chain linker strategy	33	
1.1.1.1. Attempted Synthesis of the precursor DBKA	33	
1.1.1.1.1. Synthesis of precursor monobenzylidene ketone 1	35	130
1.1.1.1.2. Synthesis of precursor aniline 2	36	131
1.1.1.1.3. Synthesis of precursor aldehyde 3	36	132
1.1.1.1.4. Synthesis of precursor DBK 4	37	134
1.1.1.1.5. Attempted conversion of DBK 4 to DBKA	38	
1.1.2. Central ring linker strategy	40	
1.1.2.1. Synthesis of precursor MCNK	40	
1.1.2.1.1. Synthesis of precursor DBK 5	41	135
1.1.2.1.2. Synthesis of precursor MCNK	42	137
1.2. Synthesis of the macromolecular 2PI	43	
1.2.1. Coupling of DBK precursor MCNK to HA	43	
1.2.2. Introducing a spacer on MCNK - extended precursor MGABA	47	
1.2.2.1. Synthesis of precursor DBK 6	48	138
1.2.2.2. Synthesis of precursor MGABA	48	140
1.2.3. Coupling of DBK precursor MGABA to HA	49	
1.2.4. Synthesis of low molecular weight HAPI from degraded HA and use of methyl- β -cyclodextrin to improve processability	51	142
1.3. Analysis of the macromolecular 2PI HAPI	54	
1.3.1. Photophysical properties	54	
1.3.2. Transmembrane migration	56	
1.3.3. Cytotoxicity assay	57	
1.3.4. 2PP direct cell encapsulation	59	
2. Cleavable 2PIs	64	
2.1. Cleavable 2PIs based on trichloromethyl-substituted 1,3,5-triazine	67	
2.1.1. Basics of trichloromethyl-substituted 1,3,5-triazines as photoinitiators	67	
2.1.2. Design of cleavable 2PIs based on trichloromethyl-substituted 1,3,5-triazine	69	
2.1.3. Quantum chemical calculations to predict cleavability of 2BC	72	
2.1.4. Synthesis of cleavable 2PI 2BC	73	
2.1.4.1. Synthesis of precursor amidine 7	75	144
2.1.4.2. Synthesis of precursor trichloromethyl triazine 8	75	145
2.1.4.3. Synthesis of 2BC and side product BC	76	146

2.1.5.	Analysis of the cleavable 2PIs BC and 2BC	78	
2.1.5.1.	Photophysical properties	78	
2.1.5.2.	2PP structuring tests	79	
2.2.	Cleavable 2PIs based on diazosulfones and diazosulfonates	85	
2.2.1.	Basics of cleavable azo initiators	85	
2.2.2.	Literature-known diazosulfones and diazosulfonates as cleavable 2PIs	87	
2.2.2.1.	Quantum chemical calculations to predict cleavability of AS1 and AS2	89	
2.2.2.2.	Synthesis of AS1 and AS2	91	
2.2.2.2.1.	Synthesis of precursor diazonium salt 9	91	149
2.2.2.2.2.	Synthesis of AS1	93	151
2.2.2.2.3.	Synthesis of AS2	94	152
2.2.2.3.	Analysis of the cleavable 2PIs AS1 and AS2	95	
2.2.2.3.1.	Photophysical properties	95	
2.2.2.3.2.	2PP structuring tests	97	
2.2.3.	Cleavable diazosulfone and diazosulfonate 2PIs with extended π -system and increased σ_{2PA}	101	
2.2.3.1.	Synthesis of diazosulfone and diazosulfonate 2PIs with extended π -system and increased σ_{2PA}	102	
2.2.3.1.1.	Attempted synthesis of AS3 and AS4 <i>via</i> diazonium salt 10	102	
2.2.3.1.2.	Attempted synthesis of AS5 and AS6	104	
2.2.3.1.2.1.	Synthesis of precursor tetrazonium salt 11	106	153
2.2.3.1.2.2.	Attempted isolation of AS5 and AS6	106	
2.2.3.1.3.	Synthesis of AS7	107	
2.2.3.1.3.1.	Synthesis of precursor tetrazonium salt 12	108	154
2.2.3.1.3.2.	Synthesis of AS7	109	156
2.2.3.2.	Analysis of the cleavable 2PI AS7	111	
2.2.3.2.1.	Photophysical properties	111	
2.2.3.2.2.	2PP structuring tests	113	
2.2.3.2.3.	Cytotoxicity assay	117	
2.2.3.2.4.	2PP direct encapsulation of human stem cells	119	
2.2.3.2.5.	Singlet oxygen formation	123	
2.2.3.2.6.	Attempted elucidation if the initiation mechanism <i>via</i> laser flash photolysis and CIDNP	125	
	EXPERIMENTAL PART	130	
	CONCLUSION	158	
	MATERIALS & METHODS	165	
	ABBREVIATIONS	175	
	REFERENCES	178	

Introduction

Tissue Engineering and Cell Encapsulation

The loss or failure of an organ or tissue is one of the most frequent, devastating, and costly problems in human health care. During the past three decades, scientists, engineers, and physicians have together created tissue engineering and regenerative medicine in an endeavor to provide functional substitutes for damaged tissue. The term regenerative medicine is often used synonymously with tissue engineering, although it more specifically often implies the use of stem cells as a cell source. Tools from a variety of fields have been applied to construct biological substitutes that can replace (or help regenerate) diseased and injured tissues, or can mimic tissues for diagnostic and research purposes.^{1,2}

The key components required for engineered tissues include:^{2,3}

- cells (differentiated cells or stem cells isolated from adult/embryonic sources)
- biocompatible scaffold materials (although scaffold free approaches have also been described)⁴
- biochemical signals (small molecules, polypeptide growth factors and nucleic acids) and physical signals (e.g. cyclic mechanical loading)
- bioreactors (providing desired conditions and external stimuli *in vitro*)

As the building blocks of biological tissues, cells play a critical role in tissue engineering. They can be isolated either from the patient receiving a therapy themselves (autologous cells) or from a different, suitable donor (allogeneic cells). Conventional approaches utilize the fully differentiated adult cell types that make up the target organ or tissue. This is problematic, as tissue engineering typically needs large numbers of cells, whereas the proliferation capability of fully differentiated adults cells is very limited, and furthermore, they tend to lose their phenotype or dedifferentiate during *in vitro* expansion.^{2,3}

An alternative cell source for tissue engineering are stem cells. Unlike other types of cells in the body, stem cells are unspecialized and capable of self-renewal for long periods, yet maintain their capacity to differentiate into multiple specialized cell types upon exposure to specific induction cues (pluripotency).³ Ethical concerns about the

use of human embryonic stem cells are a significant impediment for industrial adoption. However, recent advances have in part allowed the use of adult stem cells, induced pluripotent stem cells (iPS cells), and stem cells from placental and umbilical sources as feasible alternatives replacing embryonic cells.²

A key need for effective tissue engineering is the cellular environment that allows the cells to function as they do in the native tissue. Often the environment mimics some critical aspects of the *in vivo* setting through proper control of the materials and mechanical setting as well as the chemical milieu. Three dimensional (3D) scaffolds serve as temporary supports for cell growth and new tissue development. They are usually designed to serve at least one of the following purposes:^{2,5}

- cell attachment and perhaps migration
- retention and presentation of biochemical factors
- porous environment for adequate diffusion of nutrients, expressed products, and waste
- mechanical rigidity or flexibility

There are two main strategies in utilizing scaffolds for tissue engineering. Cells are either seeded onto prefabricated porous scaffolds, or the cells are directly encapsulated during scaffold formation. In the former strategy, a wide range of hydrophilic and/or hydrophobic precursors can be used, and the fabrication process may involve harsh solvents and/or reactants, as long as the final product is cell friendly. In cell encapsulation strategies, the process by which scaffolds form must be cytocompatible, so the number of suitable chemistries and formulations is limited. Direct cell encapsulation, however, offers several advantages:⁵

- often employable as injectable system with cells directly delivered *in vivo* to the site of interest as suspension in a liquid precursor solution
- directly curing the precursor solution at the site of interest leads to enhanced adhesion of the scaffold to adjacent tissue without requiring glue or sutures
- cell encapsulation supports higher initial cell loading and more uniform distribution / intimate cell-matrix contact compared to scaffold seeding⁶
- benefits automated tissue fabrication, since concomitant presence of cells during scaffold fabrication enables high throughput⁷

Hydrogels

Hydrogels are three-dimensional, cross-linked polymeric networks capable of absorbing large amounts of water, forming a gel that acts as a mechanical support and enables cell adhesion.⁸ They are an important class of scaffold materials due to their ability to mimic roles of the natural extracellular matrix (ECM) such as providing essential cues for cell adhesion and proliferation, while allowing the diffusion of nutrients, metabolites and growth factors.⁹

Hydrogels can be formed through a variety of gelation mechanisms, crosslinking polymer chains either by covalent, ionic, or physical bonds. Naturally occurring hydrogels are typically formed by either physical or ionic crosslinks. However, covalently crosslinked hydrogels are becoming more attractive due to better stability as well as tunability of mechanical properties and degradation. The crosslinked structure will largely dictate diffusion of ECM molecules newly synthesized by the encapsulated cells, and therefore, degradation of the scaffold should closely follow ECM synthesis and macroscopic tissue development (**Figure 1**).⁵

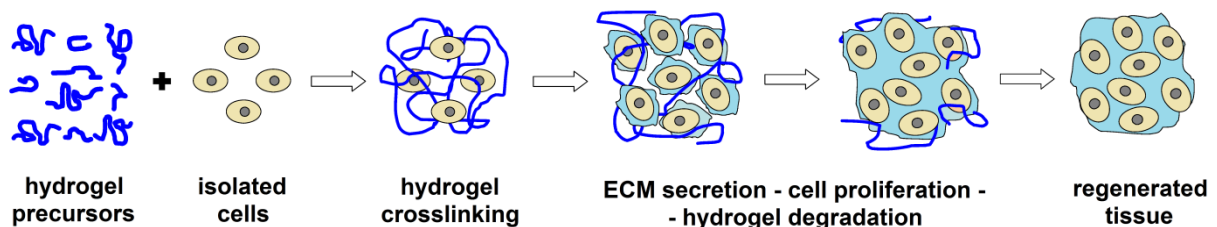


Figure 1: Schematic illustration of cell encapsulation *via* hydrogel crosslinking with subsequent tissue regeneration by ECM secretion and hydrogel degradation.^{5,10}

Besides the different gelation mechanisms, the hydrogel material itself and its need to be cell and tissue compatible are at the core of cell encapsulation.¹¹ Because cells are suspended in a liquid hydrogel precursor solution prior to encapsulation, the choice of precursors is limited to water-soluble components. Cell encapsulation strategies involving covalently crosslinked hydrogels typically employ macromolecular monomers (*i.e.* macromers, usually with molecular weight >3 kDa) derived from biocompatible polymers rather than low-molecular-weight monomers,

which are generally cytotoxic.⁵ Initial advances in extraction and preparation of ECM components led to an understanding of the material properties necessary to maintain cells *in vitro*. Naturally synthesized collagen and laminin, for example, were used to coat glass plates for tissue culture in the 1960s. This not only improved cell attachment, but also increased cell metabolism, proliferation, and viability.¹¹ While synthetic materials e.g. poly(ethylene glycol) can also be used, naturally derived polymers, such as fibrous protein based hydrogels from the ECM, provide not only the mechanical properties but the cell-ECM interactions necessary to regulate tissue development, differentiation, proliferation, and migration.¹²⁻¹⁵ The most abundant ECM components include collagen, HA and fibronectin, which have all been employed in tissue engineering constructs successfully.^{10,16,17} Gelatin, derived from collagen, exhibits excellent cell adhesion, biocompatibility and biodegradability.¹⁸⁻²¹ Since the natural physical gelation of gelatin is inhibited at physiological temperatures, its primary amine groups are modified with methacrylamide functionalities (methacrylated gelatin - gelMOD). This enables covalent crosslinking *via* radical photopolymerization, facilitating its use as scaffold material.²²

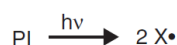
Crosslinking Mechanisms - Radical Photopolymerization

Several chemistries have been employed to facilitate the covalent crosslinking of hydrogels for cell encapsulation, with chemical crosslinking (usually step-growth polymerization) and radical chain polymerization being the most common mechanisms.⁵

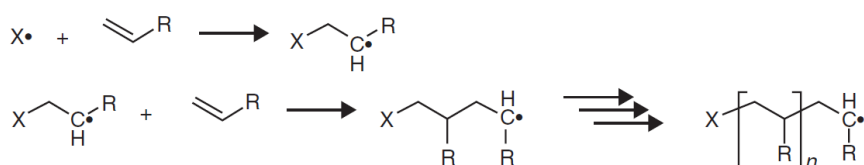
Chemical crosslinking mechanisms are attractive because they typically do not require additional components such as an initiator. However, the gelation rates are typically slower compared to radical chain polymerizations.⁵ Hyaluronan (HA) has been modified with thiol side groups, which form disulfide crosslinks in the presence of air. This mechanism was used to successfully encapsulate fibroblasts; however, the gelation process required several hours.²³ Alternatively, Michael-type addition reactions have been explored for cell encapsulation. These involve the reaction between nucleophilic thiolates as reactive thiol-species (usually slightly basic conditions required) and electrophiles such as unsaturated esters, forming thioether linkages at gelation times in the order of minutes.^{24,25}

In radical chain polymerization crosslinking, multifunctional macromers containing two or more unsaturated groups (e.g. (meth)acrylate or fumarate) are exposed to radicals formed by a suitable initiator. These radicals then propagate through multiple carbon–carbon double bonds to form high-molecular-weight kinetic chains, covalently crosslinking the network (**Figure 2**). Thermal,²⁶ redox,^{27,28} and photoinitiating conditions^{29–34} have been successfully used to encapsulate a range of cells. They are attractive because of fast polymerization, with gelation times the order of seconds to several minutes.⁵ Radical photopolymerization is particularly useful for the *in situ* formation of hydrogels as it provides unparalleled spatial and temporal control.³²

Initiation



Propagation



Termination

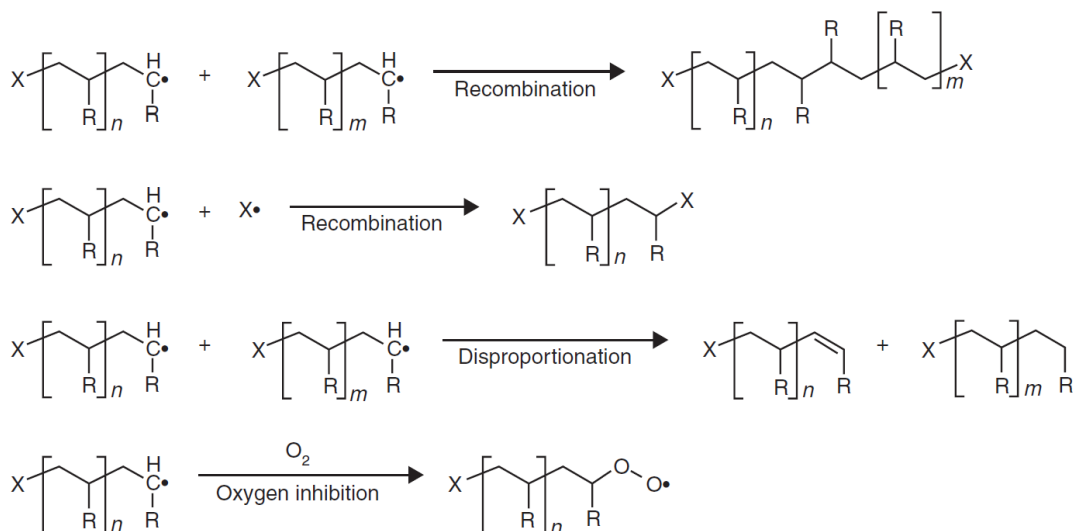


Figure 2: Mechanism of radical photopolymerization³⁵

Figure 2 shows the mechanism of radical photopolymerization in detail. The first step is the absorption of light ($h\nu$) by a key component of the photopolymerizable system - a suitable photoinitiator (PI) - and subsequent formation of initiating radicals. The radical then adds to the double bond of a monomer, turning it into a propagating

radical, which keeps adding to other monomers in multiple steps until no monomer is available or termination occurs. The modes of termination include the combination of two macroradicals or a macroradical with an initiating radical, disproportionation which produces a polymer with a terminal unsaturated group and a polymer with a terminal saturated group, and lastly addition of a macroradical to ground-state oxygen (required in the presence of cells) to form a peroxy radical with low propagating activity.³⁵

While radical photopolymerization allows cell encapsulation without significant cell settling due to the rapid reaction rates, and further benefits cells by avoiding high temperatures or extreme pH conditions,^{32,36} the presence of initiators (typically small, more or less cell permeable molecules) and the generated radicals, however, may be toxic to cells. Radical concentration will be dependent on several factors, including initiator chemistry and concentration, light intensity (directly affects radical concentration, ultraviolet (UV)-light is cytotoxic), and polymerization kinetics. Thus, the appropriate initiating conditions must be carefully considered to minimize exposure to potentially damaging PI molecules and radicals.⁵

Radical photoinitiating systems are broadly divided into two classes associated with their radical generation mechanism. Following excitation *via* light absorption, cleavable PIs (type I) dissociate into two or more radicals in a unimolecular reaction (**Figure 3**), while type II initiating systems abstract a hydrogen atom from a second, coinitiator species (**Figure 4**).³²

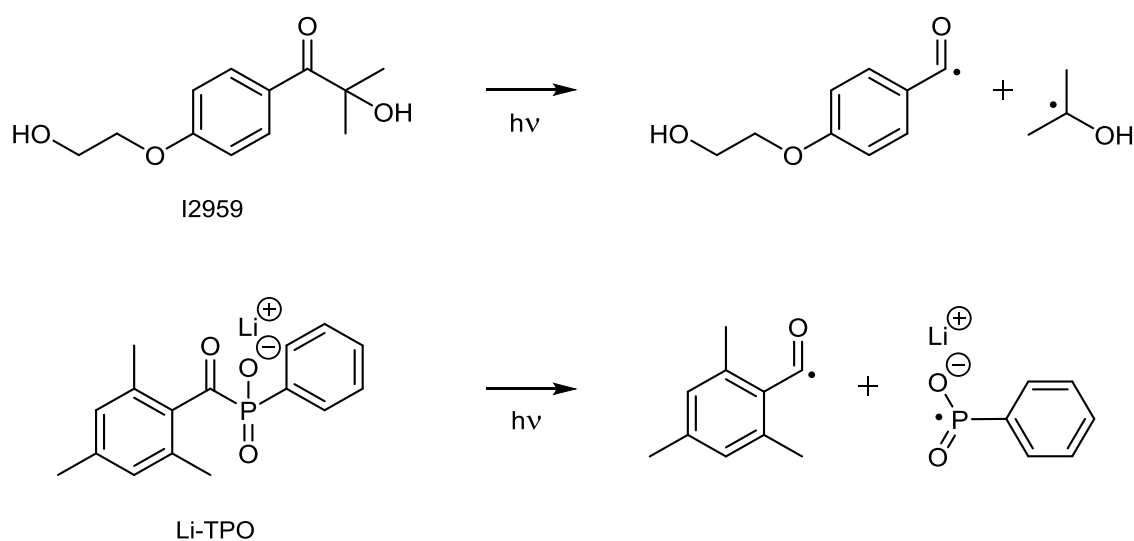


Figure 3: Radical formation of I2959 and Li-TPO *via* photocleavage.

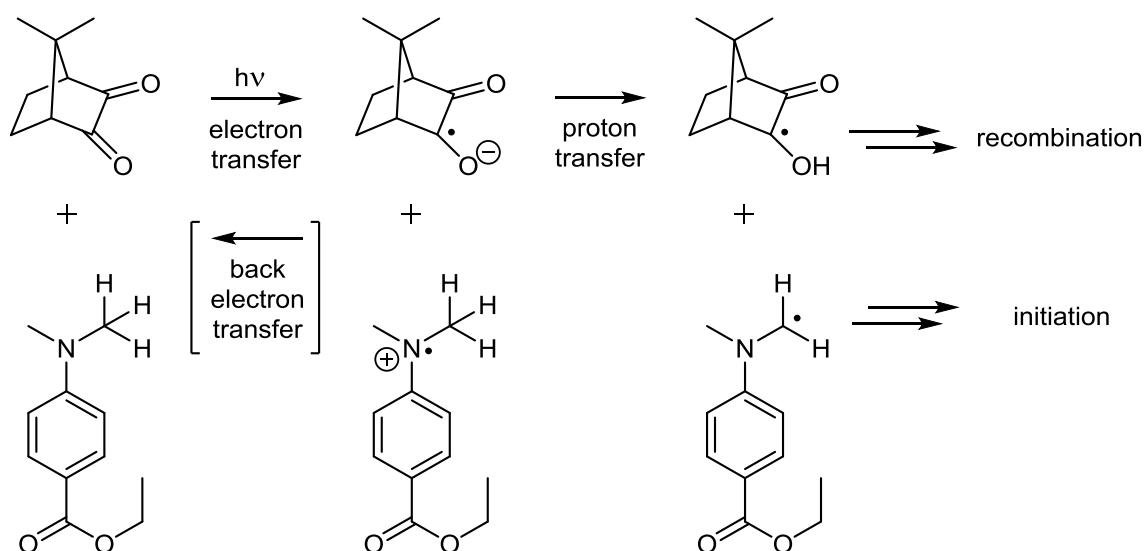


Figure 4: Radical formation mechanism of bimolecular system CQ-EDB via photoinduced electron- and proton transfer. Unwanted back electron transfer can reverse the first step and dissipate excitation energy.

The commercial cleavable UV initiator Irgacure 2959 (I2959, **Figure 3**) has been reported to exhibit relatively low cytotoxicity, and is one of the most commonly used PIs for biomaterials applications and cell encapsulation within hydrogels.^{30,32,37,38} Besides limited water-solubility (<2 wt%), a greater intrinsic shortcoming is its excitation wavelength below 360 nm, requiring the use of cytotoxic UV-radiation. The acylphosphinate Li-TPO (**Figure 3**) exhibits higher water solubility (up to 8.5 wt%), and enables cell encapsulations at lower initiator concentrations. Relative to I2959, polymerization rates with 365 nm wavelength light are increased, and absorbance above 400 nm also enables efficient visible light polymerization (more cytocompatible than UV-light).³²

Of the type II photoinitiating systems, camphorquinone (CQ)–amine combinations (e.g. CQ with ethyl 4-dimethylaminobenzoate (EDB), **Figure 4**) have been applied with some success in cellular photoencapsulation,³⁷ and Hubbell *et al.* have succeeded in employing Eosin Y (a fluorescent cellular stain) as a cytocompatible PI.^{32,39,40} In contrast to most cleavable initiators, the type II PIs CQ ($\lambda_{\text{abs}} = 470$ nm in EtOH)³⁷ and Eosin Y ($\lambda_{\text{abs}} = 470$ nm in water)⁴¹ offer the advantage of visible light absorption. However, without a coinitiator and often accelerant species they only inefficiently generate radicals to initiate photopolymerization, and their efficiency

suffers further from their bimolecular mechanism and the possibility of back electron transfer increased by the solvent cage effect in aqueous solutions.^{32,42}

Additive Manufacturing Technologies

Since they enable automated and reproducible production of complex 3D scaffold constructs from a variety of materials and in accordance to computer-aided design (CAD), additive manufacturing technologies (AMTs) have been widely used in tissue engineering and regenerative medicine as techniques complementary to cell encapsulation in simple hydrogel matrices without 3D structure.^{43,44}

Depending on scaffolding material and tissue engineering strategy, different processing techniques and methodologies have been proposed to optimize final scaffold performances in terms of external shape and size, surface morphology and internal architecture.⁴⁵ The most commonly used AMTs shall be briefly discussed here.

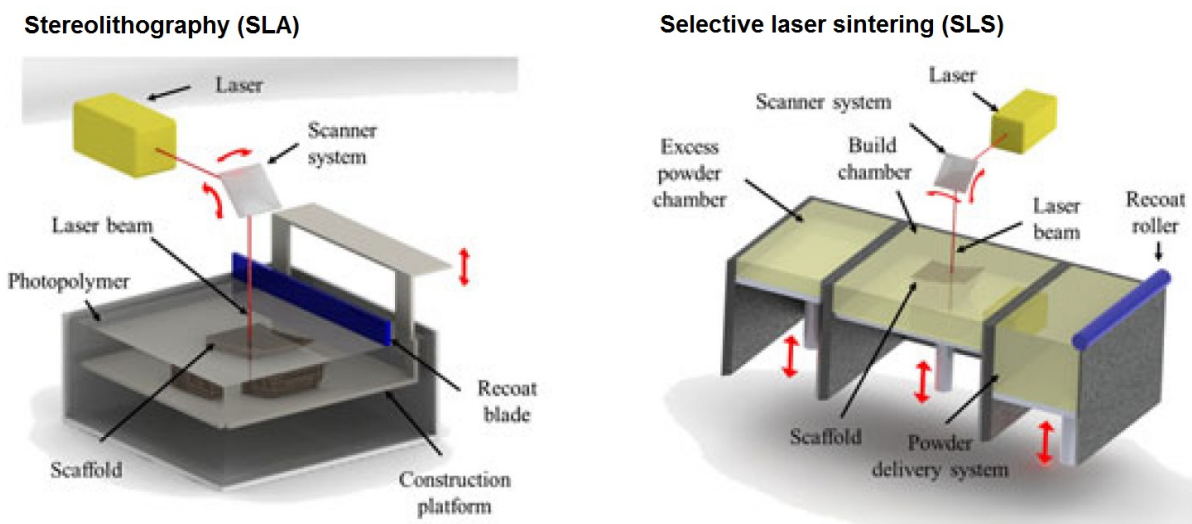


Figure 5: Schematic representation of stereolithography (SLA, **left**) and selective laser sintering (SLS, **right**).⁴⁵

Stereolithography (SLA, **Figure 5 - left**) is an AMT using a UV-laser to selectively photopolymerize a liquid resin, fabricating 3D objects in a layer-by-layer process. After the polymerization of a layer, the construction platform is lowered a given

distance and a recoat blade places a new uniform layer of resin on top of the previously built one. In order to prevent delamination between adjacent layers, the polymerization of a layer is carried out by overlapping a percentage of the previously built layer. Further processing steps after printing is finished include the removal of the non-polymerized resin and post-curing of the green part in order to improve polymerization between layers and to reduce surface irregularities.⁴⁵ At first, commercially available resins (epoxy- or acrylate-based) lacking biocompatibility and biodegradability and requiring toxic solvents were used. Examples include a porous orbital floor implant made from a slurry of hydroxyapatite in a liquid acrylic resin, where the organic components were thermally removed after SLA printing,⁴⁶ or porous scaffolds with a well-defined gyroid architecture fabricated from monoethyl fumarate-functionalized poly(D,L-lactide) and *N*-vinyl-2-pyrrolidone, that were successfully cultured *in vitro* with mouse pre-osteoblasts.⁴⁷

Selective laser sintering (SLS, **Figure 5 - right**) is based on the selective sintering of a polymer, ceramic or hybrid powder bed by a high intensity laser beam (e.g. CO₂ laser). Following the generation of a layer by selective particle bonding, a new powder bed is spread mechanically by a roller on top of the sintered layer, building up a cohesive 3D object layer-by-layer, with non-sintered areas serving as support for the subsequent layers.⁴⁵ Although studies using SLS generally aim for the production of scaffolds for bone tissue engineering (e.g. from hydroxyapatite or bioactive glass), the mechanical properties obtainable with this technique generally limit the application to non-loadbearing sites.^{48,49} A microporous polycaprolactone (PCL) scaffold intended for cardiac tissue regeneration was produced *via* SLS and successfully cultured with mouse myoblasts *in vitro*.⁵⁰ SLS has been developed primarily for industrial applications; there is only a very limited range of suitable biomaterial powders and their cost is high.⁵¹ Further concerns with the technique are the difficulty of eliminating the non-sintered material entrapped inside complex geometries, and the poor control over surface topography which is mostly defined by particle size and geometry.⁴⁵

In three-dimensional printing (3DP, **Figure 6 - left**), a binder material is deposited onto a powder layer in a controlled manner with an inkjet head. After the selective deposition of the binder, a new layer of powder is placed on top of the previous one (which acts as support for the object being built) with a roller and the binder

deposition process restarts. The construction platform containing the powder layer moves downward a distance equivalent to the thickness of the layer deposited after the fabrication of each layer. High production rates and the possibility of obtaining large-sized models at a low cost allow industrial applications.⁴⁵ 3DP has been used to produce tissue engineering scaffolds from polymeric, ceramic and composite powder materials.⁵² Kim *et al.* first reported the use of 3DP for tissue engineering, *in vitro* co-culturing hepatocytes and nonparenchymal cells on porous scaffolds made of poly(lactic-co-glycolic acid) with NaCl as the powder bed (leached out before cell seeding).⁵³ A patented 3DP technique known as TheriForm™ produces bone fillers made from β -tricalcium phosphate (TCP) as medical products.⁵⁴ Shrinkage of the scaffolds upon the sintering step is a major disadvantage of the 3DP technique and can cause distortions and fracture of the models.⁴⁵

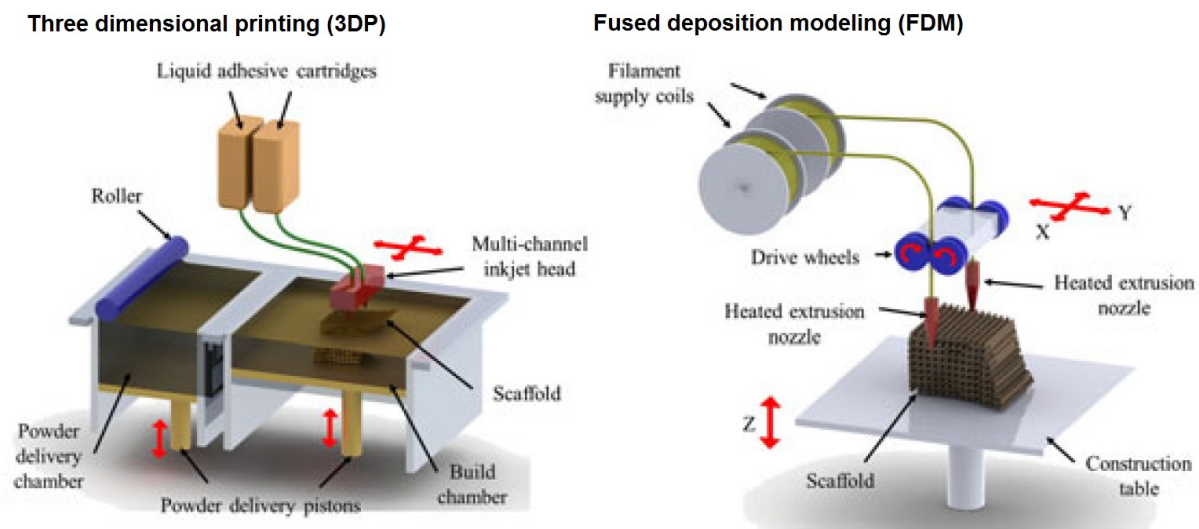


Figure 6: Schematic representation of three dimensional printing (3DP, **left**) and fused deposition modeling (FDM, **right**).⁴⁵

Fused deposition modeling (FDM, **Figure 6 - right**) is a commercially available AMT based on the extrusion of a polymeric filament through a heated nozzle. Two independent extrusion nozzles can be used to deposit different polymeric materials, one usually employed as a support material and the other to produce the 3D object. Drive wheels supply the polymeric filament to the extrusion nozzle, and the polymer melt is continuously deposited on a construction platform in a layer-by-layer process.

The motion of the extrusion head and of the construction platform allows for the deposition of the molten filament in a predefined pattern according to CAD.⁴⁵ Hutmacher *et al.* first explored the production of tissue engineering scaffolds by FDM with different pore architectures, pore sizes and porosities. PCL scaffolds were shown to support *in vitro* proliferation, differentiation and ECM production of primary human fibroblasts and periosteal cells.⁵⁵ After *in vivo* trials on surgically created defects in Yorkshire pigs model demonstrated new bone formation on FDM-fabricated PCL scaffolds,⁵⁶ similar scaffolds were approved by the FDA for craniofacial applications and are currently marketed in the form of thin interwoven meshes (Osteomesh™) or 3D implants (Osteoplug™).⁵⁷ Osteoplug™ scaffolds implanted into burr holes of 12 patients treated for a chronic subdural haematoma showed good osteointegration into the surrounding calvarial bone with no adverse events (mean follow up 16 months) in a study by Low *et al.*⁵⁸ Although its use is currently limited to a few thermoplastic polymers, the FDM technique has so far given very promising preclinical and clinical results.⁴⁵

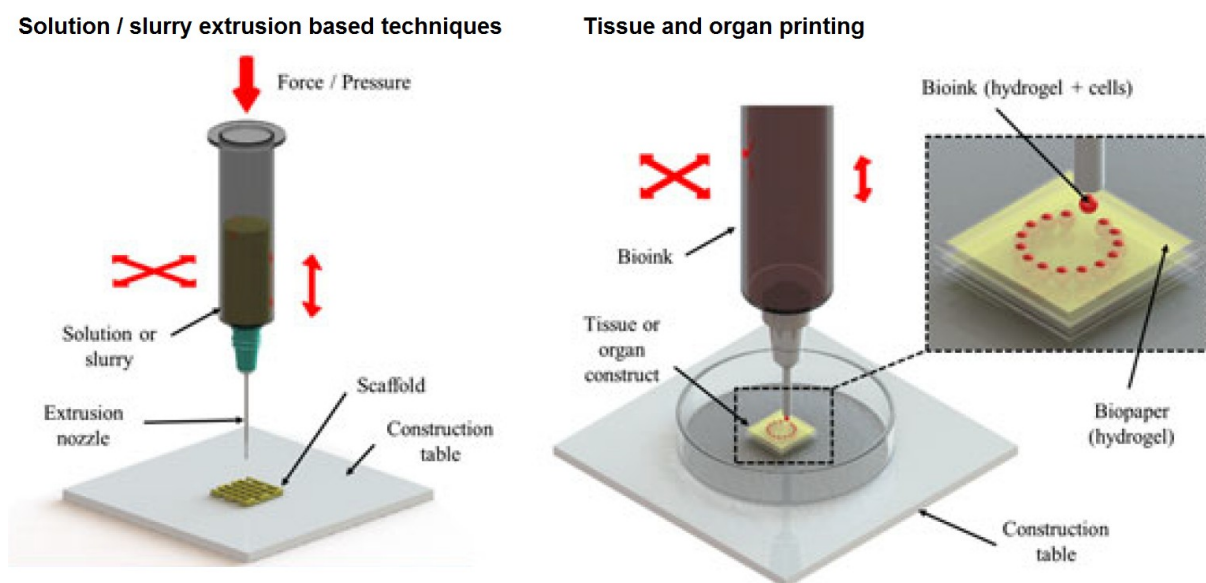


Figure 7: Schematic representation of extrusion based techniques (**left**) and tissue/organ printing (**right**).⁴⁵

In recent years, various AMTs based on the extrusion of a polymeric solution or ceramic slurry have been developed (**Figure 7- left**). In contrast to techniques such as SLS or FDM, they put little thermal stress on the processed materials, thus

avoiding concerns associated with temperature degradation of polymers and bioactive agents. However, they often involve the use of organic solvents that may compromise the biocompatibility of the scaffolds and alter the incorporated bioactive factors, if not removed completely.⁴⁵ Pressure-assisted microsyringe (PAM) is an AMT technique that combines a pressure-activated microsyringe equipped with a fine-bore exit needle with a micropositioning system to enable controlled deposition of an extruded polymeric solution. Its potential to fabricate 3D scaffolds from biodegradable polymers, such as PCL or poly(L-lactide) (PLLA) has been demonstrated.⁵⁹ Piston-assisted microsyringe (PAM2) was developed as a low-shear stress alternative system capable of direct extrusion of viscous hydrogel solutions containing cells (e.g. solutions of sodium alginate incorporating hepatocytes).⁶⁰ Low-temperature deposition manufacturing (LDM) deposits a polymeric slurry while maintaining low temperatures in a cooling chamber, with the solvent removed *via* freeze drying after the layer-by-layer fabrication of the 3D structure is finished. LDM-fabricated composite scaffolds (PLLA/TCP) showed good biocompatibility and bone regeneration during *in vivo* trials with implantation on canine radiuses.⁶¹ Robocasting (also called direct-write assembly) is an AMT capable of producing ceramic scaffolds with tailored geometry and porosity by extruding water-based, highly concentrated colloidal suspensions with minimal organic content through a nozzle into a non-wetting oil bath.⁶² Robocasting-produced bioactive glass scaffolds presented a compressive strength suitable for bone load-bearing applications,⁶³ and scaffolds made from hydroxyapatite and β -TCP loaded with an osteoinductive protein growth factor induced high amounts of newly formed bone *in vivo* in pigs.^{45,64}

Tissue or organ printing (**Figure 7- right**) employs automated technologies to produce cell-laden constructs, also taking advantage of the self-organizing properties of cells and tissues. cells and bioactive agents are deposited layer-by-layer in the form of self-assembling tissue building blocks, using hydrogels to form biopaper and/or biopink. Research activities dedicated to this approach have led to the development of laboratory-scale and commercially available manufacturing devices based on different organ biofabrication technologies, such as thermal or piezoelectric inkjet printing, 3D printing by mechanical dispensing of cells and laser assisted bioprinting.^{45,65} A thermal inkjet approach using a modified HP Deskjet to deposit aortic endothelial cells in combination with crosslinking calcium chloride into an

alginate solution demonstrated that that cells are able to attach and migrate in the printed microchannel architecture.⁶⁶ Piezoelectric drop-on-demand inkjet printing has been used to deliver suspensions of human fibroblast cells at high survival rates, however prolonged printing sessions can affect printing performance due to cell agglomeration or sedimentation inside the deposition cartridge.⁶⁷ Laser-assisted bioprinting uses laser pulses focused onto a metallic absorption layer that evaporates at the focal points, propelling a jet of cell-containing hydrogel precursor towards a lower collector hydrogel slide.⁴⁵ This allows printing cells and liquid materials with a cell-level resolution and thus high control over cell density and organization of 3D tissue constructs, and holds much promise to eventually fabricate tissue-like structures that have the physiological functionality of their native counterparts.^{68,69} Mironov *et al.* point out that developing just one robotic device - a bioprinter - is not sufficient to biofabricate human organs, but eventually automated robotic devices such as an automated tissue spheroid bioprinter, a suitable perfusion bioreactor, and non-destructive sensors/automated systems of quality control must be assembled to build an integrated organ biofabrication line.⁶⁵

Traditional AMTs have been explored to create 3D scaffolds with physiologically-relevant features to mimic the macroscopic architectures of repeating subunits on the length scale of 100–1000 μm found in tissues *in vivo*. As the understanding of the matrix biology goes deeper, there is a growing need to engineer the local microenvironment at a subcellular scale (1–10 μm) with biochemical, physical and cellular stimuli. Multiphoton microfabrication technologies show great promise to create ECM mimetic hydrogels with μm -scale resolution.⁴⁴

Two photon Induced Photopolymerization

Maria Göppert-Mayer first described simultaneous multiple-photon absorption in her doctoral thesis in 1931,⁷⁰ but even two-photon absorption (2PA) - the most probable case - remained mainly an intellectual curiosity until 1961, when Kaiser and Garrett demonstrated 2PA in a $\text{CaF}_2:\text{Eu}^{2+}$ crystal upon excitation with a continuous-wave ruby laser.⁷¹ With the advent of relatively simple, solid-state femtosecond (fs) lasers, such as titanium:sapphire (Ti:S) based systems capable of delivering extremely high peak intensities at low average laser powers (late 1980s),⁷² the interest in 2PA based technologies started gaining momentum.

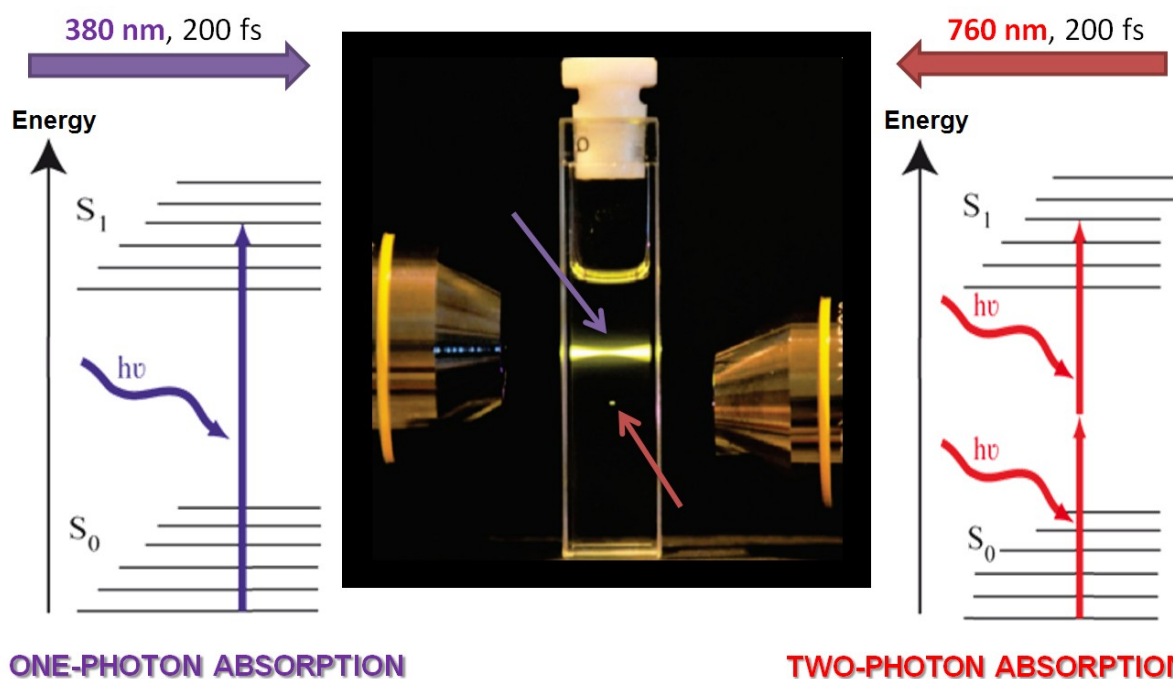


Figure 8: Simplified Jablonski-schemes and dye fluorescence illustrating differences between one- and two-photon absorption.⁷³

Figure 8 shows a dye solution exposed to two different fs-pulsed lasers focused through a microscope objective, illustrating the differences between one-photon absorption (1PA) and 2PA.⁷³ A UV-laser 1PA-excites fluorescence along its entire beam path in the dye solution, approximately following the well-known Beer-Lambert law. At sufficiently high laser intensities, an infrared (IR) laser can excite the dye by quasi-simultaneous absorption of two photons of twice the wavelength and thus half

the energy (see Jablonski-schemes, **Figure 8**) as the UV laser, causing 2PA excited frequency-upconversion fluorescence.

The following differential equation connects intensity I and the concentration c of the absorbing species with linear and non-linear absorption coefficients, α and β respectively, to describe the intensity $I(z)$ of a light beam with propagation in z -direction:

$$\frac{dI(z)}{dz} = -\alpha cI - \beta cI^2$$

In the case of 1PA the solution of this equation with the boundary condition $I(z=0) = I_0$ is the Beer-Lambert law. For 2PA with its extremely high light intensities the first (linear) term becomes negligible, leading to the following solution:

$$I(z) = \frac{I_0}{1 + I_0\beta cz}$$

A measure for the efficiency of a single absorber molecule to be excited in a 2PA process is the cross section σ_{2PA} :

$$\sigma_{2PA} = \frac{\hbar\omega\beta}{N_A c \cdot 10^{-3}}$$

Here, \hbar is the reduced Planck constant, ω the angular frequency of the absorbed photons, β the non-linear coefficient, N_A Avogadro's number and c the molar concentration.⁷⁴ A commonly used unit of σ_{2PA} is Göppert-Mayer (GM), with $1 \text{ GM} = 10^{-50} \text{ cm}^4 \text{ s photon}^{-1}$. The large scaling factor of 10^{-50} is introduced in order to obtain convenient values for common 2PA materials.

Attempts to design high σ_{2PA} compounds found that promoting factors are an extended π -conjugated core (π) of good co-planarity with various electron donor (D)- and/or acceptor (A) groups, because low-energy excitations with large transition and/or mesomeric dipole moments are thus introduced.⁷⁵ Furthermore, besides dipolar push-pull-systems, quadrupolar, octupolar (**Figure 9**) and more generally

multipolar 2PA chromophores (even dendritic and polymeric 2PA active compounds) are favorable, as higher order polarity introduces a higher chromophore density compared to dipolar structures.⁷⁶

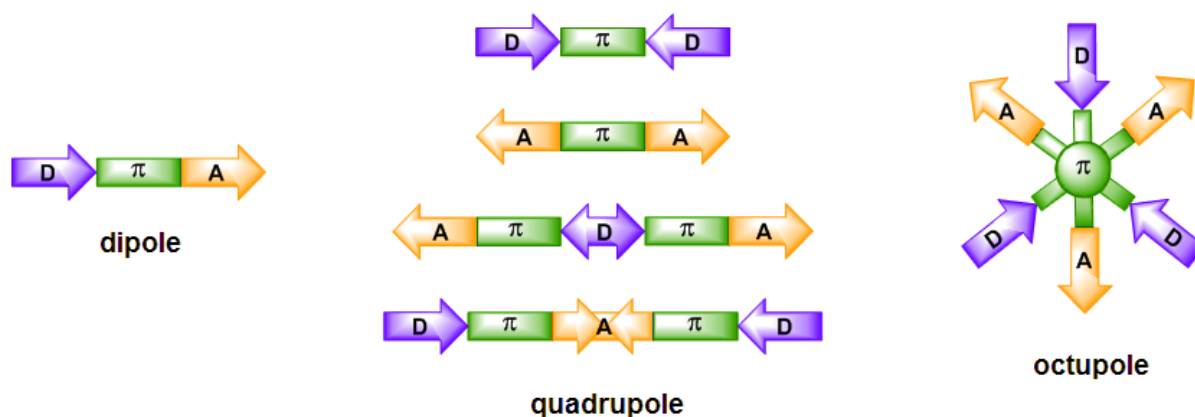


Figure 9: π -conjugated systems with polar moments of various orders, induced by donor (D) and / or acceptor (A) moieties.⁷⁷

Two-photon excited fluorescence (2PEF) and z-scan analysis are two methods currently used most often in literature to determine the σ_{2PA} value. 2PEF is a highly sensitive method requiring only minute quantities of dilute 2PA material solutions, however the method relies on reasonably strong fluorescence.⁷⁵ Z-scan (scan along the laser beam propagation direction) analysis also works for substances with extremely low fluorescence quantum yields - a desirable trait for 2PA photoinitiators (2PIs), as fluorescence is a loss channel dissipating energy away from radical generation - but requires rather high substance concentrations due to a lower sensitivity compared to 2PEF.⁷⁸ Dispersive white light continuum z-scan (WLC) is a method using a white light beam containing fs-pulses at wavelengths ranging from 600 nm to 950 nm to conveniently determine σ_{2PA} for all spectral components by performing a single z-scan.⁷⁹ Comparing measured cross sections with values from literature is usually problematic because the value is strongly dependent on the exact setup, experimental conditions and fitting calculations used, leading to different results for one and the same compound even if the same method is used.⁸⁰

The direct proportionality of 2PA to the squared light intensity has a consequence that can be taken advantage of in technology. As can be seen in **Figure 8**, the 1PA-excited fluorescence emission is observed along the entire hour-glass shaped beam

path in the cuvette, while the spatial distribution is completely different for 2PA induced fluorescence. The combination of a tightly focused laser beam and 2PA being proportional to the square of the light intensity allow only for a tiny "voxel" (volume element) of fluorescence around the very centre of the laser's focal point. This ability to induce photophysical and -chemical processes confined within a very small volume is employed in two-photon induced photopolymerization (2PP). If the focal point of a fs-pulsed laser is moved within a suitable formulation of monomers and PIs, the 2PA process allows for radical formation and "writing" of dots and lines with a high resolution down to ~60 nm, well below the diffraction limit associated with the wavelength of the laser.

Conventional SLA uses UV-lasers, where the 1PA of organic materials only allows shallow penetration so that 3D objects have to be fabricated in a layer-by-layer process applying new resin after each finished layer (**Figure 10 - left**, also see **Figure 5 - left**). 2PP allows true 3D free form fabrication, because common organic materials are highly transparent at the wavelengths of fs-pulsed Ti:S lasers (700-1000 nm) and the light can penetrate deeply into polymerizable resins (**Figure 10 - right**).^{81,82}

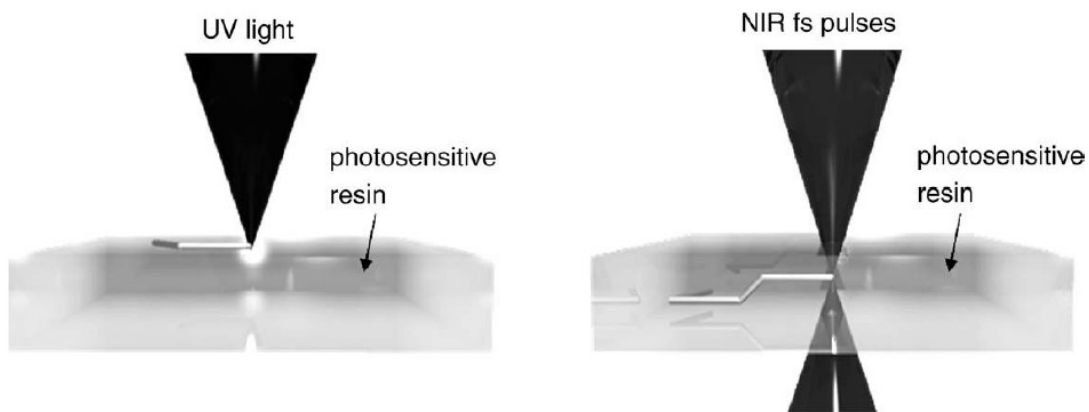


Figure 10: Comparison between one-photon polymerization (**left**) and two-photon polymerization (**right**).⁸¹

Because it enables true 3D printing with a resolution in the sub-micrometer range, 2PP has attracted considerable interest.⁸³ It has been used to fabricate parts containing ultra-small features such as photonic crystals,⁸⁴ optical waveguides,⁸⁵ micro-electronic^{86,87} or -mechanic⁸⁸ components, and scaffolds for tissue engineering.^{89,90}

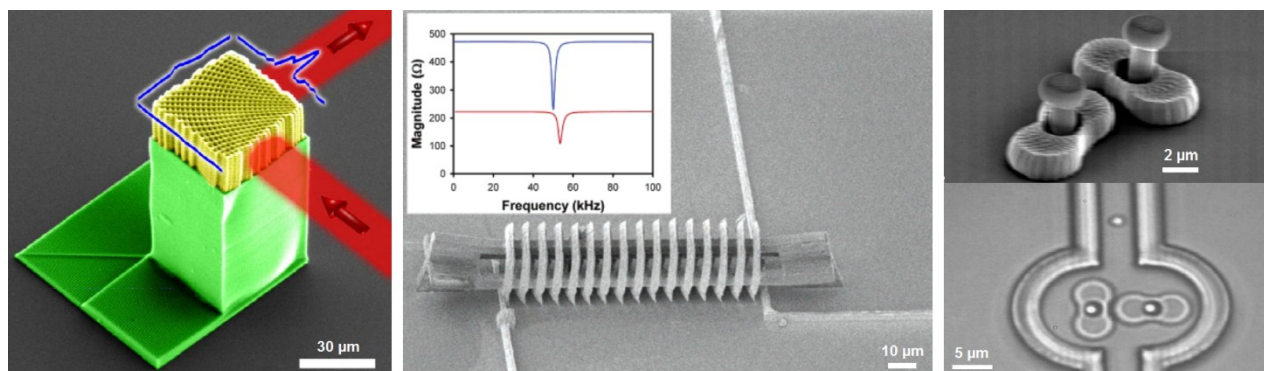


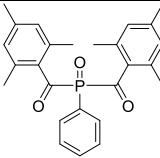
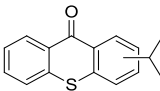
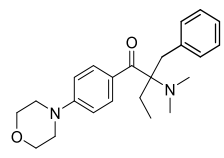
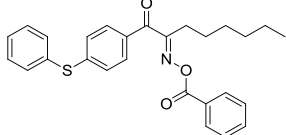
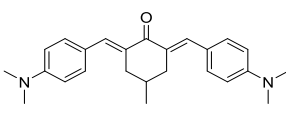
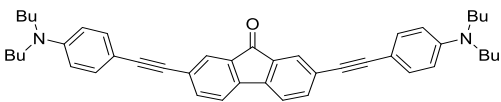
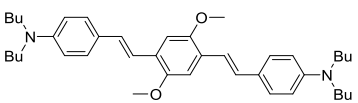
Figure 11: Examples for microdevices fabricated *via* 2PP: photonic crystal (**left**),⁸⁴ microinductor (**middle**),⁸⁷ and microfluidic pump (**right**)⁸⁸

Some examples from literature display impressive functionality of 2PP-fabricated microdevices that would be difficult to obtain with conventional techniques. 2PP was used to fabricate a three-dimensional spatially-variant photonic crystal (false-colored SEM image, **Figure 11 - left**), in which the orientation of the unit cell changes as a function of position, that directs the flow of light around a 90 degree bend while using low refractive index materials.⁸⁴ A functional 16-turn coil microinductor, with its inductive resistance depending on the frequency of the applied current, was created by selectively Cu-coating an acrylate polymer coil resting on a supporting structure composed of methacrylate polymer (**Figure 11 - middle**).⁸⁷ A lobed micropump, optically driven by means of time-divided scanning of a single laser beam, was able to create a liquid flow that moves a tracer particle at a velocity 0.2 - 0.7 $\mu\text{m/s}$ (**Figure 11 - right**).⁸⁸

Essential for obtaining high quality microstructures, as well as achieving high writing speeds, broad processing windows and low polymerization thresholds - all necessary preconditions for the industrial application of 2PP-processing - are the properties of the PI used to start the radical photopolymerization. Commercial one-photon initiators (1PIs) used in UV-light induced one-photon polymerization (1PP) of classical coatings have been and for practical reasons still are employed by some research groups by to generate microstructures *via* 2PP.^{91,92} However, due to their mostly inefficient 2PA expressed as a low σ_{2PA} ,⁹³ they suffer from limitations such as very narrow windows for ideal processing parameters and exceedingly slow achievable writing speeds. To overcome these limitations, compounds with high σ_{2PA} have been

investigated regarding their suitability as specialized, highly efficient 2PIs. An exemplary selection of commercial 1PIs investigated regarding their σ_{2PA} in a study done by Schafer *et al.*⁹³ is shown and compared to some specialized 2PIs from literature in **Table 1**.

Table 1: Organo-soluble commercial 1PIs and specially developed 2PIs, their 1PA maxima λ^{1PA}_{abs} , wavelength λ_{z-scan} used for z-scan and 2PA cross sections σ_{2PA} .

Compound	λ^{1PA}_{abs} [nm]	λ_{z-scan} [nm]	σ_{2PA} [GM]	
Irgacure 819 ⁹³		295	600	< 4
ITX ⁹³		382	760	5
Irgacure 369 ⁹³		324	670	7
Irgacure OXE01 ⁹³		328	660	31
M2CMK ⁹⁴		432	800	191
B3FL ⁹⁵		396	800	440
R1 ^{95,96}		425	800	328

The highest σ_{2PA} are usually achieved by multipolar push-pull-systems with electronic donor and acceptor groups connected *via* an extended conjugated π -systems of high co-planarity.⁹⁷ However, high σ_{2PA} alone don't guarantee high 2PI efficiency, as the energy of 2PA excited states can be dissipated *via* various other pathways competing with radical formation, such as fluorescence and phosphorescence, thermal relaxation, various isomerisation- and rearrangement-processes, and in case of systems with a bimolecular mechanism also back electron transfer. While there have been some attempts at rational design and increase of σ_{2PA} e.g. a study of Mongin *et al.* (**Figure 12**),⁹⁸ establishing reliable relationships between molecular structure and 2PI efficiency has remained a challenge as there are a multitude of factors involved, and the most efficient 2PIs up to now have been a result of serendipitous discovery.⁷⁵

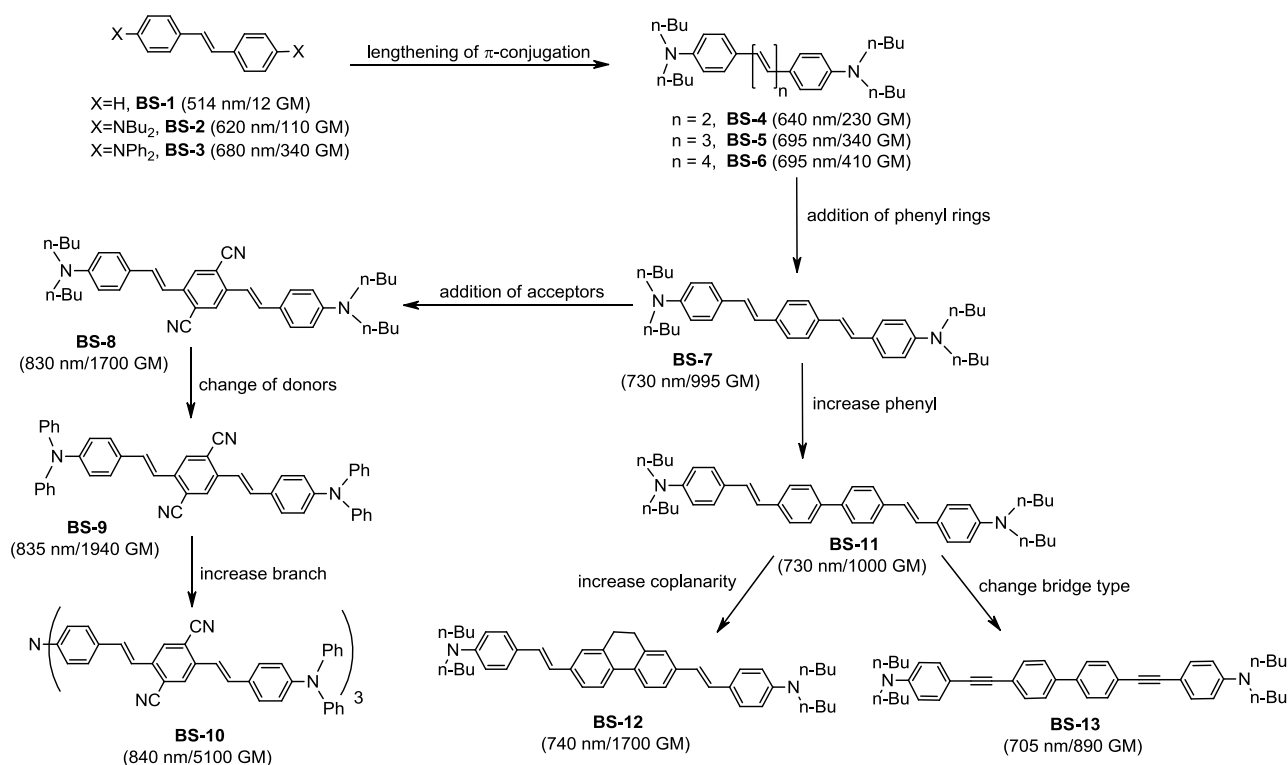


Figure 12: Schematic overview of a rational design process to increase σ_{2PA} values in brackets are the 2PA maxima and respective σ_{2PA} .⁹⁸

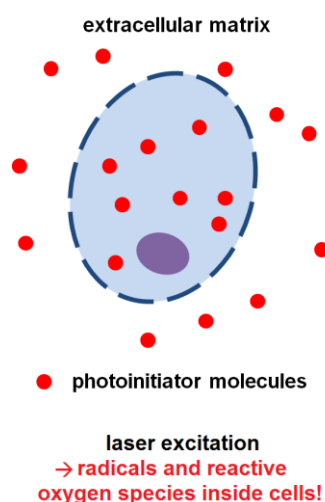
Objective

Tissue engineering approaches that aim to microengineer 3D cell cultures can mimic tissues on a small scale for diagnostic and research purposes, such as drug testing, or studying the effect of environmental cues on cell behavior. This approach is of great relevance, since conventional cell culture based on 2D matrices does not accurately reproduce the cells' natural environment and leads to significant differences in structure, function or physiology compared to living tissue.⁹⁹

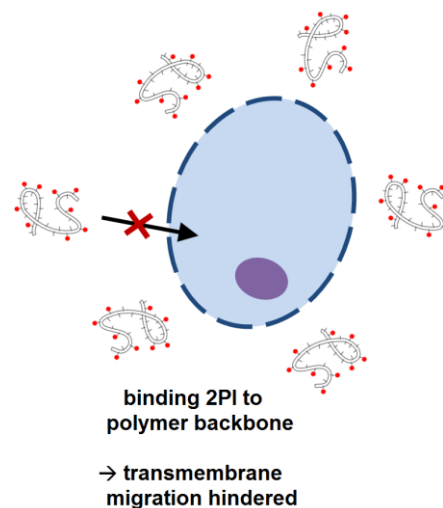
Two-photon photopolymerization (2PP) enables microfabrication in 3D with high spatiotemporal control and has been used to produce scaffolds for tissue engineering. While such scaffolds are usually pre-fabricated and then seeded with cells on the surface, direct cell encapsulation approaches are advantageous in regard to higher initial cell loading, more uniform cell distribution and a more intimate cell-matrix contact.⁶ While some success has been achieved with bacterial cell cultures, there is still a lack of studies demonstrating more sensitive cell types kept viable after 2PP encapsulation. Currently, limitations associated with the available photosensitizers and photoinitiators (PIs) used to start the covalent cross-linking processes of hydrogels are a major obstruction to progress in this field.

This thesis aims at developing novel specialized, highly effective two-photon initiators (2PIs) that enable a biocompatible 2PP cell encapsulation process. As a first approach, a macromolecular 2PI should be developed to hinder the migration of the photoactive compound through the plasma membranes inside cells, where they can otherwise directly generate toxic species upon photoexcitation.

small molecule 2PI

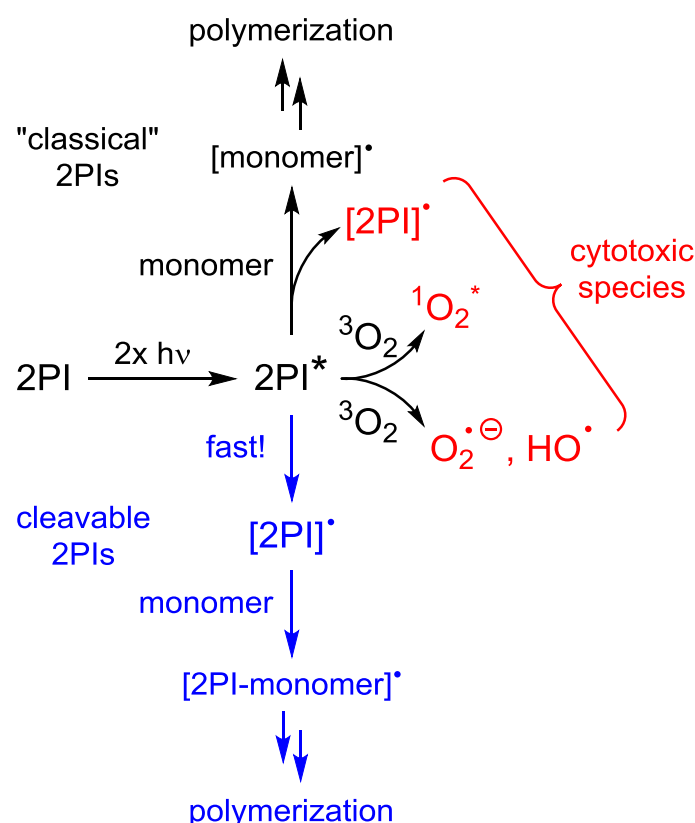


macromolecular 2PI



A further point to address is the bimolecular electron transfer-based radical generation mechanism that is assumed for "classical" 2PIs. The slow bimolecular mechanism favors side reactions such as the formation of toxic reactive oxygen species (ROS) e.g. excited singlet oxygen $^1\text{O}_2^*$, superoxide $\text{O}_2^{\bullet-}$ or hydroxyl radicals HO^\bullet . Furthermore, a cyclic mechanism is conceivable that would enable one 2PI molecule to be re-excited and form more toxic species after each cycle.

Commercial biocompatible PIs successfully used for UV-encapsulation of cells generate radicals through photocleavage. Thus, novel 2PIs with photolabile groups and suitable energy levels to facilitate rapid cleavage upon two-photon excitation should be designed. While the radicals necessary to initiate photopolymerization would still be generated, the photosensitized formation of toxic ROS could be greatly reduced with this approach.



State of the Art

While 2PP is not suitable for the fabrication of larger tissue constructs or whole organs since only very limited volumes can be processed within reasonable time frames, it offers tremendous spatial and temporal control to engineer microscopic tissue samples for diagnostic and research purposes (drug testing, studying cell behavior...). **Table 2** shows some of the water-soluble compounds that were used as PIs for 2PA-induced hydrogel crosslinking; the individual experiments are described further below.

Table 2: Water-soluble PIs used for the 2PA-induced crosslinking of hydrogels for tissue engineering applications.¹⁰⁰

Compound	σ_{2PA} [GM]	Reference
Rose Bengal	10	101
Benzophenone dimer	-	102
Irgacure 2959	-	103,104
WSPI	120	105
P2CK	136	6,106
E2CK	176	106

In recent literature, 2PP has mostly been employed for the pre-fabrication of 3D scaffolds that are subsequently seeded with cells, and a few attempts have been made to directly encapsulate cells within hydrogel matrices using the multiphoton technique.

Some examples from literature concerning the approach of pre-fabricating scaffolds and subsequently applying cells:

- Biodegradable scaffolds (enzymatic digestion by protease enzymes such as collagenase) were fabricated *via* selectively 2PA-crosslinking collagen using a modified benzophenone dimer as PI.¹⁰²
- Linear patterns were fabricated with different pitch widths (*i.e.* line separation) from either fibrinogen or bovine serum albumine (BSA) *via* 2PA-crosslinking with Rose Bengal. The purpose was to study the topographic factors and cell–matrix interactions that drive cell adhesion, spreading, differentiation, and proliferation. The morphology of human dermal fibroblasts was found to be guided by physical or geometrical factors with BSA and dominated by cell–matrix interactions in case of fibrinogen.¹⁰⁷
- A similar study engineered the mechanical properties of BSA micropillars as artificial stem cell niches by varying fabrication and reagent parameters during Rose Bengal-mediated 2PP-crosslinking. The reduced elastic modulus of the micropillars was determined *via* atomic force microscopy, and single cell traction forces of rabbit chondrocytes, human dermal fibroblasts, human mesenchymal stem cells, and bovine nucleus pulposus cells were studied.¹⁰⁸
- Primary neurons and fibroblasts were entrapped inside a cylinder fabricated from fibrinogen/BSA-mixture *via* 2PA-crosslinking with Rose Bengal.¹⁰¹ This was not a scaffold seeding approach, but by printing the hydrogel around cells, they were not directly exposed to the crosslinking conditions either.
- 2PP was applied to print precisely defined biodegradable 3D tissue engineering scaffolds from gelMOD, using Irgacure 2959 as PI. The scaffolds preserved their enzymatic degradation capability after photopolymerization,

and supported primary adipose-derived stem cell (ASC) adhesion, proliferation and differentiation into the anticipated adipogenic lineage (**Figure 13**).^{103,104}

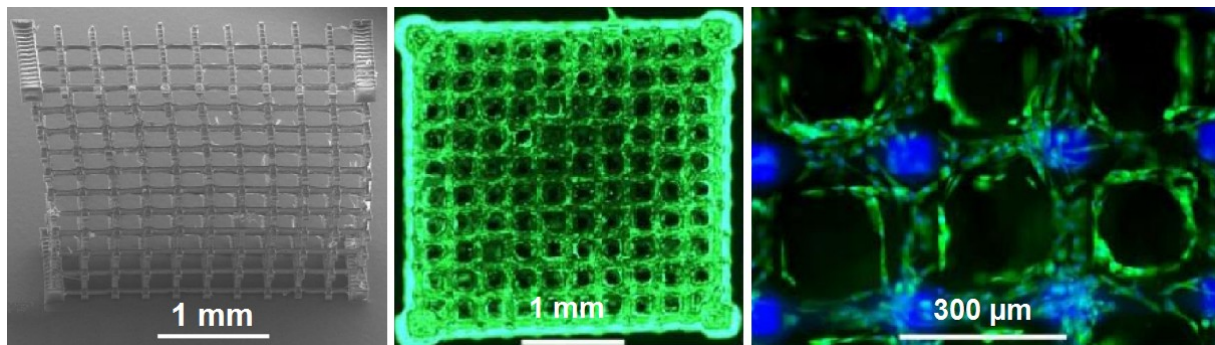


Figure 13: 3D scaffold from enzymatically degradable gelatin-based photopolymer gelMOD (**left**), seeded with adipose-derived stem cells stained green with calcein-acetoxymethyl ester (calcein-AM) (**middle and right**).^{103,104}

- A multicellular construct was engineered using laser-induced forward transfer (LIFT) to seed endothelial cells and smooth muscle cells precisely into a 2PP-prefabricated scaffold made from poly(ethylene glycol) diacrylate (PEGDA700) and Irgacure 369 as PI.¹⁰⁹

As previously mentioned in the introduction, in comparison to scaffold seeding, cell encapsulation *i.e.* directly fabricating hydrogel matrices around living cells has the advantages of supporting higher initial cell loadings, greater uniformity in cell distribution and a more intimate, defined cell-matrix contact.⁶ Furthermore, the direct encapsulation approach requires fewer processing steps and is therefore better suited for high throughput applications. However, because cells are present during scaffold fabrication, the process has far higher demands regarding the biocompatibility of printing process itself, and all materials and reagents involved. Only a few examples are described in literature where living cells were directly exposed to the conditions of the 2PP process:

- Within the human body, bacteria rarely reside as monocultures but within structured 3D communities composed of multiple bacterial species. *Staphylococcus aureus* and *Pseudomonas aeruginosa* are two opportunistic pathogens that coinfect tissues such as the lungs of cystic fibrosis patients or chronic wounds. Community attributes are believed to be mediated by

organization of individuals and populations within polymicrobial aggregates, affecting e.g. the virulence of infections. In research by Shear *et al.*, a BSA/gelatin "designer ecosystem" was 2PP printed around both suspended and settled bacteria, using Rose Bengal as 2PI. A single *S. aureus* cell was confined and grown into a clonal population in a spherical picoliter-sized BSA chamber that was free-floating in a *P. aeruginosa* culture trapped in a larger, fully enclosed, surface-attached box fabricated from gelatin. When the co-cultures were exposed to ampicillin, shells of even low-density cultures of *P. aeruginosa* produced enough β -lactamase to increase the survival of *S. aureus* to 80%, compared with a 40% survival rate without shells. Further experiments along these lines could provide insights into the underlying mechanisms involved in cellular communication and the onset of social behaviors between microbes within proximity to one another.¹¹⁰

- In the first attempt to encapsulate a larger living organism *via* 2PP, a nematode round worm (*Caenorhabditis elegans*) was immobilized in a poly(ethylene glycol) diacrylate gel scaffold using the highly efficient 2PI **WSPI** (Figure 14).

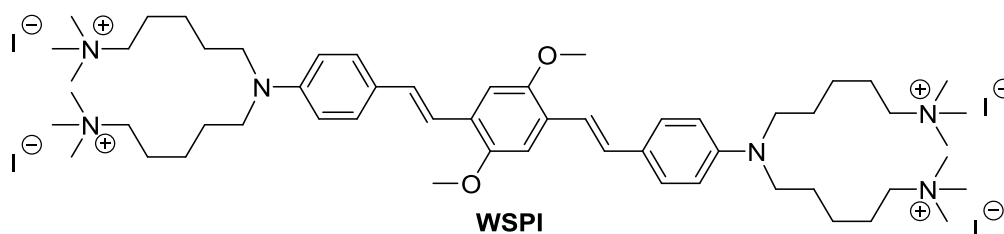


Figure 14: Specialized water-soluble 2PI **WSPI**.

While stable hydrogel structures could be obtained with water contents up to 80%, a less biocompatible ratio with 50% water content had to be used to effectively immobilize the moving worm for demonstration purposes.

The voxel was traced through the body of the animal, attaching the polymer lines to the cuticle, and firmly trapping it in the scaffold. Online video observation demonstrated that exposure to the focused beam or polymer formation around it did not trigger the animal to any specific reactions and thus did not seem to affect it. The movement of the worm, indicating its viability, was followed for 18 min after structuring.¹⁰⁵ Due to its elaborate 6-step

synthesis as well as issues with purification and storage stability, the use of **WSPI** was discontinued and no further tests with isolated cells were performed.

- Direct, multiphoton-excited crosslinking of cytoplasmic proteins was used to fabricate intracellular 3D structures in a live starfish oocyte. Photobleaching measurements determined that diffusion coefficients inside the structures were 2–3 orders of magnitude lower than in cytoplasm and 3-4 orders of magnitude lower than in free solution, and tunable by controlling the laser exposure. Such experiments could potentially be applicable to a broad range of problems in cell biology, e.g. exploring cytoskeletal dynamics or constructing channels and compartments to isolate cellular processes. Cell viability was not rigorously determined, but below a certain pulse energy/laser dose threshold the cells maintained their shape, while higher laser exposure resulted in gross distortions of cellular shape as well as leakage of the cytoplasm.¹¹¹

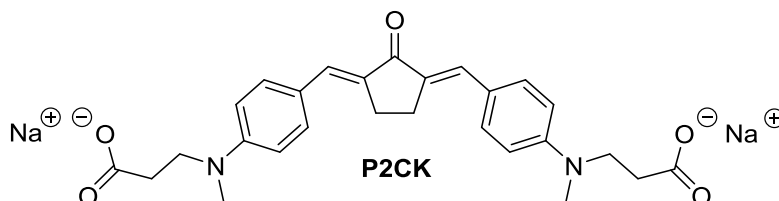


Figure 15: Specialized water-soluble 2PI **P2CK**.

- While the above-mentioned studies are focused on direct encapsulation of bacteria or lower animal cells, first attempts to explore the 2PP encapsulation of human cell cultures in dense hydrogel matrices have also been made. Human osteosarcoma cells (MG63) were encapsulated in 3D yin-yang constructs, consisting of a photosensitive hydrogel (methacrylated gelatin with up to 80% water content) crosslinked with the aid of specialized dibenzylidene ketone 2PI **P2CK** (**Figure 15**). Due to a custom 2PP printing system and the use of highly efficient **P2CK** ($\sigma_{2PA} = 136$ GM vs 10 GM for Rose Bengal), fabrication speeds of 7 mm/s could be achieved in this study. Many studies do not report the writing speed,^{110,111} however commercial systems such as the nanoscribe Photonic Professional work at speeds about 2 orders of magnitude lower, in the range of 100 $\mu\text{m/s}$.¹¹²

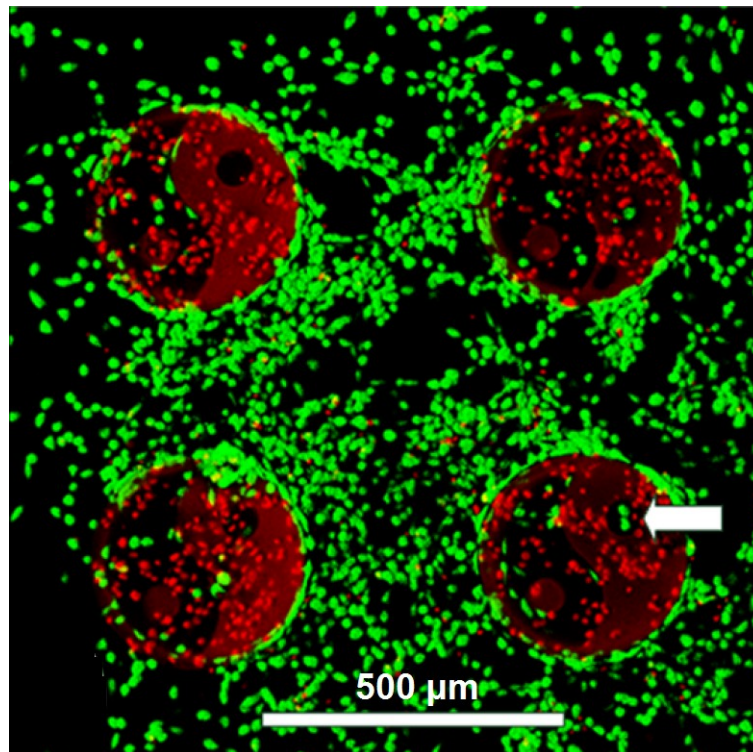


Figure 16: Viability 2PP encapsulated MG63 cells - green-stained live cells are found trapped in the cavities of the hydrogel yin-yang constructs (white arrow points to two live cells within a cylindrical cavity) as well as around the structures, while cells embedded in the material are indicated to be dead by a red stain.

After 2PP structuring, MG63 cells trapped within the cavities of the yin-yang structure (**Figure 16**) stayed viable and able to proliferate (stained green with "live"-stain cacleinAM), however the cells present in the hydrogel matrix directly within the laser exposure region were damaged or killed (stained red with "dead"-stain propidium iodide). Since control experiments demonstrated that the laser radiation itself does not damage the cells at the parameters used for encapsulation, it was concluded that the reactive species - such as free radicals and reactive oxygen species - produced during 2PP are the likely cause of the observed cell damage. While such cell-entrapping 3D constructs could be used as designer cellular microarrays to study the behavior of isolated cell groups and create 3D tissue models for drug discovery, stem cell research, and tissue engineering, the limited biocompatibility of the 2PP process using P2CK as 2PI is prohibitive.

Results & Discussion

1. Macromolecular 2PI with hindered transmembrane migration

Biocompatible classical PIs used in UV-encapsulation of cells such as I2959⁵ (**Figure 17**) have shown a lack of efficiency in 2PP based lithography, which has prompted the development of novel PIs more specialized for this field of application.⁴⁴ Among these are dibenzylidene ketone (DBK) based water-soluble 2PIs such as **P2CK** and **E2CK** (**Figure 17**),¹⁰⁶ which have proven highly efficient in the initiation of radical polymerization of hydrogel formulations based on acrylates, methacrylates as well as thiol-ene systems such as combinations of vinyl esters with multifunctional thiols.^{113–115} In this work, methacrylated gelatin (gelMOD, 97% of gelatin's primary amine groups converted to methacrylamide functionalities) is used as a photocrosslinkable hydrogel material, allowing a water content up to 90%. Cells readily bind to, proliferate, elongate, and migrate when encapsulated in microfabricated gelMOD hydrogels.¹¹⁶

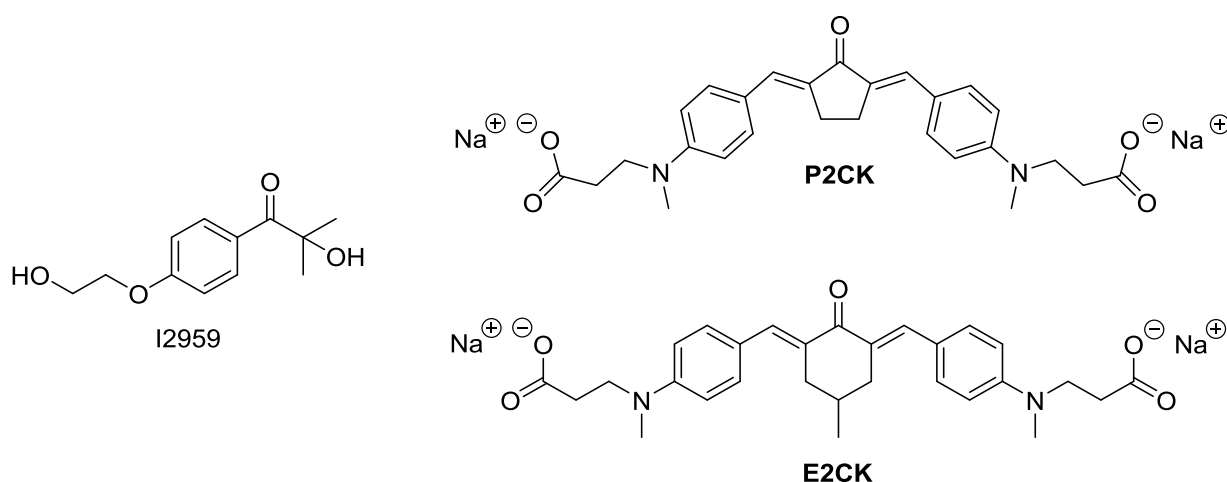


Figure 17: Classical UV-Initiator Irgacure 2959 and specialized water-soluble 2PIs **P2CK** and **E2CK**.

While **P2CK** enables 2PP printing of microscopic gelMOD-hydrogel structures with complex geometries at high fabrication speeds, living cells directly encapsulated within the structures show considerable damage and cell survival is poor. Cells that

had been in contact with the 2PI-containing material formulation but were not exposed to the laser, e.g. cells retained in the cavities of a yin-yang-structure, had significantly higher survival rates (**Figure 18 - left**). In control experiments, cells exposed to laser radiation at the same parameters as used in 2PP microfabrication but without the presence of a 2PI also did not exhibit the damage and poor survival observed in the 2PP encapsulated cells.⁶ These results demonstrate that the damaging effect on living cells in the 2PP encapsulation process is caused by phototoxicity of either the laser activated 2PI itself or a secondary reactive species generated by it.

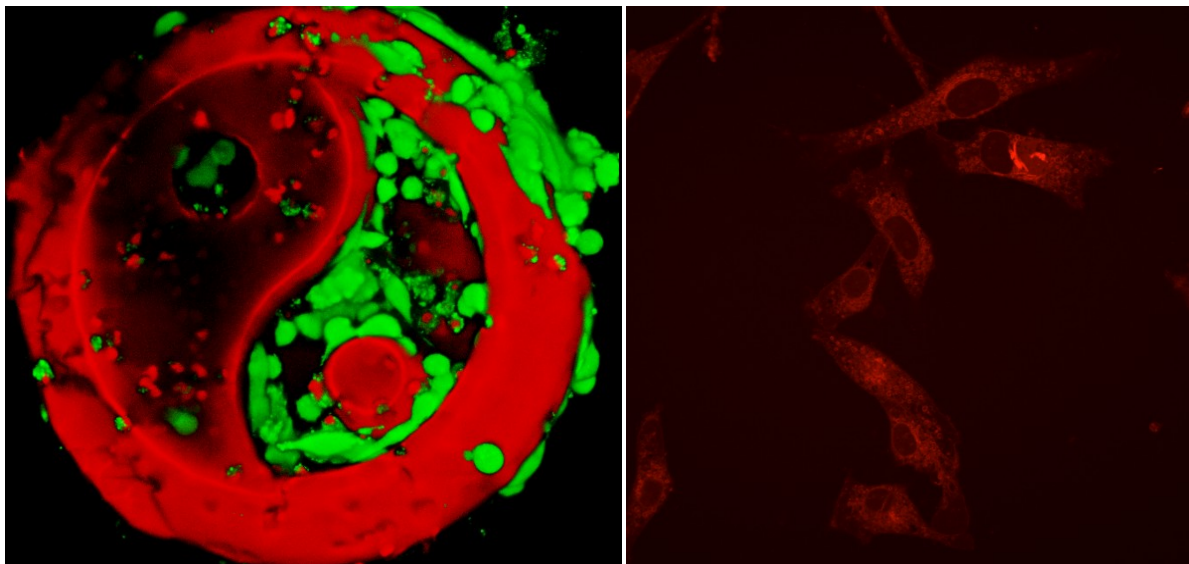


Figure 18: Cell containing 2PP-printed gelMOD hydrogel yin-yang-structure. Viability of MC3T3 cells is indicated by live/dead-staining. Viable cells, mostly found in the cavities of the structure, are stained green by calcein. The nuclei of cells with compromised membrane permeability, especially dead cells, are stained red by propidium iodide. The hydrogel itself also appears red due to the autofluorescence of residual traces of **P2CK**. (**left**); Viable MC3T3 cells incubated in **P2CK**-supplemented cell culture medium are stained due to 2PI uptake. Contrary to propidium iodide staining, the cell nuclei are not efficiently stained by **P2CK** and appear darker than other structures in the cell. (**right**)

It was hypothesized that due to the relatively small size and low molecular weight, 2PIs such as **P2CK** may pass through the cytoplasmic membrane and migrate inside cells. In order to test this hypothesis, **P2CK** was added to the culture medium of MC3T3 cells (0.1 mM final concentration) and laser scanning microscopy (LSM)-images were recorded after an incubation time of 5 min (**Figure 18 - right**). The autofluorescence that **P2CK** displays when excited by the 488 nm laser of the LSM allows the visualization of the 2PI entering and staining the cells. When the fluorescence of **P2CK** is observed using LSM settings designed for visualization of the calcein-AM/propidium iodide based live/dead-stain used in this work to assess the viability of cells,^{117,118} it passes the same filter in the microscope as the fluorescence emitted by dead-stain propidium iodide (excited by a 555 nm laser in the used setup) and thus appears in the red channel. A notable difference is that propidium iodide only enters cells when damage increases cytoplasmic membrane permeability, while **P2CK** also stains cells with intact membranes. Furthermore **P2CK** seems to mainly act as a stain for the cell membrane itself as well as organelles distributed in the cytoplasm, leaving the cell nucleus to appear relatively dark, whereas the DNA-intercalating propidium iodide almost selectively stains the nucleus.¹¹⁸ Since cells are essentially transparent for the near-infrared (NIR) light used in 2PP,¹¹⁹ 2PI molecules located inside the cells can be excited by the laser and cause photodamage by generating free radicals or reactive oxygen species (ROS) such as excited singlet oxygen $^1\text{O}_2^*$, superoxide $\text{O}_2^{\bullet-}$ or hydroxyl radicals HO^\bullet directly in the cytoplasm. Therefore, the use of a 2PI that does not easily enter cells is a promising approach to reduce the photodamage associated with 2PP direct encapsulation. To realize this goal, a straightforward strategy is to increase the 2PI size and molecular weight by linking suitable precursor such as a derivative of known and reliable 2PI systems like DBKs to a polymeric backbone, creating a macromolecular 2PI.

The most important features of a suitable material for the polymer backbone are sufficient water-solubility and high biocompatibility. Hyaluronan (HA) is a vital part of the natural extracellular matrix (ECM) of skin, cartilage, and the vitreous humor, and has been used in FDA approved biomedical products.^{120,121} Recently HA has also gained considerable interest as building block for the creation of novel bio-materials for tissue engineering and regenerative medicine applications due to its biofunctionality, as well as numerous sites for modification with reactive groups.^{122–124}

Several HA hydrogel systems have already advanced to clinical use in human and veterinary patients, particularly as dermal fillers, as intra-articular viscosupplements, for corneal and dermal wound repair, and for post-surgical adhesion prevention, among other uses.¹²⁴ Furthermore, the fact that HA is a highly negatively charged polycarboxylate poses an additional hindrance to migration through the cytoplasmic membrane, that also bears a net negative charge.¹²⁵ Thus, HA seemed ideally suited as a polymeric backbone for the creation of a water-soluble macromolecular 2PI with hindered transmembrane migration.

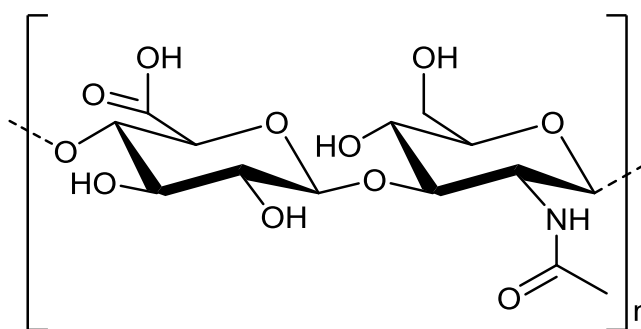


Figure 19: Structure of the repeating unit of HA

The two main functional groups of HA used for chemical modification in literature are the carboxyl and the primary hydroxyl group (**Figure 19**). Furthermore, a reactive amino group can be recovered by deacetylation of the N-acetyl group.¹²⁶ To choose a favorable approach, the properties of the precursor 2PI derivative to be linked to HA such as functional groups used for conjugation, solubility etc. should be considered. Contrary to **P2CK** and **E2CK** that were designed for good water solubility as carboxylate salts for their intended use, with a sufficiently low degree of substitution (DS) the water solubility of the macromolecular 2PI will be provided by the HA backbone, so that the DBK precursor itself does not need to be hydrophilic. While the carboxylic groups of *e.g.* **P2CK** itself could react with the hydroxyl groups of HA (or its amino groups after deacetylation), the difunctionality of **P2CK** poses a risk of crosslinking HA, leading to insoluble products. The free carboxylic acid forms of **P2CK** and **E2CK** also show very low solubility in organic solvents, so that a difficult purification of monofunctional carboxylic acid analogues may be expected. On the other hand, the carboxylic groups of HA could be reacted with functionalities on the

precursor 2PI such as hydroxyl or amino groups. Because of their generally higher nucleophilicity, amino groups would provide the benefits of better reactivity as well as chemoselectivity to avoid crosslinking *via* side reactions involving hydroxyl groups of HA. Furthermore, several methods for amidation of HA have been described in literature,¹²⁶ so that a monofunctional primary amine derivative of a DBK 2PI might be convenient to use as precursor.

Besides the functional group used for conjugation to HA, another property of the DBK precursor 2PI to be considered is the ring size of the central cycloketone. The cyclopentanone-based 2PI **P2CK** has been preferentially used in studies because a lower cytotoxicity in darkness compared to **E2CK** was demonstrated in the original publication comparing the two initiators. Moreover, **P2CK** can be obtained at higher yields (50% vs 30% for **E2CK**) and is purified more easily. Nevertheless, cyclohexanone-based **E2CK** poses the advantage of being a more efficient 2PI exhibiting larger ideal processing windows.¹⁰⁶ Due to the hindered transmembrane migration and reduced cellular uptake, the differences in cytotoxicity found with the small molecule DBK 2PIs are expected to play a less significant role in case of the macromolecular 2PI. Concerning potential phototoxicity and generation of ROS, a recent study investigated the relationship between the ring size of cyclic DBKs and the efficiency of ¹O₂-generation, attesting a quantum yield for the cyclohexanone-based system that was an order of magnitude lower than for the cyclopentanone-based compound (0.028 vs 0.26).¹²⁷ Thus, it was decided that the macromolecular 2PI should be based on a DBK precursor with a cyclohexanone central ring.

1.1. Synthesis of precursor compounds

1.1.1. Side chain linker strategy

1.1.1.1. Attempted Synthesis of the precursor DBKA

An obvious approach to obtain a monofunctionally substituted DBK is to use two different benzylidene substituents, one bearing the amino group used for linkage with HA. The lower symmetry of such a dibenzylidene ketone amine (DBKA) system is also expected to provide the side benefit of increased solubility compared to symmetrically substituted DBKs.¹²⁸ Since free primary amino groups can react under imine (Schiff base) formation with aldehydes and ketones employed as starting

materials in the condensation reactions to prepare DBKs, the amino group should be introduced after the DBK chromophore formation is complete to avoid unwanted side reactions. The complete synthetic pathway to obtain DBKA is depicted in **Figure 20**.

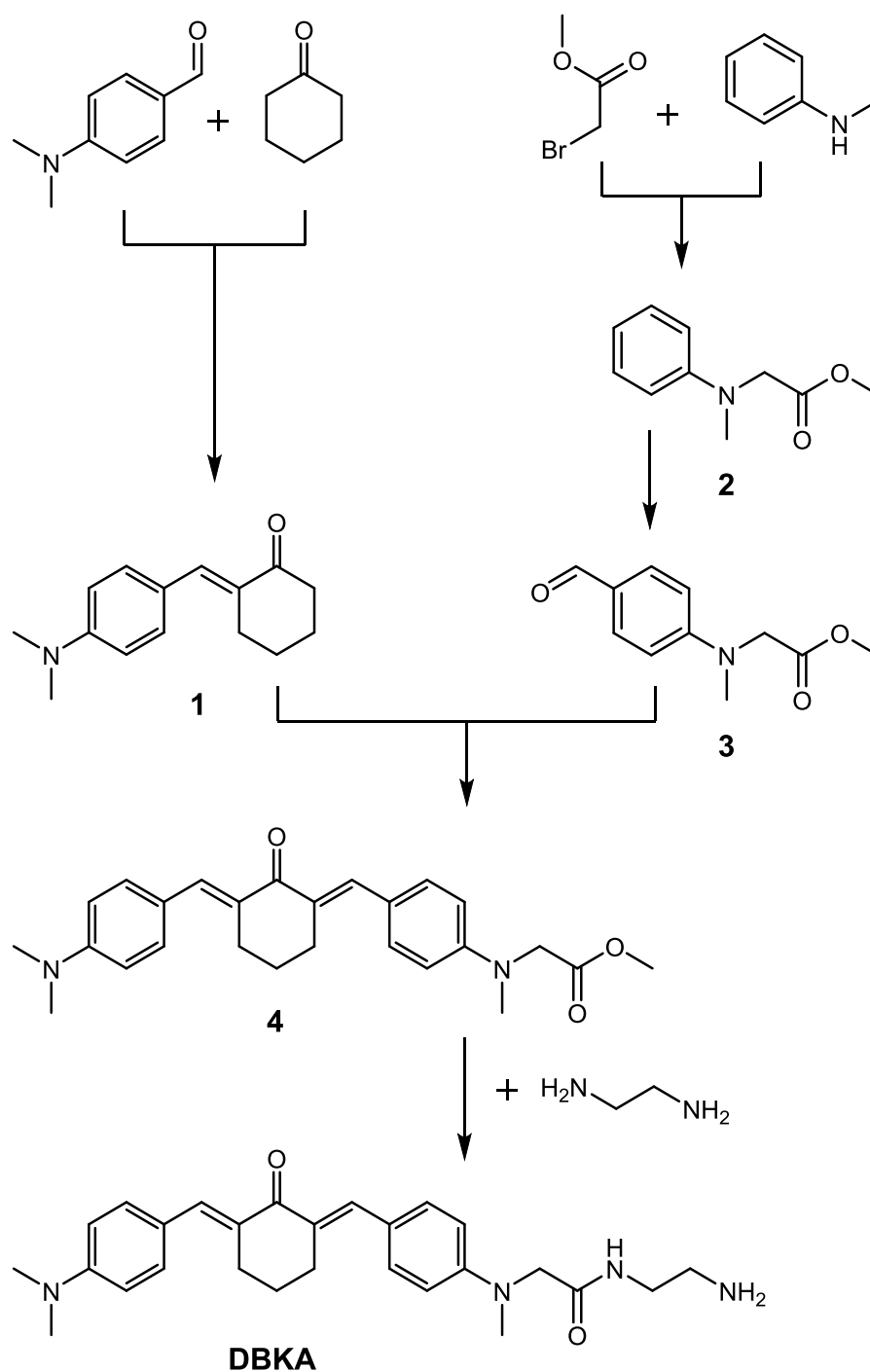
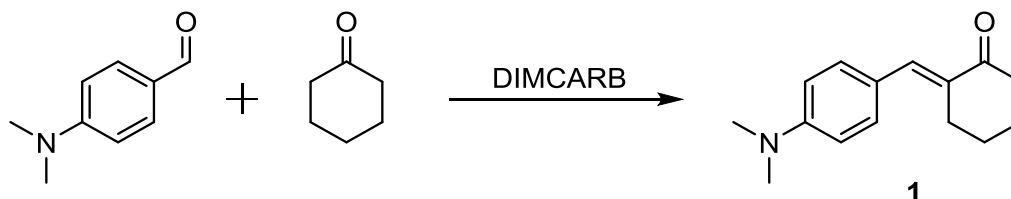


Figure 20: Synthetic pathway to DBKA

1.1.1.1.1. Synthesis of precursor monobenzylidene ketone **1**

As the first step in the synthetic sequence leading to **DBKA**, the required monobenzylidene ketone (MBK) **1** had to be prepared.

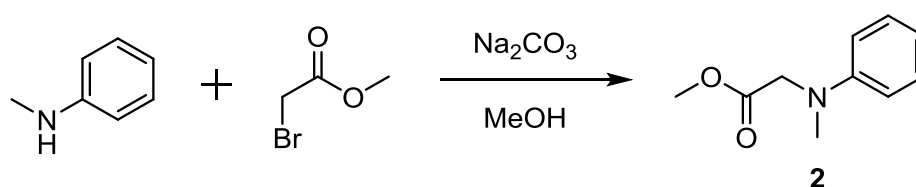


An approach to obtain a compound similar to MBK **1** was described in previous work.⁷⁷ In analogy to the original publication describing the use of DBK **M2CMK** as organo-soluble 2PI, the MBK used there was based on 4-methylcyclohexanone instead of cyclohexanone to crucially improve the solubility of the target 2PIs in acrylate based resins, which tend to be poor solvents for DBKs. Besides the effect on solubility, it was observed that the introduction of the 4-methyl substituent on the central ketone ring causes a significant drop in σ_{2PA} (191 GM for **M2CMK** vs 352 GM for the analogue without 4-methyl group), while not affecting one-photon absorption characteristics.⁹⁴ Since the solubility behavior of the macromolecular 2PI is largely determined by the hyaluronan backbone and the precursor solubility is expected to be more strongly influenced by the low symmetry of **DBKA** than a single central methyl group, unsubstituted cyclohexanone was used as starting material here to avoid potentially detrimental effects on σ_{2PA} . Previously, monobenzylidene ketones have been prepared *via* the same route as the corresponding DBKs, e.g. aldol condensation using KOH as catalyst and EtOH as solvent.⁷⁷ However, a drawback of this method is that even with an excess of ketone over aldehyde (e.g. a ratio of 2:1, in case of 4-methylcyclohexanone and 4-(dimethylamino)benzaldehyde higher excesses only marginally improve yields of the MBK product but make isolation and purification significantly more difficult) yields of the MBK are low and significant amounts of DBK are formed. This is most likely due to a higher reactivity of the MBK compared to the ketone starting material towards the aldehyde - the conjugated π -system present in the MBK expands mesomeric stabilization and thus increases formation of the enolate that acts as reactive intermediary in the first step of the aldol addition. A relatively novel method from literature makes use of the "distillable" ionic liquid dimethylammonium dimethylcarbamate (DIMCARB), which acts both as a solvent and catalyst in the formation of MBKs, and facilitates their direct preparation

with high selectivity in moderate to excellent yields.¹²⁹ By conducting the reaction between 4-(dimethylamino)benzaldehyde and cyclohexanone (1:1 ratio) in DIMCARB solution at 50°C and subsequent purification *via* column chromatography and recrystallization from n-hexane, MBK **1** was obtained in a yield of 59%.

1.1.1.1.2. Synthesis of precursor aniline **2**

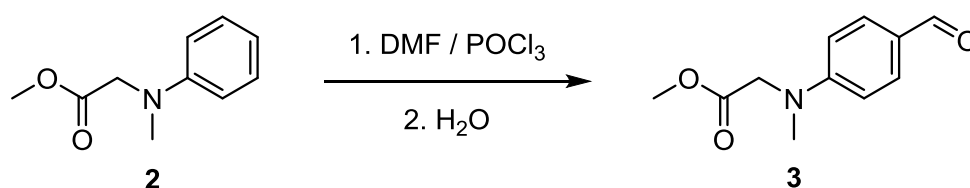
For the next step to introduce the second benzylidene substituent of **DBKA** used to attach the linker amino group, the ester substituted aldehyde **3** had to be prepared *via* another precursor, aniline **2**.



Aldehyde **3** has been used in the synthesis of DBK 2PIs before, and a suitable method for its preparation was described by Li *et al.*¹⁰⁶ in analogy to a procedure from literature for similar compounds.¹³⁰ First, the ester substituted aniline **2** was prepared by refluxing 1 equivalent *N*-methylaniline with 1.1 equivalents methyl 2-bromoacetate in MeOH, using 1.5 equivalents of solid Na₂CO₃ to trap the released HBr. After aqueous workup, pure aniline **2** was obtained at 87% yield *via* vacuum distillation.

1.1.1.1.3. Synthesis of precursor aldehyde **3**

Subsequently, the carbonyl functionality of aldehyde **3** was introduced to the para-position of aniline **2** in a Vilsmeier-Haack formylation reaction.

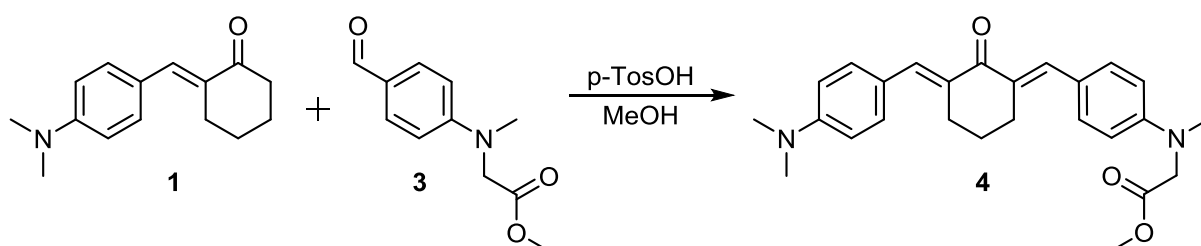


Dry DMF is treated with POCl₃ below 0°C to form a reactive chloromethyleneiminium salt, to which aniline **2** is added as DMF solution.^{131,132} Heating to 80°C for 3.5 h

leads to formation of an intermediary aryl methyleneiminium salt, which is finally hydrolyzed to the corresponding benzaldehyde **3**. Aqueous workup and recrystallization of the crude product from PE:Et₂O (4:1) afforded pure aldehyde **3** in a yield of 66%.

1.1.1.1.4. Synthesis of precursor DBK **4**

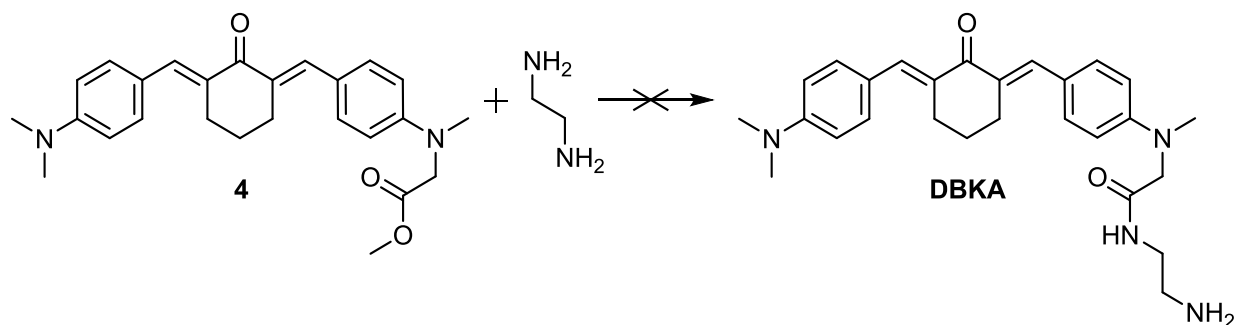
The second to last step in the sequence leading to precursor 2PI **DBKA** was the coupling reaction between MBK **1** and aldehyde **3**.



The direct coupling of aldehyde **3** with a cycloketone *via* base-catalyzed aldol condensation using excess NaOH in MeOH has been unsuccessfully attempted previously. The goal was to obtain a water-soluble DBK by performing the aldol condensation and saponification of the methyl ester groups in one step, however no DBK product was detected even with prolonged reaction times and adjustments to temperature and amounts of base.¹³² Besides the unsuitability of this approach because of its failure to yield a DBK product, the methyl ester group should be preserved here because it can further be directly substituted to introduce the linker amino group of **DBKA**. Thus, aldol condensation was attempted in dry MeOH under acidic catalysis, so that saponification was avoided and transesterification side reactions with the solvent still retain the methyl ester group. Para-toluenesulfonic acid (p-TsOH) used as a catalyst was obtained from a CHCl₃-solution of its monohydrate by removing water *via* azeotropic distillation and subsequent crystallization of the anhydrous compound.¹³³ Successful aldol condensation was observed by reacting a MeOH solution of 1 equivalent of MBK **1** with 1.2 equivalents aldehyde **3** in the presence of 0.2 equivalents p-TsOH as catalyst, stirring for 48 h at 55°C. The crude product precipitated spontaneously from the reaction mixture and was purified by recrystallization from EA, yielding DBK **4** at 77% of the theoretical amount.

1.1.1.1.5. Attempted conversion of DBK 4 to DBKA

For the final step in the sequence to the precursor **DBKA**, the methyl ester group in **DBK 4** should be amidated with ethylene diamine (using an excess to suppress the side reaction of linking together two molecules of **DBK 4**), in order to provide the free amino group functioning as linker required for further coupling to HA. However, several amidation strategies to obtain **DBKA** failed.



In the first attempt at this conversion, 1 equivalent of **DBK 4** and 3 equivalents of ethylene diamine were treated with 5 mol% NaOMe as a simple catalyst in dry toluene solution at a temperature of 50°C and under argon atmosphere, in analogy to a procedure for the direct amidation of esters developed by Oshima *et al.*¹³⁴ After 48h, TLC analysis (DCM:EA = 20:1) did not indicate the formation of **DBKA**, which should be well resolved from **DBK 4** due to its substantially higher polarity and thus lower R_F-value. Neither addition of higher amounts of NaOMe and ethylene diamine, nor raising reaction temperature to 80°C and prolonging reaction time up to 7 d helped improve this situation.

Another base-catalyzed approach for the amidation of esters published by Kim *et al.* makes use of KOt-Bu in THF, and claims full conversion of the ester substrate with short reaction times ranging from 5 - 60 min. Interestingly, Kim *et al.* found that only very low yields or trace amounts of amide were formed under water-free or oxygen-free conditions, and proposed a mechanism involving free radicals for the reaction that provided the highest yields when exposed to air and using moist THF (ca. 0.2% H₂O).¹³⁵ In accordance with the procedure, 2 equivalents of KOt-Bu were stirred in moist THF under air for 1 min, followed by the addition of 1 equivalent of **DBK 4** and 3 equivalents of ethylene diamine and continued stirring under air at room temperature. While **DBK 4** did not dissolve fully in the reaction mixture, the crystalline

orange solid changed its appearance during the reaction, becoming powdery and significantly lighter in color. In contrast to DBK **4**, the powdery solid was almost insoluble in EA and THF and showed much better solubility in alcohols such as MeOH, EtOH and iPrOH. TLC analysis (DCM:EA = 20:1) indicated full conversion of DBK **4** after 150 min, with the reaction product remaining at the starting line with this eluent mixture, and moving to an R_f -value ~ 0.5 when using DCM:MeOH:TEA = 20:1:1 as eluent. The reaction mixture was stripped of THF *in vacuo* and the solid residue partitioned between DCM and deionized water. It was noted here that not only the organic layer exhibited an intense orange color but the (due to the presence of ethylene diamine and KOt-Bu alkaline) aqueous layer as well, indicating the presence of a water-soluble DBK derivative.

Due to its free aliphatic primary amino group, **DBKA** is expected to be protonated in acidic solution and thus show increased water solubility, while the reverse is true for alkaline solutions. An aliquot of the aqueous layer was brought to pH ~ 11 with 1M aqueous KOH, but retained deep orange color even after multiple extractions with DCM. Another aliquot of the aqueous layer was adjusted to pH ~ 2 with 1M aqueous HCl, leading to the precipitation of a deep orange solid. An aliquot of the original DCM organic layer was washed with sat. NH₄Cl-solution and deionized water, then stripped of solvents *in vacuo*. The ¹H-NMR spectrum of the solid residue was almost identical in structure to DBK **4**, but with the signal of the methyl ester group at 3.73 ppm missing. It was concluded that the reaction did not lead to amidation as intended, but resulted in saponification of the ester group of DBK **4** and formation of the corresponding potassium carboxylate, which is also in line with the observed behavior of the reaction product precipitating upon acidification (reduced water solubility of the free carboxylic acid vs the carboxylate ion). While the publication by Kim *et al.* does discuss the formation of carboxylate and carboxylic acid side products when one equivalent or 10 mol% water are used, it claims high yields of amide products when using moist THF with $\sim 0.2\%$ H₂O.¹³⁵

Thus a third strategy was attempted. The successful enzymatic aminolysis of esters using lipase B from *Candida antarctica* (CAL-B) has also been described in literature. A strong dependence on solvent polarity is mentioned there, with more polar solvents such as MeCN and MTBE increasing yields and conversion rates compared to apolar solvents like n-hexane, cyclohexane or toluene.^{136,137} A solution of 1 equivalent of

DBK **4** and 3 equivalents of ethylene diamine in dry MeCN was stirred with CAL-B (immobilized on acrylic resin) at 25°C under Argon atmosphere. After 48 h, TLC did not indicate any conversion of DBK **4** to more polar products, and neither increasing the amount of ethylene diamine nor raising the reaction temperature to 50°C with prolonged reaction times lead to formation of the desired product **DBKA**.

1.1.2. Central ring linker strategy

1.1.2.1. Synthesis of precursor MCNK

Since several attempts to amidate of the ester substituted DBK **4** were unsuccessful, a different approach to obtain a suitable amino substituted DBK precursor for the macromolecular 2PI was considered. Instead of attaching the linker amino group to the side chain of a non-symmetrically substituted DBK, the central ring of a symmetrical DBK could also be used for that purpose. The introduction of substituents on the central ketone ring poses a risk of influencing σ_{2PA} disadvantageously, as was observed in the 4-methylcyclohexanone based 2PI **M2CMK** where the 4-methyl substituent was required due to poor solubility of the cyclohexanone based analogue (also see section 1.1.1.1.1. **Synthesis of precursor monobenzylidene ketone 1**).⁹⁴ However, there is an advantage regarding the synthetic procedure - when using a protected amino group in the cycloketone starting material in order to avoid imine formation side reactions, just one deprotection step is required after DBK formation *via* aldol condensation to obtain the amino functionalized precursor 2PI, while in the attempted synthesis of **DBKA**, the linker amino group was to be introduced in the last step of a lengthy sequence to avoid unwanted side reactions or more elaborate protection group strategies. The tert-butoxycarbonyl (Boc)-group is used extensively in peptide and heterocyclic synthesis for amine protection, and is not readily hydrolyzed under basic conditions.¹³⁸ Thus it is well suited as protective group during base-catalyzed aldol condensation. A suitable cycloketone, 4-(tert-butoxycarbonylamino)cyclohexanone (Boc-CNK), is even commercially available. **Figure 21** depicts the synthetic pathway to the amino-substituted precursor 2PI **MCNK**.

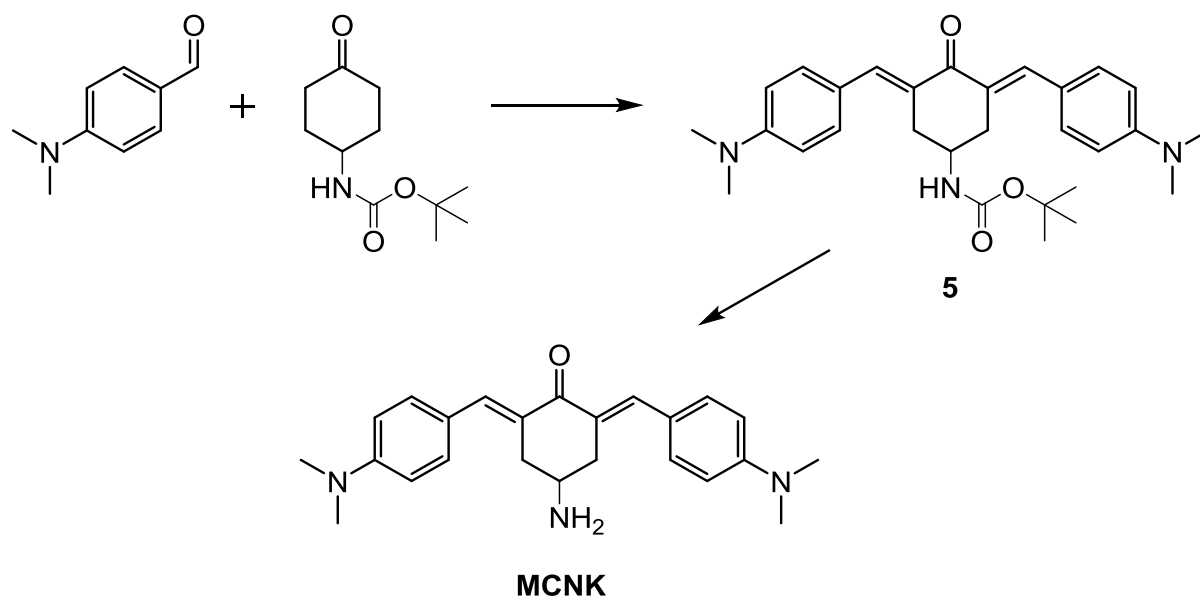
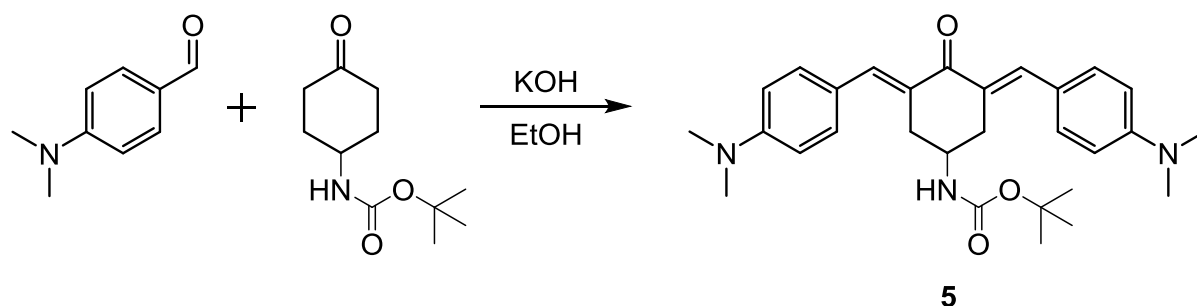


Figure 21: Synthetic pathway to **MCNK**

1.1.2.1.1. Synthesis of precursor DBK 5

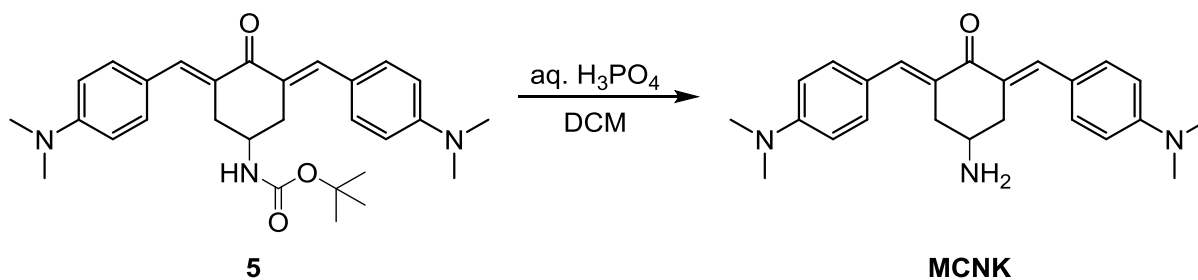
The first step of this sequence was the formation of a DBK 2PI chromophore system *via* classical aldol condensation under alkaline catalysis, resulting in the protected amine DBK 5.



A solution of 2 equivalents of 4-(dimethylamino)benzaldehyde and 1 equivalent KOH in EtOH was added to 1 equivalent of the cycloketone Boc-CNK also dissolved in EtOH, and stirred at 55°C for 24 h. The precipitation of the product started during the reaction and was completed afterwards by cooling to 4°C for 24 h to increase the yield. The precipitate was washed with cold EtOH and dried *in vacuo*. The protected amine DBK 5 was thus obtained as orange powder in a yield of 76% of the theoretical amount, with NMR-analysis indicating sufficient purity to be directly used for the next reaction.

1.1.2.1.2. Synthesis of precursor MCNK

The cleavage of the Boc-group for deprotection is commonly achieved by using strong mineral acids or trifluoroacetic acid in various solvents.¹³⁸ Here, a mild approach using aqueous H₃PO₄ was chosen,¹³⁹ as DBKs have been previously observed to form intensely blue or green colored side products when exposed to strong acids.⁷⁷



For the deprotection step, protected amine DBK **5** was suspended in DCM and treated with excess H₃PO₄ (85% aqueous solution), forming a biphasic system and leading to a visible evolution of gas (CO₂ and isobutene). The reaction mixture was subjected to vigorous magnetic stirring at room temperature to ensure effective and constant mixing of the phases. After 3 h, DBK **5** had fully dissolved and reacted, leaving a clear, slightly yellowish organic phase and a bluish grey aqueous phase containing protonated species of the product. The aqueous phase turned intensely red upon dilution with deionized water, and adjusting of the pH to ~9 with aq. NaOH led to precipitation of the product as red solid as well as white lumps of phosphate salts. Extraction of this aqueous reaction mixture with DCM with subsequent drying using Na₂SO₄ and stripping of solvents *in vacuo* yielded 95% of the theoretical amount of **MCNK** as crystalline orange flakes.

1.2. Synthesis of the macromolecular 2PI

1.2.1. Coupling of DBK precursor MCNK to HA

Following the successful preparation of the amino substituted DBK precursor **MCNK**, a suitable protocol for covalent linking of **MCNK** to HA should be chosen to complete the final synthetic step towards the hyaluronan-based macromolecular 2PI. Several approaches for the amidation of HA have been described in literature, based on coupling reagents that activate the carboxylic groups of HA such as 1-ethyl-3-[3-(dimethylamino)-propyl]-carbodiimide (EDC), 2-chloro-1-methylpyridinium iodide (CMPI), 2-chloro-dimethoxy-1,3,5-triazine (CDMT) or 1,1'-carbonyldiimidazole (CDI).¹²⁶ Amidation using EDC is performed in water as solvent and is very delicate due to a strong pH-dependency, with the optimal pH for EDC activation between 3.5-4.5 and amide formation being efficient at high pH,^{126,140} while **MCNK** is only water soluble in strongly acidic solutions. A similar problem prohibits the triazine-activated amidation using CDMT, since it is performed in a mixture of water and acetonitrile (3:2) found capable of dissolving both hyaluronic acid and CDMT,^{126,141} but not **MCNK**. Literature suggests that the CMPI-activated amidation is mainly suitable for crosslinking HA with multifunctional amines, since the CMPI-activated HA also forms ester crosslinks with its own hydroxyl groups (to be avoided at all cost to ensure good solubility of the macromolecular 2PI), and was thus not further considered.^{126,142}

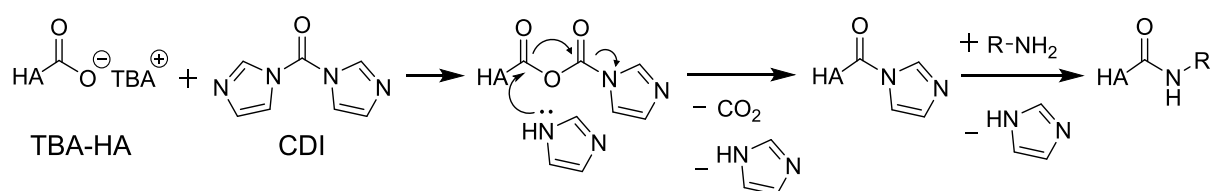
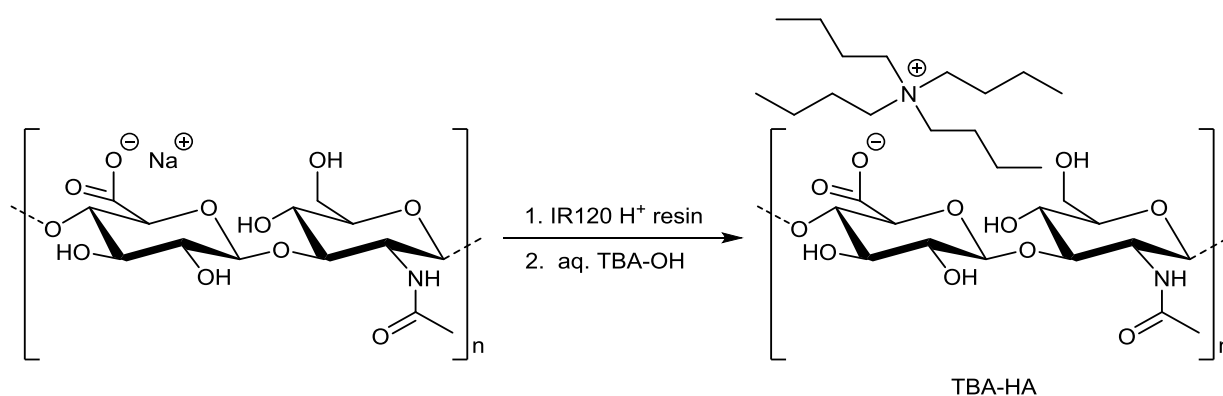


Figure 22: Mechanism of CDI-mediated amidation of HA¹²⁶

The CDI-mediated amidation of HA is performed by first reacting the tetrabutylammonium salt of HA (TBA-HA) with CDI in DMSO under acidic catalysis and subsequent addition of the amine.^{126,143} In contrast to aminolysis, alcoholysis of the intermediate acylimidazole is relatively slow and requires heating as well as strong bases as catalysts,¹⁴⁴ so that undesired auto-crosslinking reactions of HA can be avoided by conducting the reaction at room temperature. **MCNK** is well soluble in DMSO and furthermore only simple, non-toxic side products (CO₂ and imidazole) are

released,¹⁶ making this a very suitable amidation protocol. A schematic representation of the mechanism of HA-activation with CDI and the subsequent amidation step is depicted in **Figure 22**.

As a starting material and polymeric backbone for the macromolecular 2PI, bacterial HA from *Streptococcus equi* with an average molecular weight (M_n) \sim 1.6 MDa was used. The commercially available sodium salt first had to be converted to TBA-HA to achieve sufficient solubility in DMSO for the amidation procedure. TBA-HA was prepared according to a protocol described by Burdick *et al.*,¹⁴⁵ by stirring a 1 wt% solution of HA-sodium salt in deionized water with a sulfonic acidic-based ion exchange resin (Amberlite[®] IR120, hydrogen form, 3 weight equivalents) for 3 h, removing the resin beads *via* suction filtration and neutralizing the filtrate to pH 7.1 with tetrabutylammonium hydroxide solution (TBA-OH, 1M in MeOH). Freeze-drying of the neutralized filtrate yielded 95% of the theoretical amount of TBA-HA as a fluffy, fibrous solid.



For the coupling step, TBA-HA was stirred in dry DMSO until a homogenous solution was obtained. A degree of substitution (DS) of 10% of the repeating units of HA bearing the 2PI was aimed for, as low DS would necessitate the introduction of excessive amounts of HA into formulations for 2PP-printing to achieve the required 2PI-concentrations, while high DS may adversely affect the solubility of the macromolecular 2PI. Since literature¹⁴³ reports 5% amidation when using 0.1 equivalents of CDI per equivalent of HA-repeating units and 15% amidation at 0.2 equivalents of CDI, 0.15 equivalents of CDI were added to the TBA-HA solution together with 7.5 mol% of methanesulfonic acid (MsOH) as a catalyst. After 18 h of stirring under argon atmosphere, 0.3 equivalents of **MCNK** were added and stirring continued for another 24 h. The reaction was then quenched by adding saturated

aqueous NaCl-solution, followed by acetone that effects precipitation of the HA-bound **MCNK**. Residual free **MCNK** as well as excess reagents and side products of the reaction (imidazole, TBA-Cl,...) are removed by repeated washing of the precipitate with acetone and subsequent separation *via* centrifugation. For the final purification, the washed precipitate is dissolved in deionized water, dialyzed against deionized water and freeze-dried to obtain the HA-bound **MCNK** as foamy orange solid.

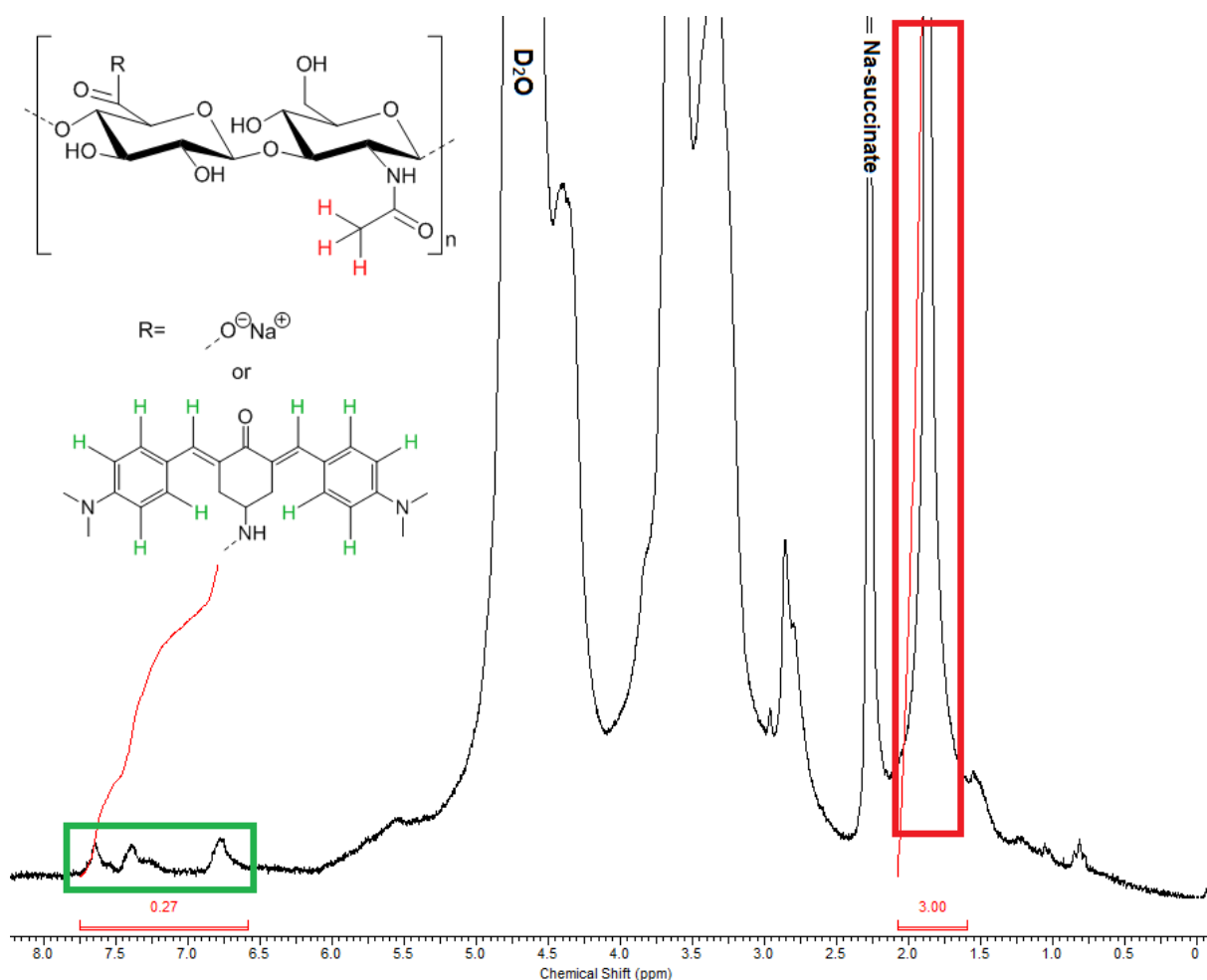


Figure 23: $^1\text{H-NMR}$ spectrum of HA-bound **MCNK**. Peak at 1.94 ppm corresponding to N-acetyl-protons of HA (red), peaks at 6.60 - 7.75 ppm corresponding to marked protons of **MCNK** (green).

The DS was determined from the $^1\text{H-NMR}$ spectrum measured in D_2O (**Figure 23**), by comparing the integral of the N-acetyl group of HA (3 protons per HA repeating unit, marked in red) to the integrals of the vinyl- and aromatic protons of **MCNK** (10 protons per 2PI unit, marked in green). For the aforementioned ratio of reagents, this

resulted in a low DS of about 3%. Repeating the reaction procedure with 0.3 equivalents CDI/0.6 equivalents **MCNK** or with 0.5 equivalents CDI/1 equivalent **MCNK** as well as increasing the reaction time after addition of the amine to 72 h only gave DS of about 4% and 5% respectively.

Since the examples from literature^{143,146} were all reactions with easily accessible amino groups on primary carbon atoms (benzylamine, octylamine, hexadecylamine...), it was considered that steric hindrance of the amino group of **MCNK**, attached to a secondary carbon atom on the cyclohexane ring in the center of the molecule, may play a role in limiting the DS. Thus, another precursor with a better accessible amino group should be prepared via introduction of a spacer group to **MCNK** in order to allow attaining higher DS.

1.2.2. Introducing a spacer on MCNK - extended precursor MGABA

A simple strategy to obtain a DBK precursor 2PI with a sterically more accessible linker amino group is to attach the latter with a suitable spacer group to the amino functionality already present in **MCNK**. Using a spacer with a carboxylic acid group for attachment to **MCNK** *via* amidation, CDI-based chemistry could be employed in a similar fashion as for linking **MCNK** to HA. However, during the step of its introduction, the new amino group needs to be protected in order to ensure that only the amino group of **MCNK** can participate in the reaction. 4-(*Tert*-butoxycarbonylamino)butyric acid (Boc-GABA-OH), a suitable spacer carrying a carboxylic acid as well as the protected amino functionality, is commercially available. The synthetic pathway to the precursor 2PI **MGABA**, carrying a sterically accessible linker amino group, is shown in

Figure 24.

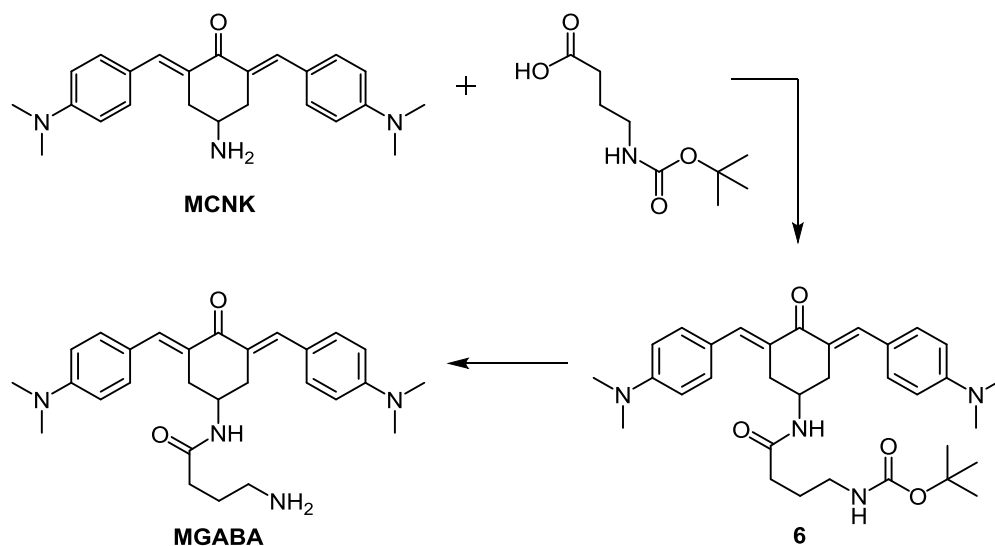
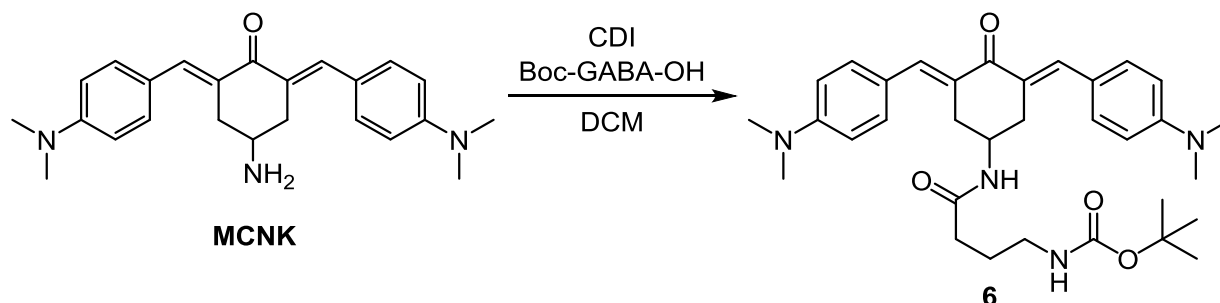


Figure 24: Synthetic pathway to **MGABA**

1.2.2.1. Synthesis of precursor DBK 6

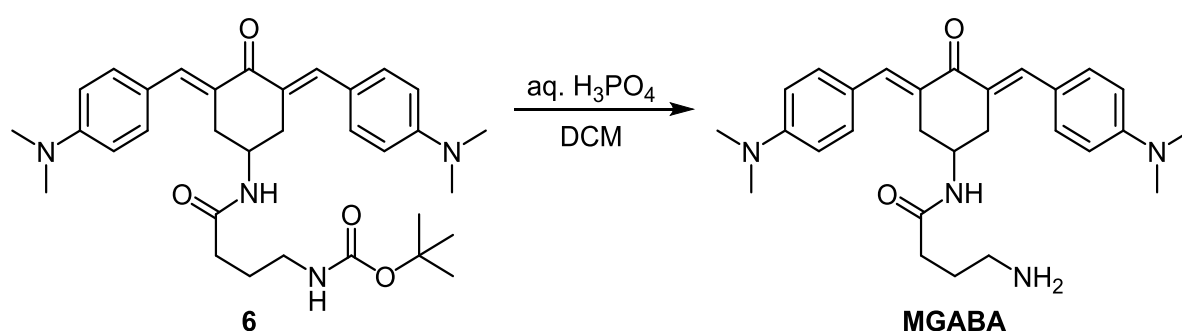
The first step in the sequence leading to **MGABA** was attaching Boc-GABA-OH to the amino group of **MCNK**.



This was carried out by dissolving 1 equivalent of Boc-GABA-OH in dry DCM and adding 1 equivalent of CDI, upon which visible formation CO_2 occurred. After 20 min of further stirring, a solution of **MCNK** in DCM was added and the mixture left to react for 18 h at room temperature. After removal of solvent (as well as some of the residual reaction by-product imidazole, which sublimates) *in vacuo*, the crude product was recrystallized from EA, giving 79% of the theoretical yield of **DBK 6** as orange crystals.

1.2.2.2. Synthesis of precursor MGABA

The cleavage of the Boc-group of **DBK 6** was carried out in analogy to the deprotection of **DBK 5**.

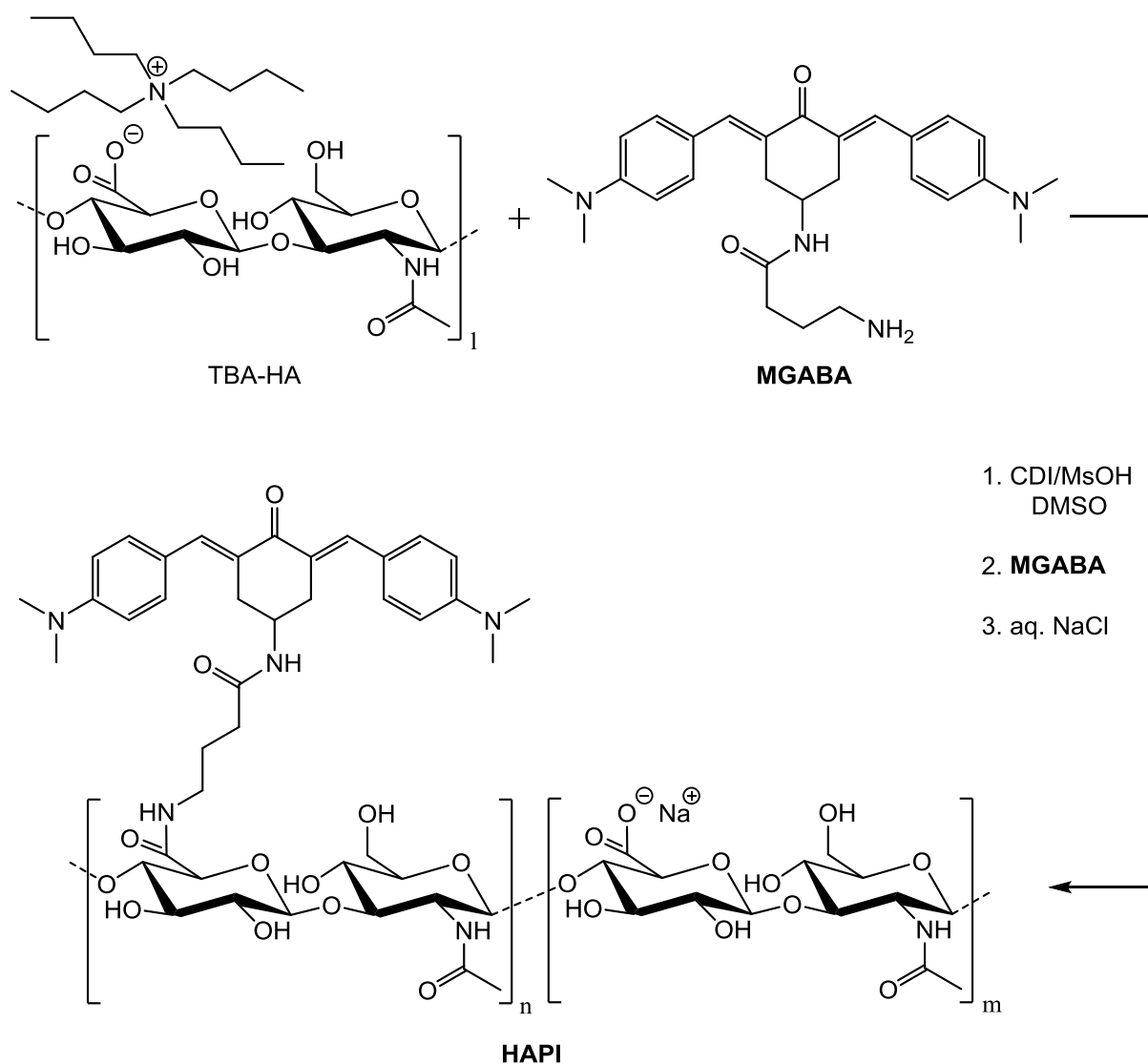


A suspension of **DBK 6** was treated for 3 h with excess H_3PO_4 (85% aqueous solution) under vigorous stirring to effect constant mixing of the biphasic system. The aqueous phase was diluted, alkalized to pH ~ 9 and extracted with DCM from which

crystalline orange flakes of **MGABA** were isolated in a yield of 94% by stripping of solvents *in vacuo*.

1.2.3. Coupling of DBK precursor **MGABA** to HA

The final step to obtain the HA-bound photoinitiator (**HAPI**) was the coupling of **MGABA** to HA, which was conducted in analogy to the reaction with **MCNK**.



TBA-HA was dissolved in dry DMSO and 0.3 equivalents of CDI as well as 7.5 mol% MsOH were added. After 18 h of stirring under argon atmosphere, 0.6 equivalents of **MGABA** were added and stirring was continued for 72 h. The workup was also conducted identically, first adding excess saturated NaCl-solution to hydrolyze

residual activated HA-carboxylate groups and exchange TBA⁻ with Na⁺ ions, then precipitating and washing the macromolecular 2PI with acetone. Finally, a solution of the macromolecular 2PI is dialyzed against deionized water and freeze-dried to obtain the HA-bound photoinitiator (**HAPI**) as foamy orange solid. A DS of 11% was calculated from the ¹H-NMR spectrum by comparing the integral of the N-acetyl group of HA to the integrals of the vinyl- and aromatic protons of the covalently bound **MGABA** (see section 1.2.1. **Coupling of DBK precursor MCNK to HA**), supporting the use of a sterically more accessible amino group in comparison to **MCNK**.

1.2.4. Synthesis of low molecular weight HAPI from degraded HA and use of methyl- β -cyclodextrin to improve processability

The macromolecular 2PI **HAPI** based on HA with a M_n of 1.6 MDa is well soluble in water by itself at a concentration equivalent to 4 mM **MGABA**. However, when mixing the **HAPI**-solution with a gelMOD-solution to obtain the hydrogel precursor formulation for 2PP printing, a problematic phenomenon occurred. Within minutes a phase separation started on a microscopic level (see **Figure 25**), and upon prolonged standing the solution separated into two distinct liquid phases, a darker reddish gel-like bottom layer that obviously contained the bulk of **HAPI**, and a lighter orange top layer deprived of the 2PI. The same effect was also observed when using hyaluronic acid vinyl ester (HAVE)¹¹⁵ instead of gelMOD as a macromer, so it is concluded that the aggregation of HAPI is not due to some interaction specific to polysaccharide/protein-mixtures.

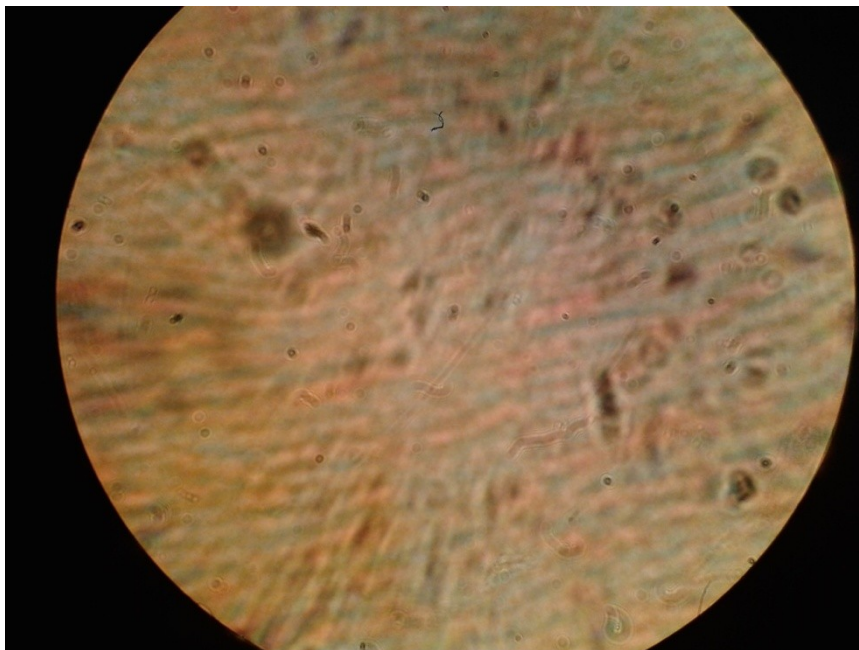


Figure 25: Phase separation - visible as alternating streaks of darker and lighter orange color - occurring when **HAPI** and gelMOD-solutions are mixed (light microscopy image, 10x magnification)

While some polymerization was observed when attempting 2PP printing of hydrogel precursor formulations with **HAPI** and gelMOD immediately after mixing, the polymerization basically stopped once the phase separation became visible and that

time frame was far too short to print any useful hydrogel structures. Thus, a solution had to be found to prevent this aggregation of **HAPI** leading to phase separation and allow for reasonable processability.

As a first approach to increase the compatibility of **HAPI** with macromers like gelMOD, it was considered to increase its solubility by using degraded HA with decreased molecular weight as a polymeric backbone for the macromolecular 2PI. While high molecular weight HA maintains homeostasis and potentially down-regulates inflammation, the generation of low molecular weight HA may act as an endogenous signal - likely mediated by cell surface receptors such as CD44 and TLR-4.¹⁴⁷⁻¹⁵⁰ Studies have demonstrated that low and very low molecular weight degradation products of HA may elicit various pro-inflammatory responses, such as a marked difference between 20 kDa and 50 kDa HA on upregulation of TNF- α expression in keratinocytes,^{150,151} or macrophages that undergo phenotypic changes dependent on molecular weight of HA that correspond to either (a) pro-inflammatory response for very low molecular weight (digest and 5 kDa) HA or (b) pro-resolving response for high molecular weight (800 and 3000 kDa) HA.¹⁴⁹ Thus while the **HAPI** solubility is expected to be highest for smaller HA fragments, a compromise had to be made in degradation to avoid the generation of higher amounts of HA with molecular weights below 20-50 kDa.¹⁵⁰

The degradation of the commercial 1.6 MDa HA sodium salt was performed by adjusting a 1 wt% solution in deionized water to pH 1 with concentrated aq. HCl and heating to 60°C under mechanical stirring for either 18 h or 24 h. The reaction mixture was subsequently neutralized using TBA-OH and dialyzed against deionized water to remove small HA fragments and excess TBA-Cl. Freeze-drying afforded white, fibrous TBA-salts of HA with M_n of 87 kDa (18 h degradation) and 50 kDa (24 h degradation), at yields of 85% and 81% respectively. The degraded TBA-HA salts were then converted to low molecular weight **HAPI** in the same fashion as the high molecular weight 1.6 MDa TBA-HA, achieving DS of 9% and 10% respectively.

While the phase separation during the preparation of hydrogel precursor formulations with gelMOD was not as immediate and pronounced when using the low molecular weight **HAPI**, it still prevented the 2PP printing of stable hydrogel structures.

However, the solvation of the lowest molecular weight **HAPI** chains could be sufficiently stabilized for 2PP printing (see section **1.3.4. 2PP direct cell encapsulation**) by the addition of 10 mM methyl- β -cyclodextrin (MBCD) for a **HAPI** concentration equivalent to 1 mM **MGABA**.

Cyclodextrins are cyclic oligosaccharides with a molecular structure approximating a truncated cone or torus, that generates a hydrophilic exterior surface and a nonpolar cavity interior (**Figure 26**). They have been used to increase water solubility and solution stability of drugs in pharmaceutical applications. The partial methylation of β -cyclodextrin (MBCD with 1.8 - 2.1 of the 3 free OH-groups per glucose unit methylated was used here) not only further increases the lipophilicity of the central cavity that is lined with skeletal carbons and ethereal oxygens of the glucose residues, but even enhances the water solubility by decreasing intramolecular hydrogen bonding that results in relatively unfavorable enthalpies of solution and low aqueous solubilities for unsubstituted β -cyclodextrin.¹⁵²

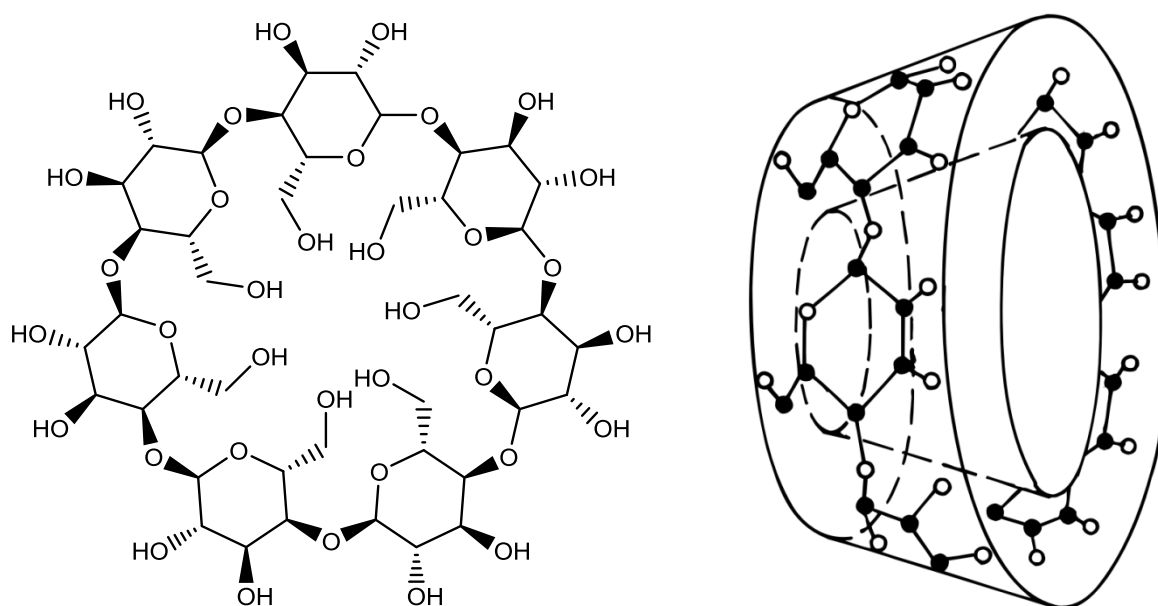


Figure 26: Chemical structure (**left**) and toroidal shape (**right**) of β -cyclodextrin.¹⁵²

A possible explanation of the stabilizing effect of MBCD on hydrogel precursor formulations containing **HAPI** and gelMOD is the formation of host-guest inclusion complexes of the cyclodextrin interior cavity with the hydrophobic parts of HA-bound **MGABA**. Thus it may weaken interactions like π - π stacking of the PI component that could contribute to the observed phase separation behavior.

1.3. Analysis of the macromolecular 2PI HAPI

1.3.1. Photophysical properties

Since a significant effect of the central ring size on the photophysical properties of DBKs has been demonstrated in literature,¹²⁷ the cyclohexanone-based system **E2CK** was chosen as a small molecule reference compound that should behave more similar to the **MGABA**-based **HAPI** in optical spectroscopy measurements than the cyclopentanone-based **P2CK**.

Both one- and two-photon optical measurements of **HAPI** and reference **E2CK** were carried out in close cooperation with Prof. Eric Vauthey and Arnulf Rosspeintner from University of Geneva.

Indeed, the one-photon absorption (1PA) spectrum of **HAPI** almost perfectly resembles both the spectral bandshape (maximum around 470 nm) and the maximum extinction coefficient (approximately $3.5 \cdot 10^4 \text{ M}^{-1} \text{ cm}^{-1}$) of the reference 2PI **E2CK** (see **Table 3** and **Figure 27**). The fluorescence maxima of **E2CK** and **HAPI** are located at ~650 nm, with fluorescence quantum yields in phosphate buffered saline (PBS) being very low (around 0.2%) and associated fluorescence lifetimes significantly below the time-resolution of the used set-up ($< 100 \text{ ps}$).¹⁵⁰

Since for unknown reasons **HAPI** did not give a signal in open aperture- or white light continuum- z-scans, 2PA spectra were recorded *via* two-photon induced fluorescence (2PEF). **HAPI** and **E2CK** again show almost identical behavior, with the wavelengths of the 2PA maxima around 830 - 840 nm and maximum σ_{2PA} in the range of 400 - 500 GM (see **Table 3** and **Figure 27**). The slightly lower maximum σ_{2PA} of **HAPI** in comparison to **E2CK** could be the result of slightly different degrees of planarity of the 2PI chromophores (different substituents on the amino-donor groups as well as on the central cyclohexanone ring) as has been previously reported for similar derivatives.⁹⁴ However, it is worth noting that this observed difference is also in the same order of magnitude as the potential error related to the very low fluorescence quantum yields as well as the error related to the NMR-determination of **HAPI**'s DS, which both affect the calculated σ_{2PA} .¹⁵⁰

Table 3: Basic photophysical properties in PBS at 20°C. λ_{abs} ... wavelength of 1PA maximum. ϵ_{max} ... molar extinction coefficient at 1PA maximum. $\lambda_{2\text{PA}}$... wavelength of 2PA maximum. $\sigma_{2\text{PA}}$... wavelength of 2PA maximum. λ_{em} ... wavelength of fluorescence maximum. ϕ ... fluorescence quantum yield in PBS.¹⁵⁰

	λ_{abs}	ϵ_{max}	$\lambda_{2\text{PA}}$	$\sigma_{2\text{PA}}$	λ_{em}	ϕ
	[nm]	[M ⁻¹ cm ⁻¹]	[nm]	[GM]	[nm]	[10 ⁻³]
E2CK	471	35000	830	480	~650	2.5
HAPI	466	35000	840	400	~650	1.8

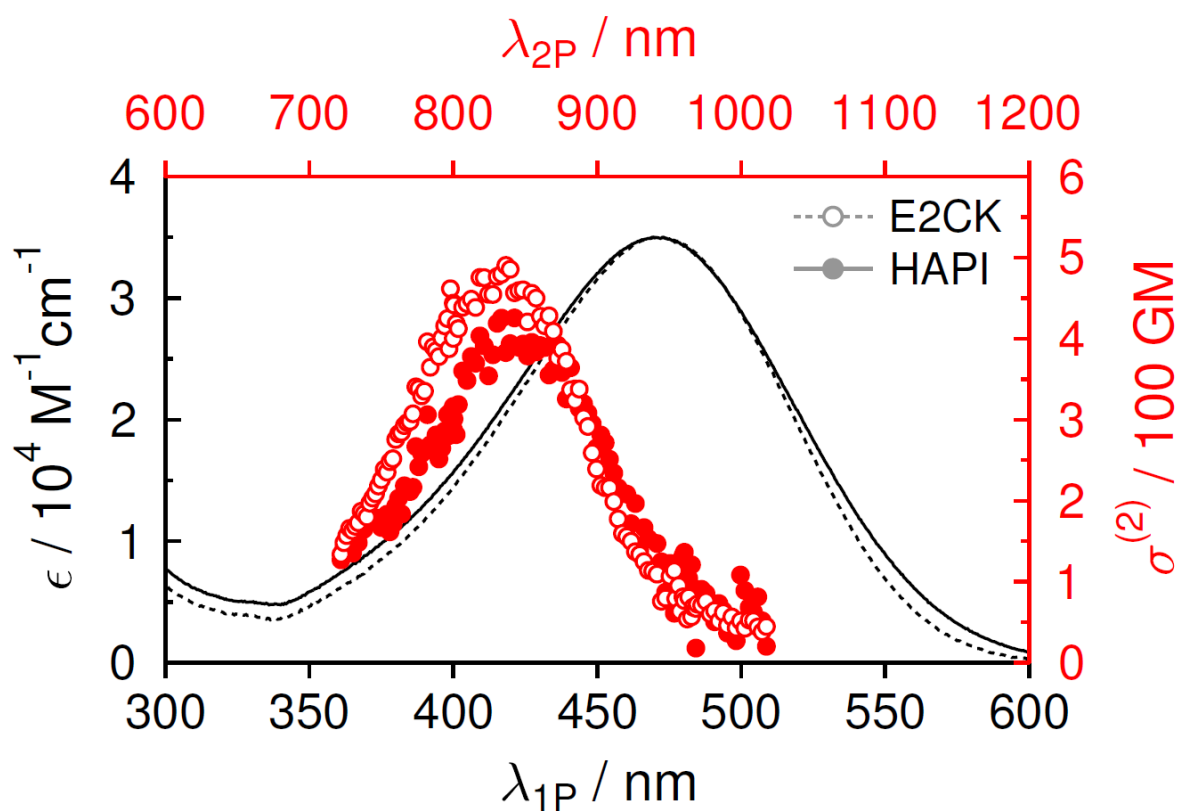


Figure 27: One-photon (black) and two-photon (red) absorption spectra of **HAPI** and **E2CK** in PBS.¹⁵⁰

1.3.2. Transmembrane migration

To prove the concept that covalently binding a small molecule 2PI to HA as a polymeric backbone hinders the transmembrane migration of the 2PI from the extracellular environment into the cytosol, live MC3T3 cells were exposed to solutions (0.1 mM 2PI concentration) of either **HAPI** or **E2CK** as a small molecule reference. The weak but visible autofluorescence ($\sim 0.2\%$ fluorescence quantum yield in aqueous solution) emitted by both **HAPI** and **E2CK** 2PI chromophores upon excitation with a 488 nm laser was used to image the 2PI distribution *via* laser scanning microscopy (LSM). In case of **E2CK**, the cells readily take up the 2PI leading to a bright fluorescent staining of various structures inside the cells (**Figure 28 - left**). **HAPI** on the other hand displays a weak fluorescence (**Figure 28 - right**, brightness digitally enhanced) in medium surrounding the cells, which themselves appear comparatively dark against the background fluorescence. This reversed fluorescence behavior of **HAPI** compared to **E2CK** strongly indicates that the transmembrane migration of a small molecule 2PI is indeed effectively hindered by covalent linkage to HA.

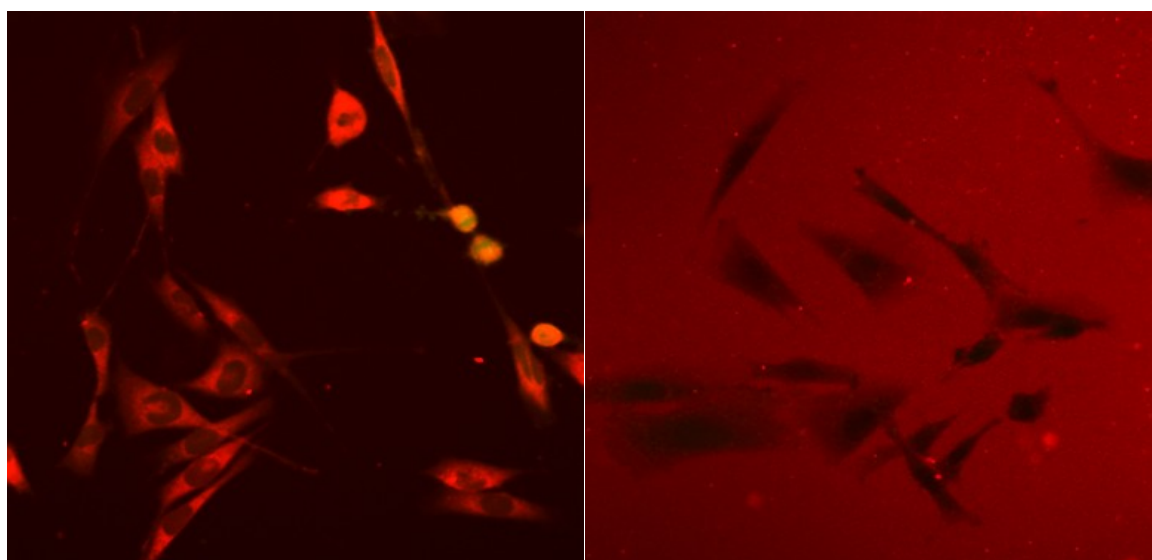


Figure 28: Visualization of the different transmembrane migration behavior of **E2CK** (**left**) and **HAPI** (**right**) *via* LSM images of their autofluorescence inside and around MC3T3 cells. To allow better visibility of darker cells against the brighter background fluorescence, the brightness and contrast of the **HAPI**-image was digitally increased compared to the **E2CK** image.¹⁵⁰

1.3.3. Cytotoxicity assay

Cells are exposed to 2PI-containing hydrogel precursor formulations both during 2PP sample preparation and the printing process itself, even if they are not directly encapsulated in the hydrogel (and thus not directly exposed to laser radiation or 2PA-induced radicals) but only trapped in cavities inside a printed structure. Therefore, while the phototoxicity of a 2PI is an aspect crucially relevant to 2PP direct cell encapsulation, the cytocompatibility of 2PIs without excitation *via* 2PA is also an important factor influencing the viability of encapsulated cells.

PrestoBlue[®] metabolic assay was used in close cooperation with Prof. Aleksandr Ovsianikov and Marica Markovic (Institute of Materials Science and Technology, TU Wien) to assess the cytocompatibility of **HAPI** in comparison to the references **P2CK** and **E2CK**, as well as the influence of MBCD that was required as a solvation stabilizer when 2PP printing with **HAPI**. For this, MC3T3 cells were first incubated with solutions of various concentrations of the aforementioned substances in α MEM cell culture medium for 5 h, a time frame long enough even for 2PP manufacturing of rather large structures. Subsequently, the PrestoBlue[®] Cell Viability test was performed, with the results displayed in **Figure 29**.

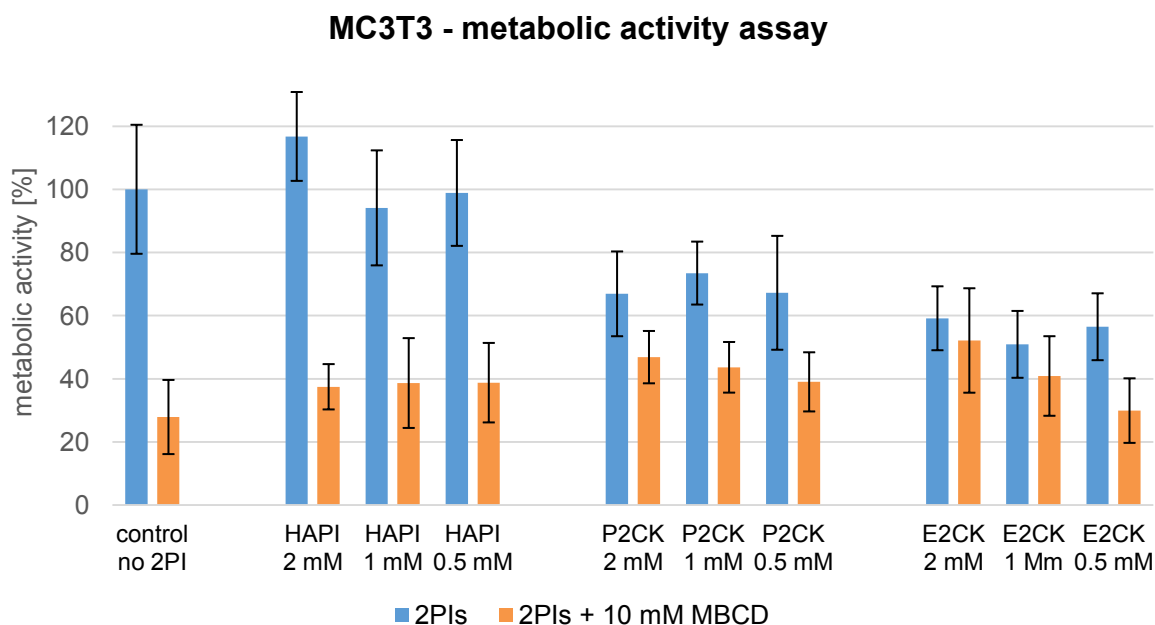


Figure 29: Effect of 5 h exposure of various concentrations of 2PIs and MBCD on the metabolic activity (determined *via* PrestoBlue[®] Cell Viability test) of MC3T3 cells. All values are given as percentage of the metabolic activity of untreated control cells.

While at 2PI concentrations of 0.5 mM - 2 mM both **P2CK** and **E2CK** caused a decrease in metabolic activity ranging from $27\pm 10\%$ to $49\pm 11\%$, indicating a significant cytotoxicity of the reference compounds, **HAPI** (without MBCD) showed no statistically significant difference compared to untreated control cells.

At a concentration of 10 mM, MBCD alone strongly decreased the metabolic activity by $72\pm 12\%$. However, when 10 mM MBCD was added to the various 2PI concentrations, the decrease only ranged from $48\pm 17\%$ to $70\pm 10\%$, with the small molecule 2PIs **P2CK** and **E2CK** attenuating the cytotoxicity of MBCD in a dose-dependent fashion. A possible explanation for this is that MBCD forms inclusion complexes with the 2PIs and thus the amount of free MBCD that can interact with the cells' biomolecules, causing toxicity, is reduced. These findings are also consistent with literature reports suggesting a cytotoxicity of MBCD that is partially ascribed to the extraction of cholesterol from the cells, and is abolished when directly adding an MBCD-cholesterol inclusion complex to the cells instead of free MBCD.¹⁵³

1.3.4. 2PP direct cell encapsulation

The most important step in order to assess the performance of **HAPI** was to employ it in its dedicated application of 2PP direct cell encapsulation. A 3D yin-yang structure (**Figure 30**), that had also been used in previous work,⁶ seemed suitable for this purpose since one half consists of through-polymerized hydrogel where cells can be embedded, while the other half of the structure is a void area where cells can be trapped but are not exposed to laser radiation during printing. This allows for a direct side-by-side comparison of laser-exposed and unexposed cells in the same structure.

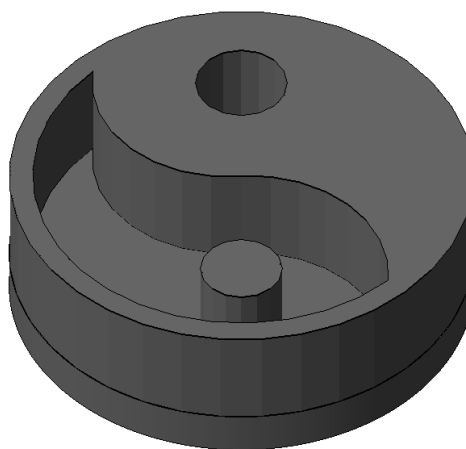


Figure 30: CAD-model of the 3D yin-yang structure (300 μm diameter), presented upside down for better visibility of the cavities. The "top" layer in the picture is joined to a glass substrate, while the "bottom" is a disc-like lid, so that the void areas are closed from all sides and allow trapping of cells.¹⁵⁰

Hydrogel precursor formulations were prepared by dissolving 15% gelMOD and either 1.0, 1.5 or 2.0 mM 2PI (**HAPI** or **P2CK**), as well as 10 mM MBCD in case of **HAPI**, in αMEM cell culture medium. In close cooperation with Prof. Aleksandr Ovsianikov and Marica Markovic, MC3T3 cells were suspended homogeneously in these formulations followed by immediate 2PP fabrication of the hydrogel yin-yang structures at 60 mW laser power and 100 mm/s writing speed. Following 2PP printing, the residual non-crosslinked gelMOD was removed by repeatedly soaking the hydrogel structures in αMEM at 37°C. At two time points, 24 h and 5 days after 2PP structuring, calcein-AM/propidium iodide live/dead stain was applied to the MC3T3 cells and LSM images were recorded (**Figure 31** & **Figure 32**).

Paradoxically, hydrogel structures printed with 1 mM **HAPI** and 10 mM MBCD were quite stable while those printed with higher concentrations of **HAPI** (that should be crosslinked more densely) displayed excessive swelling and either lost their shape or disintegrated and were washed away during cell culture medium exchanges. A possible explanation is that 10 mM MBCD is sufficient to prevent phase separation effects when using **HAPI** amounts equivalent to 1 mM 2PI, but when raising the **HAPI** concentration MBCD at 10 mM is no longer able to fully stabilize the solution, and partial phase separation interferes with the crosslinking of gelMOD.

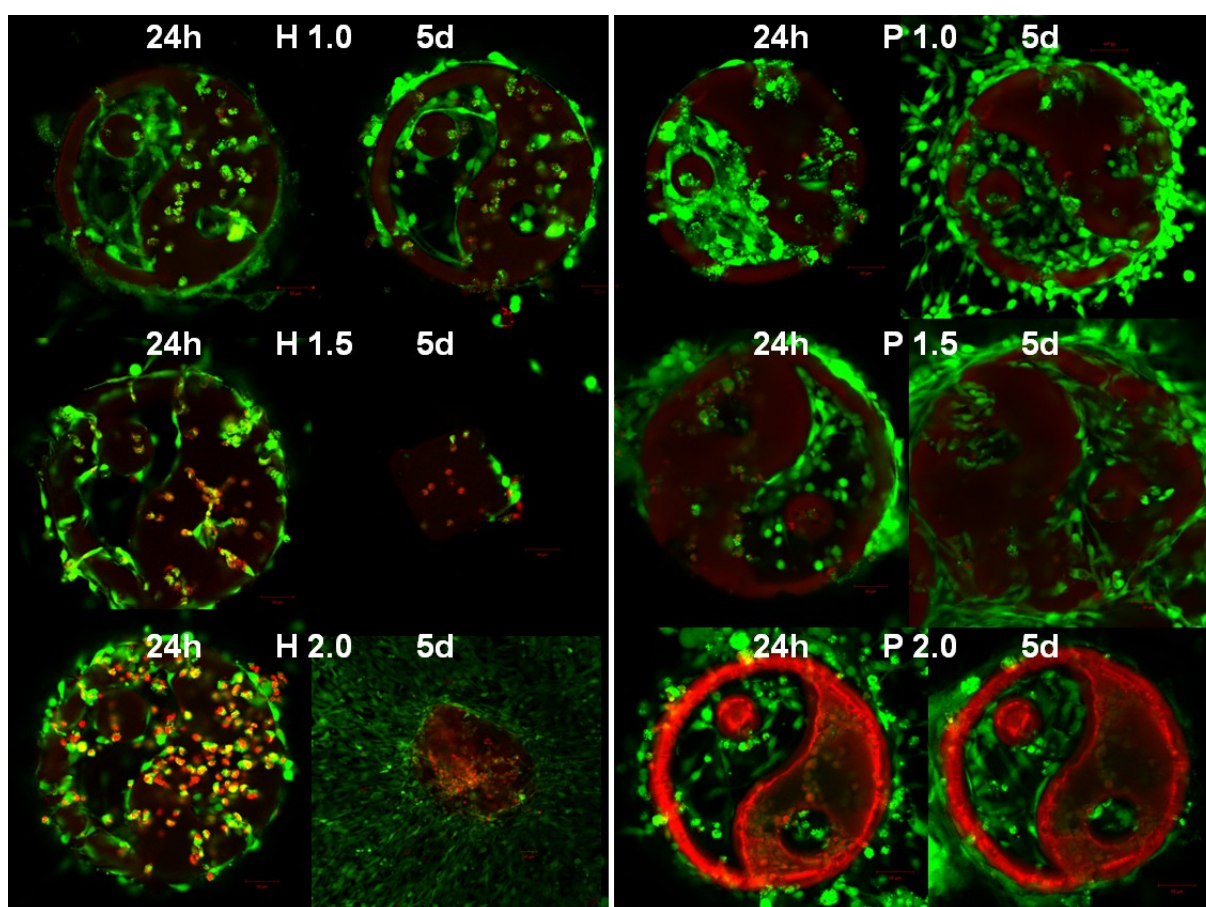


Figure 31: Examples of yin-yang hydrogel structures 2PP printed from gelMOD using either 1.0, 1.5 or 2.0 mM **HAPI** plus 10 mM MBCD (H 1.0 - H 2.0) or 1.0, 1.5 or 2.0 mM **P2CK** (P 1.0 - P 2.0). The LSM images show the encapsulated MC3T3 cells that were treated with live/dead-stain 24 h and 5 days after 2PP printing, as well as some red 2PI autofluorescence especially in case of **P2CK**. The 1.5 and 2.0 mM **HAPI** structures did not retain their integrity and shape in the days after structuring, possibly due to partial phase separation during structuring.

No attempts to print with higher amounts of MBCD were undertaken since crosslinking of 15% gelMOD with 1 mM **HAPI** and 10 mM MBCD did already produce satisfactory results, and also because PrestoBlue[®] metabolic activity assay suggests substantial MBCD toxicity even at 10 mM (see section **1.3.3. Cytotoxicity assay**). It should be noted here however, that cell survival in the hydrogel structures printed with **HAPI** plus 10 mM MBCD was much better than what may be expected from the results of the cytotoxicity assay, where > 60% reduction of MC3T3 metabolic activity was observed upon addition of 10 mM MBCD. On one hand, the exposure of the cells to the MBCD containing formulation during 2PP sample preparation and printing (assuming that MBCD was removed completely during the sample washings to remove non-crosslinked gelMOD from the printed structures) was only about 1.5 h vs 5 h in the metabolic assay. On the other hand, the amount of free MBCD available to interact with cells, and thus its toxicity, is likely significantly reduced as it binds to gelMOD that is not present in the cytotoxicity assay but comprises 15 wt% of the hydrogel precursor formulation used for 2PP printing.

Figure 32 shows close-up LSM images of yin-yang structures that are recorded in ~30 layers and then superimposed into one 3D (z-stack) image. These pictures allow an assessment of the effect that the use of **HAPI**, a polymer-bound and thus transmembrane-migration hindered 2PI, has on the viability of 2PP encapsulated cells in comparison to the small molecule reference **P2CK** that can enter cells.

The live/dead-stain applied to the MC3T3 cells uses two dyes. Calcein-AM can pass intact cell membranes and once in the cytoplasm is converted to its green fluorescent form calcein by the functioning esterase enzymes of live cells. Propidium iodide can only enter damaged cells with compromised membrane integrity (thus its use as "dead"-stain), then forming an intercalation complex with nucleic acids that is brightly fluorescent, staining cell nuclei red.^{117,118} Both structures fabricated with **HAPI** and **P2CK** trap cells in their void cavities (where the hydrogel is not exposed to the laser during 2PP structuring, and thus non-crosslinked) that spread and proliferate. After 24 h and increasingly so after 5 days, a few cells in the cavities are dead with a clearly visible, red stained nucleus, but most cells are stained bright green and look viable and healthy. Also, after 5 days the outer surface of the yin-yang structures is densely populated with MC3T3 in both cases, indicating that the hydrogel material is well tolerated and adhered to by the cells.

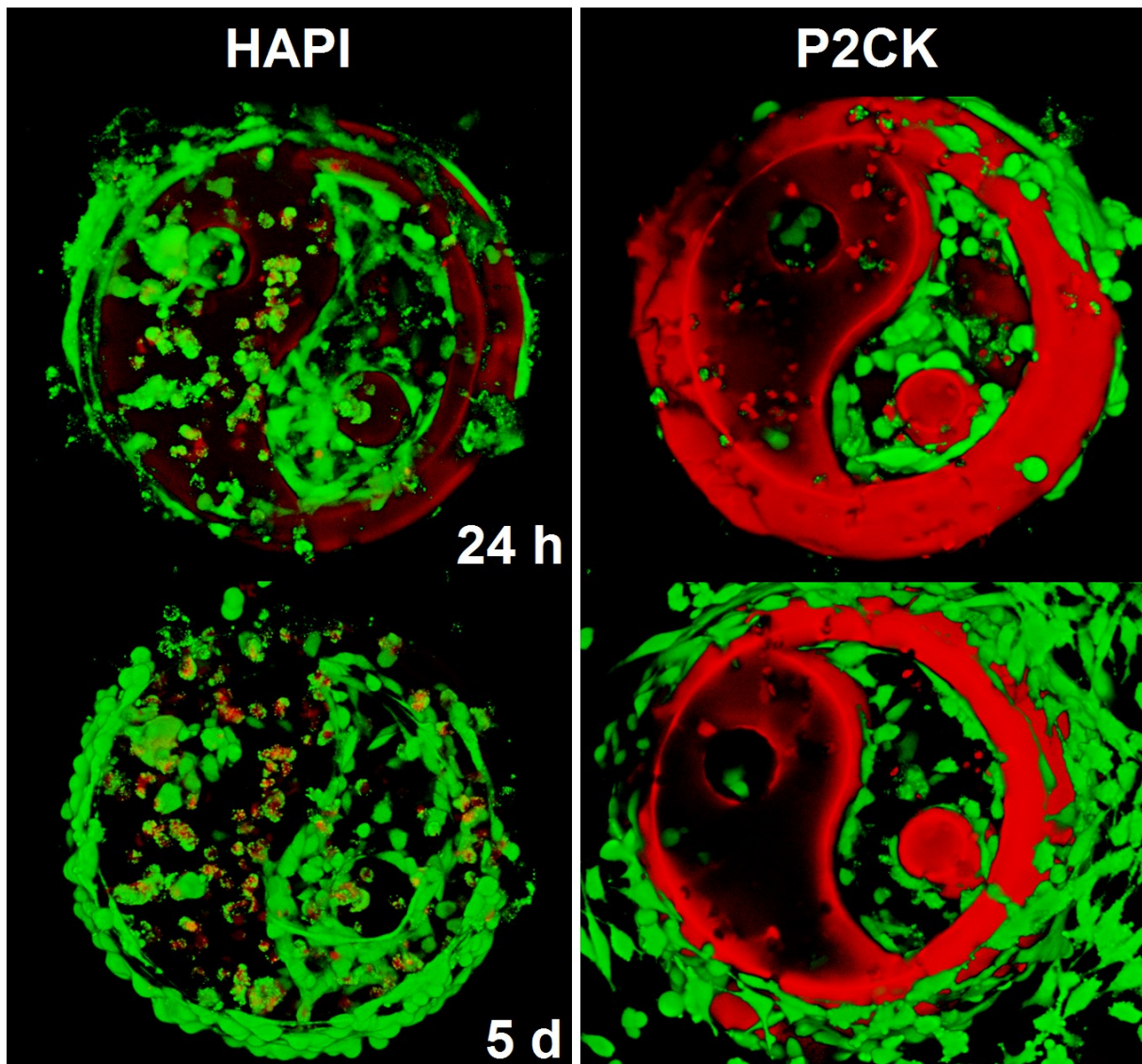


Figure 32: 3D (z-stack) LSM images of live/dead-stained MC3T3 cells 24 h (**top**) and 5 days (**bottom**) after 2PP printing, 20x magnification. The cells were encapsulated in gelMOD hydrogel yin-yang structures using either 1 mM **HAPI** and 10 mM MBCD (**left**) or 1 mM **P2CK** (**right**). In both cases, viable cells (green) spread and proliferate in the cavities and on the outer surface of the hydrogel structures. Encapsulated cells however suffer from some photodamage in case of **HAPI** (round cells, "spotted" green appearance, some nuclei stained red) and severe photodamage with **P2CK** (hardly any green cells embedded in the hydrogel, cell nuclei stained bright red).

A significant difference between structures fabricated either with **HAPI** or **P2CK** can be seen in regard to the cells actually encapsulated in the polymerized parts of the hydrogel. In case of **P2CK**, almost all encapsulated cells are dead after 24 h (**Figure 32 - top right**), indicated by their clearly defined, red stained nuclei and the almost complete absence of green stained cells. By day 5, most of the dead cells had

completely disintegrated, leaving only holes in the structure (**Figure 32 - bottom right**). It should be remarked here that the autofluorescence of residual amounts of the 2PI, especially **P2CK**, stains the whole hydrogel red. This does not truly interfere with the live/dead-stain assay however, as the staining of the cell nuclei by propidium iodide as clearly defined structures is characteristic. The encapsulated cells in the **HAPI**-crosslinked hydrogel appear photodamaged, although clearly not as extensively so as in case of **P2CK**. Both 24 h and 5 days after structuring (**Figure 32 - top left and bottom left**), **HAPI**-encapsulated MC3T3 are stained mostly green, but with a "spotted" appearance in comparison to the uniformly stained cells in the cavity of the yin-yang structure, as well as some red staining of the cell nuclei, showing that the cells have been damaged and the membrane integrity was compromised, allowing propidium iodide to enter the cells.

Thus, it is concluded that while the demonstrated hindrance of 2PI transmembrane migration into cells in case of **HAPI** is associated with a reduction in phototoxicity, the photodamage caused by the 2PP encapsulation process could not be completely eliminated *via* this strategy. Possible explanations are that the exposure of the cells' outer plasma membrane to radicals associated with 2PP still causes significant damage to the cells, or that some of the generated radical species or ROS are mobile and long-lived enough to enter the cells and damage them from within.

Besides the phototoxicity still caused by **HAPI**, further problematic issues are the observed phase separation upon mixing with hydrogel precursors affecting processability, as well as the required complex multi-step synthesis. These findings discourage further attempts to improve the macromolecular 2PI **HAPI**, so that a completely new strategy to avoid photodamage during 2PP encapsulation of cells should be conceived.

2. Cleavable 2PIs

Since the strategy of hindering transmembrane migration into cells by binding the 2PI to a polymer backbone and thus avoiding direct interaction between the laser-excited 2PI and the cells' internal structures did not sufficiently prevent cellular photodamage during 2PP encapsulation, a novel approach had to be found.

There are many examples in literature for successful encapsulation of cells in bulk hydrogel materials, using classical free radical 1PP based on UV- or even visible light. Commercial PIs such as Irgacure 2959^{30,32}, VA-086³¹ or Li-TPO^{29,32} have been used to achieve viabilities of encapsulated cells of 95% or greater. What these initiators have in common is their mechanism of radical formation. Upon photoexcitation, they generate initiating radicals *via* a fast homolytic bond cleavage,^{31,32} which could be a key to their relatively low phototoxicity.

For a new rational strategy to reduce the phototoxicity of 2PIs, it is helpful to take a closer look on the molecular mechanisms underlying 2PP. While the mechanisms of radical formation and initiation in classical 1PP have been extensively studied and described in literature,^{154–157} no such detailed studies have yet been performed in case of 2PP. The elucidation of the mechanism of radical formation of 2PP is inherently difficult to investigate, due to the very small excitation volumes of a tightly focused laser and minute amounts of active species involved, which render direct observation *e.g. via* spectroscopic methods elusive.

Cumpston *et al.* suggested that an electron transfer from the photoexcited 2PI to an electron-deficient monomer *e.g.* an acrylate might lead to the formation of radical ions or subsequent radical species that initiate the polymerization.⁹⁶ Based on this concept, a more detailed hypothetical mechanism was proposed by Lu *et al.*^{158,159} as well as Wang *et al.*¹⁶⁰

In **Figure 33** an electron-rich 2PI chromophore with a donor - π -system - donor (D- π -D)-structure is excited (represented with an asterisk *) *via* 2PA. Through a strong intramolecular charge transfer (intra-CT) from the terminal electron donor groups to the π -system, an intra-exciplex with particularly high electron density at the π -core is formed. Electrons could then be transferred from the electron rich parts of the intra-exciplex to electron-deficient double bonds of a monomer, forming radical ions, with the energy barrier for this "electron hopping" drastically reduced by the short-range

molecular interaction promoted by the monomer being present in bulk or at least high concentrations. The radical ions can then either initiate polymerization, or the process can simply be reversed *via* back electron transfer.¹⁵⁸

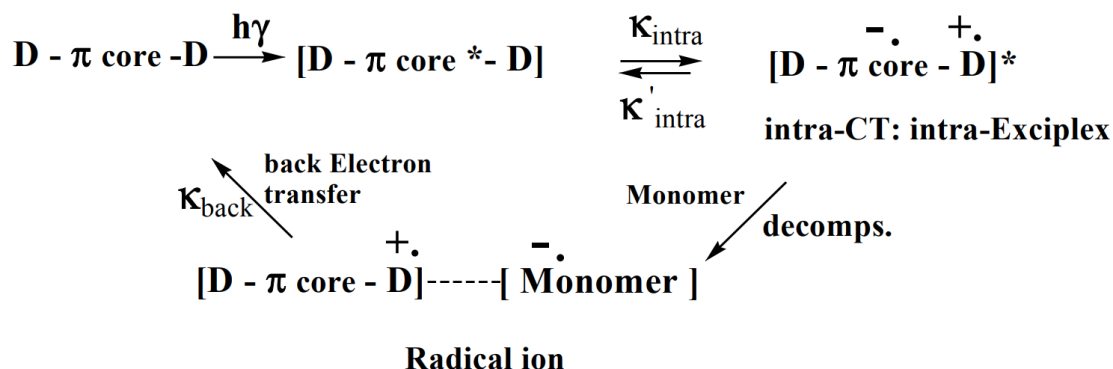


Figure 33: Hypothetical mechanism of radical formation in 2PP.¹⁵⁸

It is also thinkable that two of the formed radical ions dimerize to a dianion (as observed in the polymerization of styrene initiated by sodium naphthalenide¹⁶¹) that is subsequently oxidized to a diradical (initiating polymerization) by the 2PI radical cations, effectively resulting in a regeneration of the 2PI, which can in turn start the process anew (**Figure 34**).

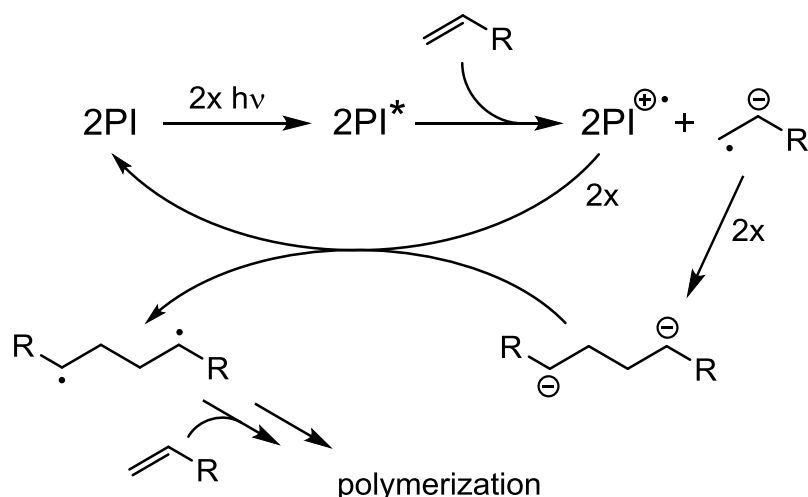


Figure 34: Hypothetical 2PP mechanism with dimer-diradical formation from the monomer and resulting regeneration of the 2PI.

In conclusion, classical 1PP encapsulation of cells makes use of PIs that generate initiating radicals *via* a fast homolytic bond cleavage, while 2PP most likely requires excited states with longer lifetimes to enable bimolecular electron transfer reactions

from the 2PI to the monomer. Previous studies considered that in detrimental side reactions, long lived 2PI excited states might also transfer energy or electrons to molecular oxygen, thus generating $^1\text{O}_2^*$ or $\text{O}_2^{\bullet-}$, HO^\bullet and other reactive oxygen species (ROS) respectively (**Figure 35**).⁶ It is well established that ROS are capable of inflicting biological damage¹⁶² and may hence be to a significant extent responsible for the phototoxicity encountered in 2PP.

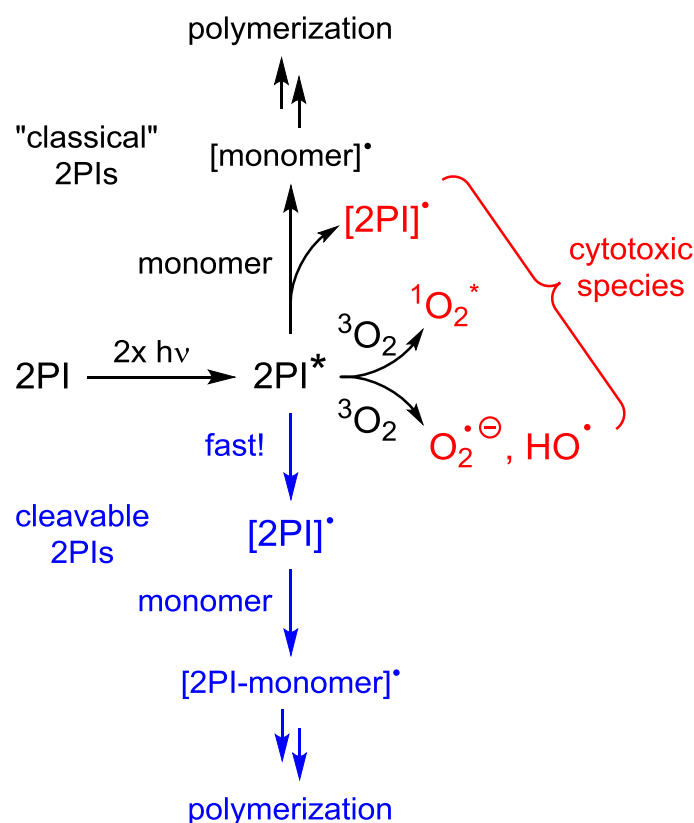


Figure 35: Different mechanisms regarding the formation of initiating radicals and cytotoxic ROS for "classical" and novel, cleavable 2PIs.⁶

While classical cleavable 1PIs that have shown good cytocompatibility in UV-photoencapsulation of cells are not suitable for 2PP due to their mostly exceedingly low $\sigma_{2\text{PA}}$,⁹³ the "classical" efficient 2PIs suffer from a slow bimolecular mechanism of radical formation and are liable to unwanted side reactions such as the formation of cytotoxic ROS. Thus, a promising approach would be to combine features promoting large $\sigma_{2\text{PA}}$ such as strong electron donor/acceptor groups and extended π -systems with structural moieties enabling direct radical formation *via* fast cleavage to avoid side reactions generating ROS (**Figure 35**).

2.1. Cleavable 2PIs based on trichloromethyl-substituted 1,3,5-triazine

2.1.1. Basics of trichloromethyl-substituted 1,3,5-triazines as photoinitiators

Organic halogen compounds, which are capable of generating free radicals such as a chlorine or a bromine free radical upon exposure to light, have been widely used as PIs in photopolymerizable compositions.¹⁶³ Derivatives of halomethyl-1,3,5-triazines are widely mentioned in the patent literature^{163–167} and have been used in the field of photopolymerization alone as cleavable PIs, or in the presence of a sensitizer or/and co-initiators in photoinitiating systems, reacting in that case through an electron transfer mechanism.^{168,169}

Among these derivatives, (trichloromethyl)-1,3,5-triazines (CTs) are an important class of PIs for free-radical initiated photoimaging systems. Although by itself, 2,4,6-tris(trichloromethyl)-1,3,5-triazine (TCT) is not a practical PI, photosensitization and chromophore substitution have been used to extend its spectral response to longer wavelengths.¹⁷⁰

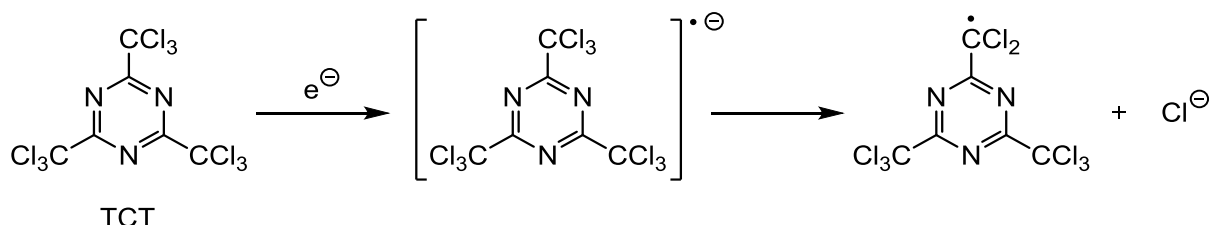


Figure 36: TCT as radical forming compound after electron transfer from other species such as sensitizer dyes.¹⁷¹

TCT produces radicals e.g. upon bimolecular electron transfer (**Figure 36**) from photoexcited sensitizer dyes (**Figure 37**) such as benzothiazine¹⁷² or cyanine dyes,^{171,173} or even isopropylthioxanones (ITX),¹⁷⁴ allowing photocuring *via* visible or near IR light. In some cases, additional electron donating components such as tertiary aromatic amines¹⁶⁹ or aryl borate salts¹⁷³ are included, giving rise to the recovery of the initial dye and a new initiating species, resulting in a significantly increased efficiency of such multicomponent systems.^{157,168,169}

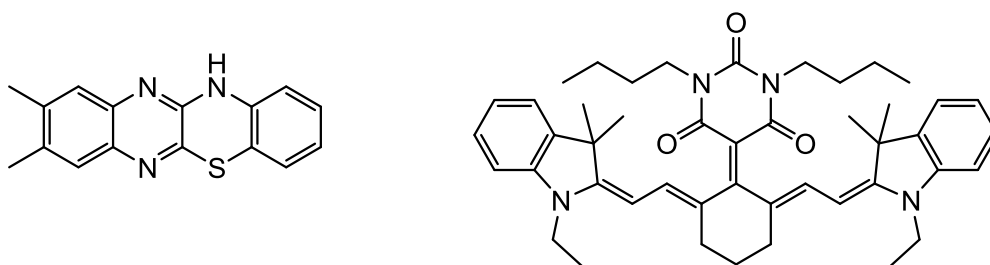


Figure 37: Examples for benzothiazine-based (**left**) and cyanine-based (**right**) sensitizer dyes used in conjunction with TCT.

Other CTs have been prepared with a chromophore system directly linked to the triazine ring, either with or without direct electronic conjugation (**Figure 38**). The extension of the conjugated π -system and introduction of an electron-donating substituent by replacing one of the trichloromethyl-groups of TCT with a 4-methoxyphenyl-group (compound TA in **Figure 38**) leads to a red-shift of the absorption maximum from 275 nm to 330 nm. The performance regarding polymerization rate and monomer conversion when used in dye/amine/triazine-tricomponent initiator systems is also increased vs TCT.¹⁶⁸

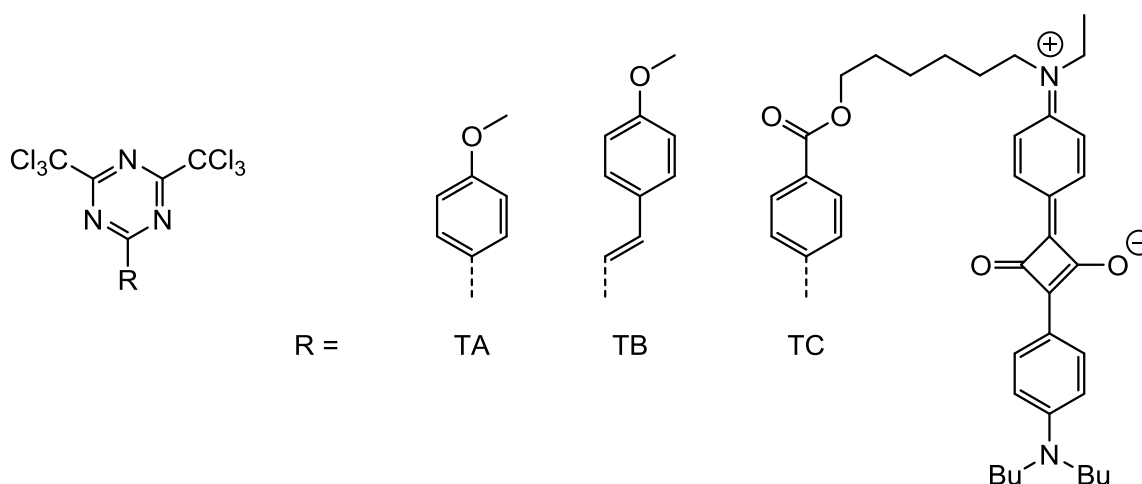


Figure 38: Examples for chromophore-substituted bis(trichloromethyl)-1,3,5-triazine derivatives. TA and TB bear an electron-donating methoxy substituent in conjugation to the triazine moiety *via* phenylene or styrylene groups respectively.^{168,175} A squarylium dye is linked to the triazine system in TC with a non-conjugated C₆ spacer group, with the close proximity between sensitizing dye and sensitized acceptor resulting in a faster electron transfer rate compared to the unlinked pair.¹⁷⁶

Insertion of an additional vinyl-group results in 2-(4-methoxystyryl)-4,6-bis(trichloromethyl)-1,3,5-triazine (compound TB in **Figure 38**) with a further red-shifted absorption maximum at 373 nm. TB on its own is already capable of radical formation *via* direct cleavage when excited with a visible light LED (405 nm), surpassing established commercial acylphosphine oxide-initiators in the radical polymerization of (meth)acrylates, and exhibiting even higher efficiency when combined with tertiary amines.¹⁷⁵

In an attempt to speed up the bimolecular electron transfer of dye-sensitized (trichloromethyl)-1,3,5-triazine initiating systems, triazine-linked squarylium dyes (example TC in **Figure 38**) have been prepared and proven to indeed result in 4.4 to 15-times faster polymerization rate (C_6 and C_2 alkylene spacer respectively) than the corresponding unlinked two-component system.¹⁷⁶

2.1.2. Design of cleavable 2PIs based on trichloromethyl-substituted 1,3,5-triazine

A major reason for established commercial cleavable 1PIs only being of very limited suitability for 2PP lies in their exceedingly low σ_{2PA} at 800 nm, resulting from their short conjugated π -systems as well as λ_{abs} typically being well below 400 nm, often below 300 nm.

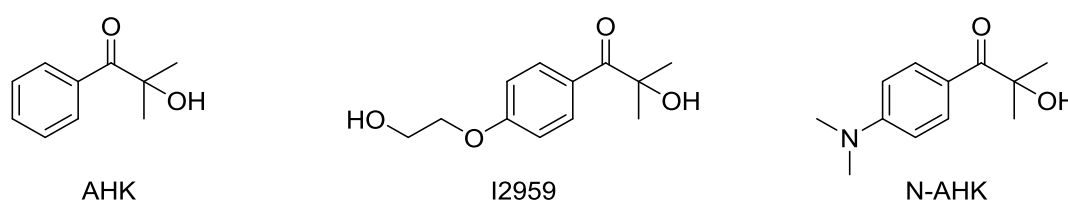


Figure 39: Examples for cleavable α -hydroxy ketone 1PIs.

α -Hydroxy ketones are an important class of commercial cleavable 1PIs. Jockusch *et al.* investigated the effects that para-substituents on the benzoyl chromophore have on photocleavage. Their findings indicate that while the simple benzoyl-group of AHK (**Figure 39 - left**) promotes n, π^* -nature of the lowest triplet state T_1 and favors fast and efficient cleavage from T_1 upon irradiation, the introduction of a dimethylamino-group in N-AHK (**Figure 39 - right**) changes the configuration of the lowest triplet

states to π,π^* -transitions and results in a lack of α -cleavage from T_1 . Alkoxy-substitution such as in the biocompatible, water-soluble I2959 (**Figure 39 - middle**) represents an intermediate for which α -cleavage occurs efficiently, but at a relatively slow rate.¹⁷⁷

While alkoxy-substituted triazine initiator TB acts as a highly efficient cleavable 1PI at 405 nm ($\lambda_{\text{abs}} = 373$ nm), it still seems prudent to design a cleavable triazine 2PI with an extended π -system as well as strong electron donor groups (dialkylamino instead of alkoxy) to increase $\sigma_{2\text{PA}}$ and shift λ_{abs} closer to the region of established DBK 2PIs, ranging from 430 - 480 nm.⁹⁴ However, the resulting compound would most likely have to be able to cleave from a π,π^* -triplet state in order to act as an efficient 2PI.

Since the development of successful procedures for synthesis and purification is generally more complicated for large planar π -systems bearing strongly hydrophilic groups to ensure good water-solubility, organosoluble derivatives should be prepared first to allow basic studies before deciding if the effort to make water-soluble compounds is warranted.

Thus, a proposed structure for a cleavable trichloromethyl-substituted 1,3,5-triazine 2PI **2BC** (**Figure 40**) is based on replacing the methoxy-group of TC with a dibutylamino-group as a stronger electron donor bearing butyl-groups that support good solubility, as well as replacing one of the trichloromethyl-substituents with a second (dibutylamino)styryl-unit to elongate the π -system and ensure high $\sigma_{2\text{PA}}$.

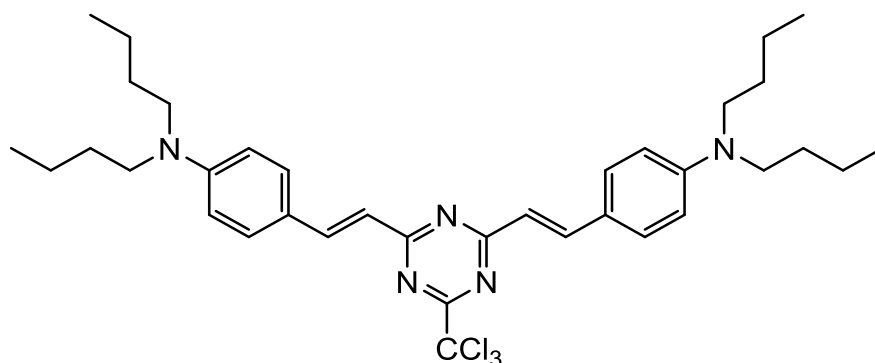


Figure 40: Proposed cleavable 2PI **2BC**.

An issue of concern lies in the fact that along with a red-shift of λ_{abs} and increased $\sigma_{2\text{PA}}$, singlet and triplet energies decrease as π -conjugation length expands, due to the reduction in the energy difference between neighboring orbitals.^{178,179} Eventually the energy of the excited triplet state may be too low to effect photodissociation of cleavable moieties, in this case the C-Cl bond. This could be a reason why no efficient cleavable 2PIs have been described in literature to date. Therefore, before **2BC** is prepared, quantum chemical calculations should first be performed to estimate the nature and energy levels of the involved excited states and predict if C-Cl bond cleavage is energetically favorable.

2.1.3. Quantum chemical calculations to predict cleavability of **2BC**

Quantum chemical calculations were carried out in cooperation with Prof. Tom Scherzer and Sergej Naumov from the Leibniz Institute for Surface Modification (IOM) in order to predict the cleavability of **2BC**. Calculations of energy levels (**Figure 41**) were performed at the B3LYP/6-31G(d,p)//PBF(THF, $\epsilon=7.6$) level of theory, for a simplified version of **2BC** where the dibutylamino-groups had been replaced with dimethylamino-substituents (greatly reduces calculation effort while result is not changed fundamentally), in THF solution.

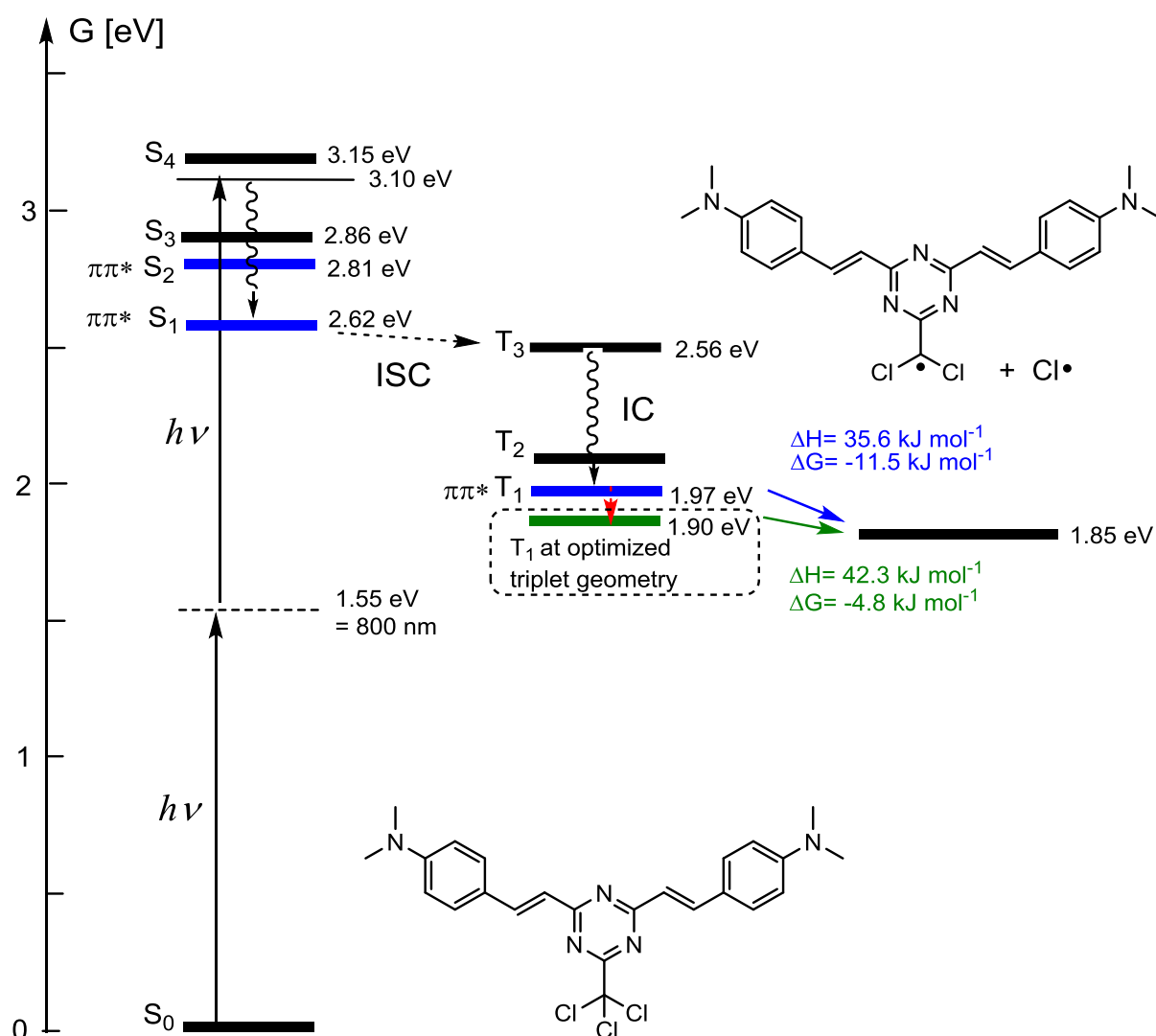


Figure 41: Calculated Jablonski-Scheme for the dimethylamino-analogue of **2BC**.

Axis shows Gibbs free energy in eV.

Figure 41 shows that degenerate 2PA at 800 nm is sufficient to lead to an excited state above singlet state S_3 , from where the system can vibrationally relax to excited singlet S_1 . Intersystem crossing (ISC) leads to excited triplet T_3 that transitions to T_1 via internal conversion (IC). The involved states S_1 and T_1 are indeed of π, π^* -nature, and the cleavage of one C-Cl-bond is endothermic both from the geometrically optimized and non-optimized triplet T_1 . However, the dissociation into two particles, the carbon-based radical and the chlorine radical is entropically favorable, so that the reactions are exergonic and spontaneous cleavage from excited triplet T_1 is possible.

2.1.4. Synthesis of cleavable 2PI 2BC

A series of multipolar (dibutylamino)styryl-1,3,5-triazines was prepared in previous work,⁷⁷ and proved to initiate 2PP with similar efficiency as DBK 2PIs such as **M2CMK**. The syntheses of **BTrz**, **2BTrz** and **3BTrz** (**Figure 42**) all start from precursor 2,4,6-trimethyl-1,3,5-triazine (Trz) and proceed via Knoevenagel condensation with 4-(dibutylamino)benzaldehyde under alkaline catalysis with KOH in MeOH. Trz itself can be simply obtained by trimerization of either ethyl acetimidate¹⁸⁰ or MeCN.¹⁸¹

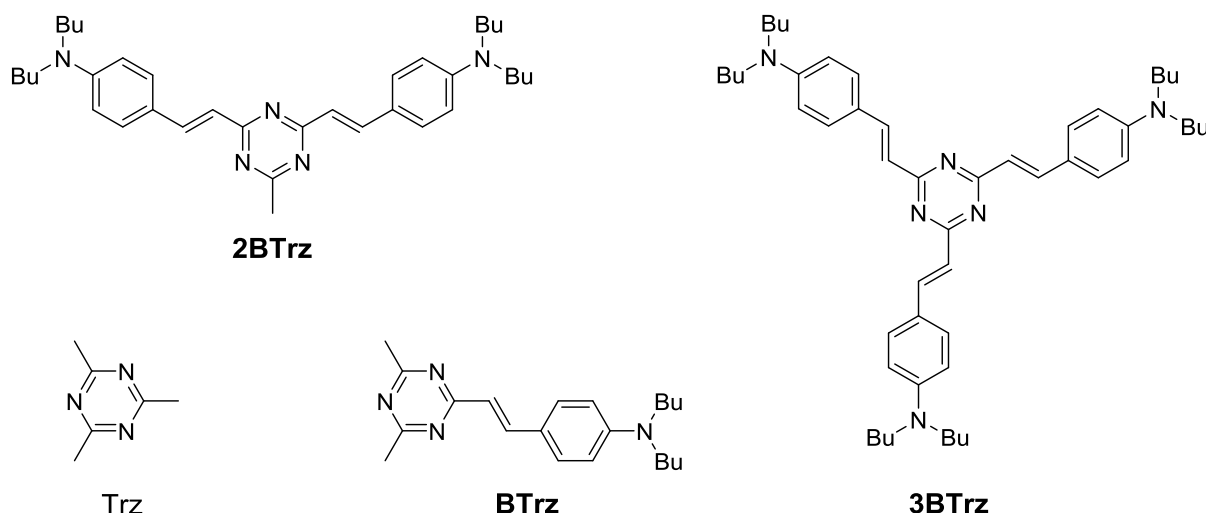


Figure 42: Triazine-based 2PIs **BTrz**, **2BTrz** and **3BTrz** prepared from precursor Trz in previous work.⁷⁷

2BC can be prepared in a similar fashion to **2BTrz**, however the replacement of one methyl-group of Trz with a trichloromethyl-group results in some important differences that will be discussed below. The complete synthetic pathway to **2BC** is depicted in **Figure 43**.

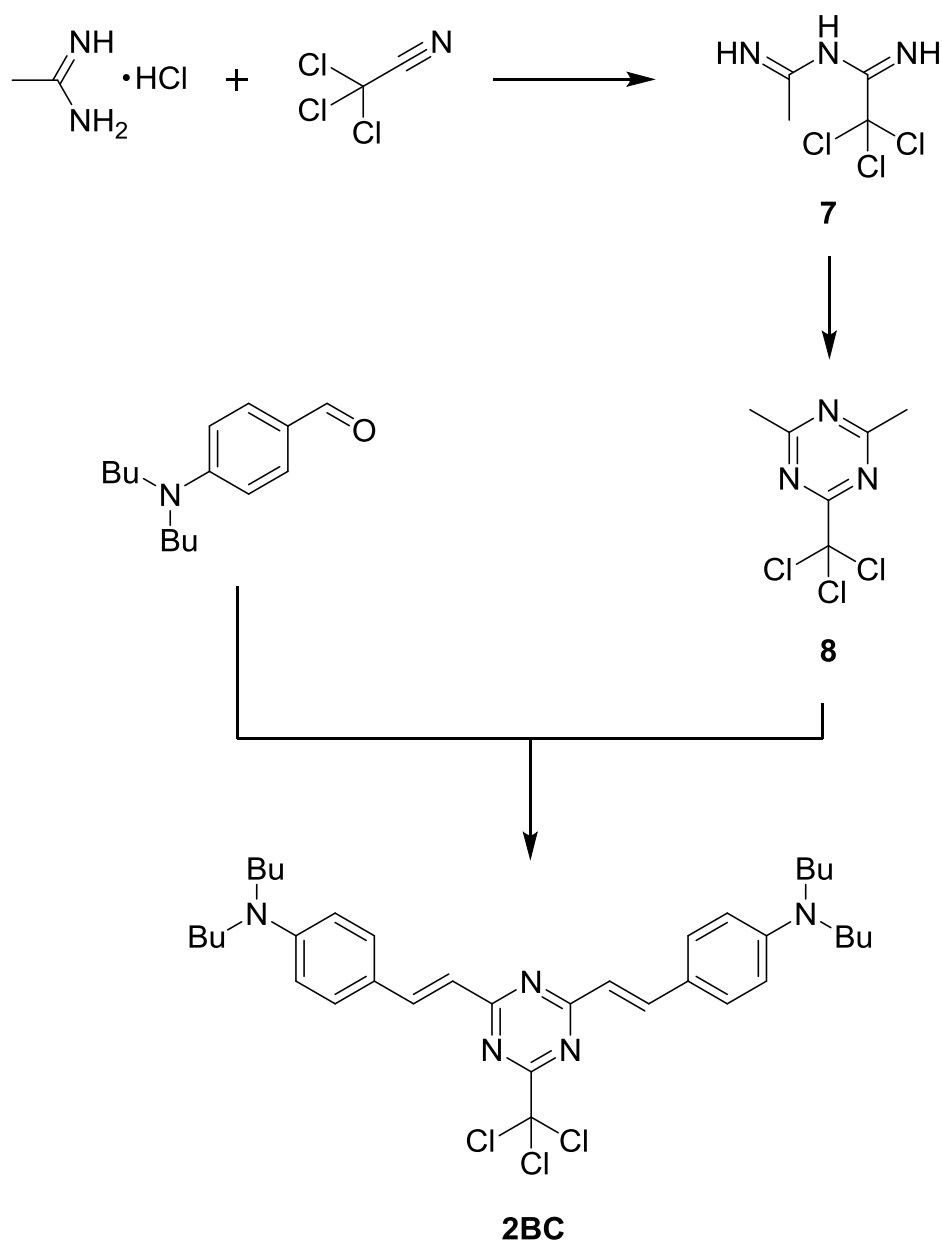
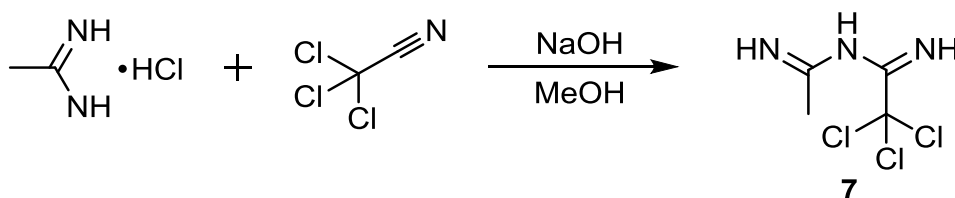


Figure 43: Synthetic pathway to **2BC**.

2.1.4.1. Synthesis of precursor amidine 7

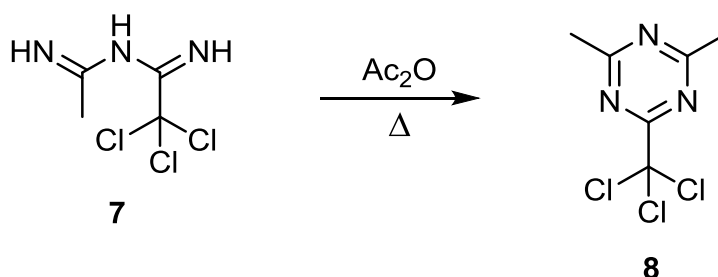
Due to its substitution pattern with two methyl groups and one trichloromethyl-group, the intermediate trichloromethyl-triazine **8** can no longer be obtained by a simple trimerization reaction. Cotrimerization of trichloroacetonitrile with MeCN mainly yields 2-methyl-4,6-bis(trichloromethyl)-1,3,5-triazine, even if an excess of MeCN is used, and is not a reasonably practicable method to prepare triazine **8**.¹⁸² Instead, it is prepared in a two step sequence from acetamidine and trichloroacetonitrile *via* the intermediate amidine **7** and acetylation of this product.¹⁸³



For this, a solution of 1 equivalent acetamidine hydrochloride in MeOH is treated with 1 equivalent NaOH to obtain acetamidine freebase. After dropwise addition of 1 equivalent trichloroacetonitrile the reaction is conducted at room temperature for 18 h. The residue left behind after removing the solvent *in vacuo* is Soxhlet-extracted with PE to separate sticky pinkish-brown impurities from the crude product. The product crystallizes from PE-solution upon cooling to 4°C as shiny colorless platelets, yielding amidine **7** at 52% of theory.

2.1.4.2. Synthesis of precursor trichloromethyl triazine 8

To prepare the precursor triazine **8**, in a one-pot procedure one of the imino groups of amidine **7** is acetylated and cyclization effected by condensing the introduced carbonyl group with the remaining imino functionality.

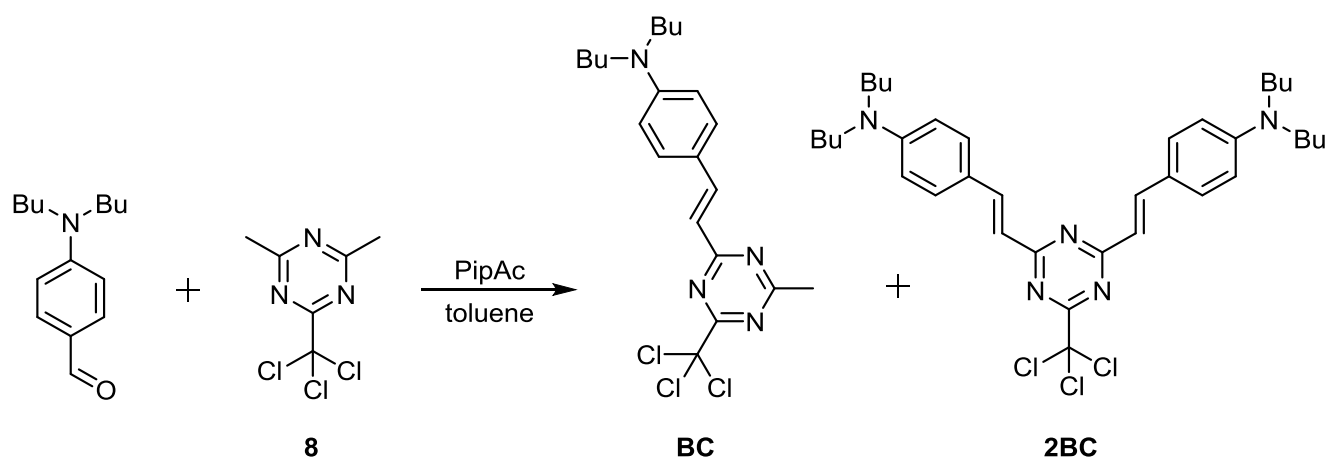


Amidine **7** was dissolved in Ac_2O and held at reflux for 1.5 h before pouring the reaction mixture into water containing ice, leading to the product separating as impure brown crystals. The patent suggests recrystallization from aqueous acetonitrile, however this is not a suitable method as the bp of the water/acetonitrile azeotrope is around 77°C , well above the melting point of triazine **8** stated to be $69 - 71^\circ\text{C}$.¹⁸³ Instead, pure triazine **8** was obtained in a yield of 59% of theory as colorless crystals by Kugelrohr distillation of the crude product.

2.1.4.3. Synthesis of 2BC and side product BC

In contrast to the synthesis of triazine 2PIs **BTrz** - **3BTrz** (Figure 42), the Knoevenagel condensation of the precursor triazine with 4-(dibutylamino)-benzaldehyde cannot be performed with KOH in MeOH. The trichloromethyl-group is lost in this reaction because of its liability to nucleophilic substitution by OH^- and MeO^- -ions, due the electron-deficient 1,3,5-triazine being prone to nucleophilic attack and the CCl_3^- -carbanion being a good nucleofuge owing to the inductive effect of the electronegative chlorine atoms.

A patent describing the preparation of chromophore substituted bis(trichloromethyl)-triazines mentions the use of piperidinium acetate (PipAc) as a catalyst.¹⁶⁶



The procedure¹⁶⁶ of melting precursor triazine and 4-(dibutylamino)benzaldehyde in the presence of PipAc and keeping the mixture at 140°C led to good yields after only a few hours in case of **BTrz** - **3BTrz**.⁷⁷ However, this method could not be used in the synthesis of **2BC** - products with the trichloromethyl-group replaced by piperidine

were formed *via* nucleophilic substitution, as indicated by NMR-analysis and non-cleavability of the isolated products.

In the successful synthesis of **2BC**, the mono-styrylated compound **BC** was also obtained as a side product.

To perform the condensation reaction, 1 equivalent of triazine **8**, 1.75 equivalents of 4-(dibutylamino)benzaldehyde and 0.3 equivalents of PipAc were kept at reflux in toluene for 80 h under argon atmosphere, removing the water formed in the condensation reaction by means of a Dean-Stark-trap. The reaction mixture was diluted with DCM and extracted with NH₄Cl-solution and deionized water to remove PipAc. The brown residue left upon removal of the solvents *in vacuo* was separated via column chromatography, using toluene as eluent. After elution of **2BC**, polarity was increased by using toluene with 15% Et₂O to also elute the mono-styrylated compound **BC** that is formed as an intermediate in the formation of **2BC** and possibly also acts as cleavable 2PI. Both compounds were glassy solids after removal of solvents *in vacuo* and were subsequently crystallized from n-pentane to yield pure **2BC** at 26% and **BC** at 38% of theory. It should be noted here that **2BC**, and to a lesser extent **BC**, are extraordinarily sensitive to visible light, requiring the whole synthesis, purification and handling to be conducted in a red-light laboratory with LEDs narrowly emitting around 620 nm as the sole source of light.

2.1.5. Analysis of the cleavable 2PIs **BC** and **2BC**

2.1.5.1. Photophysical properties

To evaluate the basic photophysical properties, UV/Vis spectra of the trichloromethyl-triazines should be measured and compared to reference compounds.

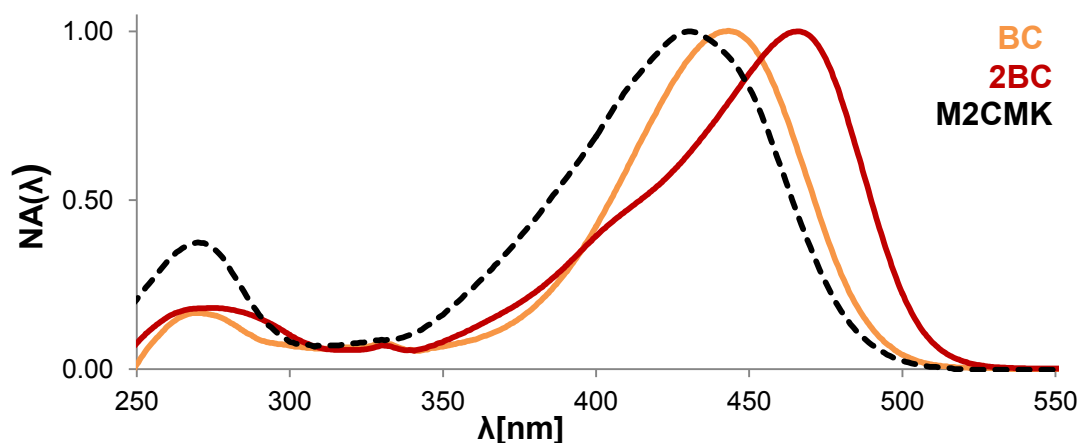


Figure 44: Normalized 1PA spectra of **BC**, **2BC** and **M2CMK** in THF solution.

The 1PA spectra of **BC** and **2BC** are shown in **Figure 44**. In comparison to the non-cleavable reference compounds⁷⁷ **BTrz** ($\lambda_{\text{abs}} = 412 \text{ nm}$, $\epsilon_{\text{max}} = 4.3 \cdot 10^4 \text{ M}^{-1}\text{cm}^{-1}$) and **2BTrz** ($\lambda_{\text{abs}} = 433 \text{ nm}$, $\epsilon_{\text{max}} = 8.0 \cdot 10^4 \text{ M}^{-1}\text{cm}^{-1}$) shown in **Figure 42**, **BC** ($\lambda_{\text{abs}} = 443 \text{ nm}$, $\epsilon_{\text{max}} = 5.2 \cdot 10^4 \text{ M}^{-1}\text{cm}^{-1}$) and **2BC** ($\lambda_{\text{abs}} = 467 \text{ nm}$, $\epsilon_{\text{max}} = 9.5 \cdot 10^4 \text{ M}^{-1}\text{cm}^{-1}$) both exhibited substantially red-shifted 1PA maxima and higher molar extinction coefficients. This is likely due to the inductive effect of the trichloromethyl-group on the triazine-ring, increasing its character as electronic acceptor and thus the intramolecular charge transfer of the push-pull systems. Compared to the quadrupolar DBK reference compound **M2CMK** ($\lambda_{\text{abs}} = 430 \text{ nm}$, $\epsilon_{\text{max}} = 4.7 \cdot 10^4 \text{ M}^{-1}\text{cm}^{-1}$), the 1PA of quadrupolar triazine **2BC** is red-shifted by 37 nm and the extinction coefficient is about twice as high.

Although the 1PA merely tails out above 500 nm, the cleavable triazine 2PIs show an extraordinary sensitivity to 1PA of visible light. A sample of **2BC** kept inside a brown glass vial decomposed within minutes, turning black, upon exposure to the ambient light of an orange light laboratory where special fluorescent tubes and filter foils ensure a cut-off of light <520 nm wavelength. When excluding light completely by covering a vial containing **2BC** kept at room temperature with aluminum foil, no such

change occurred even after days. Convenient handling of the cleavable triazine 2PIs was only possible in dark rooms with red LEDs emitting around 620 nm as the sole light source.

Due to longer irradiation times required for such experiments and the light sensitivity of the compounds resulting in formation of intensely colored decomposition products, no reliable fluorescence or 2PA spectra/cross sections were measured for **BC** and **2BC**.

2.1.5.2. 2PP structuring tests

To assay the performance of **2BC** and also **BC** as 2PIs, they should be employed in 2PP microfabrication of 3D structures at different laser intensities and writing speeds. As reference compounds, the non-cleavable triazines **2BTrz** and **BTrz** as well as the DBK 2PI **M2CMK** were tested under the same conditions.

The 2PIs were dissolved in a mixture of acrylate resins (ethoxylated-(20/3)-trimethylolpropane triacrylate (ETA) / trimethylolpropane triacrylate (TTA) molar ratio = 1:1) at a concentration of 5 $\mu\text{mol/g}$ resin and arrays of defined woodpile structures were 2PP-printed at 800 nm, varying the laser power (10 - 100 mW) and writing speed (0.32 - 100 mm/s).

During structuring, the cleavable trichloromethyl-triazine 2PIs **2BC** (**Figure 45**) and **BC** (**Figure 46**) behaved fundamentally different from the non-cleavable reference 2PIs **2BTrz** (**Figure 47**), **BTrz** (**Figure 48**) and **M2CMK** (**Figure 49**). Since LSM-images were inadequate to demonstrate the 3D-nature of the differences between the printed woodpile-structures, they were gold-sputtered and scanning electron microscopy (SEM-)images were recorded.

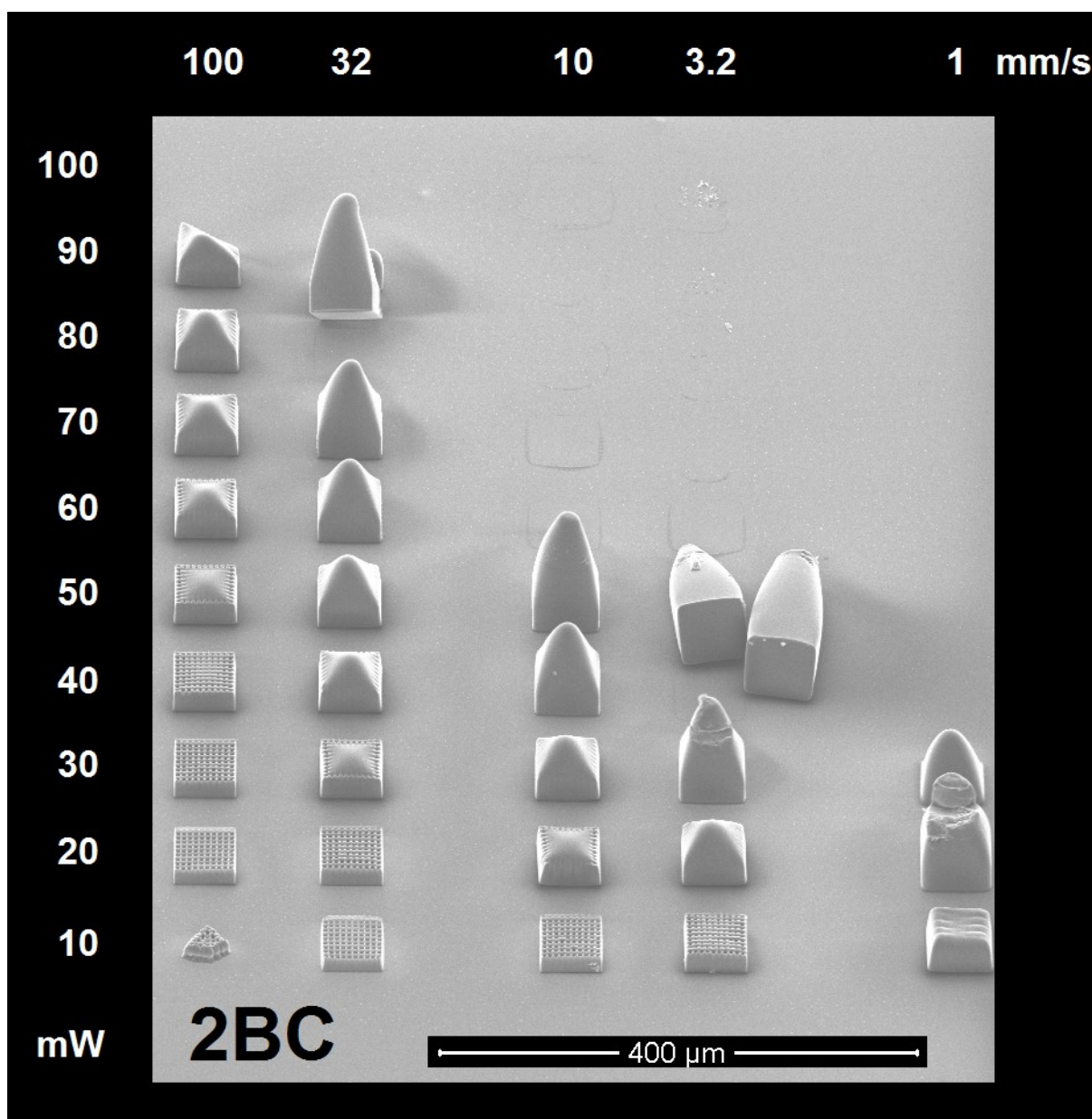


Figure 45: Woodpile-structures 2PP-printed with **2BC**.

While **2BC** clearly had the lowest polymerization threshold of the investigated compounds, with a collapsed structure visible at 10 mW laser power and the highest tested speed of 100 mm/s, the ideal processing window with woodpile structures of high quality is very small compared to the other 2PIs. At higher laser powers and lower writing speeds, a kind of overpolymerization occurred that was not previously witnessed with other 2PIs. Printed polymer lines were no longer separate from each other, but growing together and eventually forming bizarre dome-like structures of bulk polymer. The process was accompanied by the formation of dark, intensely

colored decomposition products eventually obstructing the view on the structuring process that was observed live *via* a CCD-camera. The dome-like polymer structures themselves were also colored amber to brown by these photodarkening products. Despite using a methacrylate-modified glass substrate to covalently link the polymer structures to the glass and keep them firmly attached, the high polymerization shrinkage led to spalling and loss of most of the dome-like structures in the high-energy segment of the woodpile-array printed with **2BC** (**Figure 45**).

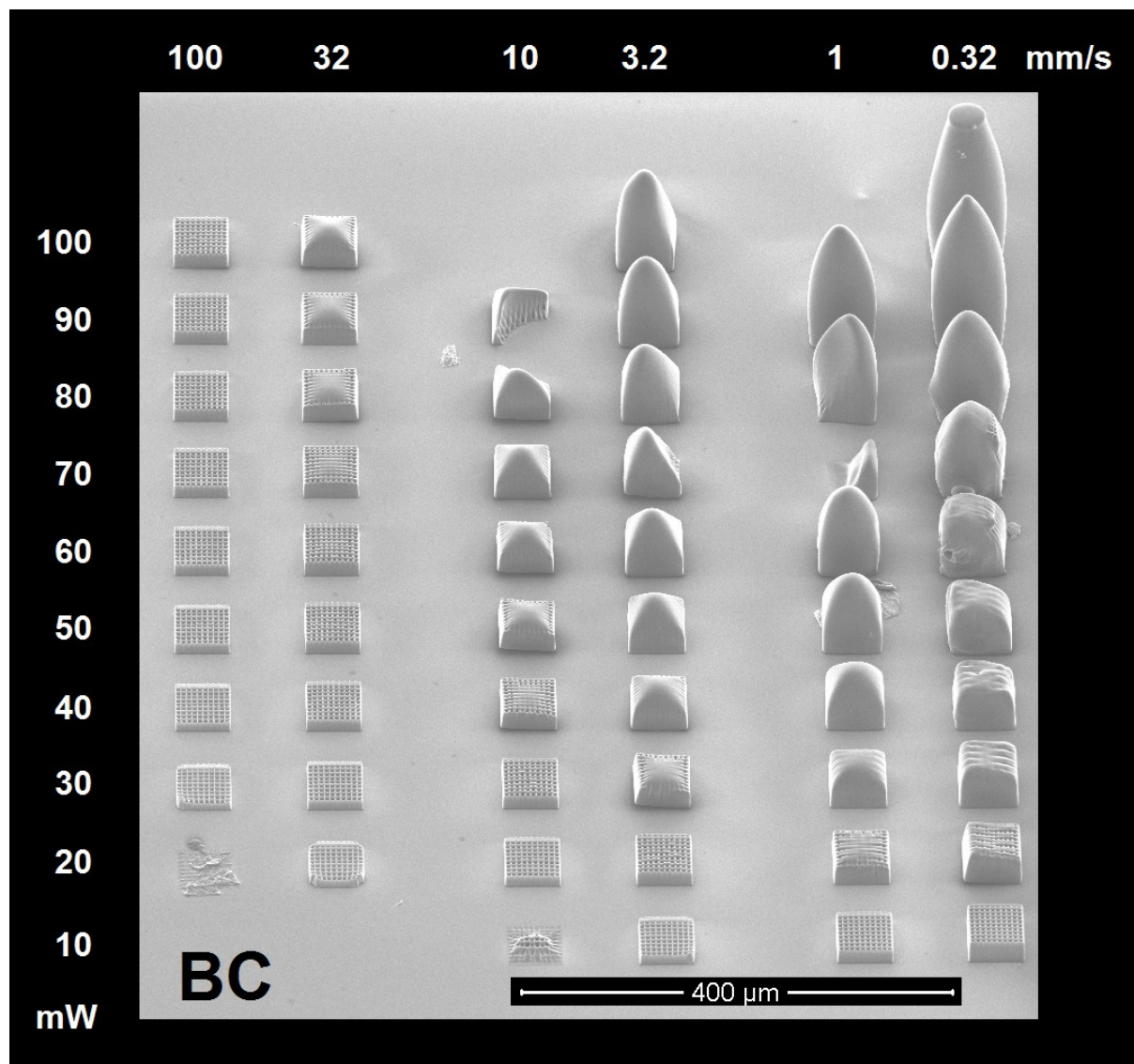


Figure 46: Woodpile-structures 2PP-printed with **BC**.

While similar photodarkening and overpolymerization processes were observed in case of **BC** (**Figure 46**), the polymerization threshold is higher (10 mW at 10 mm/s and 20 mW at 100mm/s) and the complete loss of printing resolution is also shifted to

higher energies. This is presumably due to the smaller conjugated π -system associated with **BC** lacking one of the two aminostyryl-groups of **2BC**, resulting in less efficient 2PA. The dome-structure printed at 100 mW and 0.32 mm/s grew to a multiple of the intended height of the woodpile-structure, touching the cover slide opposing the glass substrate and leading to a planar "tip" of the structure (**Figure 46**). The dome-like structures observed at higher laser energies in case of the trichloromethyl-triazine 2PIs all grew along the beam propagation direction of the laser, far outside the voxel of laser intensity sufficiently focused to facilitate 2PP. A plausible explanation for this behavior is that the dark decomposition products formed at higher laser energies spread by diffusion, leading to 1PA of the NIR laser light and subsequently to photo- or even thermal polymerization of the acrylate resin through local overheating.

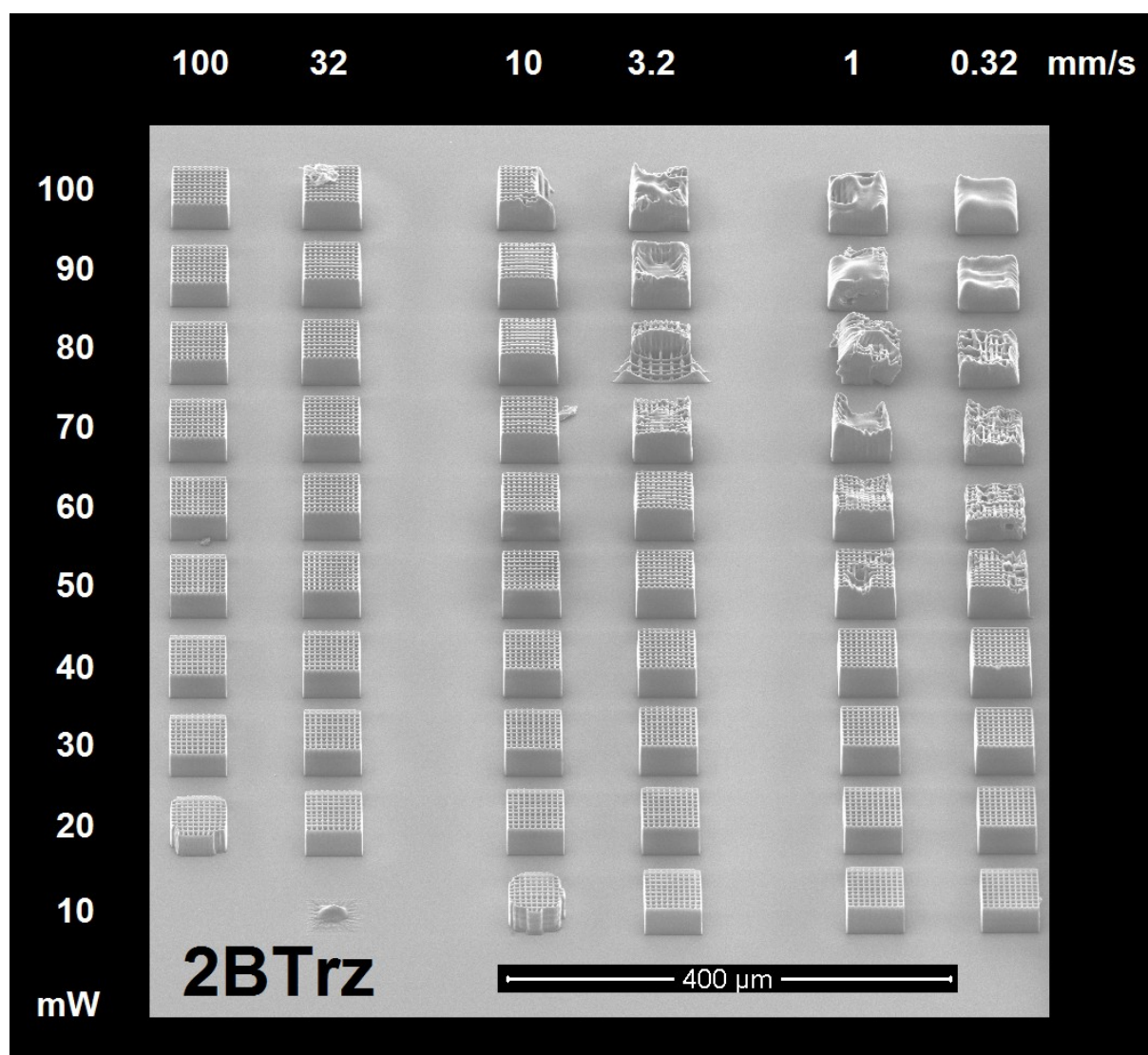


Figure 47: Woodpile-structures 2PP-printed with **2BTrz**.

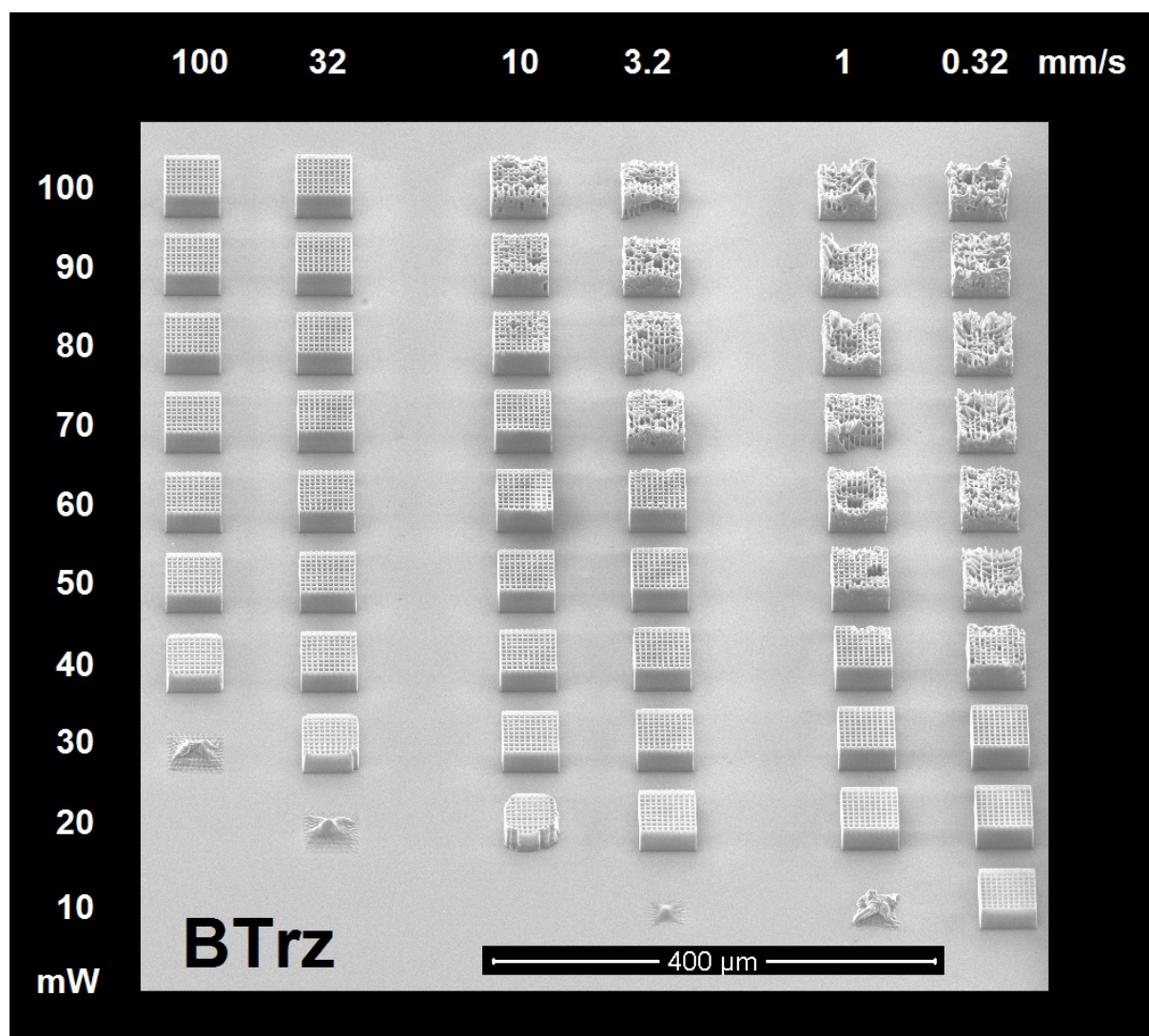


Figure 48: Woodpile-structures 2PP-printed with **BTrz**.

No similar effects were observed with any of the reference 2PIs. While the polymerization thresholds of **2BTrz** and **M2CMK** were comparable, slightly higher than the threshold of **2BC** and lower than **BC** and **BTrz**, **2BTrz** had the largest processing window for well-defined woodpile-structures. Due to the atypical overpolymerization effects, all of the reference 2PIs, even **BTrz**, had larger ideal processing windows than the trichloromethyl-triazine 2PIs.

In conclusion, because of these uncontrollable effects the cleavable trichloromethyl-triazine 2PIs are not suitable for 2PP-printing of well-defined structures. Furthermore the extreme sensitivity to visible light, requiring red-light laboratories with narrow-band light sources only, make the handling of compounds such as **2BC** inconvenient in comparison to established 2PIs. Since it is assumed that the behavior of water-

soluble derivatives would not be fundamentally different, the development of halomethyl-triazine 2PIs was abandoned in favor of different cleavable systems.

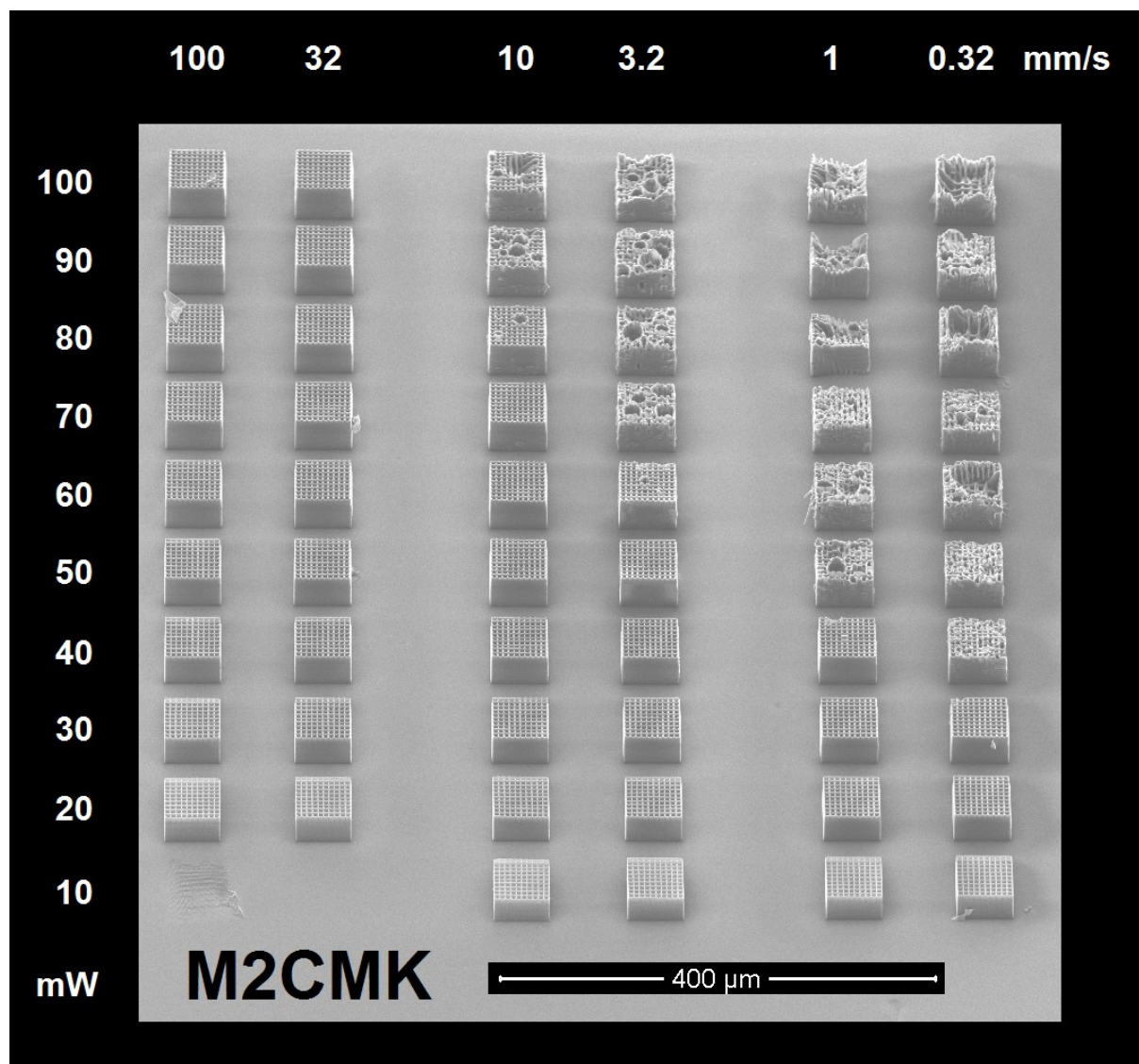


Figure 49: Woodpile-structures 2PP-printed with **M2CMK**.

2.2. Cleavable 2PIs based on diazosulfones and diazosulfonates

2.2.1. Basics of cleavable azo initiators

The quantum chemical calculations performed for **2BC** (Figure 41) indicated the importance of the positive entropy associated with homolytic cleavage of one 2PI molecule into two radicals, making the endothermic process exergonic and thus spontaneous.

This entropy increase is particularly relevant as a driving force in case of some initiators that form multiple radicals as well as a gaseous reaction product (e.g. nitrogen) with high entropy. VA-086, an aliphatic azo initiator that recently was successfully used in UV-encapsulation of live cells,³¹ is structurally similar to the well known initiator 2,2'-azobis(isobutyronitrile) (AIBN) that has been widely used to initiate radical polymerization. Azo initiators such as VA-086 or AIBN can be cleaved thermally or photolytically, resulting in two carbon-based radicals and gaseous nitrogen (Figure 50).

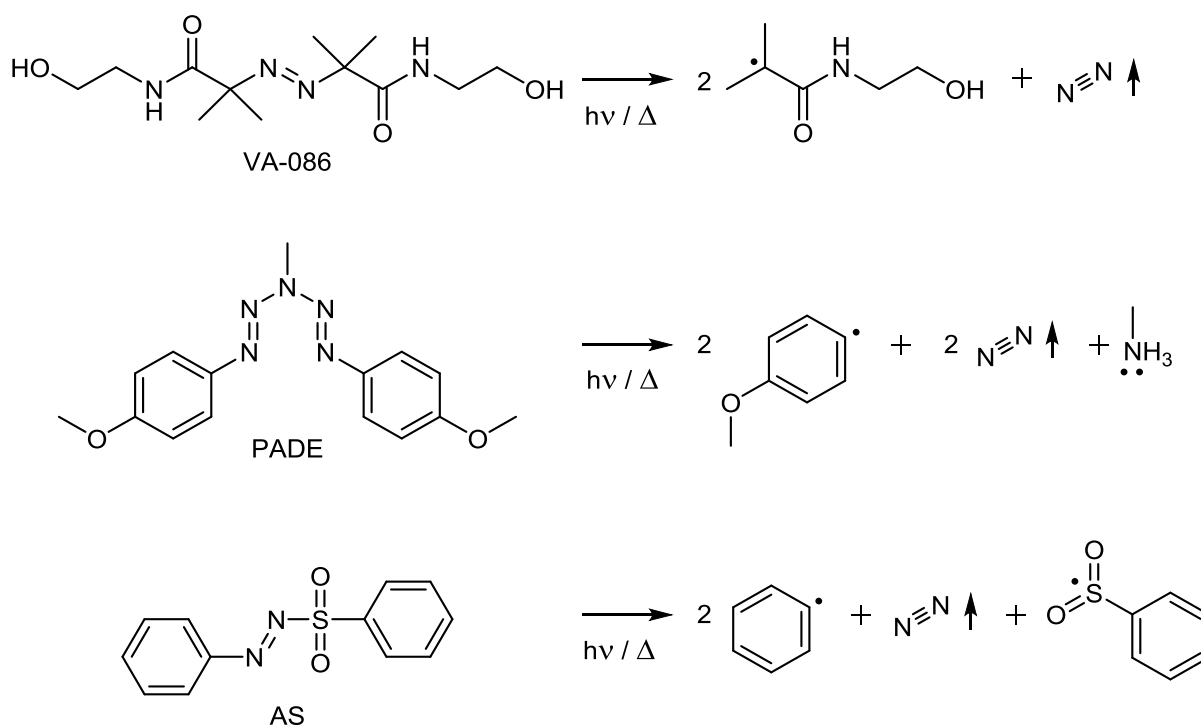


Figure 50: Reaction products resulting from thermal- or photoinduced cleavage of initiators containing an azo-group.¹⁸⁴

Pentaaza-1,4-dienes such as PADE (**Figure 50**), cleaving under formation of phenyl-radicals, have been successfully used in the photopolymerization of acrylates,¹⁸⁵ and also been tested in 2PP-printing in previous work.⁷⁷ Although the cleavability of PADE could be directly observed under 2PP conditions through its formation of nitrogen bubbles, the performance as 2PI was not satisfactory, with high polymerization thresholds and unacceptable quality of printed woodpile test-structures. Preliminary attempts to replace the methoxy-substituents of PADE with dimethylamino-groups to increase σ_{2PA} lead to a compound that was so unstable that it could not be isolated.

Aryl diazosulfones (e.g. AS, **Figure 50**) are a further class of azo-group containing substances that can act as radical initiators. Besides gaseous nitrogen, their cleavage leads to phenyl- and sulfonyl-based radicals that can initiate polymerization.

2.2.2. Literature-known diazosulfones and diazosulfonates as cleavable 2PIs

The array of purposes diazosulfones (**Figure 51 - left**) and the closely related, water-soluble diazosulfonates (**Figure 51 - right**) have been employed for is diverse, ranging from building blocks and reagents in organic synthesis^{186–189} to radical polymerization,^{190,191} spin traps,¹⁹² film coatings,¹⁹³ diazo copying¹⁹⁴ and fungicides.¹⁹⁵



Figure 51: Structural motifs of diazosulfones (**left**) and diazosulfonates (**right**).

The application of a biocompatible, water-soluble diazosulfonate 2PI is of particular interest when considering the tentatively assumed mechanism of 2PP initiation considered for established bimolecular initiators such as **P2CK**. Through a cyclic mechanism of electron transfer to and back electron transfer from the monomer (see **Figure 34**), one "classical" 2PI molecule could be 2PA excited multiple times, each time also potentially generating cytotoxic ROS besides initiating radicals (see **Figure 35**). Radical formation via fast homolytic cleavage leaves less time for bimolecular side reactions such as the generation of ROS. Compared to the cleavable trichloromethyl-triazine based 2PIs described above, cleavable diazosulfonates pose an additional advantage in that regard. While **2BC** and **BC** retain a chromophore system still capable of 2PA (compare reference compounds **2BTrz** and **BTrz**) even after dissociation of all three C-Cl bonds, 2PA-induced cleavage of diazosulfones and diazosulfonates leads to an irreversible decomposition of the chromophore, avoiding the possibility of multiple cycles of ROS-generation after the first successful formation of initiating radicals.

Although patent literature does mention radical photopolymerization induced by diazosulfones,¹⁹¹ only an account of thermally activated polymerization of methyl methacrylate was found in a research paper.¹⁹⁰ The compound used there was (3-methylphenyl)azophenylsulfone ($\lambda_{\text{abs}} = 302 \text{ nm}$, $\epsilon_{\text{max}} = 15.1 \cdot 10^4 \text{ M}^{-1}\text{cm}^{-1}$ in CHCl_3), which performed similar to AIBN as thermal initiator. The same publication also

describes (4-methoxyphenyl)azophenylsulfone ($\lambda_{\text{abs}} = 349 \text{ nm}$, $\epsilon_{\text{max}} = 22.6 \cdot 10^4 \text{ M}^{-1} \text{ cm}^{-1}$ in CHCl_3), however mentions nothing about its initiation capabilities. A kinetic study on the thermolysis of diazosulfones found that electron-donating substituents on the phenylazo-group strongly influence the rates of thermal decomposition, with the decomposition temperatures of the solid compounds being around 70°C for the 3-methyl-, 110°C for the 4-methoxy- and 130°C for the 4-(dimethylamino)-derivative respectively.¹⁹⁶

An ideal 2PI should be efficiently excited and form radicals *via* 2PA while being as thermally stable as possible. So it is serendipitous that the 4-(dimethylamino)-derivative has the highest thermal stability in the series, as its 1PA maximum (not stated in literature, a publication from 1977 mentions the UV-spectrum not being recorded because of instability under the measurement conditions¹⁸⁹) likely corresponds better to the intended 2PA wavelength of 800 nm than that of e.g. the 4-methoxy-derivative.

Two simple 4-(dimethylamino)-derivatives, the diazosulfone **AS1** and the water-soluble diazosulfonate **AS2** (**Figure 52**), have been long known in literature^{196,197} but have not yet been tested as PIs. Thus, quantum chemical calculations are used to confirm that photocleavage is energetically favorable, and **AS1** as well as **AS2** should be prepared and their properties and performance as 2PIs investigated.

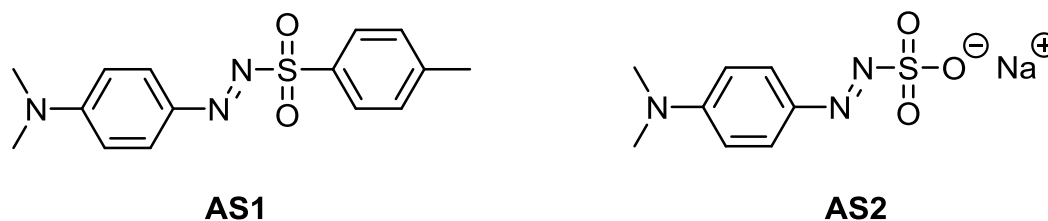


Figure 52: Literature-known^{196,197} diazosulfone **AS1** and diazosulfonate **AS2**.

2.2.2.1. Quantum chemical calculations to predict cleavability of AS1 and AS2

Quantum chemical calculations were carried out in close cooperation with Prof. Tom Scherzer and Sergej Naumov from the Leibniz Institute for Surface Modification (IOM) in order to confirm the homolytic cleavability of **AS1** and **AS2**. **Figure 53** shows that **AS1** is a metastable compound, with its spontaneous decomposition from the ground state being only kinetically hindered. The cleavage after 2PA, ISC to T_2 and radiationless transition to optimized triplet geometry, is also strongly exergonic.

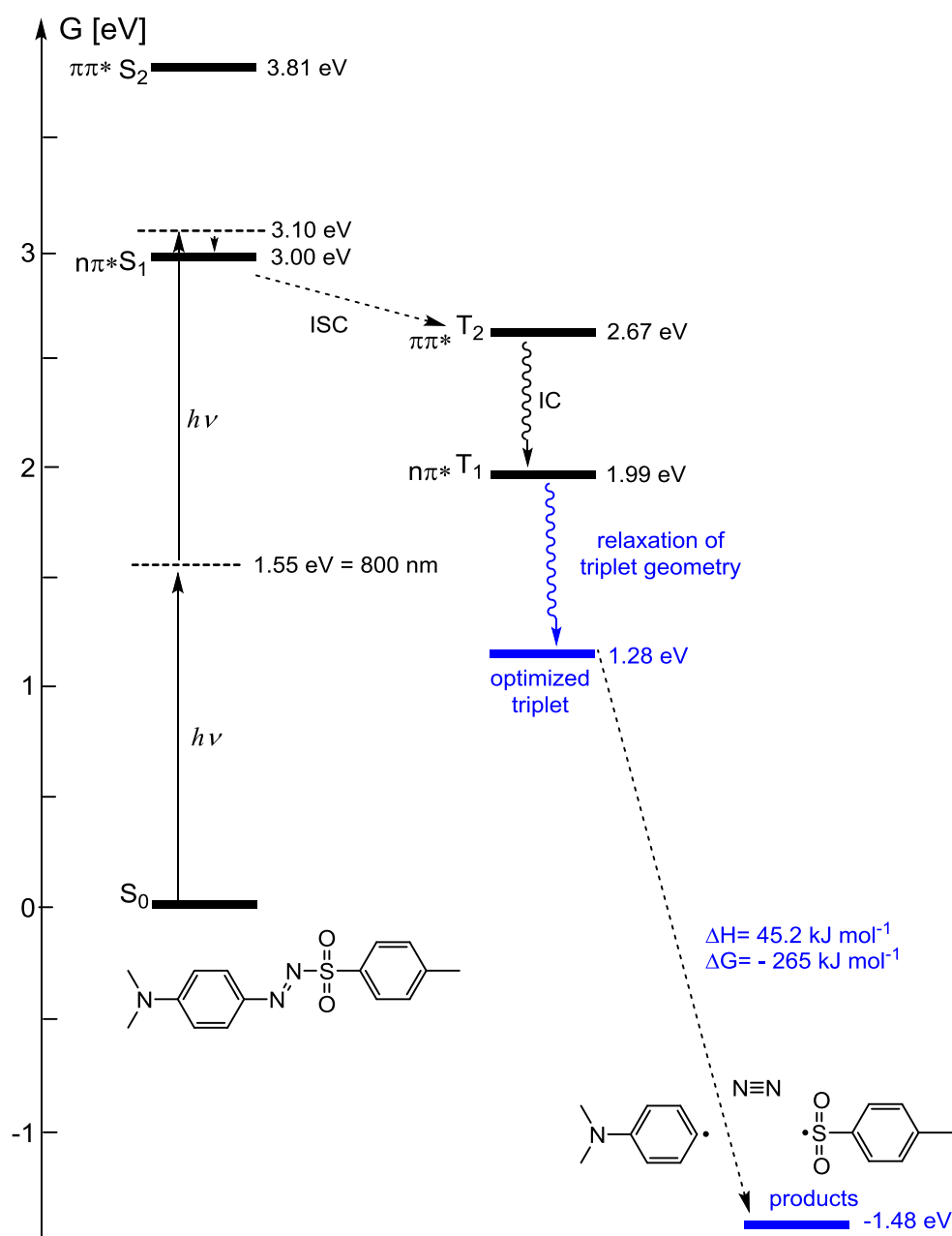


Figure 53: Calculated Jablonski-Scheme for **AS1**. Axis shows Gibbs free energy.

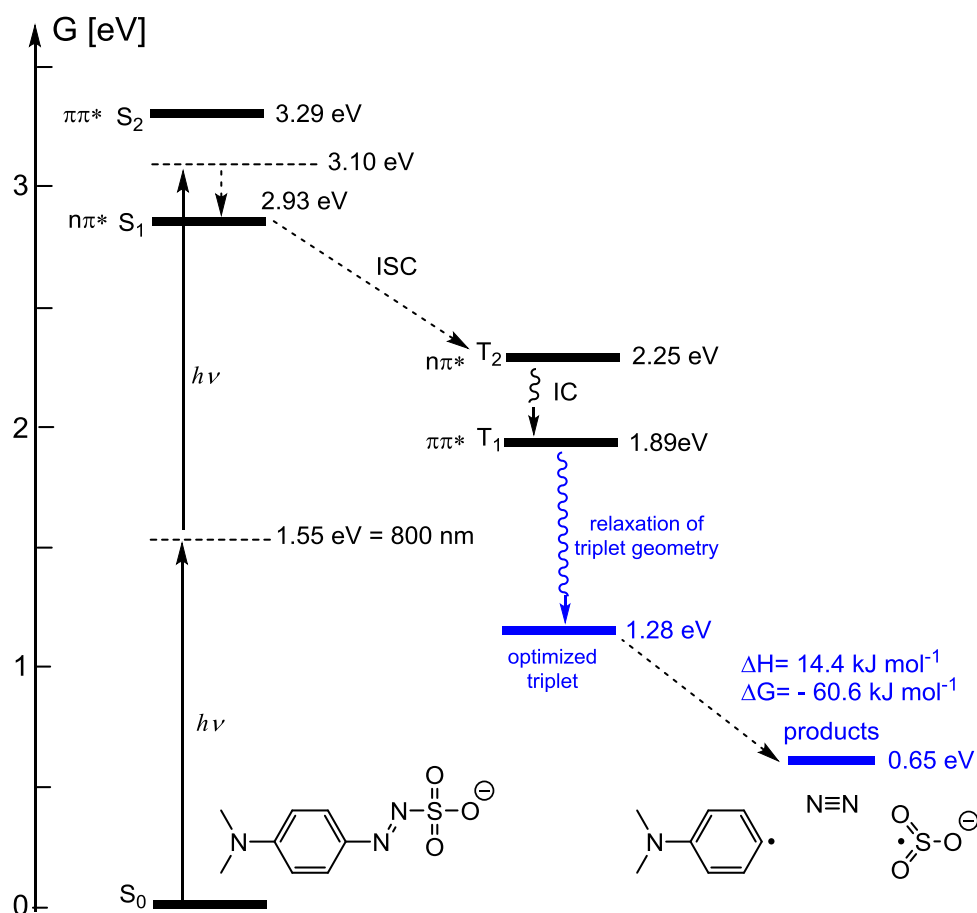


Figure 54: Calculated Jablonski-Scheme for **AS2**. Axis shows Gibbs free energy.

Figure 54 demonstrates that in contrast to **AS1**, **AS2** is a stable compound regarding the decomposition under homolysis of the C-N- and S-N-bonds to the azo group. Although the dissociation of **AS2** into nitrogen and radicals is far less exergonic at $\sim -61 \text{ kJ mol}^{-1}$ in comparison to **AS1** at -265 kJ mol^{-1} . While the cleavage reaction of **2BC** (**Figure 41**) is roughly as endothermic as the cleavage of **AS1** and about 3 times as endothermic as the dissociation of **AS2**, it is clear that the entropy of formation of gaseous nitrogen is a major driving force making photocleavage significantly more exergonic compared to the trichloromethyl-triazines.

It should be noted that while for both **AS1** and **AS2** S1 is predicted to be of n,π^* -nature, the lowest excited triplet T_1 from which cleavage occurs is n,π^* for **AS1** and π,π^* in case of **AS2**, which could be attributed to the difference in electron distribution caused by the presence of the negatively charged oxygen-atom in **AS2**.

2.2.2.2. Synthesis of AS1 and AS2

Both diazosulfones and diazosulfonates are known since the late 19th century. They are prepared by coupling diazonium salts of the corresponding amines with alkali arylsulfonates or alkali sulfites, respectively.¹⁹⁰

The synthetic pathways to **AS1** and **AS2** are shown in **Figure 55**. The dihydrochloride of *N,N*-dimethyl-1,4-phenylenediamine is first converted to diazonium salt **9**, which acts as the common precursor for both **AS1** and **AS2**.

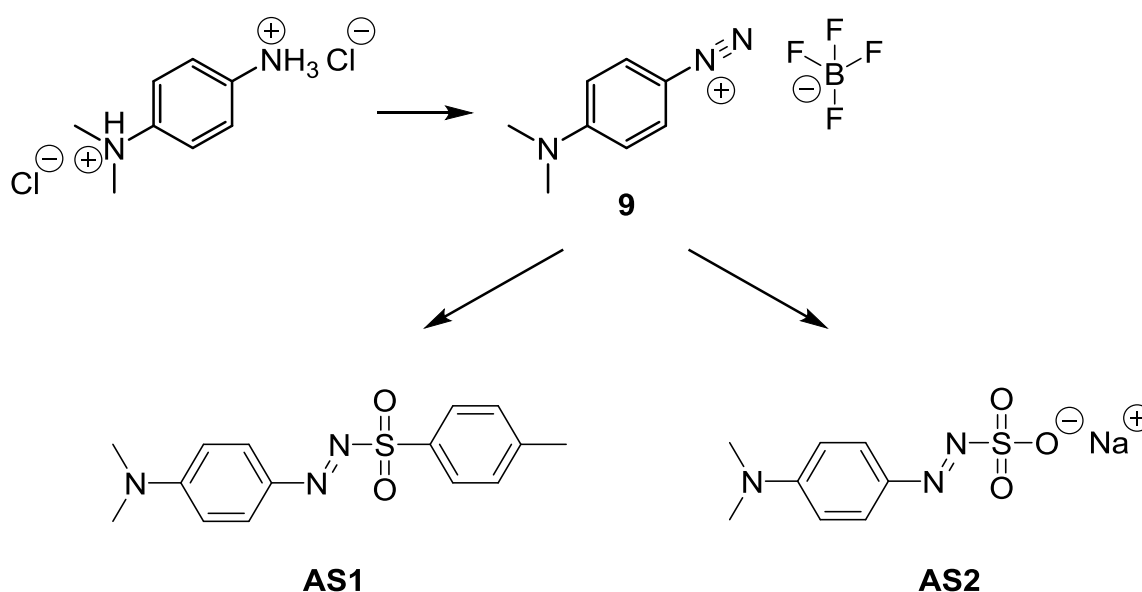


Figure 55: Synthetic pathways to **AS1** and **AS2**.

2.2.2.2.1. Synthesis of precursor diazonium salt **9**

Diazonium salts are important intermediates e.g. in the synthesis of aromatic azo compounds that are widely used as dyes, pigments, therapeutic agents etc.¹⁹⁸ For this application, aromatic amines are typically diazotized with NaNO₂ in strongly acidic aqueous solution (**Figure 56**). The nature of the counter-ion of the diazonium salt strongly influences its stability.¹⁹⁸ If HCl is used as mineral acid, the resulting diazonium chlorides are usually not isolated but immediately converted through further reactions in a one-pot procedure, as they are unstable and can decompose explosively.

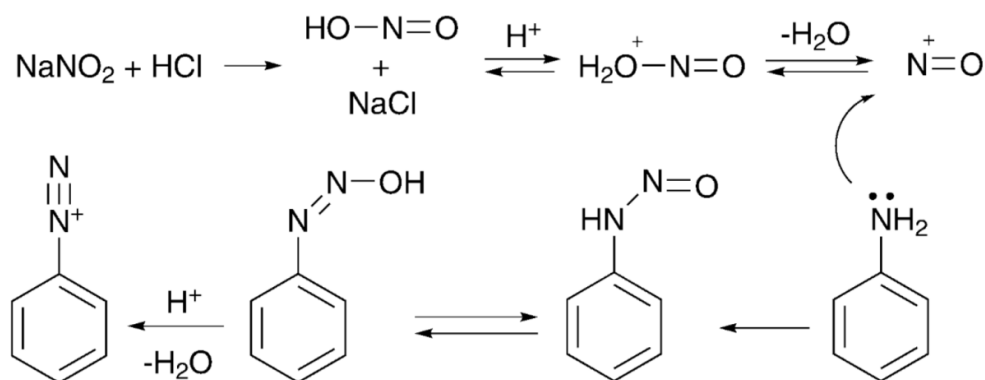
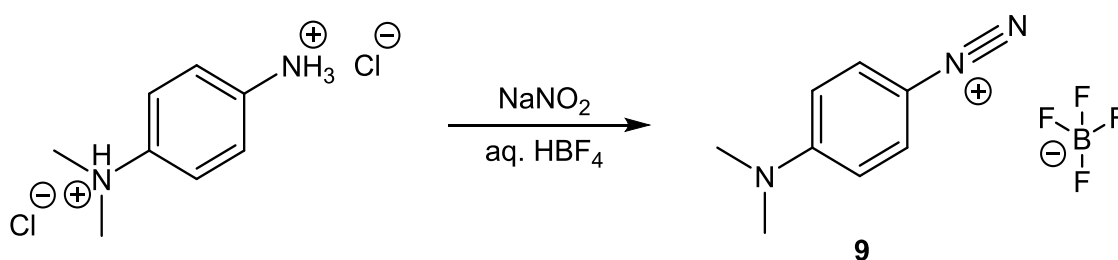


Figure 56: The reactive nitrosonium cation is formed *via* protonation of NaNO_2 and subsequently converts aniline to the benzenediazonium cation.¹⁹⁸

More conveniently, salts such as tetrafluoroborates, disulfonimides, hexafluorophosphates and zinc chlorides are stable in the solid form and can be stored for long periods of time.¹⁹⁸ Diazonium tetrafluoroborates are remarkably stable and insensitive to shock as dry solids, and many can be handled safely in quantities of several kilograms.¹⁹⁹

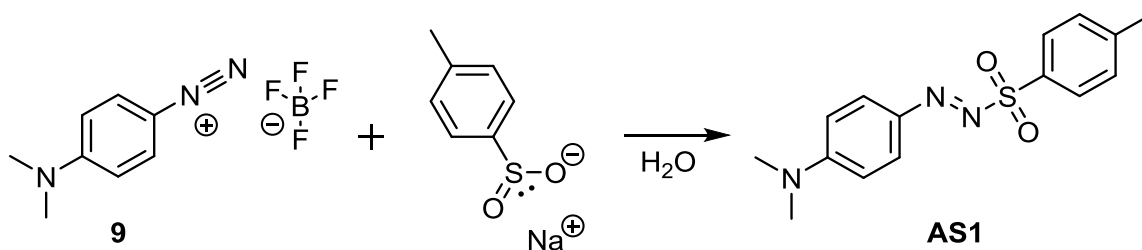
Thus, diazonium tetrafluoroborate **9** was chosen as suitable precursor for **AS1** and **AS2**, and prepared according to literature.²⁰⁰



A solution of *N,N*-dimethyl-1,4-phenylenediammonium dichloride in 20% aq. HBF_4 was treated with NaNO_2 at a temperature between 0 - 5°C and the resulting precipitate washed with 5% aq. HBF_4 , MeOH and Et_2O . Diazonium salt **9** was obtained as deeply yellow, light sensitive ($\lambda_{\text{abs}} = 380 \text{ nm}$, $\epsilon_{\text{max}} = 40.3 \cdot 10^4 \text{ M}^{-1} \text{ cm}^{-1}$)²⁰⁰ powder at a yield of 81% of theory.

2.2.2.2. Synthesis of AS1

Diazosulfones can be obtained in a one-pot procedure from anilines by diazotization using NaNO_2 and HCl , buffering the filtered solution with sodium acetate and finally adding sodium p-toluenesulfinate (NaTS).¹⁸⁹ However, in contrast to other diazosulfones, in case of **AS1** two publications specifically recommend the isolation of diazonium tetrafluoroborate **9** and subsequent reaction with NaTS in neutral aqueous solution.^{189,196}

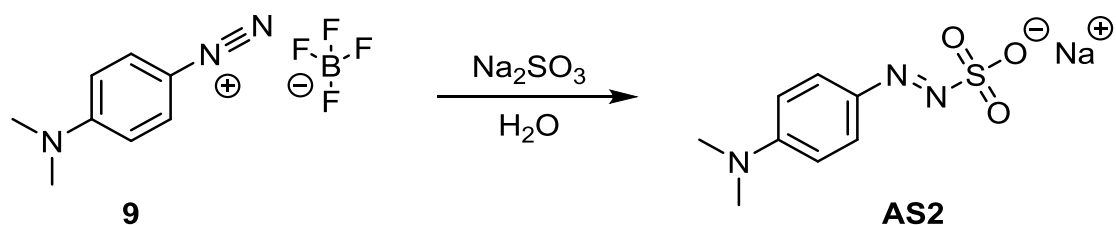


Thus, for the synthesis of **AS1**, 1 equivalent of diazonium salt **9** was suspended in water and an aqueous solution of 1.1 equivalents NaTS was added dropwise under magnetic stirring. After allowing the reaction to complete for 18 h at room temperature, the resulting dark orange precipitate is collected and recrystallized from EA. Care is taken to work quickly, as prolonged heating during recrystallization leads to decomposition of **AS1**, resulting in formation of impurities that darken the color of the solution and eventually separate as brown oily droplets that contaminate the recrystallized product.

AS1 can also be obtained by reacting diazonium salt **9** with NaTS in DCM suspension and removing unreacted solids from the resulting DCM-solution of **AS1** by filtration, however the crude product obtained *via* this method was less pure compared to the water-based method.

2.2.2.2.3. Synthesis of AS2

A facile synthesis of **AS2** and substituted derivatives studied for the use in a photographic development system was described in literature.²⁰¹



An aqueous solution of 1.1 equivalents Na_2SO_3 is added dropwise to a suspension of 1 equivalent diazonium salt **9** in water. The reaction mixture is heated to 70°C and stirring continued for 1h. The product crystallizes upon cooling and is purified by recrystallization from deionized water at 70°C . Although care was taken to avoid excessive heating in both cases, it should be noted here that **AS2** is considerably more thermally stable with a decomposition temperature above 260°C vs 140°C for **AS1**.

2.2.2.3. Analysis of the cleavable 2PIs AS1 and AS2

2.2.2.3.1. Photophysical properties

To investigate their basic photophysical properties, UV/Vis and 2PA spectra of **AS1** and **AS2** should be measured and compared to the DBK reference compounds **M2CMK** and **P2CK** (Figure 57).

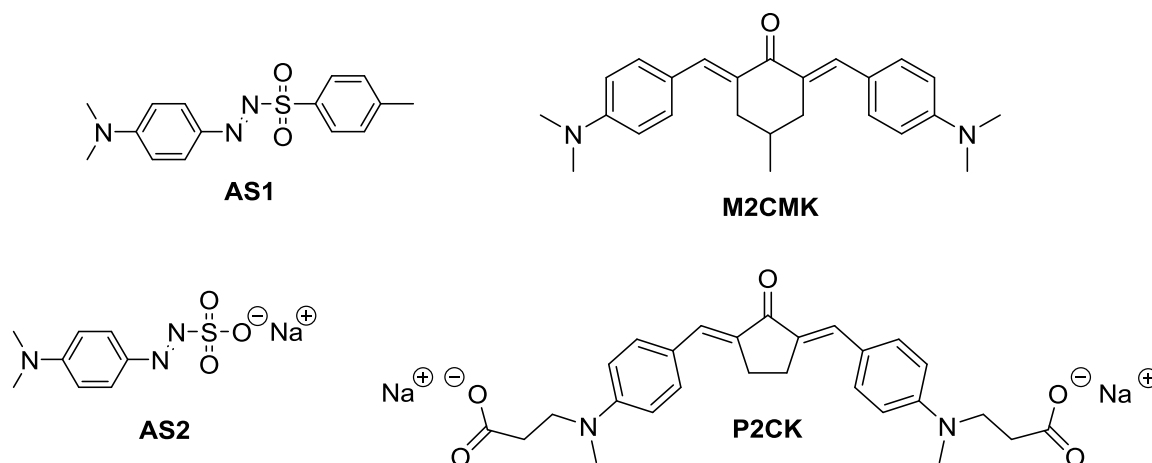


Figure 57: Chemical structures of **AS1** and **AS2**, and the DBK references **M2CMK** and **P2CK**.

The 1PA spectra of **AS1** and **AS2** as well as the references **M2CMK** and **P2CK** are depicted in Figure 58. The organo-soluble **AS1** ($\lambda_{\text{abs}} = 431 \text{ nm}$, $\epsilon_{\text{max}} = 3.0 \cdot 10^4 \text{ M}^{-1} \text{cm}^{-1}$) has its 1PA maximum almost at the same wavelength as reference **M2CMK** ($\lambda_{\text{abs}} = 430 \text{ nm}$, $\epsilon_{\text{max}} = 4.7 \cdot 10^4 \text{ M}^{-1} \text{cm}^{-1}$). The absorption coefficient of **AS1** is considerably smaller though, possibly due to a reduced size of the conjugated π -system compared to **M2CMK**.

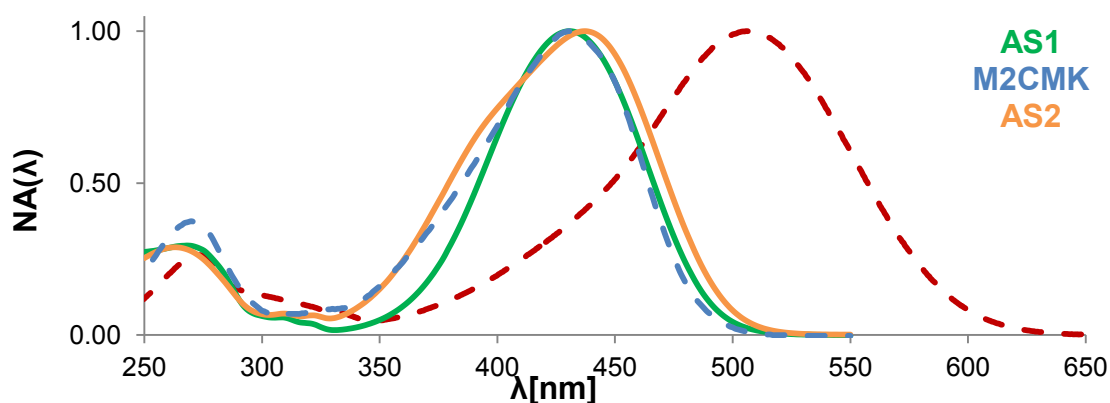


Figure 58: Normalized 1PA spectra of **AS1** and **M2CMK** (in THF solution) as well as **AS2** and **P2CK** (in PBS solution).

The water-soluble **AS2** ($\lambda_{\text{abs}} = 437 \text{ nm}$, $\epsilon_{\text{max}} = 2.4 \cdot 10^4 \text{ M}^{-1}\text{cm}^{-1}$) has a similar, slightly red-shifted 1PA maximum **AS1** and **M2CMK**, although a direct comparison between the compounds based on these spectra is difficult due to difference in polarity between THF and the water-based PBS. In comparison to the water-soluble reference 2PI **P2CK** ($\lambda_{\text{abs}} = 506 \text{ nm}$, $\epsilon_{\text{max}} = 5.5 \cdot 10^4 \text{ M}^{-1}\text{cm}^{-1}$), the 1PA of **AS2** is blue-shifted almost 70 nm, and less than half as intense.

In cooperation with Prof. Wolfgang Husinsky and Aliasghar Ajami from the Institute of Applied Physics, TU Wien, white light continuum (WLC) 2PA spectra of the compounds were also measured and are shown in **Figure 59**.

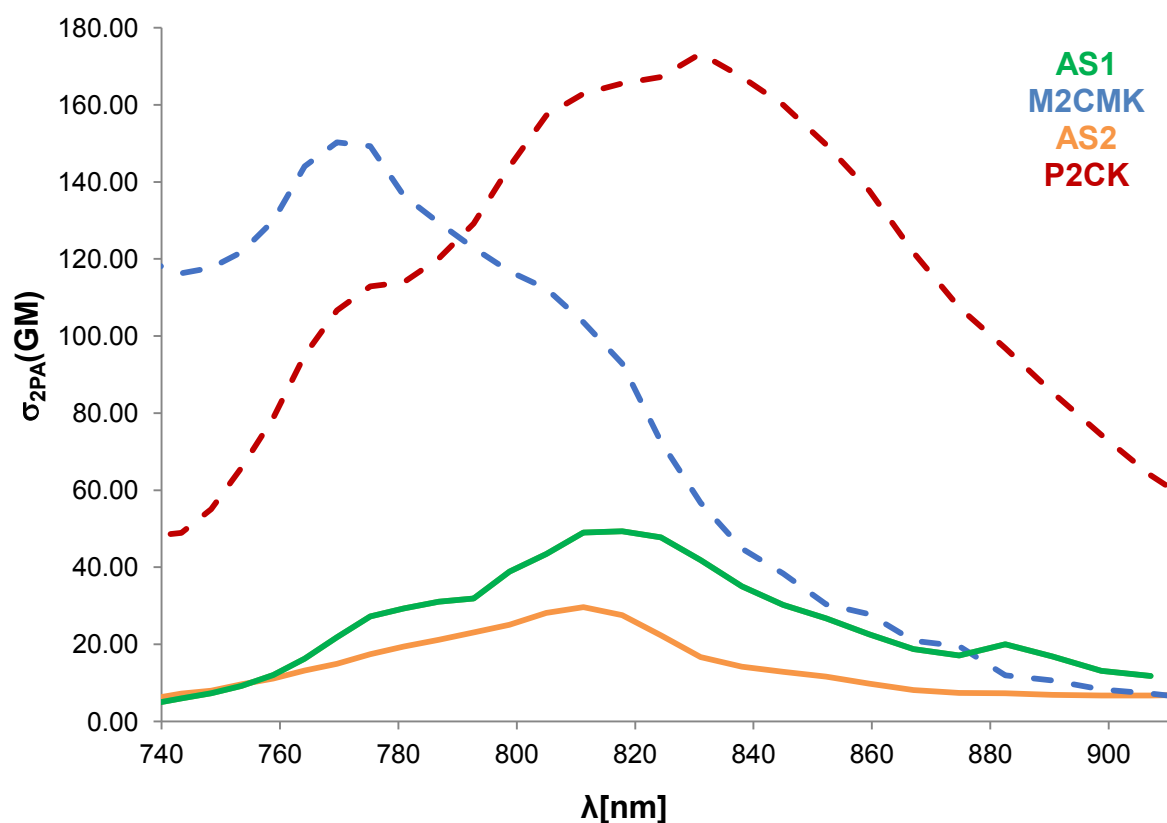


Figure 59: WLC 2PA spectra of **AS1** and **M2CMK** (in THF solution) as well as **AS2** and **P2CK** (in PBS solution).

Both **AS1** ($\lambda_{2PA} = 818 \text{ nm}$, $\sigma_{2PA} = 49 \text{ GM}$) and **AS2** ($\lambda_{2PA} = 811 \text{ nm}$, $\sigma_{2PA} = 30 \text{ GM}$) exhibit only a fraction of the σ_{2PA} of the DBK reference compounds **M2CMK** ($\lambda_{2PA} = 770 \text{ nm}$, $\sigma_{2PA} = 150 \text{ GM}$) and **P2CK** ($\lambda_{2PA} = 831 \text{ nm}$, $\sigma_{2PA} = 173 \text{ GM}$), likely a result of the small conjugated π -systems of the azo compounds.

2.2.2.3.2. 2PP structuring tests

In order to assess the performance of **AS1** and **AS2** as 2PIs, arrays of 3D test structures should be 2PP-fabricated at different laser intensities and writing speeds.

For the organo-soluble **AS1**, **M2CMK** was chosen as the reference 2PI and a mixture of acrylate resins (ETA/TTA = 1:1) as the material for the formulations. To account for the different size π -systems of the 2PIs, **AS1** was applied at 10 $\mu\text{mol/g}$ resin and **M2CMK** only at 5 $\mu\text{mol/g}$, a concentration commonly used for this reference. Similar to **M2CMK**, **AS1** did not readily dissolve in the acrylate resin mixture, and acetone was added as a co-solvent that is then removed *in vacuo* before 2PP-printing. The attempt to aid dissolution by ultrasonication of the mixture at 40°C for 20 min led to formation of a viscous polyacrylate gel, indicating that **AS1** also acts as a thermal initiator. Thus, for **AS1** a larger amount of acetone had to be used, and dissolution of the 2PI as well as removal of the co-solvent were performed at room temperature.

Arrays of defined woodpile structures were 2PP-printed at 800 nm with **AS1** and **M2CMK** (**Figure 60** and **Figure 62**), varying the laser power (10 - 150 mW) and writing speed (20 - 200 mm/s). For visual assessment of the structure quality, LSM-imaging of residual 2PI autofluorescence was employed as a time efficient alternative to recording SEM-images that require careful drying and gold-sputtering of the printed structures.

While **M2CMK** led to acceptable printing results even at the lowest energy of 10 mW at 200 mm/s, the polymerization threshold for **AS1** was quite high, at 60 mW for the tested speed range. The first good quality structures with no defects such as collapsed edges were obtained at a laser power of 100 mW. Conforming with the higher polymerization threshold in case of **AS1**, the onset of overpolymerization effects and cavity formation in the printed structures due to decomposition of the material was also at slightly higher powers than for **M2CMK**. The performances of **AS1** and **M2CMK** were similar at laser powers above 100 mW, but the ideal processing window of **AS1** was considerably smaller than that of the reference. Thus, the performance of the DBK 2PI **M2CMK** was clearly superior, even though it was applied at only half the concentration of **AS1**.

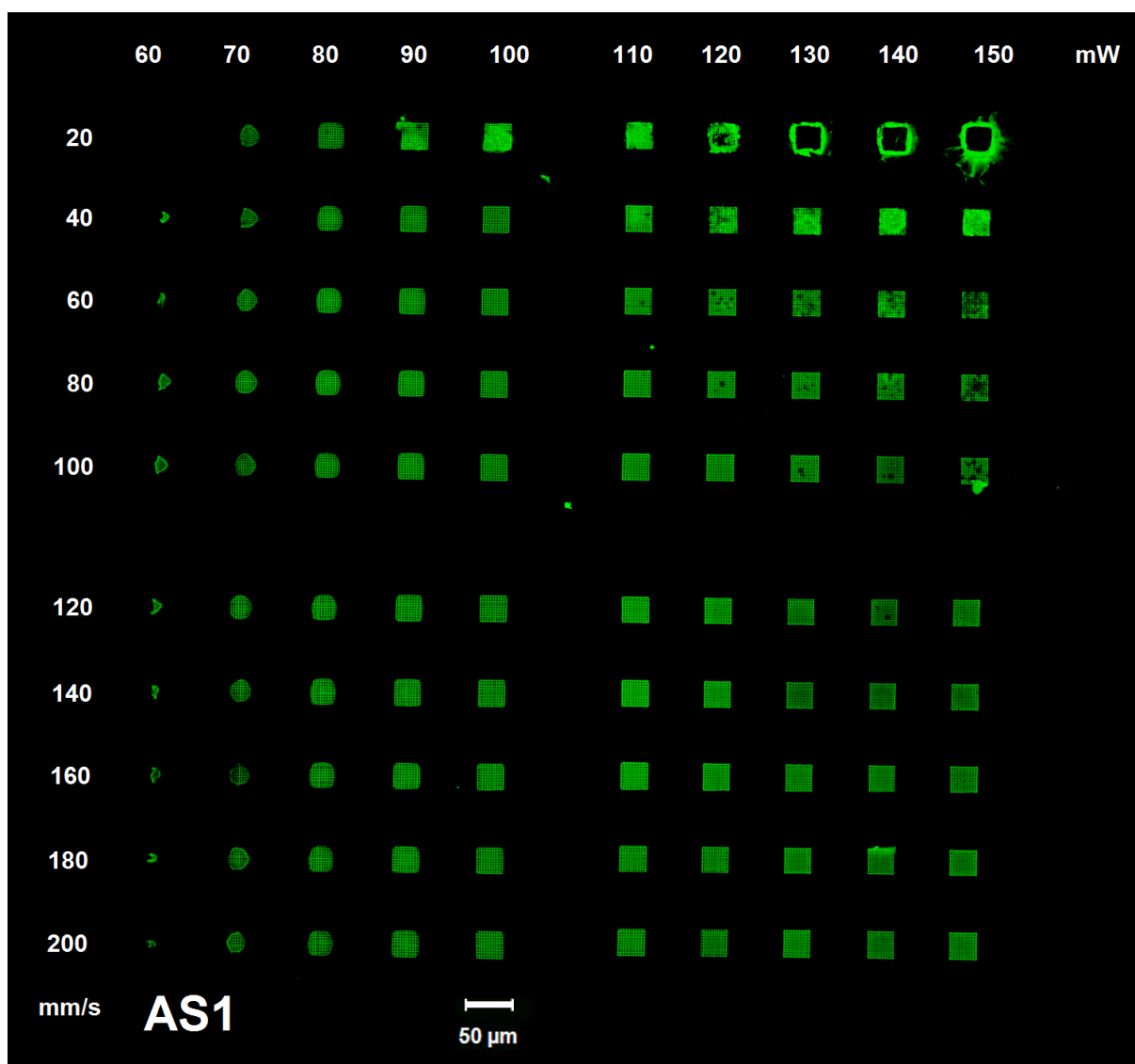


Figure 60: Woodpile-structures 2PP-printed with **AS1** (10 μmol/g resin).

In case of the water-soluble **AS2**, as similar speed-power-screening was performed in comparison to DBK reference **P2CK**. A reactive, water-miscible monomer was required, so poly(ethylene glycol) diacrylate (PEGDA700) was used at 50 wt% in PBS as the hydrogel precursor. Furthermore, due to excessive swelling and lack of mechanical stability, woodpiles are not practical as test structures for hydrogels. Instead, dense cubes were 2PP-printed with **AS2** at 8 mM (high concentration required due to low σ_{2PA}) and **P2CK** at 1 mM, varying the laser power from 10 to 120 mW and the writing speed from 20 to 200 mm/s. The LSM-images (**Figure 61** and **Figure 63**) present a situation similar to the organo-soluble 2PIs. The polymerization threshold for the tested speed range was relatively high at 50 mW in case of **AS2**, while good quality structures were obtained from 60 to 120 mW, except for the

highest tested power at the two lowest speeds of 20 and 40 mm/s leading to overpolymerization. At only 1/8th the concentration of **AS2**, the reference **P2CK** led to good printing results over the entire power range from 10 to 120 mW, with the only cubes of unacceptable quality occurring from 120 mm/s upwards at 10 mW, and with 20 mm/s at 120 mW.

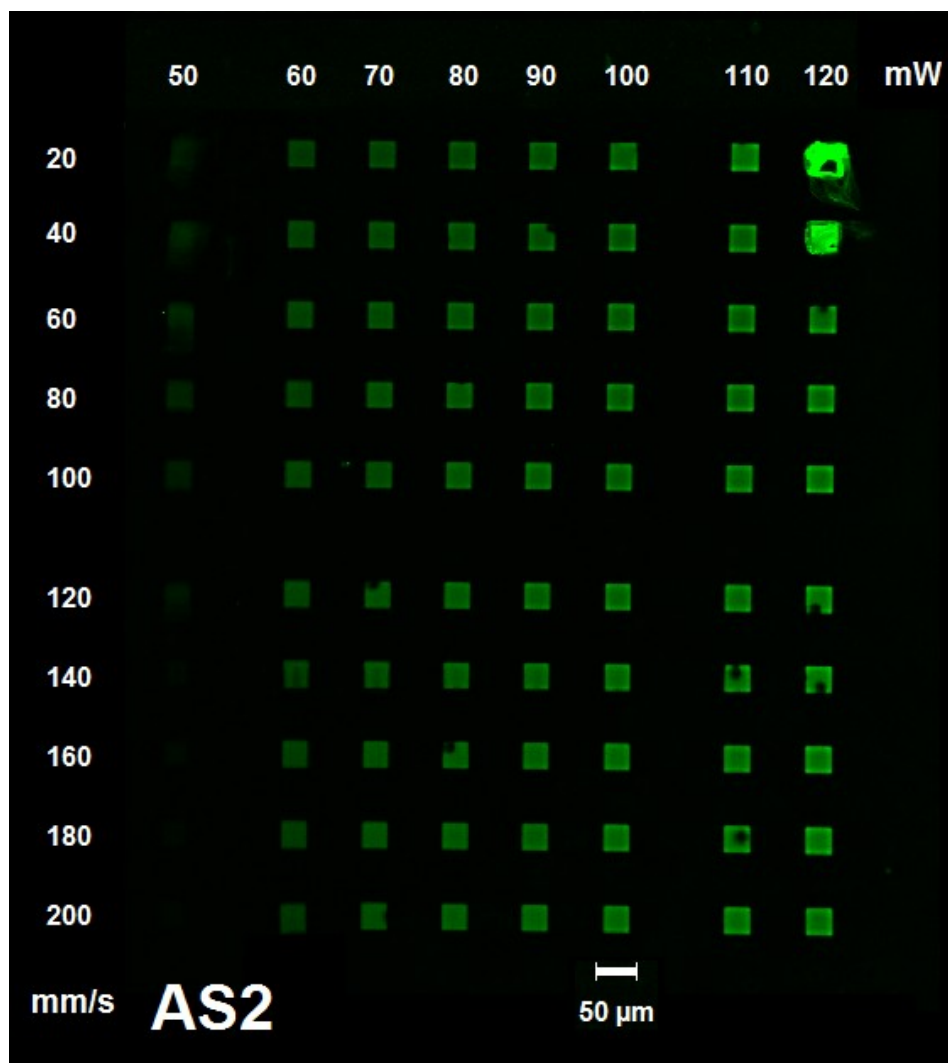


Figure 61: Hydrogel-cubes 2PP-printed with **AS2** (8 mM).

It should be noted here that while bubble formation due to thermal decomposition of the material is commonly encountered with organo-soluble 2PIs at higher energies (**Figure 60** and **Figure 62**), it is not usually observed with hydrogels. Occasional, random inclusion of larger bubbles in the hydrogel cubes was observed with **AS2** even at powers as low as 70 mW (**Figure 61**), while no bubbles occurred with **P2CK** (**Figure 63**). This could be due to formation of gaseous N_2 from **AS2**, suggesting its 2PP mechanism might indeed be based on 2PA-induced photocleavage.

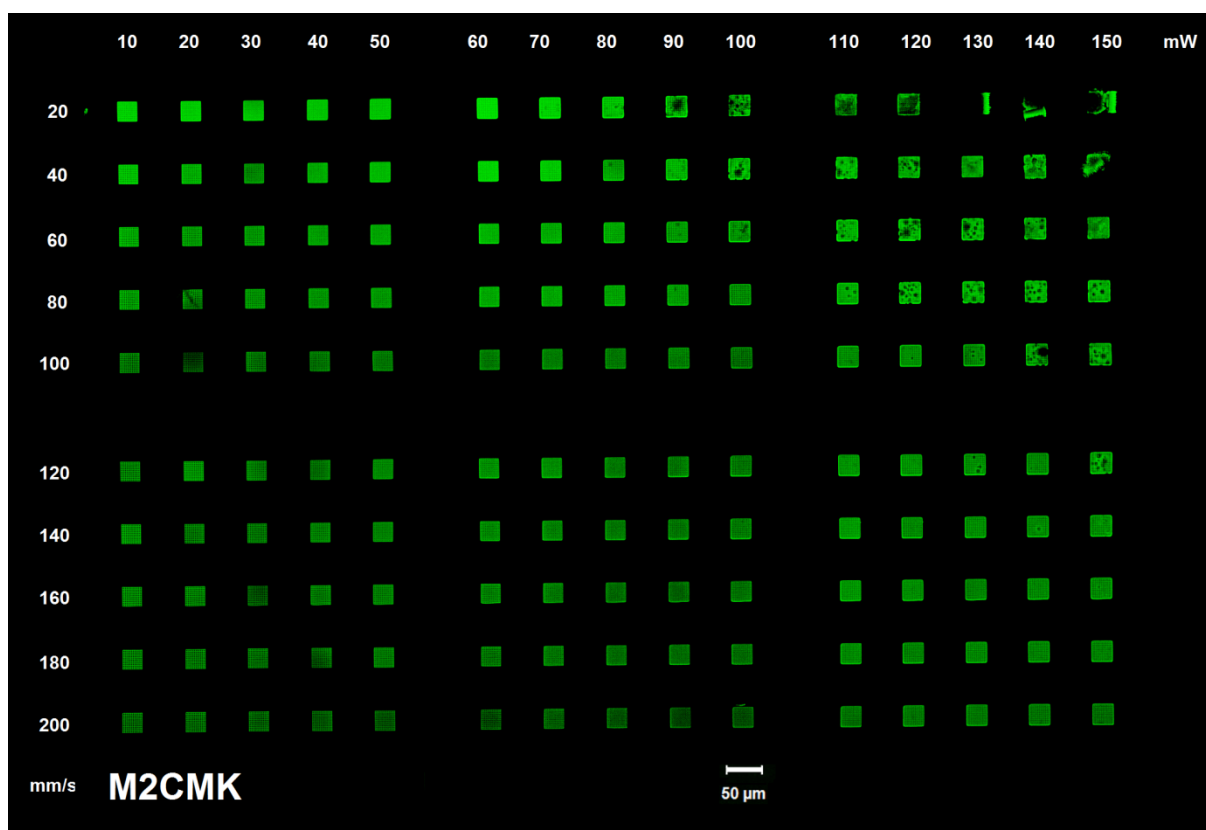


Figure 62: Woodpile-structures 2PP-printed with **M2CMK** (5 $\mu\text{mol/g}$ resin).

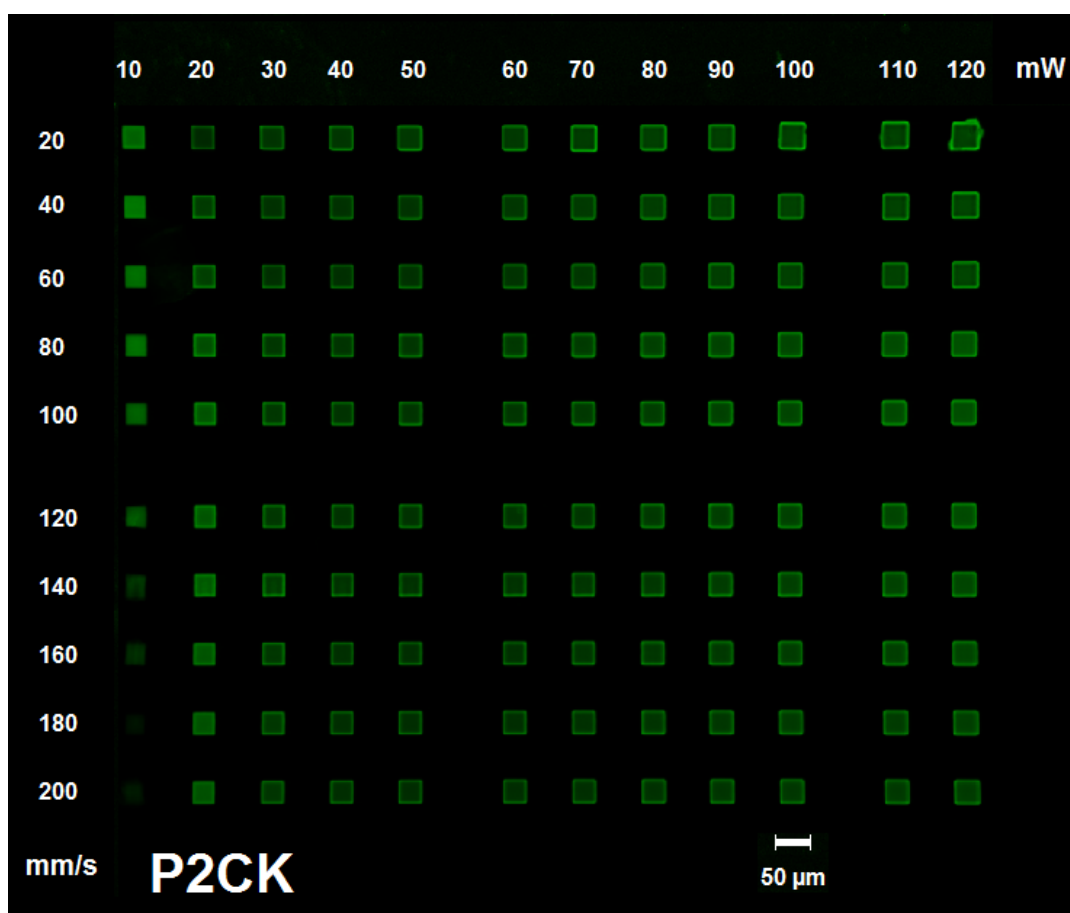


Figure 63: Hydrogel-cubes 2PP-printed with **P2CK** (1 mM).

2.2.3. Cleavable diazosulfone and diazosulfonate 2PIs with extended π -system and increased σ_{2PA}

In regard to the concept of reducing 2PI phototoxicity *via* fast cleavage that avoids bimolecular processes such as ROS formation, the possible N_2 -bubble formation that occurred when structuring with **AS2** is a promising result. The bubbles formed while printing dense hydrogels also behave different from those encountered with woodpile-structures in viscous resins, which form even with non-cleavable 2PIs after onset of thermal decomposition effects and are associated with deteriorating structure quality. Governed by the forces of buoyancy and surface tension, the many small bubbles that form tend to stay on the flat top surface of the growing hydrogel structure, and eventually coalesce there into one big bubble (**Figure 64**). Thus, the bubbles only rarely get trapped inside the hydrogel structures, conveniently avoiding undesired structural defects and pores.

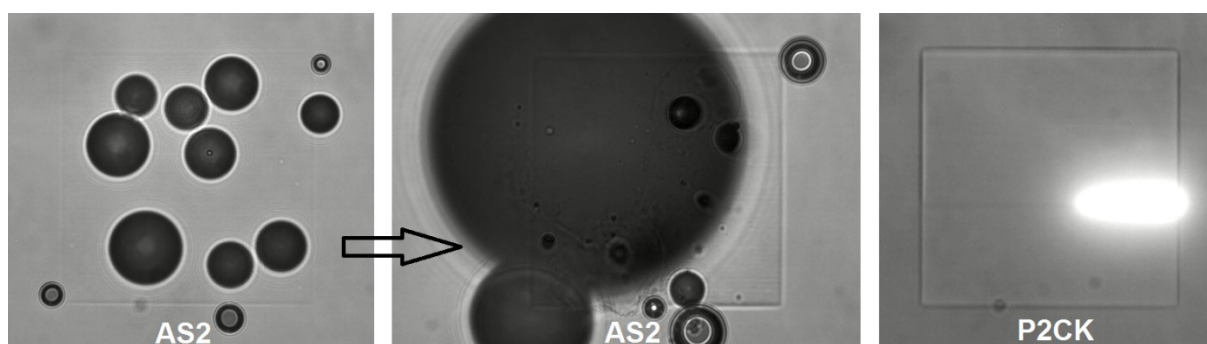


Figure 64: Bubble formation and coalescence observed during 2PP-structuring with **AS2**. Using the same structuring parameters with **P2CK** (laser voxel can be traced *via* 2PA excited fluorescence), no bubbles are formed. Images recorded with CCD-camera during 2PP-printing.

However, even at high concentrations the azo initiators **AS1** and **AS2** showed inferior performance and far narrower ideal processing windows compared to **M2CMK** and **P2CK**, likely as direct result of their σ_{2PA} being only a fraction of that of the DBK 2PI references. Thus, the next logical step is to design and prepare diazosulfone and diazosulfonate 2PIs with increased σ_{2PA} . Since the dimethylamino-substituent present in **AS1** and **AS2** is already one of the strongest electronic donor groups available, a reasonable approach is to extend the length of the conjugated π -system.

2.2.3.1. Synthesis of diazosulfone and diazosulfonate 2PIs with extended π -system and increased σ_{2PA}

2.2.3.1.1. Attempted synthesis of AS3 and AS4 via diazonium salt 10

The azo initiators **AS3** and **AS4** (Figure 65) are analogous to **AS1** and **AS2**, but with a styrylene-group inserted between the diazo-group and the 4-(dimethylamino)phenyl-ring to increase the conjugation length and consequently σ_{2PA} .

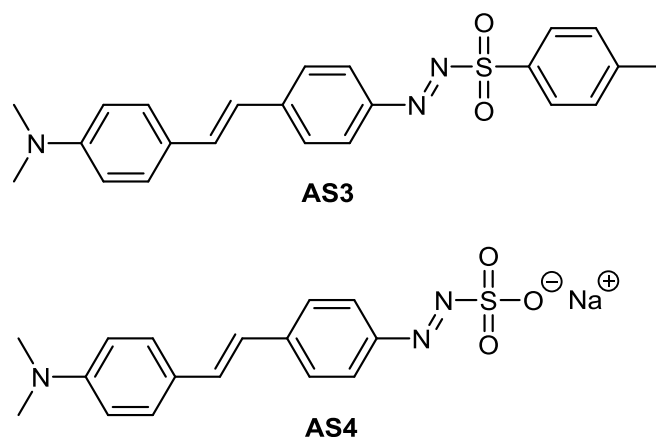


Figure 65: Azo initiators with extended π -system: diazosulfone **AS3** and diazosulfonate **AS4**.

Again, both **AS3** and **AS4** could be obtained *via* a common precursor, diazonium salt **10**, with the synthetic pathways shown in Figure 66. 4-Amino-4'-(*N,N*-dimethylamino)stilbene (ADS), a suitable aniline precursor for diazonium salt **10**, is commercially available as a mixture of (*E*)- and (*Z*)-isomers.

However, when attempting the synthesis of diazonium salts, the low solubility of ADS in various solvents was highly problematic. The preparation of diazonium salt **10** analogous to the procedure²⁰⁰ for diazonium tetrafluoroborate **9** failed due to insolubility in either 20% or 50% aq. HBF_4 . Similarly, the diazotization of ADS with isopentyl nitrite to obtain diazonium salt **10** analogues with trifluoroacetate-²⁰² or *o*-benzenedisulfonimide-anions²⁰³ failed due to insufficient solubilities in DCM/MeCN and acetic acid, respectively.

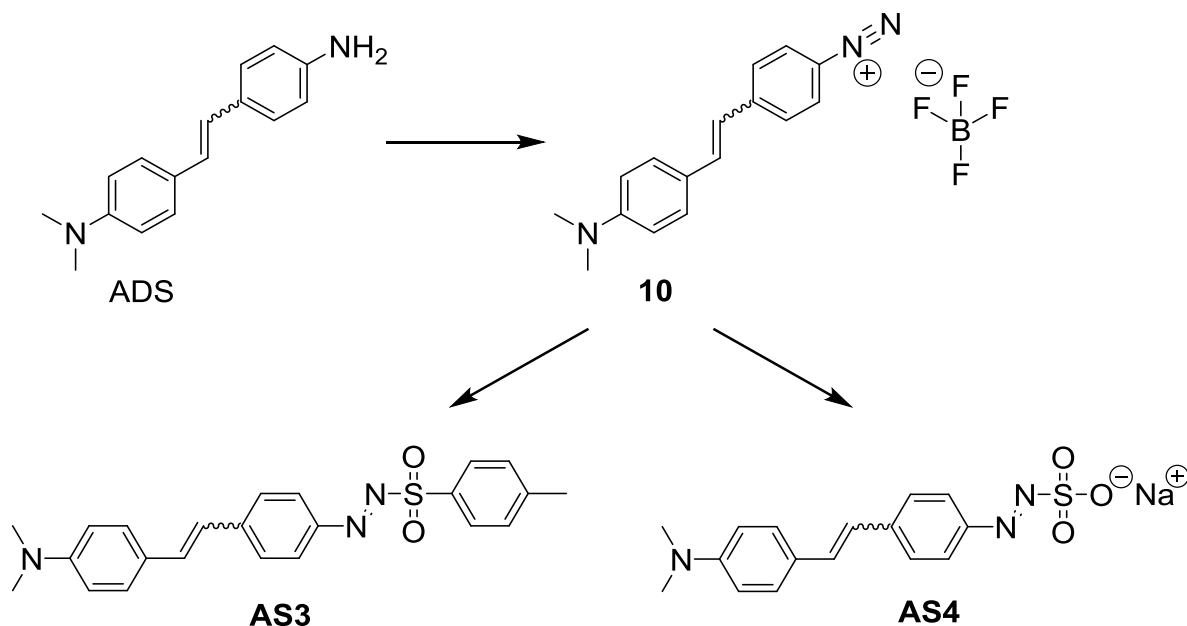


Figure 66: Synthetic pathways to **AS3** and **AS4**.

Zarei *et al.* described a solvent-free method to directly prepare diazosulfones from stable diazonium salts supported on sulfonated silica gel a solid reagent.^{204,205} For this method, silica sulfuric acid was first prepared according to literature by dripping chlorosulfonic acid onto magnetically stirred silica gel 60, followed by shaking for 30 min while removing the HCl-gas that is formed with a water-jet vacuum pump.²⁰⁶ ADS is then ground with silica sulfuric acid and NaNO₂ in a mortar with a pestle, first as a dry mixture to homogenize, then with a few drops of water to form the intermediate diazonium silica sulfate. Solid NaTS is then added and grinding continued for a few more minutes.²⁰⁵ Marked intensifications of the pinkish-orange color of ADS both after addition of NaNO₂/water and later NaTS indicate that a reaction might indeed have taken place, however the potential product **AS3** could not be efficiently extracted with either EA, acetone, DCM or CHCl₃. This might be simply due to exceedingly low solubility of **AS3** in these solvents, or potentially also due to a strong adsorbing interaction between the mildly alkaline dimethylamino-group of **AS3** and silica sulfuric acid. Among the 22 examples for diazosulfones prepared by this method in literature,²⁰⁵ none with amino-substituents were mentioned.

Lastly, the isolation of **AS3** and **AS4** was attempted *via* the chloride-analogue of diazonium salt **10**, which occurs as reactive intermediate in a one-pot procedure for the synthesis of an azido-compound.²⁰⁷ Here, ADS is dissolved in concentrated HCl and diazotized at -10°C with NaNO_2 . Since the reaction with either NaTS or Na_2SO_3 requires buffering of the strongly acidic solution used for diazotization, a procedure for diazosulfones by Kreher *et al.* was followed that uses only $\sim 12\%$ aq. HCl which is buffered with sodium acetate after diazotization is completed.¹⁸⁹ Brownish, practically insoluble precipitates were formed in both cases after addition of either NaTS or Na_2SO_3 , so that further attempts to obtain **AS3** and **AS4** were discontinued.

Rapid decomposition of diazonium salt **10** might also be a reason for the failed synthetic attempts, since it is mentioned in a publication were many of the stilbene-diazonium salts were not isolated due to thermal instability and rapidly declining purity, but only observed spectroscopically *in situ*.²⁰⁸

2.2.3.1.2. Attempted synthesis of AS5 and AS6

In the further pursuit of azo initiators with extended π -system, the dimethylamino donor substituent in the push-pull D- π -A molecules should be exchanged for a second diazosulfone or diazosulfonate-group, resulting in the A- π -A structures **AS5** and **AS6** (Figure 67). This should lead to increased solubility of the precursors as well as the azo initiators, especially of diazosulfonate **AS6**, bearing two ionic groups.

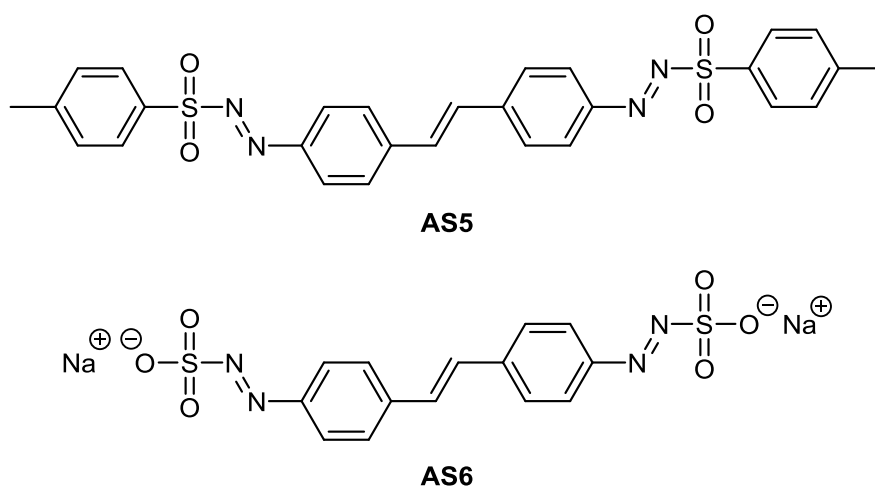


Figure 67: Azo initiators with extended π -system: diazosulfone **AS5** and diazosulfonate **AS6**.

Figure 68 presents the synthetic pathways to **AS5** and **AS6**, which could be synthesized from the common precursor tetrazonium salt **11**.

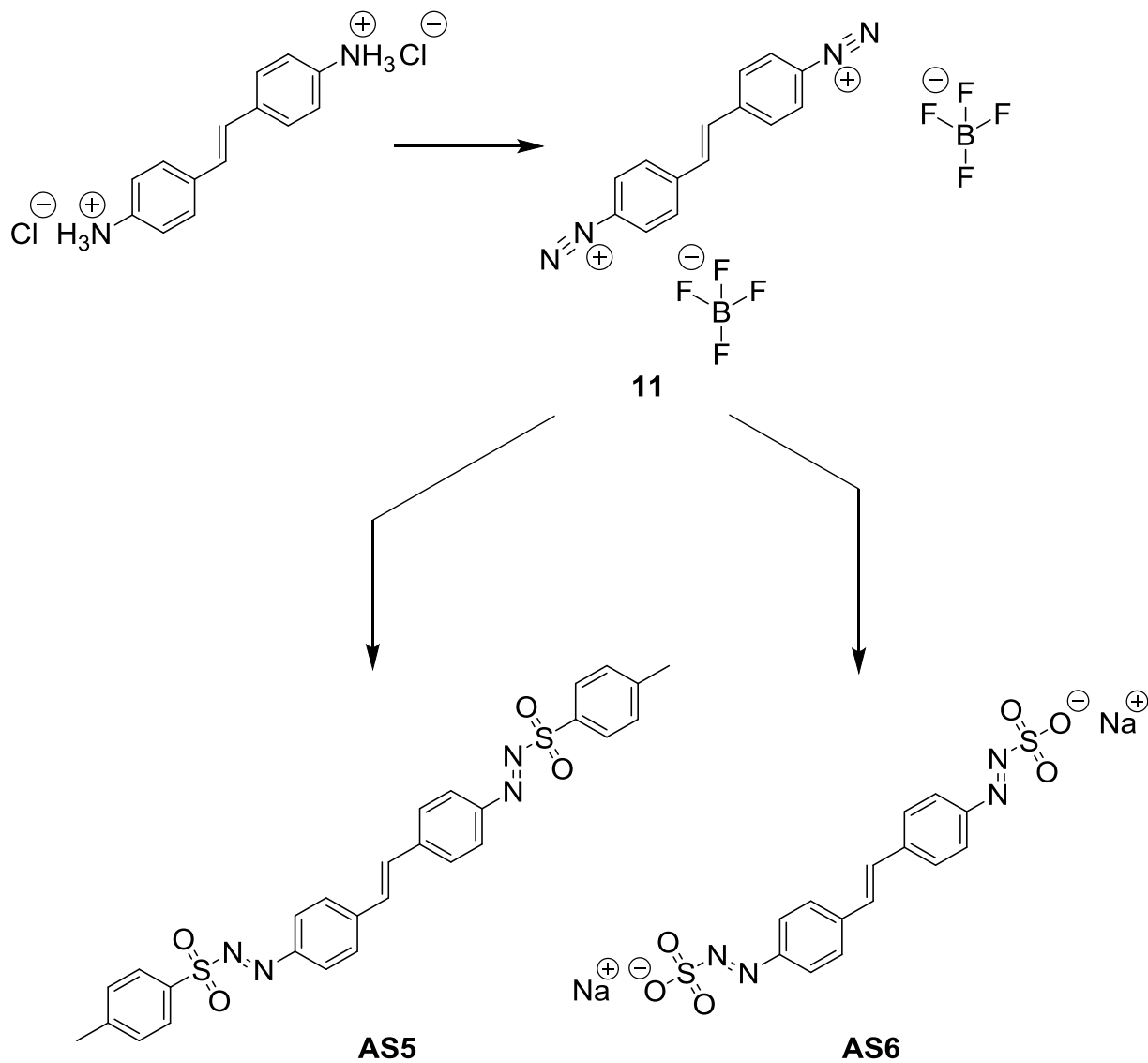
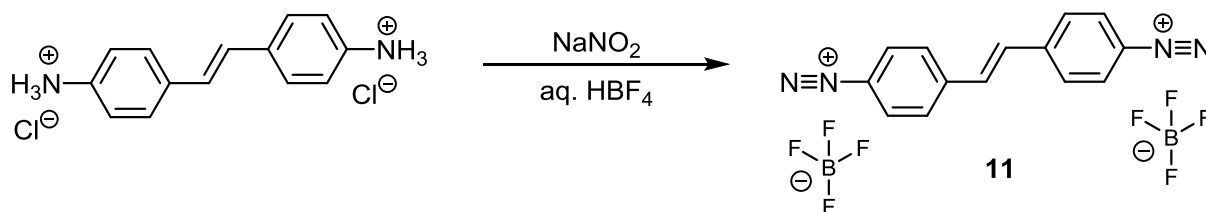


Figure 68: Synthetic pathways to **AS5** and **AS6**.

2.2.3.1.2.1. Synthesis of precursor tetrazonium salt **11**

Tetrazonium salt **11** was synthesized in analogy to the method for diazonium salt **9**.²⁰⁰



(E)-4,4'-diaminostilbene dihydrochloride is dissolved in 20% aq. HBF_4 and treated with 2.1 equivalents aq. NaNO_2 at a temperature between 0 - 5°C. The product precipitates as a brownish-orange solid. Dark impurities are also formed than appear as floating crumbs that can be decanted after centrifugation of the aqueous reaction mixture. The precipitate was then washed with deionized water, MeOH and Et_2O , collecting the solids *via* centrifugation after each washing. Tetrazonium salt **11** was obtained at a yield of 70% of theory by drying the washed centrifugate *in vacuo* at room temperature.

2.2.3.1.2.2. Attempted isolation of **AS5** and **AS6**

For the coupling step to prepare **AS5**, tetrazonium salt **11** was suspended in deionized water and 3 equivalents of NaTS were added as an aqueous solution. The formation of voluminous brown flakes indicated a reaction taking place, however ^1H -NMR-analysis of the crude product revealed various signals from impurities in the aromatic region. The brown flakes were extracted with DCM, the resulting orange suspension filtered, stripped of solvent *in vacuo* and the residue purified *via* column chromatography using DCM:EA = 5:1 as the eluent. During rotary evaporation of the eluent solvent, substantial decomposition of **AS5** occurred even when "heating" with room temperature water and despite protection from light, so no reliable spectral data of the pure compound could be obtained. It seems that extension of the π -system and lack of an electron donor group, which increases thermal stability of diazosulfones according to literature,¹⁹⁶ exacerbates the stability issues already encountered with **AS1**. Moreover, the solubility of crude **AS5** in ETA/TTA acrylate resin was very low. Thus, further attempts to prepare an organo-soluble diazosulfone 2PI with extended π -system were abandoned.

Based on the considerably higher decomposition temperature of **AS2** above 260°C vs 140°C for **AS1**, **AS6** is also expected to be more thermally stable in comparison to **AS5**. However, when attempting to react tetrazonium salt **11** with Na₂SO₃, either no reaction took place or the resulting product was almost insoluble, as the supernatant solution obtained from centrifugation of the aqueous reaction mixture showed only a slight yellowish tinge instead of the intense yellow to orange color typical for diazosulfonates, and almost no residue was left after evaporation of water from this solution. Thus, the next step to prepare a water-soluble, biocompatible diazo-sulfonate 2PI was modification of **AS6** to increase the solubility of the system.

2.2.3.1.3. Synthesis of AS7

In order to increase the water-solubility of **AS6**, further hydrophilic moieties should be introduced in addition to the two solubility-providing diazosulfonate-groups in the periphery of the molecule. The use of additional sulfonate groups on the aromatic π-system core seemed particularly favorable for a variety of reasons. Aromatic sulfonate groups are widely used in commercial acid dyes as strongly water-solubilizing substituents, having the advantage of easy synthetic availability as well as being negatively charged in aqueous solution over an extremely broad pH range.²⁰⁹ A suitable sulfonated analogue to the precursor used in the attempted preparation of **AS5** and **AS6** is 4,4'-diaminostilbene-2,2'-disulfonic acid (amsonic acid), which is manufactured in large quantities as raw material for optical brighteners.²¹⁰

Figure 69 shows the synthetic pathway to diazosulfonate **AS7** from amsonic acid via tetrazonium salt **12**. Besides the low thermal stability observed with **AS5**, its low solubility in organic solvents and acrylate resins is expected to substantially further decrease by the introduction of highly polar and hydrophilic sulfonate- or sulfonic acid groups. Thus, no attempts are undertaken to prepare an organo-soluble diazosulfone based on tetrazonium salt **12**, even though such a derivative was mentioned among the claims of a patent describing diazosulfone PIs.¹⁹¹

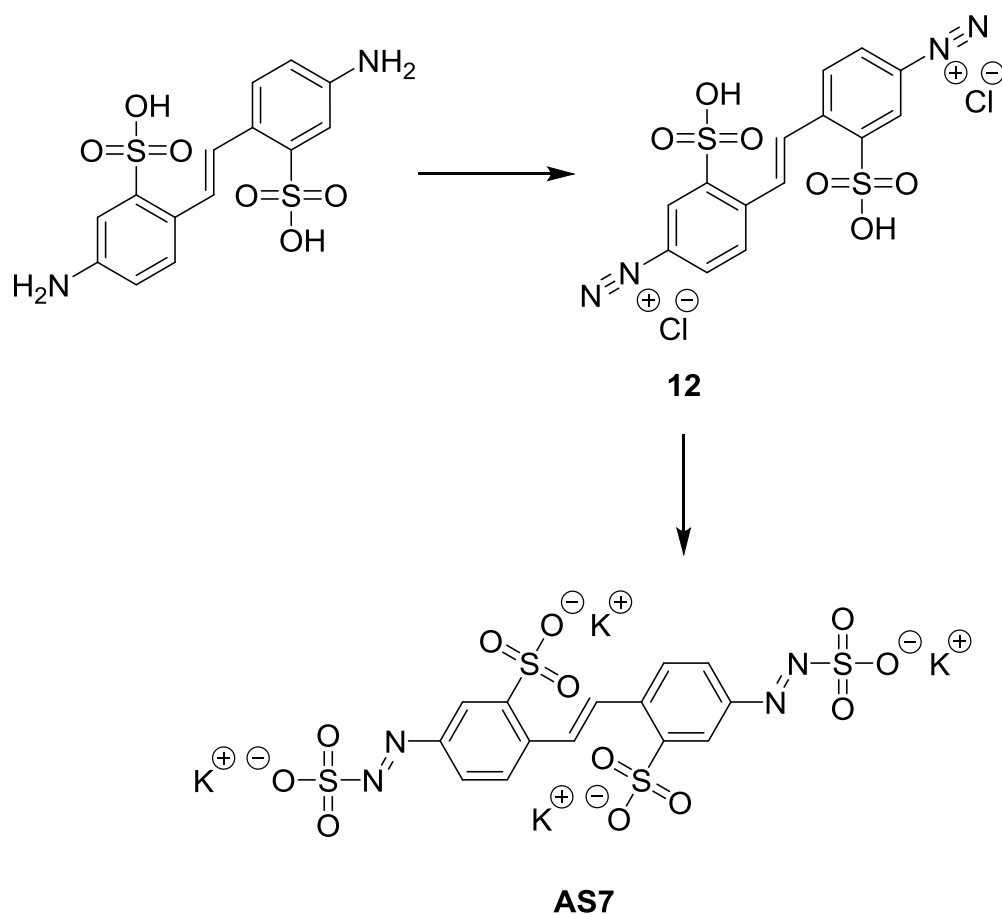
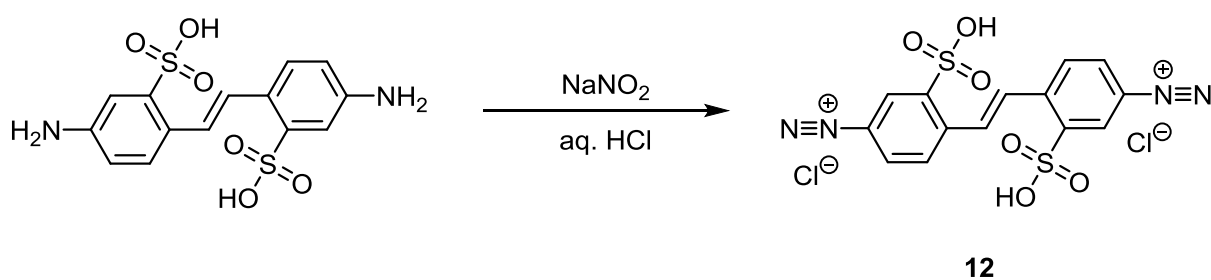


Figure 69: Synthetic pathway to **AS7**.

2.2.3.1.3.1. Synthesis of precursor tetrazonium salt **12**

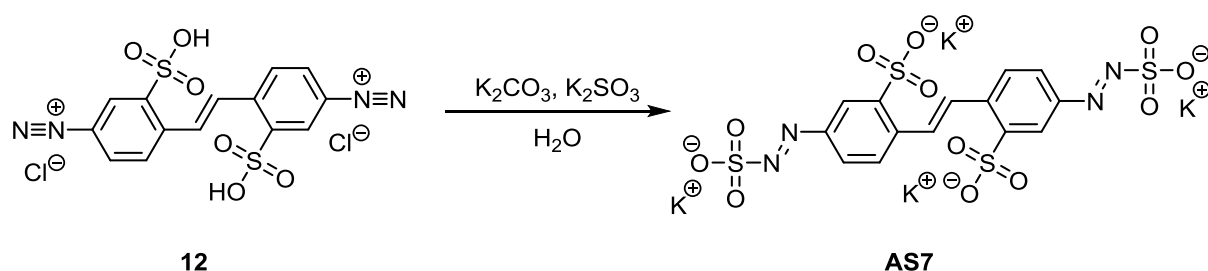
Tetrazonium salt **12** was prepared with chloride-anions since this salt conveniently remains an undissolved solid in acidic solution, whose synthesis has been described in detail in patent literature where it is used in the manufacture of water-soluble azo dyes.²¹¹



The patent even specifies the diazotization of amsonic acid at an elevated temperature of 35°C, however it was found here that addition of NaNO₂ without sufficient cooling can lead to runaway reactions with formation of dark impurities and brown NO₂-gas. Thus, amsonic acid was suspended in deionized water, conc. HCl was added and the stirred suspension cooled to ~0°C before slowly adding an aqueous solution of NaNO₂ so that the temperature always stays below 5°C. The suspension is then stirred at room temperature for 30 min and at 35°C for another 2.5 h. During diazotization the brownish-white color of amsonic acid changes to an intense canary yellow. The solid product is collected by centrifugation, washed with deionized water, MeOH and Et₂O and dried *in vacuo* to obtain tetrazonium chloride **12** at a yield of 83% of theory. The ¹H-NMR-spectrum indicated sufficient purity for further use, however no reliable ¹³C-NMR-spectra could be recorded due to a very low solubility of the compound.

2.2.3.1.3.2. Synthesis of AS7

For the final coupling step to obtain **AS7**, tetrazonium salt **12** should be reacted with Na₂SO₃.



In the attempted isolation of the sodium salt of **AS7** by reacting an aqueous suspension of tetrazonium salt **12** with Na₂CO₃ to neutralize the sulfonic acid groups and Na₂SO₃ to convert the diazonium- to diazosulfonate-groups, it was found that the solubility of this sodium salt is so high that it does not readily precipitate from solution. Neither cooling nor salting out *via* addition of NaCl as suggested by literature²¹² could affect precipitation, so that a different approach had to be used. Since literature mentions a generally lower solubility of potassium diazosulfonates vs the sodium salts,²¹² the synthesis of **AS7** from tetrazonium salt **12** was repeated

using K_2CO_3 and K_2SO_3 , leading to successful isolation of the product as finely crystalline, orange powder at a yield of 50%.

To obtain pure samples of **AS7**, the exact amount of water used as solvent for the reaction as well as the manner of addition of K_2CO_3 and K_2SO_3 are critical. It is crucial to conduct the reaction in relatively concentrated solution, otherwise yields are drastically reduced or **AS7** does not precipitate at all (since the water-solubility of the potassium salt still is excellent). On the other hand, if the reaction mixture is too concentrated, dark impurities are formed that are not easily separated from the product. Furthermore, it was found that portionwise addition of K_2CO_3 and K_2SO_3 mixed homogeneously as solids leads to best results, while introducing them to the reaction mixture consecutively or as solutions also encourages the formation of side products. Recrystallization of the crude product from the minimal amount of water required for dissolution at 70°C leads to removal *e.g.* of traces of unreacted carbonate-ions, that can otherwise be observed in ^{13}C -NMR-spectra of crude **AS7** samples with a variable chemical shift ranging from 161-168 ppm, the exact value depending on the pH of the measured solution.²¹³

2.2.3.2. Analysis of the cleavable 2PI **AS7**

2.2.3.2.1. Photophysical properties

To evaluate the photophysical properties of **AS7**, UV/Vis and 2PA spectra should be measured and compared to those of DBK reference compound **P2CK** (Figure 70).

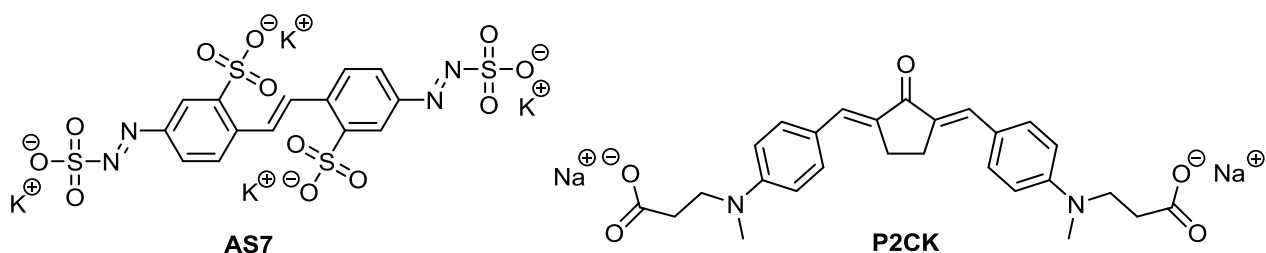


Figure 70: Chemical structures of **AS7** and DBK reference **P2CK**.

The 1PA spectra of **AS7** and the DBK reference compound **P2CK** are shown in Figure 71.

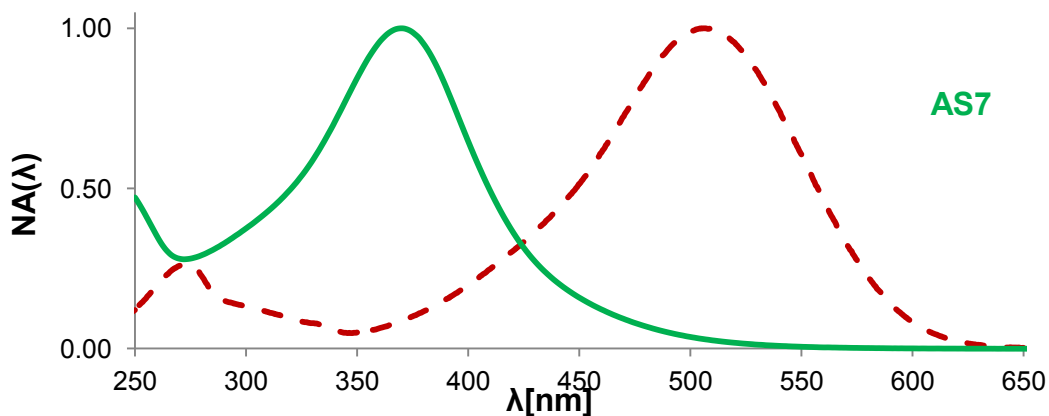


Figure 71: Normalized 1PA spectra of **AS7** and **P2CK** (in PBS solution).

The 1PA of **AS7** ($\lambda_{\text{abs}} = 370 \text{ nm}$, $\epsilon_{\text{max}} = 2.2 \cdot 10^4 \text{ M}^{-1}\text{cm}^{-1}$) is considerably blue-shifted in regard to the other water-soluble 2PIs, by 136 nm in comparison to **P2CK** ($\lambda_{\text{abs}} = 506 \text{ nm}$, $\epsilon_{\text{max}} = 5.5 \cdot 10^4 \text{ M}^{-1}\text{cm}^{-1}$) and 67 nm compared to **AS2** ($\lambda_{\text{abs}} = 437 \text{ nm}$, $\epsilon_{\text{max}} = 2.4 \cdot 10^4 \text{ M}^{-1}\text{cm}^{-1}$, see Figure 58). The reason for this blue-shift is likely due to **AS7** being an A- π -A-system with four electronic acceptor groups, but no strong electron donors such as alkylamino substituents. This also results in an absorption coefficient

ϵ_{\max} less than half of that of **P2CK** and also lower than **AS2**, despite **AS7** having an extended π -system with two diazosulfonate groups in conjugation to each other.

The 2PA of **AS7** was investigated in cooperation with Prof. Wolfgang Husinsky and Aliasghar Ajami from the Institute of Applied Physics, TU Wien, with the WLC 2PA spectra of the compounds shown in **Figure 72**.

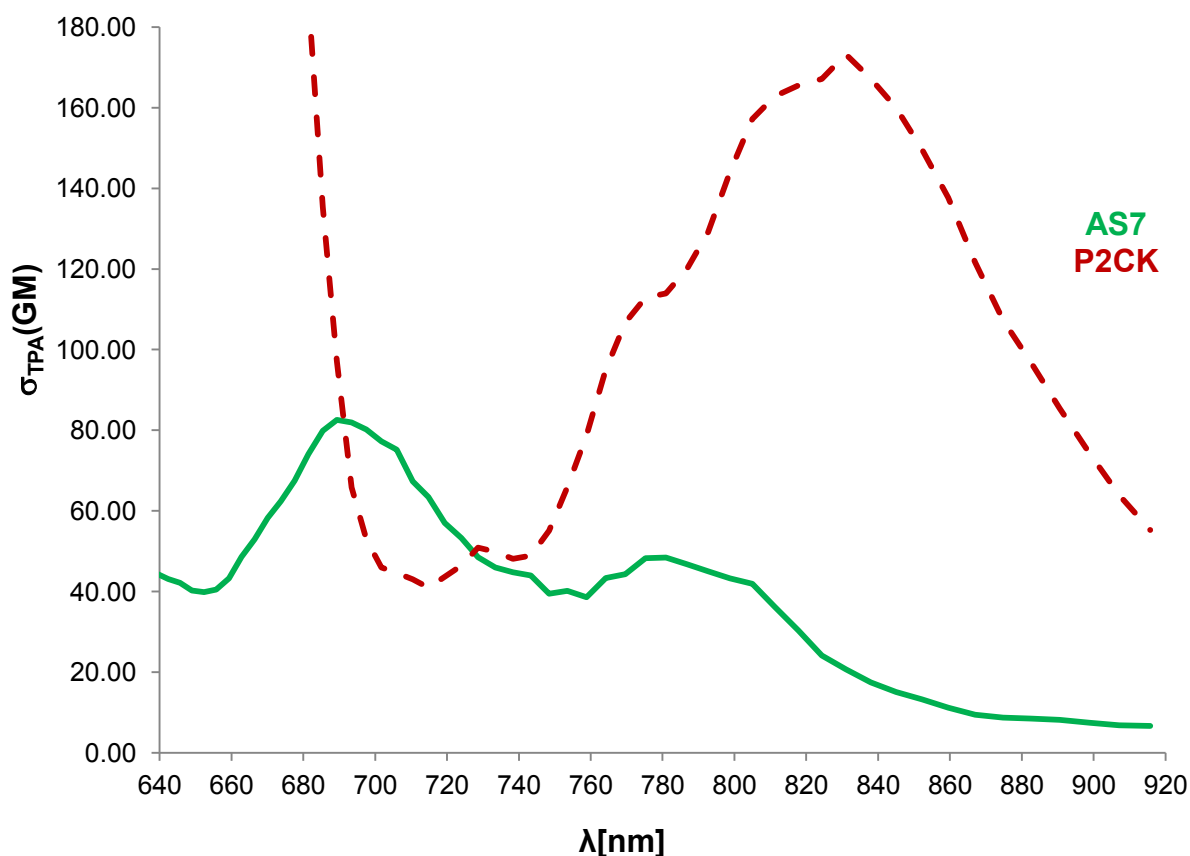


Figure 72: WLC 2PA spectra of **AS7** and **P2CK** (in PBS solution).

In most of the investigated spectral region, the $\sigma_{2\text{PA}}$ of **AS7** is considerably lower than that of the reference **P2CK**.

AS7 exhibits two local 2PA maxima ($\lambda_{2\text{PA},1} = 689$ nm, $\sigma_{2\text{PA},1} = 83$ GM; $\lambda_{2\text{PA},2} = 781$ nm, $\sigma_{2\text{PA},2} = 48$ GM), both far below the local maximum of **P2CK** ($\lambda_{2\text{PA}} = 831$ nm, $\sigma_{2\text{PA}} = 173$ GM). At 800 nm, the $\sigma_{2\text{PA}}$ of **AS7** is 43 GM and that of **P2CK** is 145 GM. Since the sizes of the conjugated π -systems of the two different compounds are comparable, the most likely reason for the low $\sigma_{2\text{PA}}$ is **AS7**'s lack of strong electron donor groups such as the alkylamino substituents present in **P2CK**.

2.2.3.2.2. 2PP structuring tests

As a first assessment of the 2PI performance of **AS7**, arrays of hydrogel cubes were 2PP-fabricated at different laser intensities and writing speeds. For this purpose, both **AS7** and **P2CK** were dissolved at 1 mM concentration in a formulation of 50 wt% PEGDA700 in PBS, and dense cubes were 2PP-printed at laser power varying from 10 to 120 mW and writing speeds from 20 to 200 mm/s. LSM-images of the printed cubes show that while **AS7** (**Figure 73**) is less efficient as a 2PI than **P2CK** (**Figure 74**) at an equal concentration of 1 mM, its ideal processing window is substantially larger than that of **AS2** (**Figure 61**) even when tested at an elevated concentration of 8 mM to compensate for its smaller size conjugated π -system. It should also be noted here that under these parameters, cubes printed with **AS7** did not show any visible N_2 -bubble inclusions, in contrast to those printed with **AS2**.

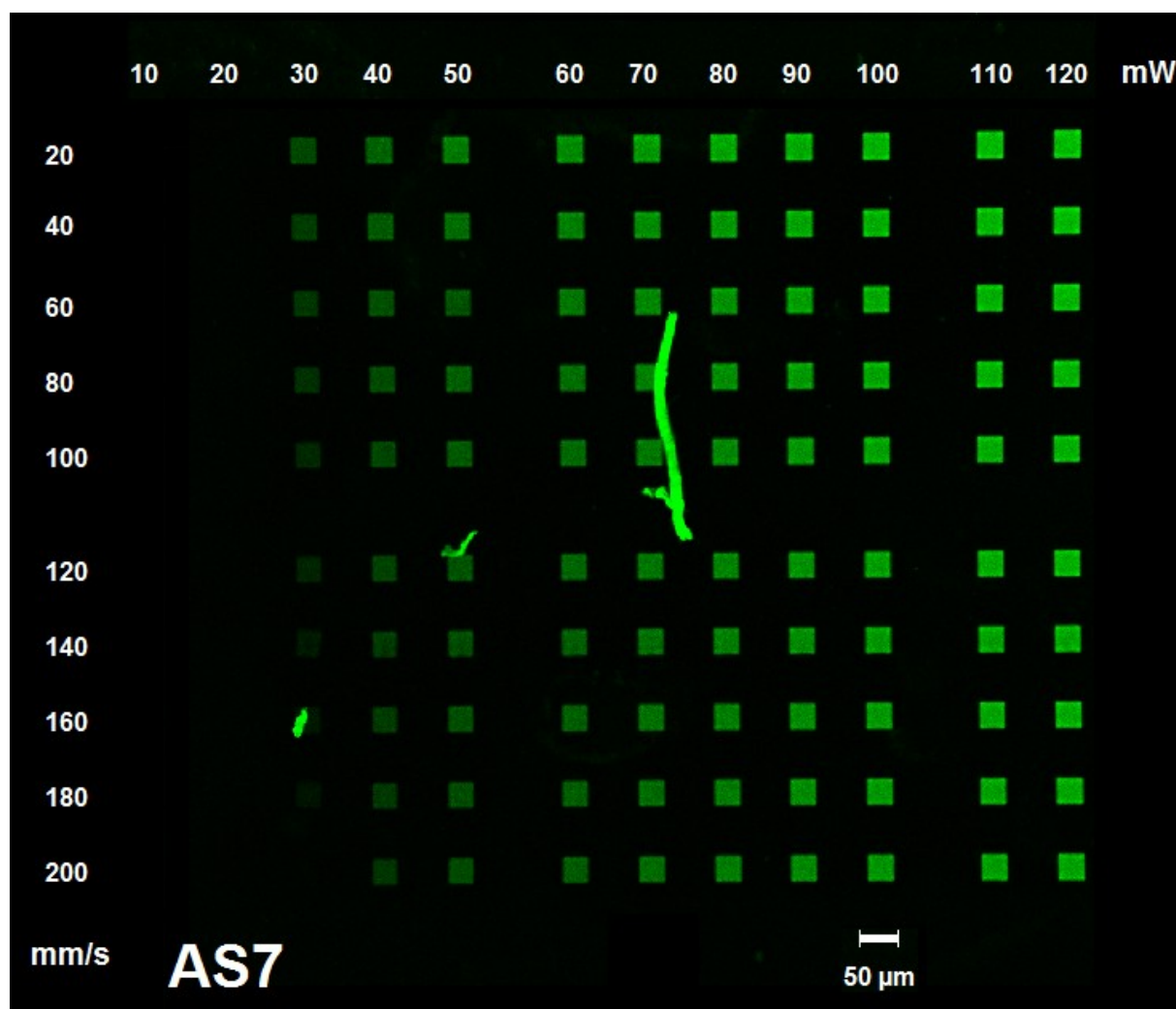


Figure 73: Hydrogel-cubes 2PP-printed with **AS7** (1 mM).

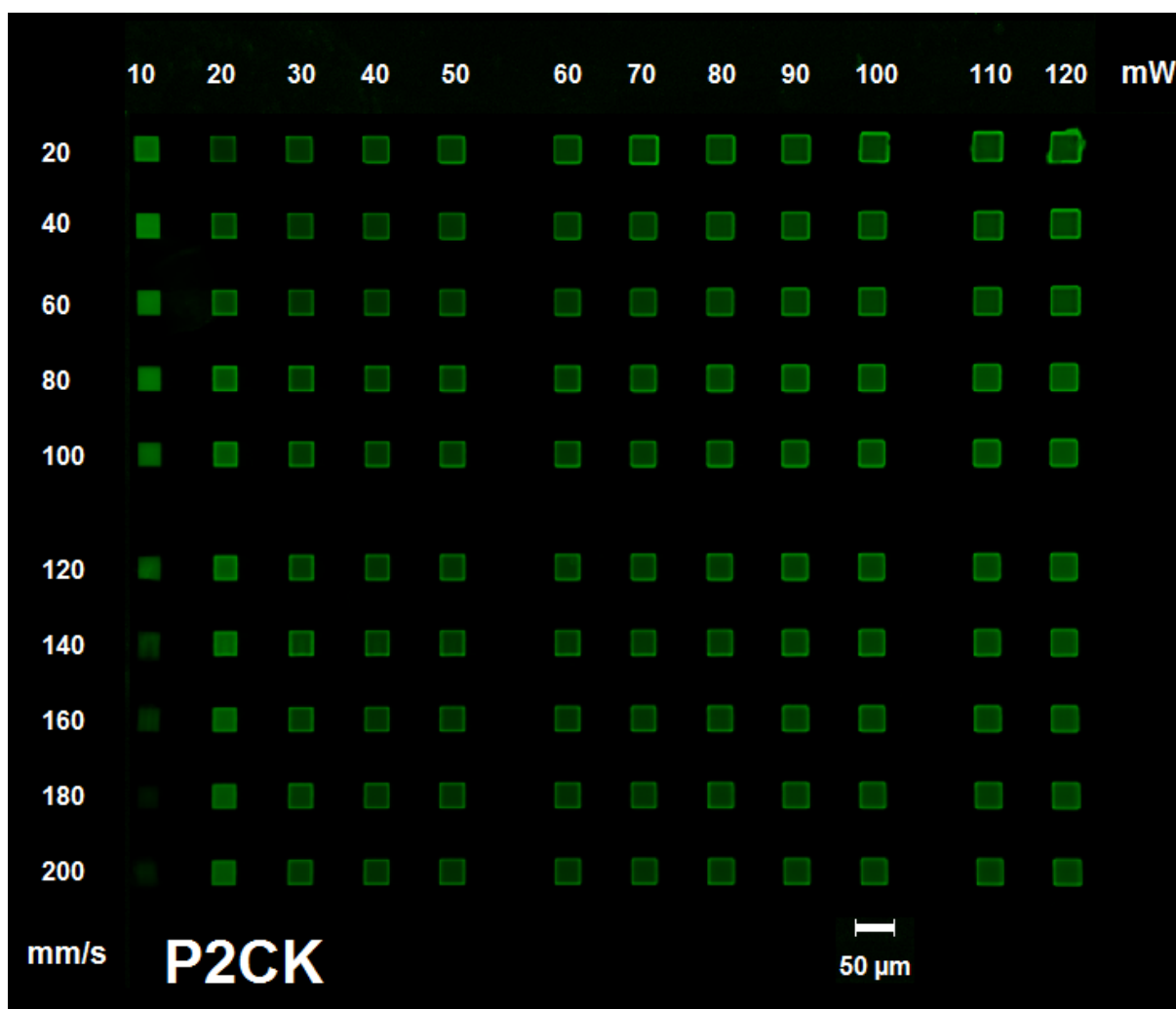


Figure 74: Hydrogel-cubes 2PP-printed with **P2CK** (1 mM).

In order to provide a more detailed comparison between **AS7** and **P2CK**, the (phototoxic) benchmark currently used in 2PP cell encapsulation experiments, further 2PP structuring tests were performed in close cooperation with Prof. Aleksandr Ovsianikov and Agnes Dobos. The aim was to investigate under which parameters a hydrogel printing performance more similar to 1 mM **P2CK** could be achieved. Thus, polymerization thresholds as well as the swelling of printed hydrogels were measured, using either **AS7** or **P2CK** at concentrations of 1 and 2 mM in a 10 wt% solution of gelMOD in EGM-2 cell culture medium.

Hydrogel cubes were printed at a wavelength of 800 nm, laser powers ranging from 45 - 100 mW and high writing speeds from 100 - 1000 mm/s. The minimal laser powers required for structuring were recorded as fabrication thresholds (**Figure 75**).

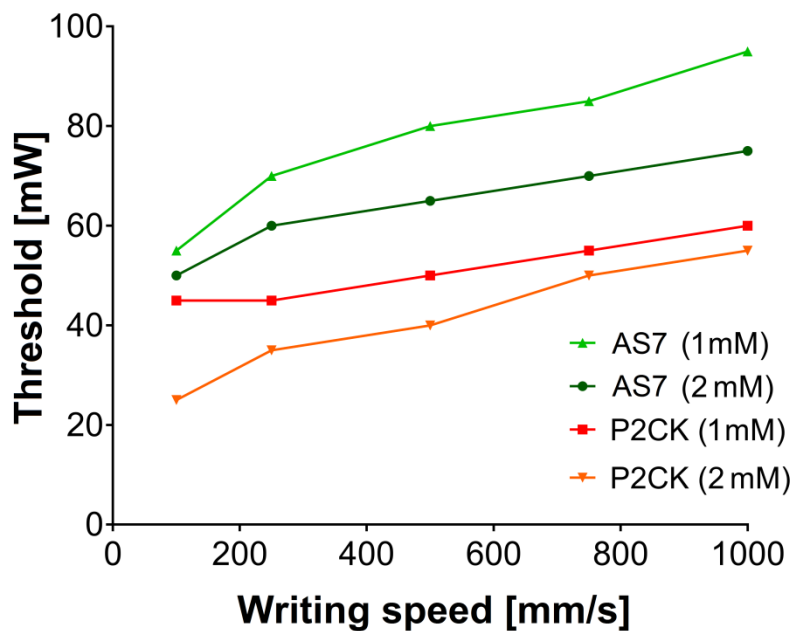


Figure 75: Dependency of hydrogel structuring thresholds on writing speeds when using **AS7** and **P2CK** at either 1 or 2 mM concentration.²¹⁴

While **AS7** consistently required higher laser powers to initiate the polymerization than the reference **P2CK**, at a concentration of 2 mM **AS7** did not have more than 15 mW higher threshold values than 1 mM **P2CK** at any of the tested writing speeds.

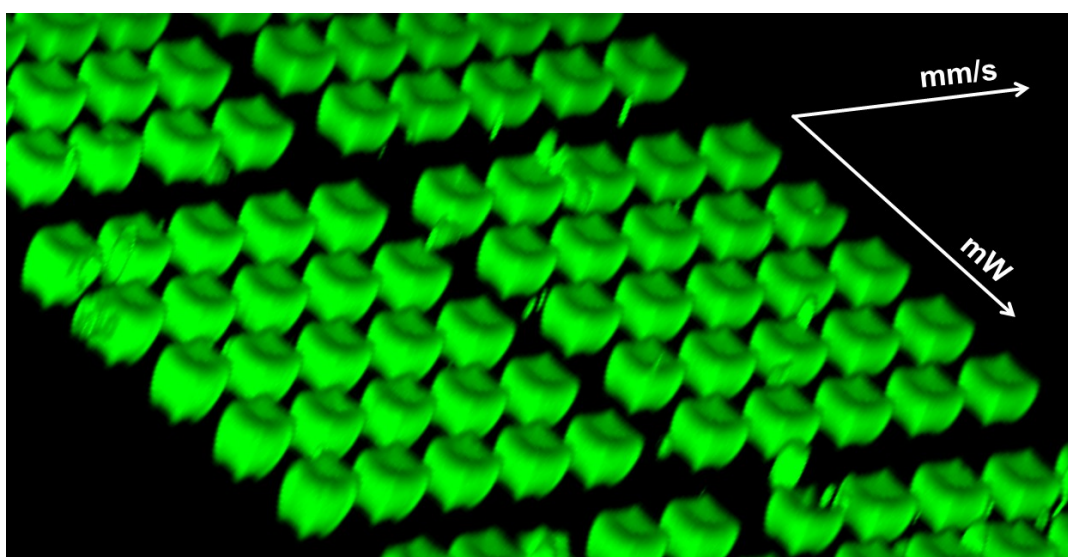


Figure 76: 3D LSM image demonstrating the dependency of hydrogel swelling on 2PP-printing laser power and writing speed.

At a given PI and hydrogel precursor concentration, the laser power and writing speed during 2PP-printing both directly affect the crosslink density of the hydrogel, with lower speeds and higher powers resulting in a more densely crosslinked gel. In turn, the water uptake of a printed hydrogel structure and the resulting swelling after printing are higher for structures that are crosslinked only loosely. Thus, the swelling of hydrogel cubes depends on and is a measure for their crosslink density (**Figure 76**). This can be taken advantage of to compare the crosslink density of hydrogel cubes fabricated under different conditions, with the aid of the following equation where Q is defined as the swelling ratio, and P_t and P_b are the perimeters of hydrogel cube slices at the top and bottom of the structure, respectively:

$$Q = \frac{P_t - P_b}{P_b} \cdot 100\%$$

Figure 77 shows the measured swelling ratios for hydrogel cubes fabricated with either 2 mM **AS7** or 1 mM **P2CK** at different laser powers and two different writing speeds (100 and 500 mm/s). The swelling ratios of cubes printed using **AS7** at the double concentration of **P2CK** are similar to each other in the tested speed and power range. In conclusion, 2 mM **AS7** can be used in 2PP-printing of hydrogels to achieve a performance comparable to 1 mM **P2CK**.

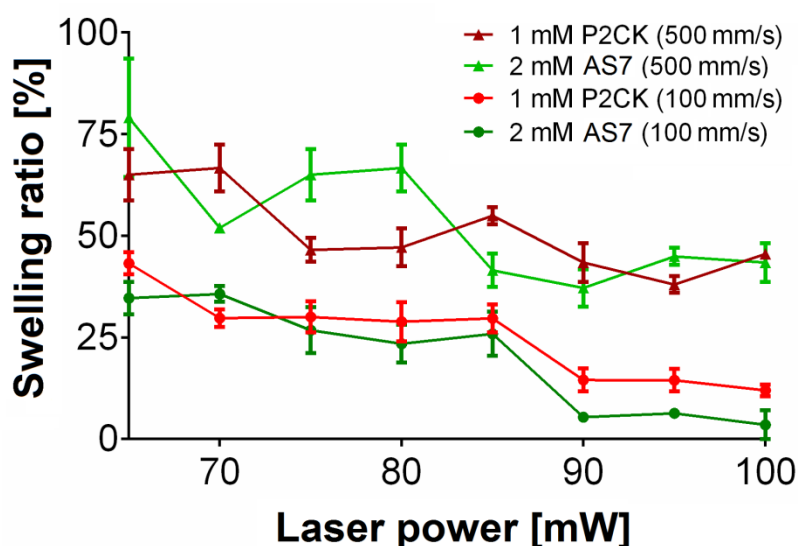


Figure 77: Dependency of hydrogel structure swelling on laser power at different writing speeds and 2PI concentrations.²¹⁴

2.2.3.2.3. Cytotoxicity assay

During sample preparation and the 2PP printing process itself, cells are invariably exposed to 2PI-containing formulations for extended periods of time. This is also the case for cells that are not directly encapsulated in the hydrogel, but only to be trapped in pores or cavities of a printed structure. These cells are not exposed to laser radiation in the presence of the 2PI and hence not directly subject to its phototoxicity, but the cytocompatibility in darkness is still crucial.

Thus, the cytocompatibility of **AS7** was evaluated in comparison to **P2CK** by performing a PrestoBlue[®] metabolic assay in close cooperation with Prof. Aleksandr Ovsianikov, Marica Markovic and Agnes Dobos. MC3T3 cells were exposed to various concentrations of either **AS7** or **P2CK** in α MEM cell culture medium for 3 h and the PrestoBlue[®] Cell Viability test was performed subsequently.

While **P2CK** exhibited significant cytotoxicity at concentrations above 1 mM, causing a dose-dependent decrease of metabolic activity ranging from 35 \pm 6% to 50 \pm 6%, **AS7** did not lead to any significant reduction of metabolic activity even at a concentration of 4 mM (**Figure 78**).

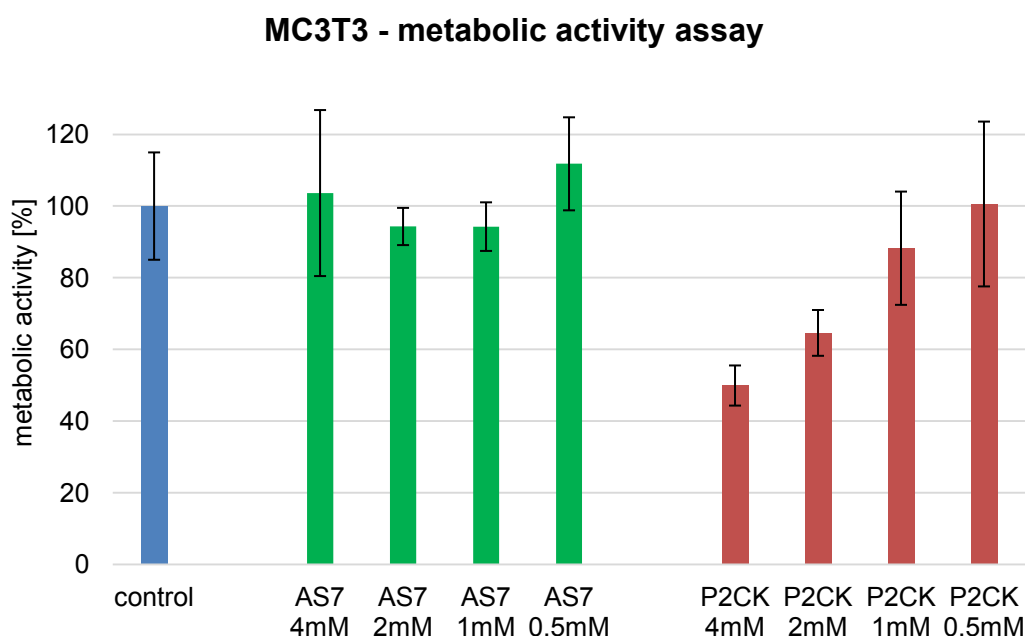


Figure 78: Effect of 3 h exposure of various concentrations of **AS7** and **P2CK** on the metabolic activity (determined *via* PrestoBlue[®] Cell Viability test) of MC3T3 cells. All values given as percentage of the metabolic activity of untreated control cells.

Due to the promising results of **AS7** not causing any significant cytotoxicity for MC3T3 even at concentrations far higher than what is required for efficient 2PP structuring, similar tests were also performed with human adipose derived stem cells (ASC/TERT1), a cell type more sensitive and expensive to cultivate than MC3T3.

PrestoBlue® Cell Viability test was performed on ASC/TERT1 cells that had previously been exposed to various concentrations of either **AS7** or **P2CK** in EGM-2 cell culture medium for 3 h. While **P2CK** was still well tolerated by ASC/TERT1 at 0.5 mM (a concentration too low for practicable 2PP cell encapsulation), concentrations between 1 to 4 mM caused strong dose-dependent decreases in metabolic activity (greater reduction than observed with MC3T3), ranging from 57±2% to 86±4%. In contrast, **AS7** showed high cytocompatibility in the investigated concentration range, with only slight reductions in metabolic activity ranging from 6±5% to 18±6% (**Figure 79**).

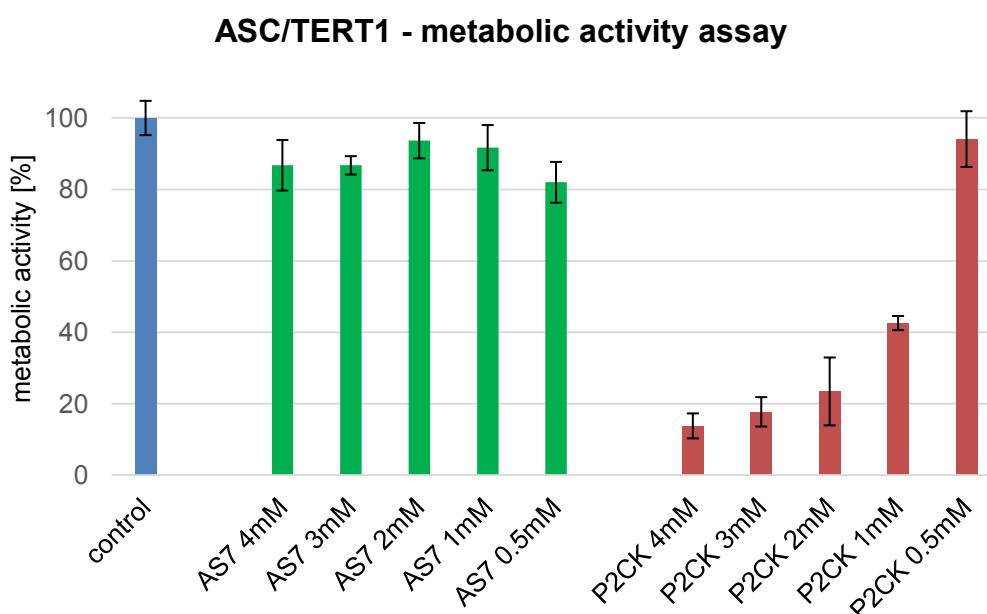


Figure 79: Effect of 3 h exposure of various concentrations of **AS7** and **P2CK** on the metabolic activity (determined *via* PrestoBlue® Cell Viability test) of ASC/TERT1 cells.

All values given as percentage of the metabolic activity of untreated control cells.

2.2.3.2.4. 2PP direct encapsulation of human stem cells

To assess the performance of **AS7** in its dedicated application of 2PP direct cell encapsulation, 3D hydrogel structures in the shape of a "TU Wien"-logo (**Figure 80**) were fabricated in close cooperation with Prof. Aleksandr Ovsianikov and Agnes Dobos. Similar to the 3D yin-yang structure (**Figure 30**), the TU Wien-logo presents cells encapsulated in the polymerized hydrogel next to cells trapped in cavities that are not exposed to laser radiation, allowing for a direct side-by-side comparison.



Figure 80: CAD-model of the TU Wien logo (dimensions 500 × 500 × 125 μm). The "top" layer in the picture is joined to a glass substrate, while the "bottom" is a through-polymerized lid (omitted in the picture for better visibility), so that the void "letter" areas are closed from all sides and allow trapping of cells.

Since AS7 showed excellent cytocompatibility results in the PrestoBlue[®] Cell Viability assay, encapsulation of human stem cells ASC/TERT1 was directly pursued.

Hydrogel precursor formulations were prepared by dissolving 10% gelMOD and either 2 mM **AS7** or 1 mM **P2CK** in EGM-2 cell culture medium. After homogeneously suspending ASC/TERT1 cells in the formulations, TU Wien logos were printed immediately at 80 mW laser power and 250 mm/s writing speed, followed by careful removal of residual non-crosslinked gelMOD by repeatedly soaking the hydrogel structures in EGM-2 at 37°C. Calcein-AM/propidium iodide live/dead stain was applied at two time points (24 h and 5 days after 2PP printing) to record LSM images (**Figure 81**).

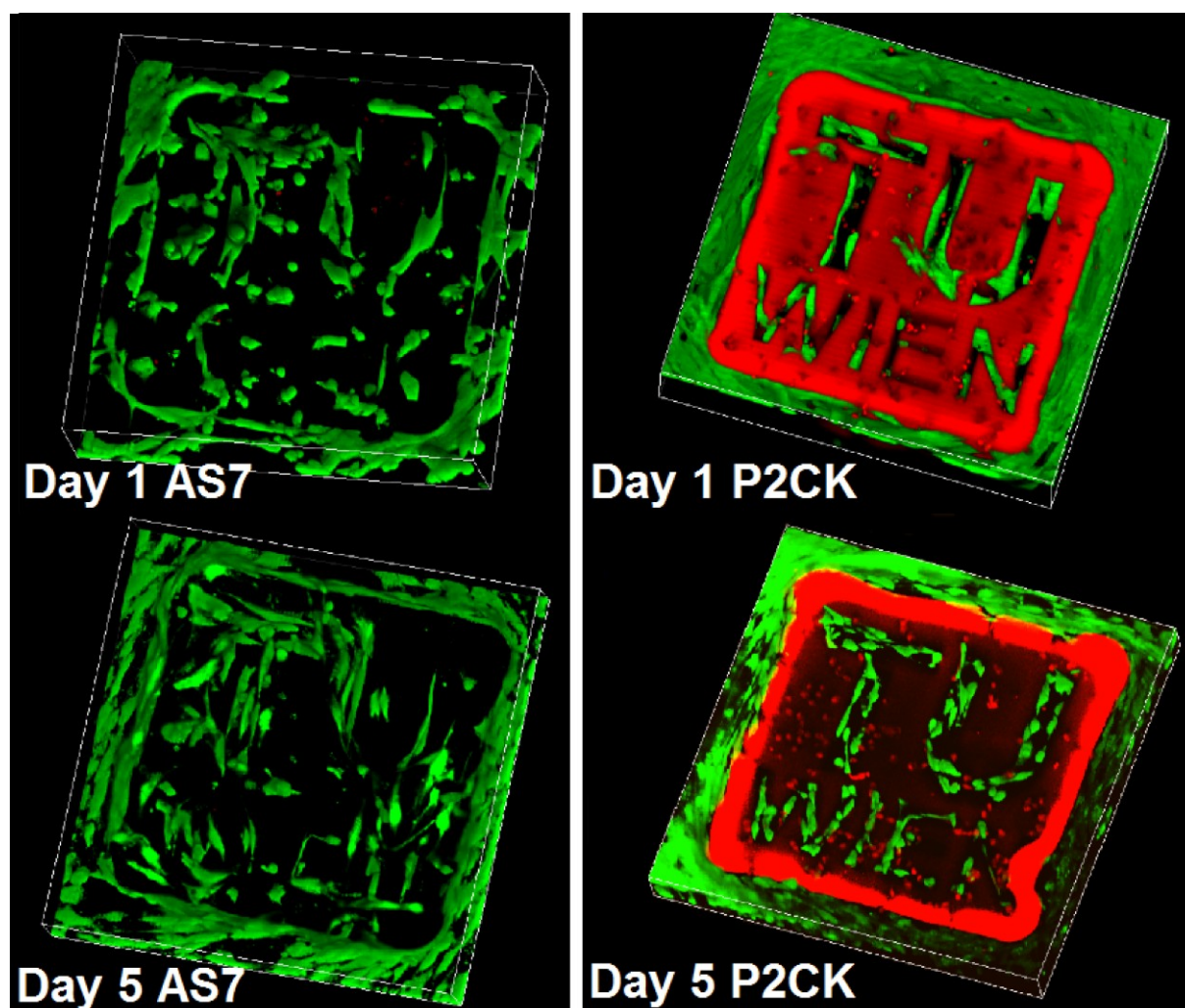


Figure 81: 3D (z-stack) LSM images of live/dead-stained ASC/TERT1 cells 24 h (top) and 5 days (bottom) after 2PP printing, 20x magnification. The cells were encapsulated in gelMOD hydrogel TU Wien logos using either 2 mM **AS7** (left) or 1 mM **P2CK** (right). In both cases, viable cells (green) spread and proliferate in the cavities and on the outer surface of the hydrogel structures. When using **AS7**, almost all cells encapsulated in the hydrogel as well as the cells in the cavities are viable (stained green) and show healthy morphology 5 days after structuring. With **P2CK** in turn, viable cells spread and proliferate in the cavities and on the outer surface of the hydrogel structure, while almost no cells encapsulated with **P2CK** survive the first 24 h (hardly any green cells in the hydrogel, cell nuclei stained bright red).²¹⁴

In order to also obtain a quantitative measure of the survival of ASC/TERT1, cells were encapsulated *via* 2PP printing in larger hydrogel cubes with a side length of 300 μm . The same formulations as in the TU Wien logo experiments at laser powers ranging from 80 - 110 mW and a fast writing speed of 1000 mm/s were used.

Live/dead stain was applied at two time points (24 h and 5 days after 2PP printing) and the live cells were counted in the 3D LSM images using ImageJ FIJI software. **Figure 82** shows examples of hydrogel cubes with encapsulated cells used for automated counting, while

Figure 83 presents the counting results.

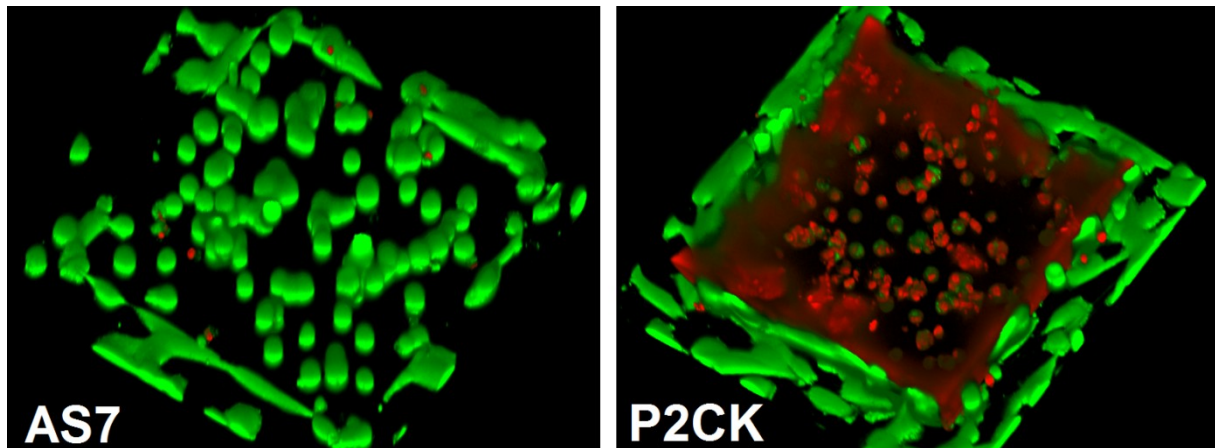


Figure 82: Examples (100 mW laser power) of hydrogel cubes used for cell survival quantification *via* automated counting. Live/dead-stained ASC/TERT1 cells 24 h after encapsulation in gelMOD cubes using either 2 mM **AS7** (left) or 1 mM **P2CK** (right).

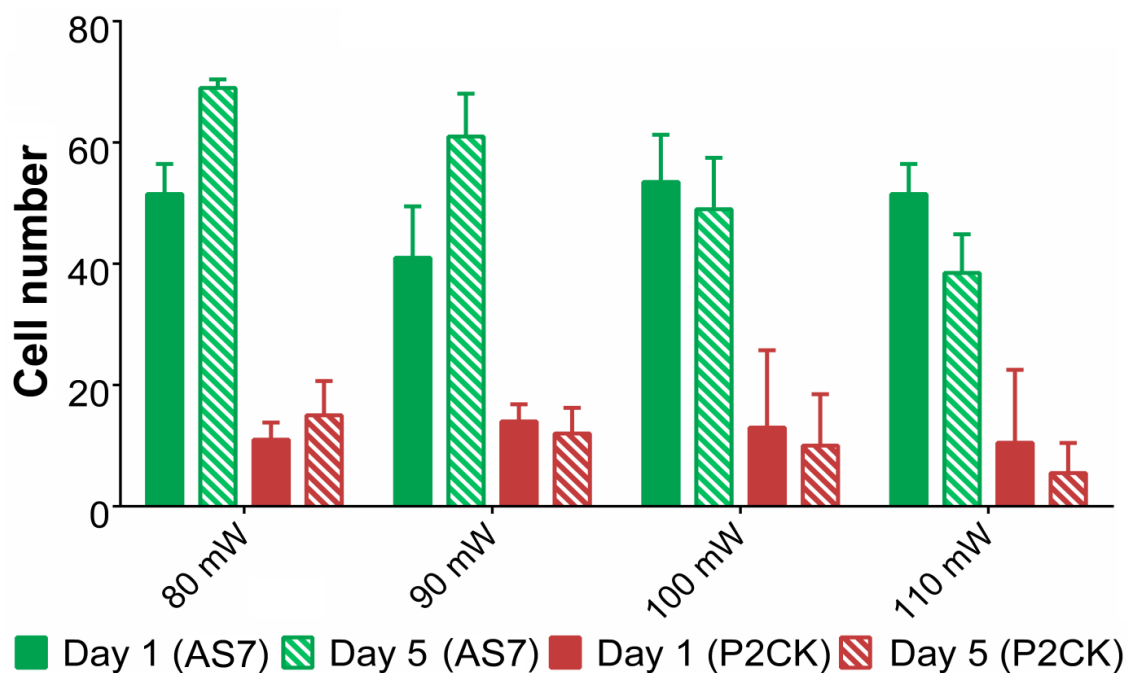


Figure 83: Results of the automated counting of viable cells that survived encapsulation in hydrogel cubes as shown in **Figure 82**.²¹⁴

Several important differences are observed when comparing the hydrogels printed and cells encapsulated with either **AS7** or **P2CK**, as shown in **Figure 81** and **Figure 82**.

As observed in previous experiments, the autofluorescence of residual **P2CK** left after 2PP structuring bleeds through into the LSM-channel recording the fluorescence of the dead-stain, causing the whole hydrogel structure to appear red and sometimes opaque. While **P2CK** also weakly and diffusely stains cells (the cell nucleus less so than other structures, see **Figure 18 - right**), this does not truly interfere with identifying the dead stained cells, as the intense fluorescence of propidium iodide is confined to the cell nuclei and thus characteristic. However, the fluorescence exhibited by **P2CK** mostly is not an useful feature and can obstruct clear view in LSM images. In case of **AS7**, no such fluorescence is observed. In fact, attempts to measure the fluorescence emission spectra and quantum yields were unsuccessful. Thus, the transmembrane migration behavior and possible intracellular accumulation of **AS7** also could not be investigated in experiments similar to those performed with **HAPI** and **E2CK** (see **Figure 28**). If a direct LSM-visualization of hydrogels printed with **AS7** is desired (appearing just as dark space in **Figure 81** and **Figure 82**), this can be achieved e.g. by addition of fluorescein-O-methacrylate to the hydrogel precursor formulation before 2PP structuring.

Regarding the behavior of the cells, a striking improvement in cytocompatibility is seen with **AS7** over **P2CK**. In the TU Wien logo structures, the use of **P2CK** as 2PI (**Figure 81 - right**) resulted in spreading and proliferation only of the cells trapped in the "letter"-cavities of the structure, *i.e.* the cells that were not exposed to the focused fs-laser radiation. Almost all cells encapsulated in the hydrogel with **P2CK** were severely photodamaged (cell nuclei stained red by propidium iodide) 24 h after encapsulation, with the few viable cells (stained green by calcein) remaining in the hydrogel dying before the next LSM-image was recorded after 5 days. In case of **AS7** however (**Figure 81 - left**), both cells trapped in the cavities and cells encapsulated in the hydrogel showed no signs of phototoxicity in the live/dead-stain assay. Either cells were stained green 24 h and 5 days after structuring, as well as showing signs of spreading and proliferation during that period.

The difference between the two 2PIs is also well visible in the hydrogel cubes fabricated for the cell counting experiments. Almost all of the cells encapsulated with

AS7 (**Figure 82 - left**) were healthy and viable, showing no morphological differences compared to cells that were attached to the outside of the hydrogel cube or the surrounding glass substrate. Membrane damage was indicated only in a few cells by the cell nuclei being stained red. With **P2CK**, cell membrane integrity was compromised during 2PP encapsulation, so that almost all the cells had nuclei stained red by propidium iodide (**Figure 82 - right**). Despite an equal cell density in the formulation before 2PP printing, 3 to 6 times as many viable cells were found in the cubes fabricated with **AS7** compared to those printed with **P2CK**, and cells were proliferating between day 1 and day 5 in the structures fabricated at 80 or 90 mW (

Figure 83).

In conclusion, the novel diazosulfonate 2PI **AS7** behaved completely differently in 2PP cell encapsulation experiments, exhibiting a vastly improved biocompatibility compared to the well established DBK reference **P2CK**.

2.2.3.2.5. Singlet oxygen formation

In an attempt to investigate the reason for the improved cytocompatibility of **AS7** during the photoencapsulation process, singlet oxygen luminescence measurements were performed in cooperation with Prof. Roman Dedic from the Charles University.

Formation of $^1\text{O}_2$ sensitized by **P2CK** and **AS7** after irradiation at 420 nm (only 1PA possible in the measuring setup) was determined by direct time-resolved detection of $^1\text{O}_2$ infrared luminescence at 1270 nm. **P2CK** showed only a very weak signal in the first 1 μs after the excitation pulse at 1 mM, a concentration typically used for 2PP structuring. The lifetime of $^1\text{O}_2$ in water is naturally short (3.5 μs), so D_2O (~68 μs lifetime) saturated with oxygen was used as a solvent for further measurements to obtain better signal quality due to higher quantum yield of phosphorescence.^{215,216} The signal quality was also improved by lowering **P2CK** concentration to 0.1 mM, with further lowering of 2PI concentration to 20 μM leading to an almost disappearing luminescence signal. This can be explained by the fact that **P2CK** could act both as sensitizer and quencher in the formation of $^1\text{O}_2$, with the quenching effect being dominant at 1 mM. The quenching of $^1\text{O}_2$ by **P2CK** is also expressed in the shortening of $^1\text{O}_2$ lifetime (compared to pure D_2O) to 16 ± 4 μs (**Figure 84**, red line).

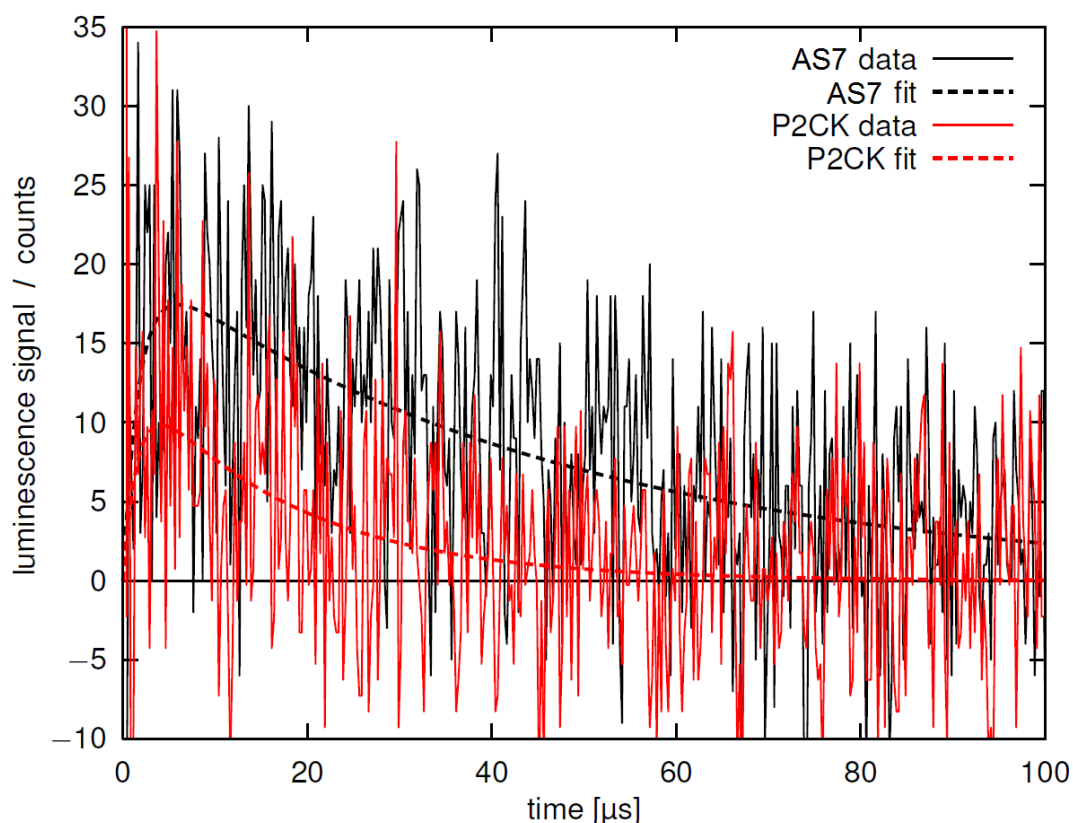


Figure 84: Luminescence signal (solid) together with respective fits (dotted) of excited $^1\text{O}_2$ generated by 100 μM **AS7** (black) and the reference **P2CK** (red) in D_2O saturated by oxygen.²¹⁴

In contrast to what was expected from cell encapsulation experiments, **AS7** (**Figure 84**, black line) showed a four times stronger signal than **P2CK**, indicating that it acts as a more potent photosensitizer of $^1\text{O}_2$. This could be explained by the fact that at a concentration of 100 μM , the quenching of $^1\text{O}_2$ by **AS7** is much lower compared to **P2CK**. The longer $^1\text{O}_2$ lifetime of ~ 40 μs using **AS7** in D_2O would also support this conclusion. Nevertheless, the efficiency of $^1\text{O}_2$ generation is exceedingly weak in both cases. Compared to compounds used in photodynamic therapy such as porphyrins (compared to tetraphenylporphine tetrasulfonate (TPPS4) in the same experimental setup, data not shown), the luminescence is two to three orders of magnitude lower.^{47,48} This suggests that $^1\text{O}_2$ -formation alone is not the only cause of photodamage observed in the 2PP-encapsulation of cells with **P2CK**. For example, the formation of $\text{O}_2^{\bullet-}$ via bimolecular electron transfer²¹⁷ from the 2PI to O_2 could be lower in case of **AS7**, due to its lack of electron donating groups and reduced electron density of the π -system compared to **P2CK**. Further experiments will be required to investigate the differences in ROS-formation induced by **AS7** or **P2CK**.

2.2.3.2.6. Attempted elucidation of the initiation mechanism *via* laser flash photolysis and CIDNP

The actual mechanisms of 2PA induced radical formation are inherently difficult to elucidate, since only minute amounts of active species are formed and confined in a very small excitation volume of a tightly focused laser. However, as a first approximation, the 1PA induced photochemistry of **AS7** and **P2CK** should be investigated.

In cooperation with Prof. Georg Gescheidt-Demner and Anna Eibel from TU Graz, chemically induced dynamic nuclear polarization (CIDNP) and laser flash photolysis (LFP) experiments were performed.

CIDNP-spectroscopy is a type of NMR-experiment that makes use of the coupling between electron spins and nuclear spins in radicals, leading to a nuclear spin polarization that greatly enhances the intensity of certain signals.²¹⁸ **Figure 85** and **Figure 86** show the NMR-spectra of **AS7** (1 mM in D₂O) and **P2CK** (0.5 mM in D₂O) before and during CIDNP, where radicals should be generated by irradiation with a 355 nm laser.

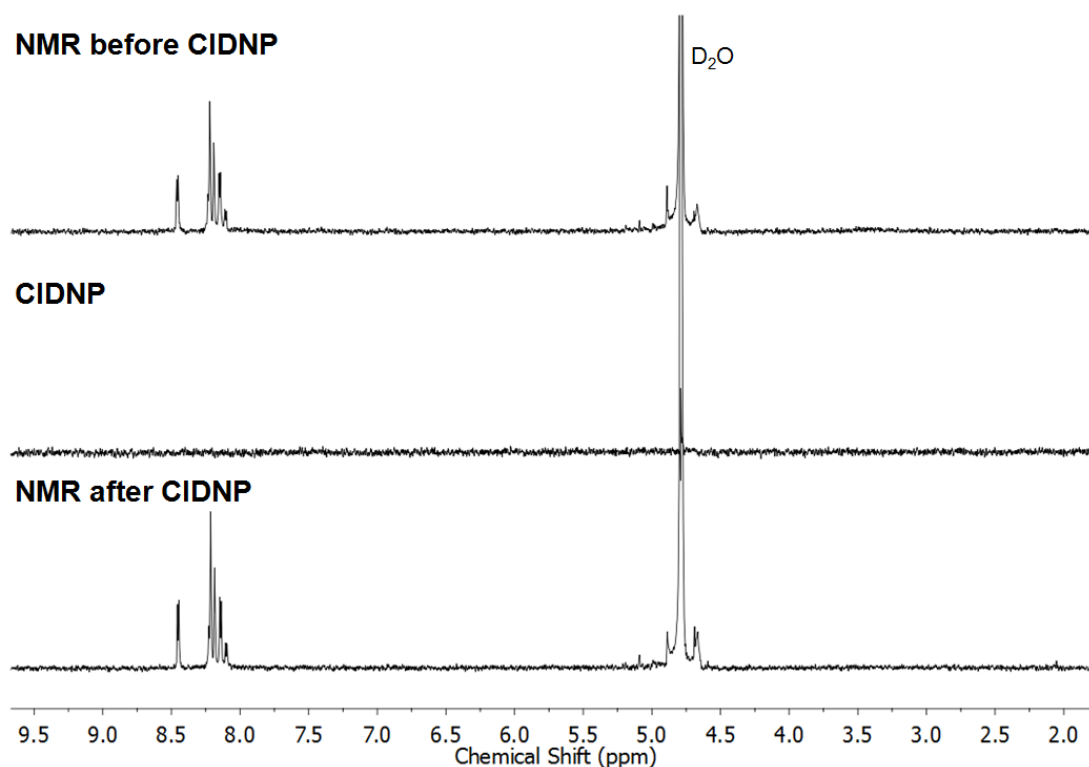


Figure 85: ¹H-NMR and -CIDNP (355 nm laser excitation) spectra of **AS7**.

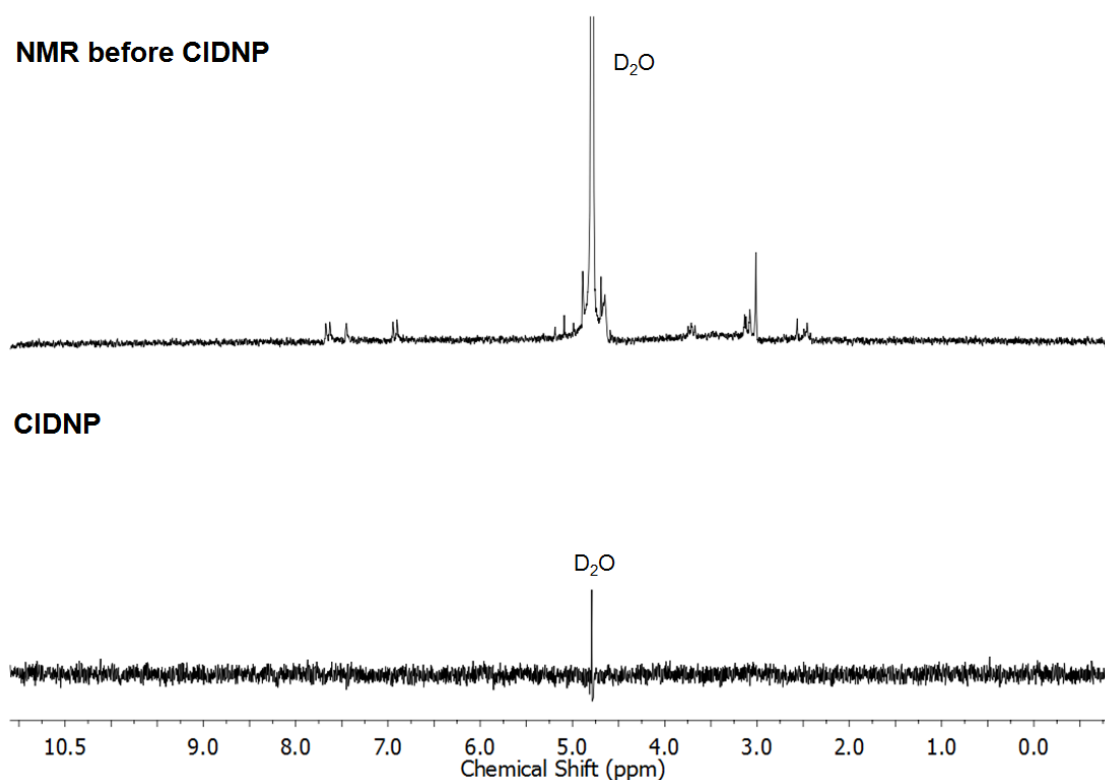


Figure 86: ¹H-NMR and -CIDNP(355 nm laser excitation) spectra of **P2CK**.

No CIDNP signals were observed. Besides the laser wavelength not being suitable for radical generation from the 2PIs (although **AS7** shows strong absorption at 355 nm), the detection could also be unsuitable in regard to the lifetime of the formed radicals. Addition of methyl methacrylate (slightly soluble in D₂O) also did not lead to observable CIDNP signals.

The LFP, also performed with a 355 nm pump laser, similarly did not yield any signals from transient absorbing species in the observed range from 350 - 650 nm (**Figure 87** and **Figure 88**).

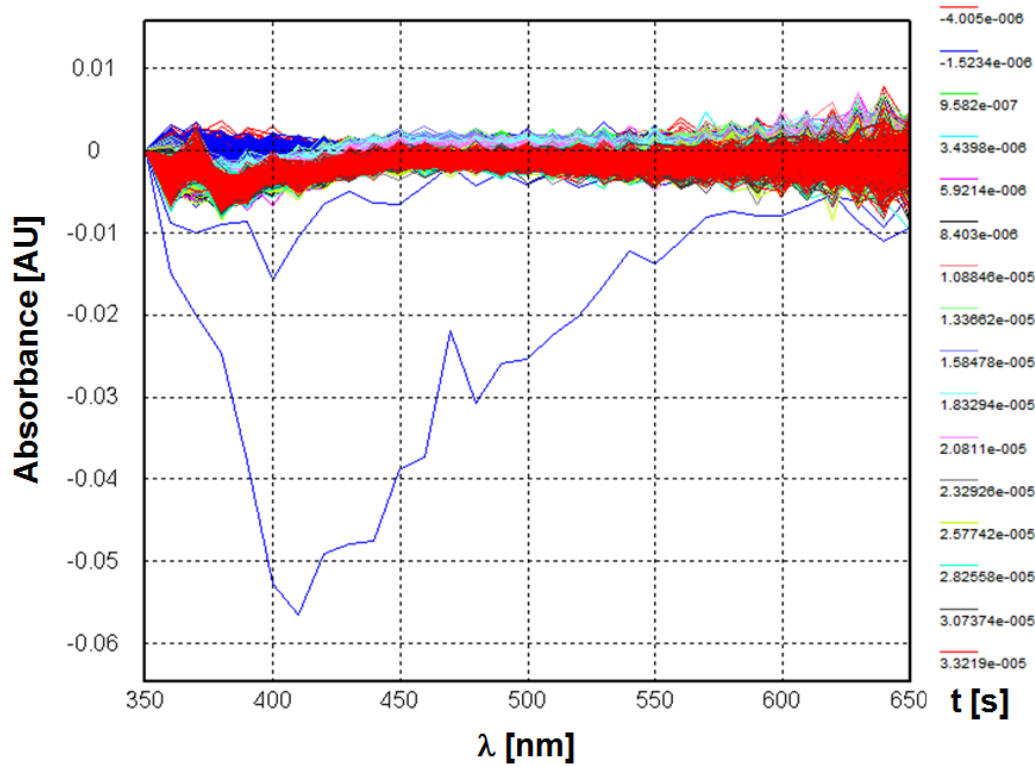


Figure 87: Laser flash photolysis (355 nm) of AS7.

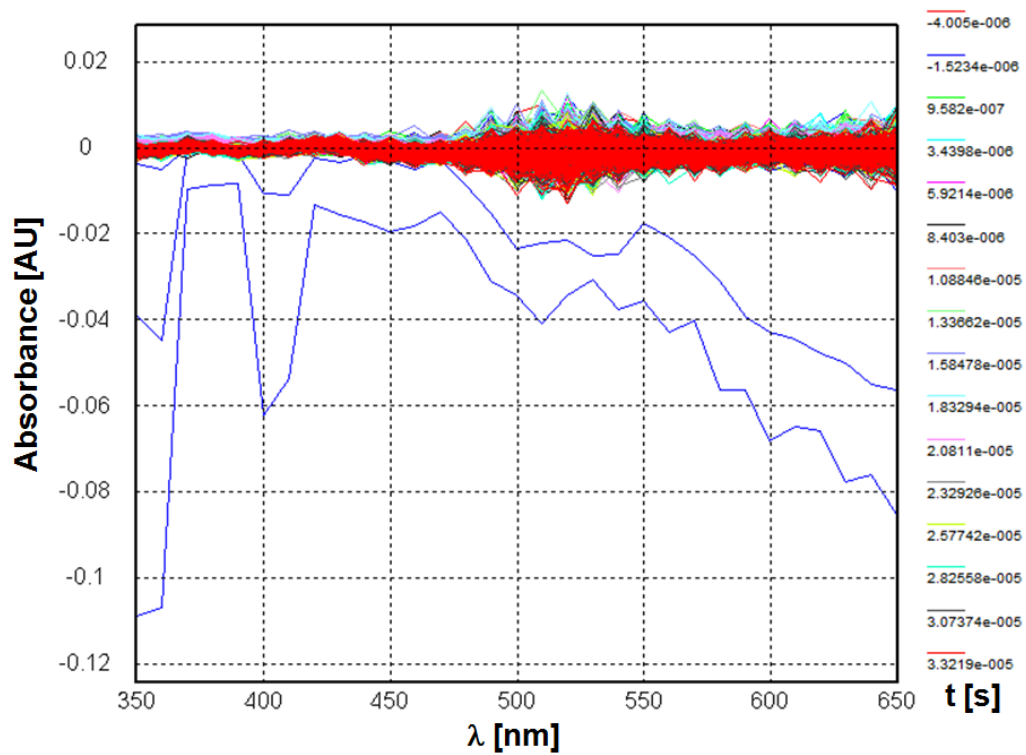


Figure 88: Laser flash photolysis (355 nm) of P2CK.

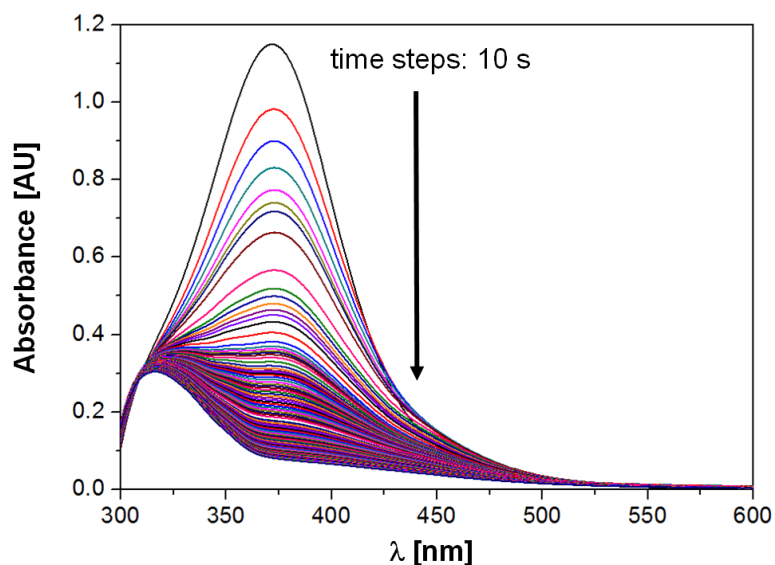


Figure 89: UV/Vis-spectra during photolysis of **AS7** with a 385 nm LED.

UV/Vis-spectra recorded from solutions of **AS7** (~0.05 mM in water, **Figure 89**) in time steps of 10 s during irradiation with a 385 nm LED demonstrated photolysis of the 2PI at that wavelength. The same experiment showed no or very slow photobleaching of **P2CK** (~0.03 mM in water, **Figure 90**). While the change in **AS7** absorption spectra is too uncharacteristic to allow conclusions regarding the photoproducts, this is indicative of a cleavable mechanism in case of **AS7** but not **P2CK**.

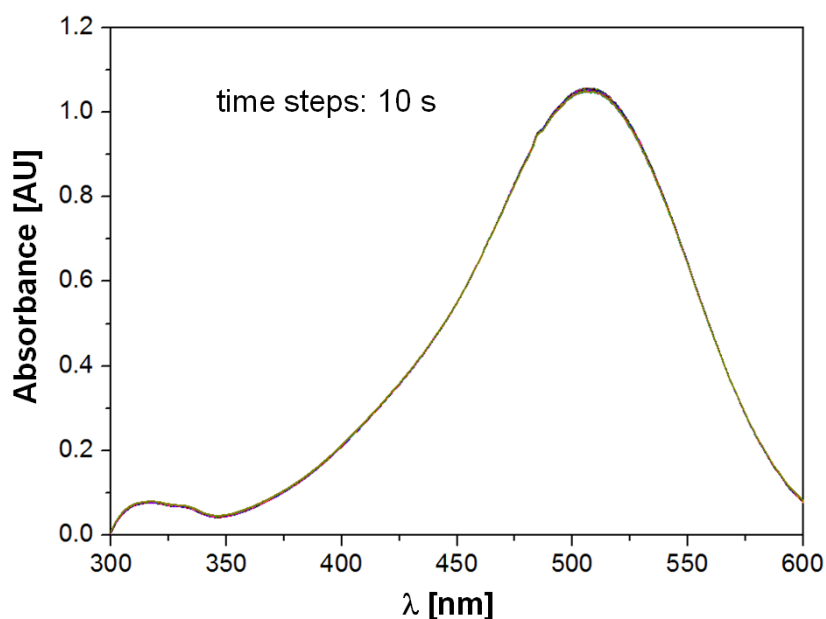


Figure 90: UV/Vis-spectra during attempted photolysis of **P2CK** with a 385 nm LED.

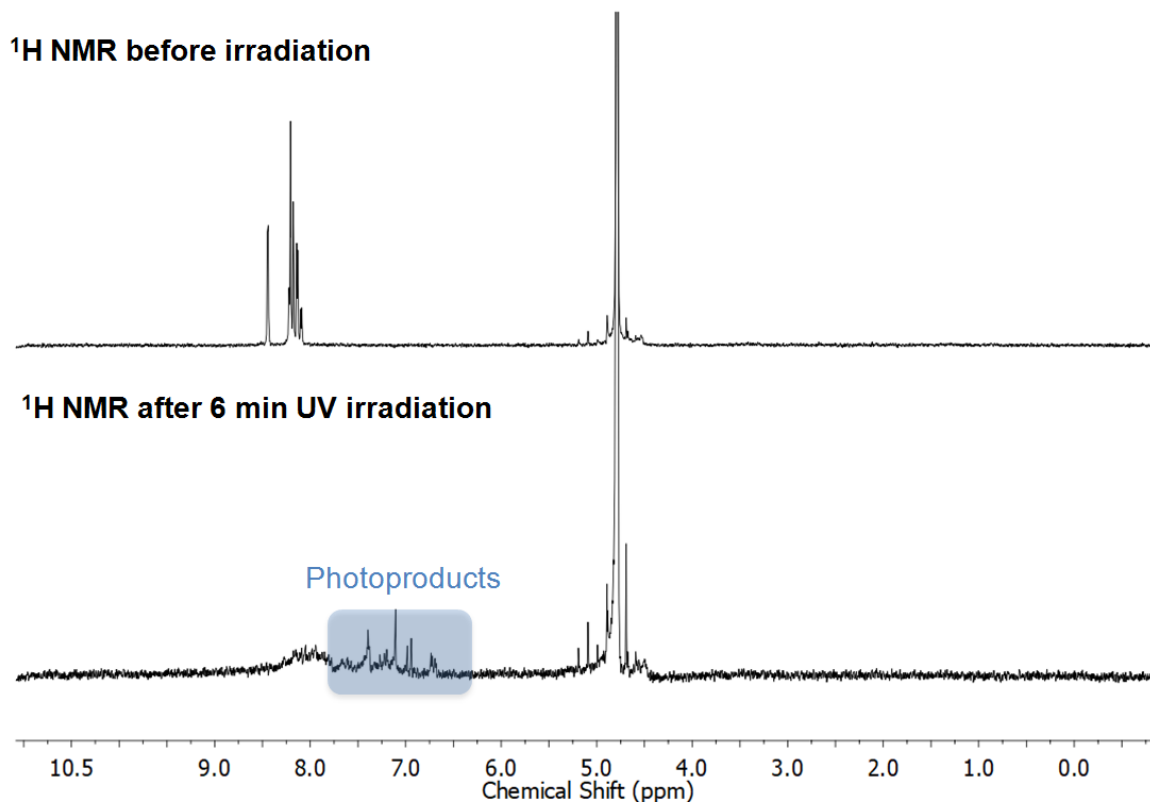


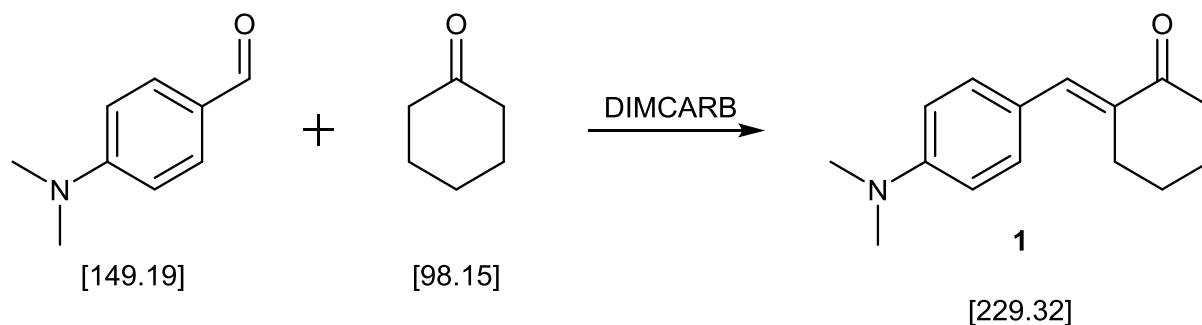
Figure 91: ^1H -NMR before and after photolysis of **AS7** with a Hg-Xe UV-lamp.

Photolysis of a 2 mM solution of **AS7** in D_2O with a Hg-Xe UV-lamp could achieve complete decomposition of the 2PI to aromatic photoproducts (**Figure 91**).

In conclusion, the elucidation of the mechanism of even 1PA induced radical formation from **AS7** requires further studies and possibly also a change of the hardware (e.g. the exciting laser, detection) of the experimental setups for CIDNP and LFP.

Experimental Part

1.1.1.1.1. (2E)-2-[4-(dimethylamino)phenyl]methylene]cyclohexanone (1)



Reagents	MW [g/mol]	[mg]	[mL]	[mmol]	[eq.]
4-(dimethylamino)benzaldehyde	149.19	870		5.83	1.0
cyclohexanone	98.15	572		5.83	1.0
dimethylammonium dimethyl- carbamate (DIMCARB)			9		

Procedure

All steps were performed in an orange light room. DIMCARB (9 mL) was added to 4-(dimethylamino)benzaldehyde (870 mg, 5.83 mmol, 1.0 eq) with magnetic stirring under argon atmosphere. After the visible formation of CO₂-gas had stopped, the mixture was heated to 50°C and cyclohexanone (572 mg, 5.83 mmol, 1.0 eq) was added subsequently. Stirring at 50°C was continued for 48 h, leading to the formation of a bright orange precipitate. After removal of DIMCARB *in vacuo* the bright orange solid residue was dissolved in DCM (50 mL), extracted with aq. H₂SO₄ (0.5 M, 40 mL), the organic layer dried with Na₂SO₄ and stripped of solvent *in vacuo*. The bright orange residue was purified further by column chromatography (PE:EA = 4:1, 235 g silica gel 60) and subsequent recrystallization from n-hexane, yielding monobenzylidene ketone **1** as fine yellow needles.

Yield

789 mg yellow needles (59% of theory)

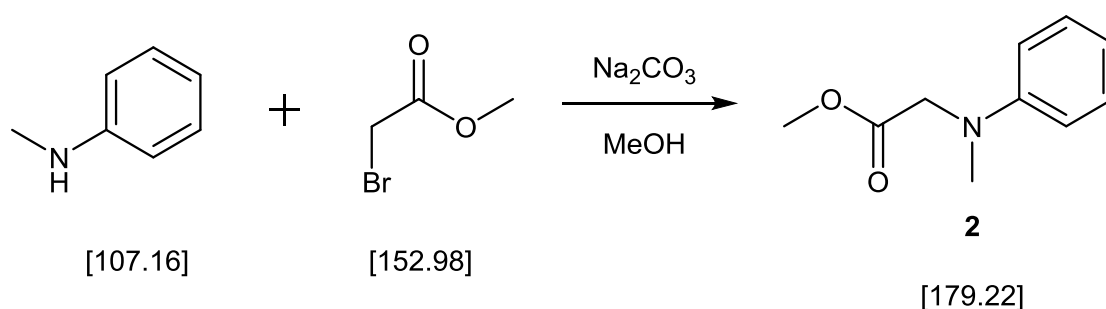
Analysis

TLC: $R_f = 0.32$ (PE:EA = 4:1)

mp: 127 - 128°C (lit. 127 - 128°C)²¹⁹

¹H NMR (200 MHz, CDCl₃) δ (ppm) = 7.55 (1H, s, -C=CH), 7.40 (2H, d, $J = 8.8$ Hz, -N-ar-H^{3,5}), 6.69 (2H, d, $J = 8.8$ Hz, -N-ar-H^{2,6}), 3.00 (6H, s, -N(CH₃)₂), 2.86 (2H, dt, $J = 1.9$ and 6.3 Hz, -CH₂-C=O), 2.50 (2H, t, $J = 6.7$ Hz, -CH₂-C=CH), 1.69 - 1.98 (4H, m, -CH₂-CH₂-)

¹³C-NMR (50 MHz, CDCl₃) δ (ppm) = 201.0 (1C, -C=O), 150.4 (1C, N-ar-C¹), 141.1 (1C, -C=CH), 137.1 (1C, -C=CH), 132.5 (2C, N-ar-C^{3,5}), 123.3 (1C, N-ar-C⁴), 111.4 (2C, N-ar-C^{2,6}), 40.0 (2C, -N(CH₃)₂), 39.8 (1C, -CH₂-C=O), 29.0 (1C, -CH₂-C=CH), 23.7 + 23.1 (2C, -CH₂-CH₂-)

1.1.1.1.2. N-methyl-N-phenylglycine methyl ester (2)

Reagents	MW [g/mol]	[g]	[mL]	[mmol]	[eq.]
N-methylaniline	107.16	10.7		100	1.0
methyl 2-bromoacetate	152.98	16.9		110	1.1
Na ₂ CO ₃	105.99	15.9		150	1.5
MeOH			150		

Procedure

Sodium carbonate (15.9 g, 150 mmol, 1.5 eq) was added to a solution of freshly distilled N-methylaniline (10.7 g, 100 mmol, 1.0 eq) and methyl 2-bromoacetate (16.9

g, 110 mmol, 1.1 eq) in MeOH (150 mL). The reaction mixture was held at reflux with magnetic stirring under argon atmosphere for 18 h. After cooling to room temperature, the reaction mixture was filtered and stripped of solvent *in vacuo*. The residue was dissolved in EA (250 mL), extracted with deionized water (3 x 100 mL), the organic layer dried with Na₂SO₄ and stripped of solvent *in vacuo*. The oily residue was purified by vacuum distillation to afford aniline **2** as yellow oil.

Yield

15.7 g yellow oil (87% of theory)

Analysis

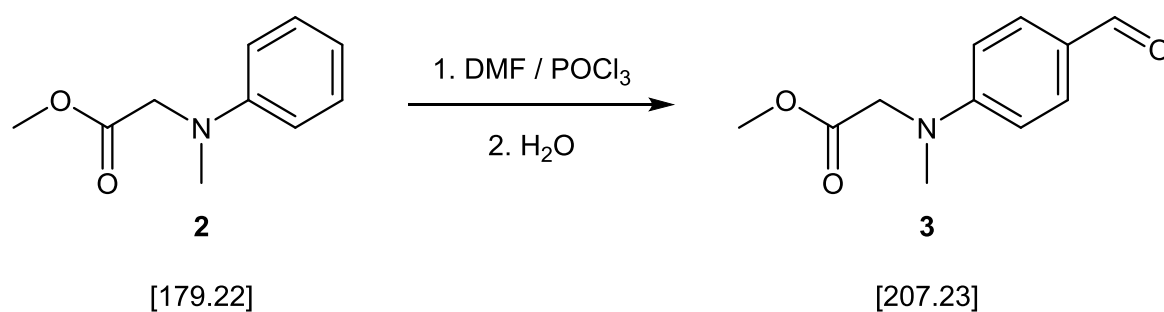
TLC: $R_f = 0.25$ (PE:EA = 9:1)

bp: 70 - 76°C (27 mbar)

¹H NMR (200 MHz, CDCl₃) δ (ppm) = 7.20 - 7.07 (2H, m, -N-ar-H^{3,5}), 6.71 - 6.53 (3H, m, -N-ar-H^{2,4,6}), 3.96 (2H, s, -N-CH₂-), 3.59 (s, 3H, -COO-CH₃), 2.95 (3H, s, -N-CH₃)

¹³C-NMR (50 MHz, CDCl₃) δ (ppm) = 171.4 (1C, -COO-CH₃), 148.7 (1C, N-ar-C¹), 129.1 (2C, N-ar-C^{3,5}), 117.2 (1C, N-ar-C⁴), 112.1 (2C, N-ar-C^{2,6}), 54.1 (1C, -N-CH₂-COO), 51.7 (1C, -COO-CH₃), 39.3 (1C, -N-CH₃)

1.1.1.1.3. *N*-(4-formylphenyl)-*N*-methylglycine methyl ester (**3**)



Reagents	MW [g/mol]	[g]	[mL]	[mmol]	[eq.]
aniline 2	179.22	10.0		56	1.0

POCl ₃	153.33	8.6	56	1.0
dry DMF			47	

Procedure

Freshly distilled POCl₃ (8.6 g, 56 mmol, 1.0 eq) was added dropwise to dry DMF (35 mL) under argon atmosphere and magnetic stirring, maintaining an internal temperature between -5°C and 0°C. Once addition of POCl₃ was completed the reaction mixture was stirred for another 30 min, keeping the temperature below 0°C. A solution of aniline **2** (10.0 g, 56 mmol, 1.0 eq) in dry DMF (12 mL) was then added, the reaction mixture heated to 80°C and stirred for 3.5 h at that temperature. The mixture was then cooled to room temperature, poured into ice water and stirred vigorously for 18 h. Subsequently, the pH of the solution was adjusted to 7-8 by adding aq. NaOH (1 mol/L, 200 mL), the formed precipitate collected *via* suction filtration, dissolved in DCM (200 mL) and washed with deionized water (4 x 400 mL). The organic layer was dried with Na₂SO₄ and stripped of solvent *in vacuo*. The solid residue was recrystallized from PE:Et₂O (4:1, 2.8 L) and dried *in vacuo* to obtain aldehyde **3** as white crystals.

Yield

7.6 g white crystals (66% of theory)

Analysis

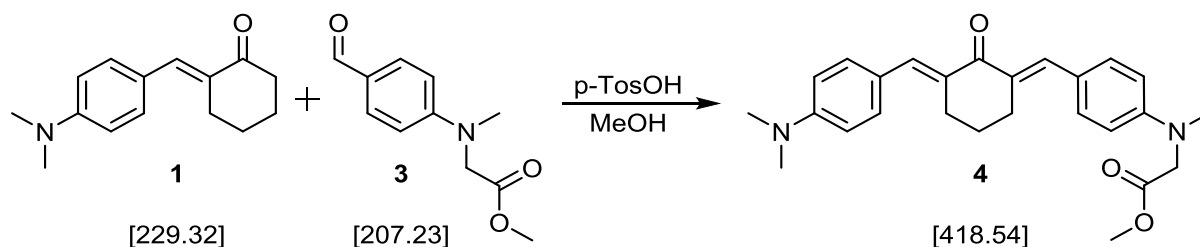
TLC: R_f = 0.35 (PE:EA = 3:2)

mp: 73 - 74°C (lit. 75 - 78°C)²²⁰

¹H NMR (200 MHz, CDCl₃) δ (ppm) = 9.73 (1H, s, H-C=O), 7.72 (2H, d, J=9.0 Hz, -N-ar-H^{3,5}), 6.67 (2H, d, J=9.2 Hz, -N-ar-H^{2,6}), 4.13 (2H, s, -N-CH₂-COO-), 3.71 (3H, s, -COO-CH₃), 3.12 (3H, s, N-CH₃)

¹³C-NMR (50 MHz, CDCl₃) δ (ppm) = 190.2 (1C, H-C=O), 170.1 (1C, -COO-CH₃), 153.2 (1C, N-ar-C¹), 131.8 (2C, N-ar-C^{3,5}), 126.2 (1C, N-ar-C⁴), 111.2 (2C, N-ar-C^{2,6}), 53.6 (1C, -N-CH₂-COO), 52.1 (1C, -COO-CH₃), 39.5 (1C, -N-CH₃)

1.1.1.1.4. (1E,3E)-N-[4-[[3-[[4-(dimethylamino)phenyl]methylene]-2-oxocyclohex-1-ylidene]methyl]phenyl]-N-methyl-glycine methyl ester (4)



Reagents	MW [g/mol]	[mg]	[mL]	[mmol]	[eq.]
MBK 1	229.32	500		2.18	1.0
aldehyde 3	207.23	542		2.62	1.2
p-TsOH	156.20	75		0.44	0.2
MeOH			8		

Procedure

All steps were performed in an orange light room. MBK **1** (500 mg, 2.18 mmol, 1.0 eq), aldehyde **3** (542 mg, 2.62 mmol, 1.2 eq) and p-TsOH (75 mg, 0.44 mmol, 0.2 eq) were dissolved in dry MeOH (8 mL). The reaction mixture was magnetically stirred under argon atmosphere at 55°C for 48 h. The resulting yellow precipitate was collected *via* vacuum filtration and washed with cold MeOH (2 mL). DBK **4** was obtained as fine orange needles by recrystallization from EA and drying *in vacuo*.

Yield

703 mg orange needles (77% of theory)

Analysis

TLC: R_f : 0.53 (DCM/EE 20:1)

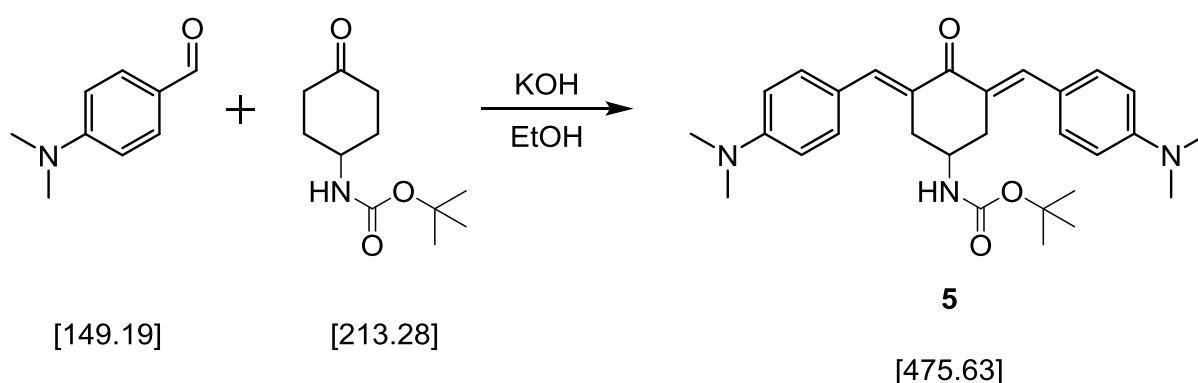
mp: 160 - 162°C

$^1\text{H NMR}$ (200 MHz, CDCl_3) δ (ppm) = 7.72 - 7.82 (2H, m, $-\text{C}=\text{CH}-$), 7.37 - 7.50 (4H, m, N-ar- $\text{H}^{3,5}$), 6.61 - 6.77 (4H, m, N-ar- $\text{H}^{2,6}$), 4.10 (2H, s, $(\text{CH}_3)\text{N}-\text{CH}_2\text{COO}-$), 3.73 (3H, s, $-\text{COO}-\text{CH}_3$), 3.10 (3H, s, $(\text{CH}_3)\text{N}-\text{CH}_2\text{COO}-$), 3.00 (6H, s, $(\text{CH}_3)_2\text{N}-$), 2.83 -

2.96 (4H, m, -CH₂-CH₂-CH₂-), 1.79 (2H, quin, J = 5.8 Hz, -CH₂-CH₂-CH₂-)

¹³C-NMR (50 MHz, CDCl₃) δ (ppm) = 189.8 (1C, O=C(-C=CH-)₂), 170.8 (1C, -CH₂-COO-), 150.2 (1C, (CH₃)₂N-ar-C¹), 148.7 (1C, -CH₂-N-ar-C¹), 137.1 + 136.4 (2C, -C=CH-), 132.8 (1C, -C=CH), 132.3 (4 C, -N-ar-C^{3,5}), 132.1 (1C, -C=CH-), 125.2 + 124.0 (2C, N-ar-C⁴), 111.5 (4 C, -N-ar-C^{2,6}), 53.8 (1C, CH₃-N-CH₂-), 51.9 (1C, -COO-CH₃), 40.0 (2C, (CH₃)₂N), 39.3 (1C, -CH₂-N-CH₃), 28.6 + 28.5 (2C, -CH₂-CH₂-CH₂-), 23.0 (1C, -CH₂-CH₂-CH₂-)

1.1.2.1.1. (3E,5E)-N-[3,5-bis[[4-(dimethylamino)phenyl]methylene]-4-oxo-cyclohexyl]carbamic acid 1,1-dimethylethyl ester (5)



Reagents	MW [g/mol]	[mg]	[mL]	[mmol]	[eq.]
4-(dimethylamino)benzaldehyde	149.19	1000		6.70	2.0
Boc-CNK	213.28	715		3.35	1.0
KOH	56.10	188		3.35	1.0
EtOH			10		

Procedure

All steps were performed in an orange light room. To a magnetically stirred solution of Boc-CNK (715 mg, 3.35mmol, 1.0 eq) in EtOH (5 mL), a solution of 4-(dimethylamino)benzaldehyde (1 g, 6.70 mmol, 2.0 eq) and KOH (188 mg, 3.35

mmol, 1.0 eq) in EtOH (5 mL) was added. The reaction mixture was heated to 55°C and stirred for 24 h. After cooling to room temperature, the reaction mixture was further cooled to 4°C in the fridge and the resulting orange precipitate of DBK **5** was recovered by suction filtration 24 h later, washed with cold EtOH and dried *in vacuo*.

Yield

1.21 g orange powder (76% of theory)

Analysis

TLC: R_f : 0.55 (DCM/MeOH/NH₄OH 90:10:1)

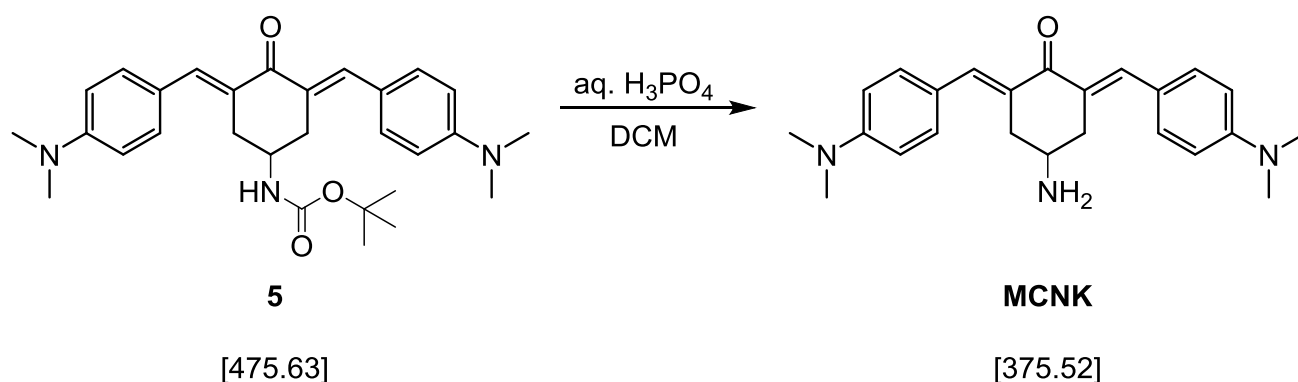
mp: 219 - 222°C

HR-MS m/z: [M+H]⁺ calculated for C₂₉H₃₈N₃O₃ 476.2908;
found 476.2932

¹H NMR (200 MHz, CDCl₃): δ (ppm) = 7.88 (2H, s, -C=CH-), 7.42 (4H, d, J = 8.9 Hz, N-ar-H^{3,5}), 6.69 (4H, d, J = 8.9 Hz, N-ar-H^{2,6}), 4.58 - 4.90 (1H, m, -CH₂-CH-CH₂-), 4.09 (1H, bs, -NH-COO-), 2.72 - 3.25 (16H, m, -CH₂-CH-CH₂-, (CH₃)₂N-), 1.37 (9H, s, -COO-C(CH₃)₃)

¹³C NMR (50 MHz, CDCl₃): δ (ppm) = 188.3 (1C, O=C(-C=CH-)₂), 155.1 (1C, -NH-COO-), 150.6 (2C, N-ar-C¹), 139.9 (2C, -C=CH-), 132.6 (4 C, -N-ar-C^{3,5}), 128.1 (2C, -C=CH-), 123.6 (2C, N-ar-C⁴), 111.6 (4C, -N-ar-C^{2,6}), 79.3 (1C, -COO-C(CH₃)₃), 45.2 (1C, -CH₂-CH-CH₂-), 40.1 (4C, (CH₃)₂N-), 34.4 (2C, -CH₂-CH-CH₂-), 28.4 (3C, -COO-C(CH₃)₃)

1.1.2.1.2. (2E,6E)-4-amino-2,6-bis[[4-(dimethylamino)phenyl]methylene]
cyclohexanone (MCNK)



Reagents	MW [g/mol]	[mg]	[mL]	[mmol]	[eq.]
DBK 5	475.63	875		1.84	1.0
H ₃ PO ₄			2		
DCM			7.5		

Procedure

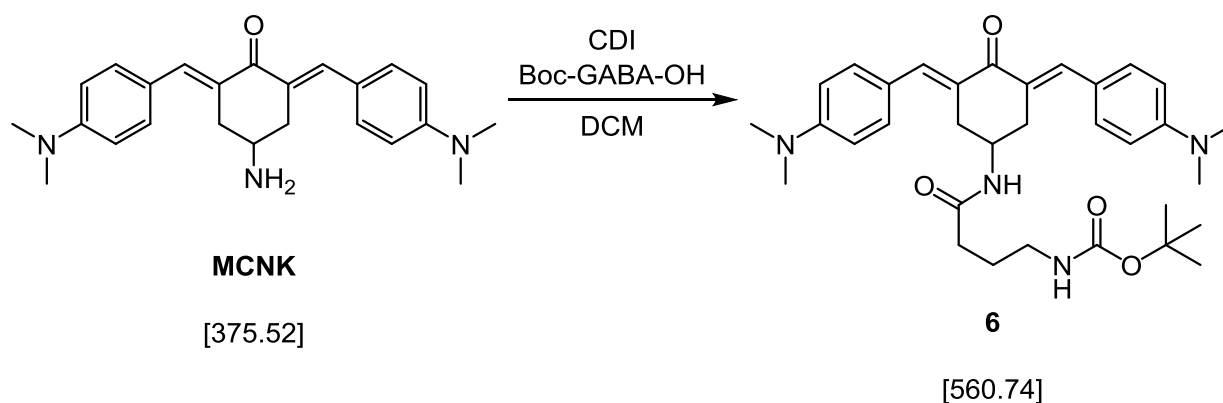
All steps were performed in an orange light room. Phosphoric acid (85% aqueous solution, 2 mL) was added to a suspension of DBK **5** (875 mg, 1.84 mmol) in DCM (7.5 mL) and stirred vigorously to ensure constant mixing of the phases. After 3 h stirring at room temperature, the solids had dissolved resulting in an almost colorless organic phase and a bluish grey aqueous phase. Deionized water (25 mL) was added, the reaction mixture cooled to 0°C and NaOH (50% aqueous solution) was added drop-wise to bring the aqueous phase to pH ~9. The aqueous phase was extracted with DCM (3 x 75 mL), adding more water as necessary to dissolve remaining solid phosphate salts. The combined organic layers were dried over Na₂SO₄ and stripped of solvent *in vacuo*, resulting in orange flakes of **MCNK**.

Yield

656 mg orange flakes (95% of theory)

AnalysisTLC: R_f: 0.25 (DCM/EA 20:1)

mp: 158 - 160°C

HR-MS m/z: [M+H]⁺ calculated for C₂₄H₃₀N₃O 376.2383;
found 376.2394¹H NMR (200 MHz, CDCl₃): δ(ppm) = 7.82 (2H, s, -C=CH-), 7.43 (4H, d, J = 9.0 Hz, N-ar-H^{3,5}), 6.69 (4H, d, J = 9.0 Hz, N-ar-H^{2,6}), 3.10 - 3.30 (3H, m, -CH₂-CH-CH₂-, -CH₂-CH-CH₂-), 3.00 (12H, s, (CH₃)₂N-), 2.55 - 2.83 (2H, m, -CH₂-CH-CH₂-), 1.39 (2H, s, -NH₂)¹³C NMR (50 MHz, CDCl₃): δ(ppm) = 188.8 (1C, O=C(-C=CH-)₂), 150.5 (2C, N-ar-C¹), 138.5 (2C, -C=CH-), 132.5 (4 C, -N-ar-C^{3,5}), 129.6 (2C, -C=CH-), 123.9 (2C, N-ar-C⁴), 111.6 (4 C, -N-ar-C^{2,6}), 47.0 (1C, -CH₂-CH-CH₂-), 40.1 (4C, (CH₃)₂N-), 38.1 (2C, -CH₂-CH-CH₂-)**1.2.2.1. (3E,5E)-N-[4-[[3,5-bis[[4-(dimethylamino)phenyl]methylene]-4-oxocyclohexyl]amino]-4-oxobutyl]carbamic acid 1,1-dimethylethyl ester (6)**

Reagents	MW [g/mol]	[mg]	[mL]	[mmol]	[eq.]
MCNK	375.52	556		1.48	1.0
Boc-GABA-OH	203.24	300		1.48	1.0

CDI	162.15	239	1.48	1.0
DCM			13	

Procedure

All steps were performed in an orange light room. Boc-GABA-OH (300 mg, 1.48 mmol) and CDI (239 mg, 1.48 mmol) were dissolved in anhydrous dichloromethane (3 mL) and stirred for 20 min after cessation of the initial gas formation. A suspension of MCNK (556 mg, 1.48 mmol) in dichloromethane (10 mL) was added and the resulting mixture stirred for 18 h. After removal of the solvent *in vacuo*, the solid residue was recrystallized from EA to obtain pure DBK **6**.

Yield

830 mg orange crystals (79% of theory)

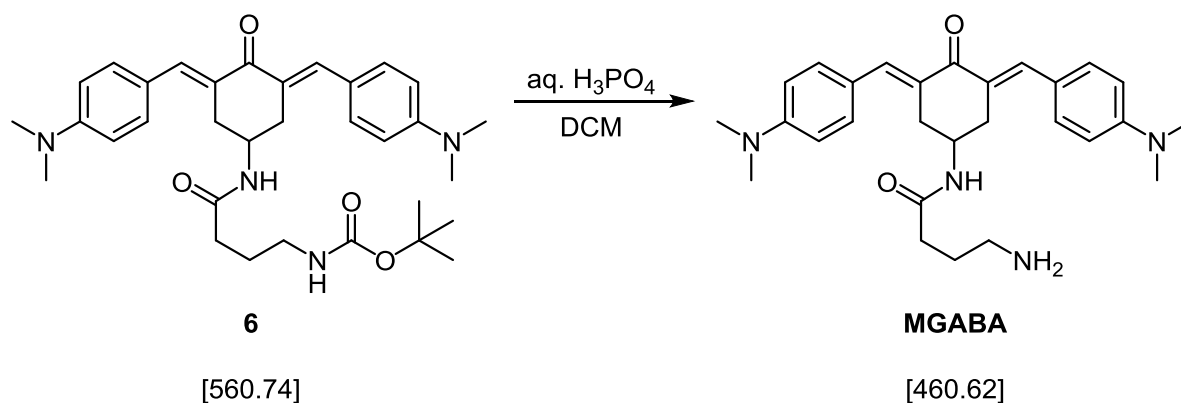
Analysis

TLC:	R _f : 0.60 (EA)
mp:	decomposition > 250°C
HR-MS m/z:	[M+H] ⁺ calculated for C ₃₃ H ₄₅ N ₄ O ₄ 561.3435; found 561.3461

¹H NMR (200 MHz, CDCl₃): δ(ppm) = 7.85 (2H, s, -C=CH-), 7.37 (4H, d, J = 8.9 Hz, N-ar-H^{3,5}), 6.64 (4H, d, J = 8.9 Hz, N-ar-H^{2,6}), 6.49 (1H, d, J = 7.0 Hz, -NH-CO-CH₂-), 4.86 (1H, bs, -NH-COO-), 4.25 - 4.49 (1H, m, -CH₂-CH-CH₂-), 2.90 - 3.22 (18H, m, -CH₂-CH-CH₂-, (CH₃)₂N-, -CH₂-NH-COO-), 2.13 (2H, t, J = 7.0 Hz, -NH-CO-CH₂-), 1.70 (2H, quin, J = 6.8 Hz, -CH₂-CH₂-CH₂-), 1.40 (9H, s, -COO-C(CH₃)₃)

¹³C NMR (50 MHz, CDCl₃): δ(ppm) = 188.3 (1C, O=C(-C=CH-)₂), 172.1 (1C, -NH-CO-CH₂-), 156.3 (1C, -COO-C(CH₃)₃), 150.6 (2C, N-ar-C¹), 140.1 (2C, -C=CH-), 132.7 (4C, -N-ar-C^{3,5}), 127.9 (2C, -C=CH-), 123.5 (2C, N-ar-C⁴), 111.7 (4C, -N-ar-C^{2,6}), 79.1 (1C, -COO-C(CH₃)₃), 44.2 (1C, -CH₂-CH-CH₂-), 40.1 (4C, (CH₃)₂N-), 39.7 (1C, -CH₂-NH-COO-), 33.9 + 33.6 (3C, -CH₂-CH-CH₂-, -NH-CO-CH₂-), 28.4 (1C, -COO-C(CH₃)₃), 26.2 (1C, -CH₂-CH₂-CH₂-)

1.2.2.2. (3E,5E)-4-amino-N-[3,5-bis[[4-(dimethylamino)phenyl]methylene]-4-oxocyclohexyl]butanamide (MGABA)



Reagents	MW [g/mol]	[mg]	[mL]	[mmol]	[eq.]
DBK 6	560.74	600		1.07	1.0
H ₃ PO ₄			2		
DCM			5		

Procedure

All steps were performed in an orange light room. Phosphoric acid (85% aqueous solution, 2 mL) was added to a suspension of DBK **6** (600 mg, 1.07 mmol) in DCM (5 mL) and stirred vigorously to ensure constant mixing of the phases. After 3 h stirring at room temperature, the solids had dissolved resulting in an almost colorless organic phase and a bluish grey aqueous phase. Deionized water (25 mL) was added, the reaction mixture cooled to 0°C and NaOH (50% aqueous solution) was added dropwise to bring the aqueous phase to pH ~9. The aqueous phase was extracted with DCM (3 x 75 mL), adding more water as necessary to dissolve remaining solid phosphate salts. The combined organic layers were dried over Na₂SO₄ and stripped of solvent *in vacuo*, resulting in orange flakes of **MGABA**.

Yield

464 mg orange flakes (94% of theory)

Analysis

TLC: $R_f = 0.14$ (DCM/MeOH/NH₄OH 90:10:1)

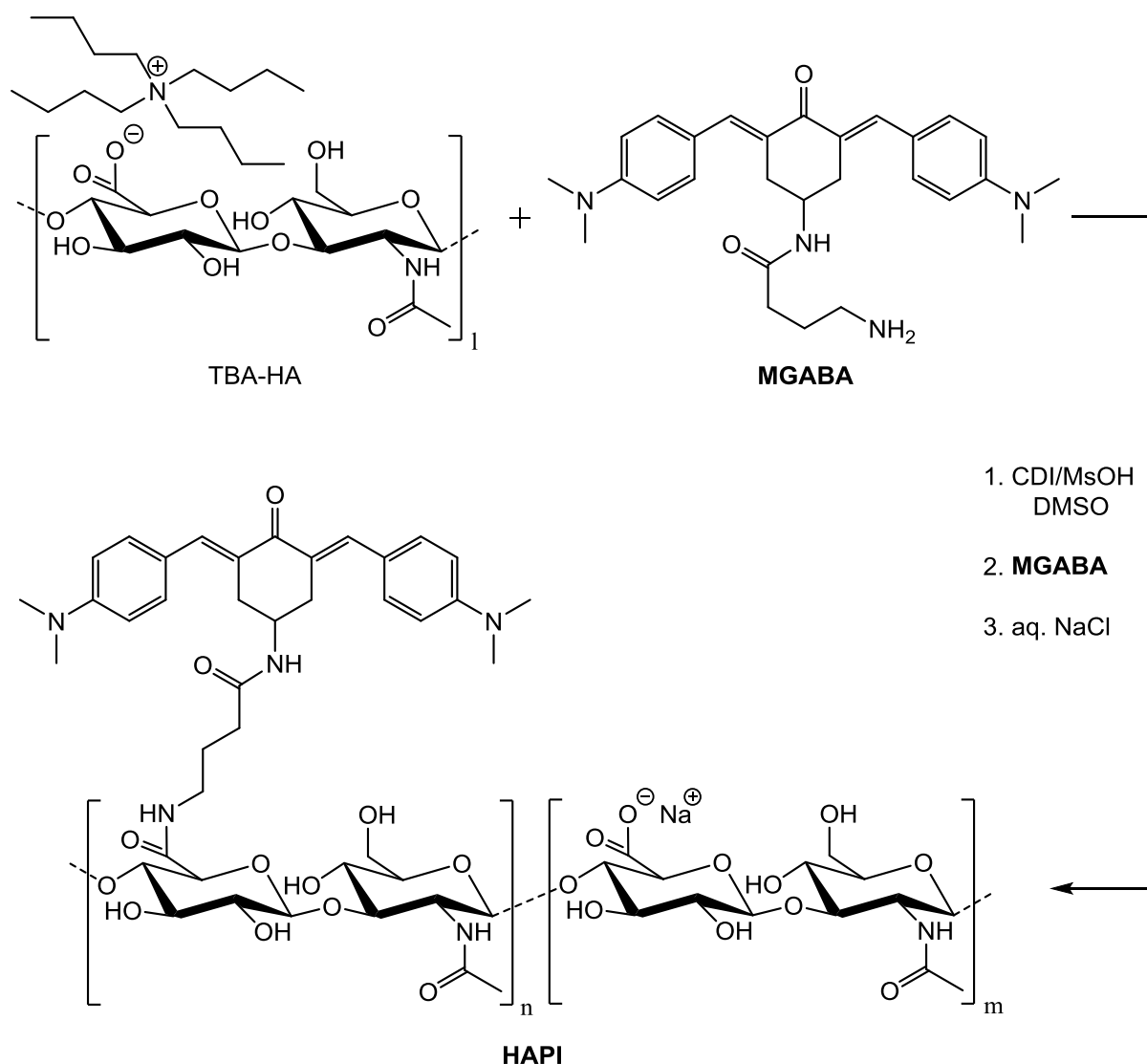
mp: 146 – 148°C

HR-MS m/z: [M+H]⁺ calculated for C₂₈H₃₇N₄O₂ 461.2911;
found 461.2919

¹H NMR (200 MHz, CDCl₃): δ (ppm) = 7.85 (2H, s, -C=CH-), 7.36 (4H, d, $J = 8.8$ Hz, N-ar-H^{3,5}), 6.74 (1H, d, $J = 7.8$ Hz, -NH-CO-CH₂-), 6.63 (4H, d, $J = 8.8$ Hz, N-ar-H^{2,6}), 4.27 - 4.48 (1H, m, $J = 4.7$ and 4.7 and 7.8 Hz, -CH₂-CH-CH₂-), 3.06 (4H, d, $J = 4.7$ Hz, -CH₂-CH-CH₂-), 2.97 (12H, s, (CH₃)₂N-), 2.57 (2H, t, $J = 7.0$ Hz, -CH₂-NH₂), 2.14 (2H, t, $J = 7.2$ Hz, -NH-CO-CH₂-), 1.62 (2H, *quin*, $J = 7.0$ Hz, -CH₂-CH₂-CH₂-), 1.31 (2H, s, -NH₂)

¹³C NMR (50 MHz, CDCl₃): δ (ppm) = 188.3 (1C, O=C(-C=CH-)₂), 172.5 (1C, -NH-CO-CH₂-), 150.6 (2C, N-ar-C¹), 140.1 (2C, -C=CH-), 132.7 (4C, -N-ar-C^{3,5}), 127.9 (2C, -C=CH-), 123.4 (2C, N-ar-C⁴), 111.6 (4C, -N-ar-C^{2,6}), 43.8 (1C, -CH₂-CH-CH₂-), 41.4 (1C, -CH₂-NH₂), 40.0 (4C, (CH₃)₂N-), 34.2 + 33.7 (3C, -CH₂-CH-CH₂-, -NH-CO-CH₂-), 29.0 (1C, -CH₂-CH₂-CH₂-)

1.2.4. Hyaluronan-based photoinitiator (HAPI)¹⁵⁰



For low molecular weight HAPI, sodium hyaluronate (1.5 g, 1.6 MDa) was degraded by dissolving in deionized water (150 mL), adjusting to pH 1.00 with conc. HCl (~11 M) and mechanical stirring at 60°C for 24 h. After cooling down to room temperature and adjusting to pH 7.00-7.05 with TBA-OH (1M in MeOH), the reaction mixture was stirred for 1 h and the white precipitate that formed was removed by centrifugation. The resulting clear solution was dialyzed against deionized water to remove small oligomers and excess TBA-Cl. Freeze-drying afforded 1.22 g tetrabutyl ammonium hyaluronate (TBA-HA) as a white fibrous solid.

The following steps were performed in an orange light room. An aliquot of TBA-HA (125 mg, 200 μmol HA repetition units, 1 eq.) was dissolved in dry DMSO (12 mL) under argon atmosphere. After addition of CDI (9.8 mg, 60 μmol , 0.3 eq.) and MsOH

(1.46 mg, 15 μmol , 0.075 eq.) stirring was continued for 18 h, then **MGABA** (55.6 mg, 120 μmol , 0.6 eq.) was added and the clear orange solution stirred for another 72 h. Brine (1.2 mL) was added dropwise to the reaction mixture and after 2 h stirring at room temperature, acetone (35 mL) was added. The resulting orange precipitate was separated by centrifugation and washed with acetone (3x 45 mL) by stirring vigorously and subsequent centrifugation. The precipitate was then dissolved in deionized water (25 mL), the resulting red solution dialyzed against deionized water and freeze-dried to obtain **HAPI** as a bright orange fibrous solid.

Yields

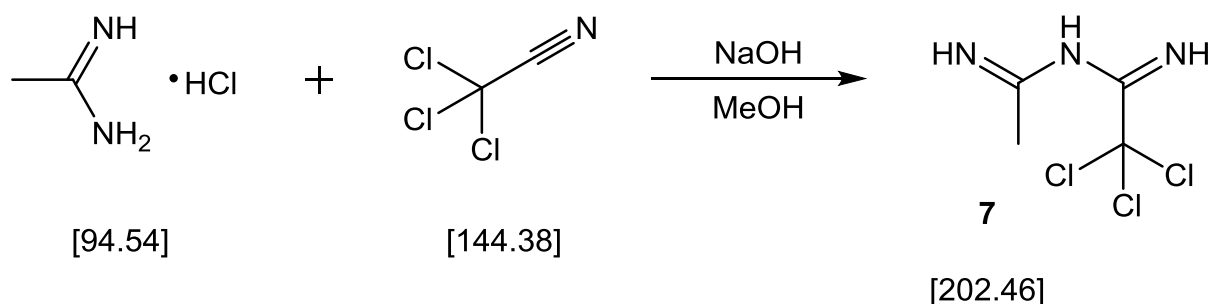
degradation step: 1.22g white fibrous solid (81% of theory),

modification step: 83 mg orange fibrous solid (95% of theory)

Analysis

M_n (GPC of TBA-HA, 24h degradation time): 50 kDa

^1H NMR (200 MHz, D_2O) of HAPI: $\delta(\text{ppm}) = 7.57$ (0.19H [varies with DS], *bs*), 7.01 - 7.45 (0.40H [varies with DS], *m*), 6.28 - 6.86 (0.39H [varies with DS], *m*), 4.19 - 4.64 (2H, *m*), 3.17 - 4.02 (10H, *m*), 2.52 - 3.03 (1.70 H [varies with DS], *m*), 1.92 (3H, *bs*)

2.1.4.1. 2,2,2-Trichloro-*N*-(1-iminoethyl)ethanimidamide (**7**)

Reagents	MW [g/mol]	[g]	[mL]	[mmol]	[eq.]
acetamidine hydrochloride	94.54	5.50		58.2	1.0
trichloroacetonitrile	144.39	8.40		58.2	1.0
NaOH	40.00	2.33		58.2	1.0
MeOH			25		

Procedure

A solution of NaOH (2.33 g, 58.2 mmol, 1.0 eq.) in MeOH (25 mL) was added to acetamidine hydrochloride (5.50 g, 58.2 mmol, 1.0 eq.), forming a white suspension. Freshly distilled trichloroacetonitrile (8.40 g, 58.2 mmol, 1.0 eq., bp 80 - 84°C at 1 atm) was added dropwise to the suspension under magnetic stirring and external cooling with a water bath (~15°C), leading to a pinkish tinge. Stirring was continued at room temperature for 18 h and the reaction mixture stripped of the solvent *in vacuo*, leaving behind a pinkish-brown solid residue. Soxhlet-extraction of this residue was performed with PE (200 mL) for 18 h. The resulting clear solution was left to crystallize at 4°C, and the product collected *via* suction filtration and drying *in vacuo*, yielding amidine **7** as shiny platelets.

Yield

6.15 g of colorless platelets **7** (52% of theory)

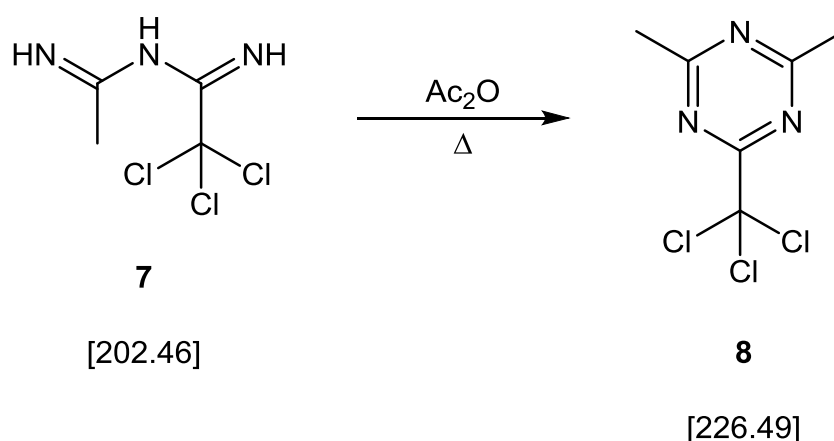
Analysis

mp: 94 - 95°C (lit. 92 - 94°C)¹⁸³

^1H NMR (200 MHz, CDCl_3) δ (ppm) = 10.49 + 9.27 + 6.29 (3H, *br. s.*, $\text{HN}=\text{CCH}_3\text{-NH}$ -; $\text{HN}=\text{CCH}_3\text{-NH}$ -; $\text{HN}=\text{CCCl}_3\text{-NH}$ -), 2.20 (3H, *s*, $\text{HN}=\text{CCH}_3\text{-NH}$ -)

^{13}C -NMR (50 MHz, CDCl_3) δ (ppm) =

2.1.4.2. 2,4-Dimethyl-6-(trichloromethyl)-1,3,5-triazine (8)



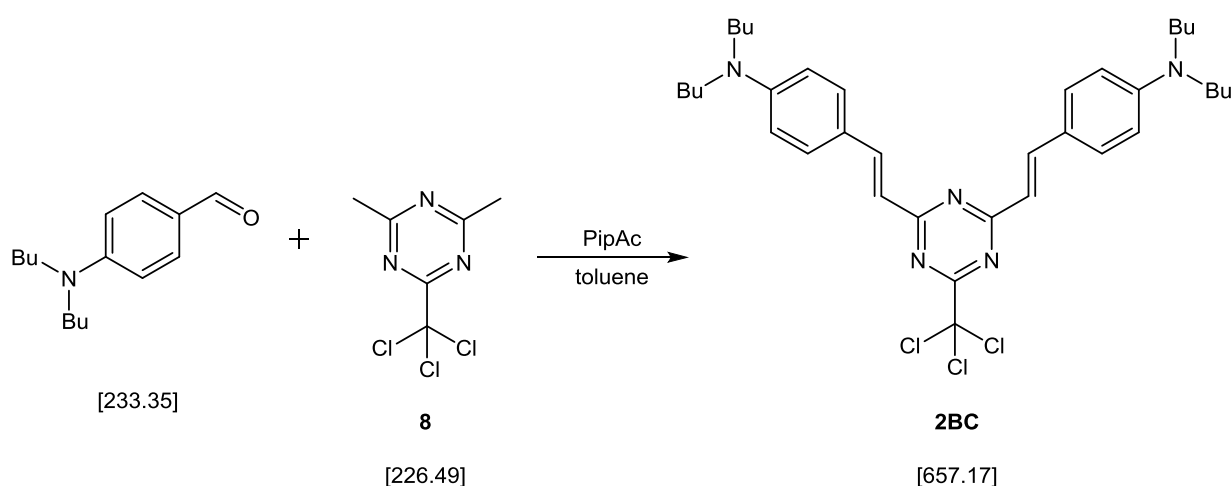
Reagents	MW [g/mol]	[g]	[mL]	[mmol]	[eq.]
2,2,2-trichloro- <i>N</i> -(1-iminoethyl)ethanimidamide (7)	202.46	4.90		24.2	1.0
Ac_2O			25		

Procedure

A solution of amidine **7** (4.90 g, 24.2 mmol, 1.0 eq.) in Ac_2O (25 mL) was held at reflux for 1.5 h, leading to an intensification of color from slightly yellow to brown. The reaction mixture was poured onto ice/water (200 mL) and after 20 min of magnetic stirring the aqueous phase is sucked off through a glass frit. The resulting brown crystals were purified by Kugelrohr distillation (40°C at 3 mbar) to yield triazine **8** as a colorless crystalline mass.

Yield

3.21 g of colorless crystals **8** (59% of theory)

Analysismp: 74 - 75°C (lit. 69 - 71°C)¹⁸³¹H NMR (200 MHz, CDCl₃) δ (ppm) = 2.76 (6H, s, CH₃-trz)¹³C-NMR (50 MHz, CDCl₃) δ (ppm) = 178.3 (2C, trz-C^{2,4}), 173.0 (1C, trz-C⁶), 95.5 (1C, trz-CCl₃), 25.7 (2C, trz-CH₃)**2.1.4.3. 4,4'-[(6-Trichloromethyl-1,3,5-triazine-2,4-diyl)di-(1E)-2,1-ethenediyl]bis[N,N-dibutylbenzenamine] (2BC)**

Reagents	MW [g/mol]	[mg]	[mL]	[mmol]	[eq.]
2,4-dimethyl-6-(trichloromethyl)- 1,3,5-triazine (8)	226.49	500		2.21	1.0
4-(dibutylamino)benzaldehyde	233.35	902		3.86	1.75
PipAc	145.20	96		0.66	0.3
toluene			5		

Procedure

All steps of this protocol were performed in a red light lab (LEDs with λ_{\max} = 620 nm as the only light source). A 10 mL round bottom flask fitted with a Dean-Stark-trap (prefilled with toluene) and reflux condenser was charged with triazine **8** (500 mg, 2.21 mmol, 1.0 eq.), 4-(dibutylamino)benzaldehyde (902 mg, 3.86 mmol, 1.75 eq.),

PipAc (96 mg, 0.66 mmol, 0.3 eq.) and toluene (5 mL). The solution was kept at reflux for 80 h under argon atmosphere. After cooling to room temperature, the resulting dark brown solution was taken up in DCM (150 mL), washed with saturated NH_4Cl -solution (3 x 50 mL) and deionized water (100 mL). The organic phase was dried with Na_2SO_4 and the solvent removed *in vacuo* to yield a brownish residue. The mixture was separated *via* column chromatography (toluene with 0-15% Et_2O , 113 g silica gel 60, detection $\lambda = 295$ nm). **2BC** eluted as first major peak from the column using toluene without Et_2O . The pure product was obtained by removal of the solvents and drying *in vacuo* at 40°C with subsequent crystallization of the resultant glassy solid from n-pentane.

Yield

383 mg of reddish-brown fine crystals **2BC** (26% of theory)

Analysis

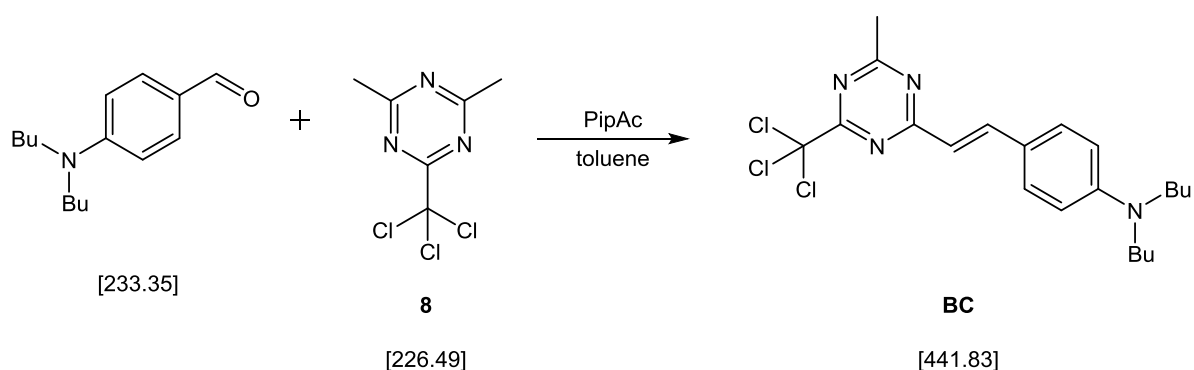
TLC: $R_f = 0.70$ (toluene)

mp: $102 - 105^\circ\text{C}$

^1H NMR (200 MHz, CDCl_3) δ (ppm) = 8.32 (2H, *d*, $J = 15.7$ Hz, $-\text{CH}=\text{CH}-\text{ar}$), 7.60 (4H, *d*, $J = 8.8$ Hz, $\text{Bu}_2\text{-N-ar-H}^{3,5}$), 7.01 (2H, *d*, $J = 15.7$ Hz, $-\text{CH}=\text{CH}-\text{ar}$), 6.68 (4H, *d*, $J = 8.6$ Hz, $\text{Bu}_2\text{-N-ar-H}^{2,6}$), 3.37 (8H, *t*, $J = 7.4$ Hz, $-\text{N}(\text{CH}_2-\text{CH}_2-\text{CH}_2-\text{CH}_3)_2$), 1.54 - 1.75 (8H, *m*, $-\text{N}(\text{CH}_2-\text{CH}_2-\text{CH}_2-\text{CH}_3)_2$), 1.25 - 1.54 (8H, *m*, $-\text{N}(\text{CH}_2-\text{CH}_2-\text{CH}_2-\text{CH}_3)_2$), 1.03 (12H, *t*, $J = 7.2$ Hz, $-\text{N}(\text{CH}_2-\text{CH}_2-\text{CH}_2-\text{CH}_3)_2$)

^{13}C -NMR (50 MHz, CDCl_3) δ (ppm) = 173.0 (2C, $\text{trz-C}^{2,4}$), 172.3 (1C, trz-C^6), 149.8 (2C, $\text{Bu}_2\text{-N-ar-C}^1$), 144.2 (2C, $-\text{CH}=\text{CH}-\text{ar}$), 130.5 (4C, $\text{Bu}_2\text{-N-ar-C}^{3,5}$), 122.1 (2C, $\text{Bu}_2\text{-N-ar-C}^4$), 119.1 (2C, $-\text{CH}=\text{CH}-\text{ar}$), 111.4 (4C, $\text{Bu}_2\text{-N-ar-C}^{2,6}$), 93.4 (1C, trz-CCl_3), 50.7 (4C, $-\text{N}(\text{CH}_2-\text{CH}_2-\text{CH}_2-\text{CH}_3)_2$), 29.4 (4C, $-\text{N}(\text{CH}_2-\text{CH}_2-\text{CH}_2-\text{CH}_3)_2$), 20.2 (2C, $-\text{N}(\text{CH}_2-\text{CH}_2-\text{CH}_2-\text{CH}_3)_2$), 13.9 (2C, $-\text{N}(\text{CH}_2-\text{CH}_2-\text{CH}_2-\text{CH}_3)_2$)

4-[(1*E*)-2-(4-Methyl-6-trichloromethyl-1,3,5-triazin-2-yl)ethenyl]-*N,N*-dibutylbenzenamine (BC)



Reagents	MW [g/mol]	[mg]	[mL]	[mmol]	[eq.]
2,4-dimethyl-6-(trichloromethyl)-1,3,5-triazine (8)	226.49	500		2.21	1.0
4-(dibutylamino)benzaldehyde	233.35	902		3.86	1.75
PipAcO	145.20	96		0.66	0.3
toluene			5		

Procedure

All steps of this protocol were performed in a red light lab (LEDs with $\lambda_{\max} = 620$ nm as the only light source). **BC** was obtained from the reaction mixture from the synthesis of **2BC** by separation *via* column chromatography (toluene with 0-15% Et₂O, 113 g silica gel 60, detection $\lambda = 295$ nm). **BC** was eluted from the column after **2BC** by increasing solvent polarity using toluene with 15% added Et₂O. The pure product was obtained by removal of the solvents and drying *in vacuo* at 40°C with subsequent crystallization of the resultant glassy solid from n-pentane.

Yield

371 mg of ochre fine crystals **BC** (38% of theory)

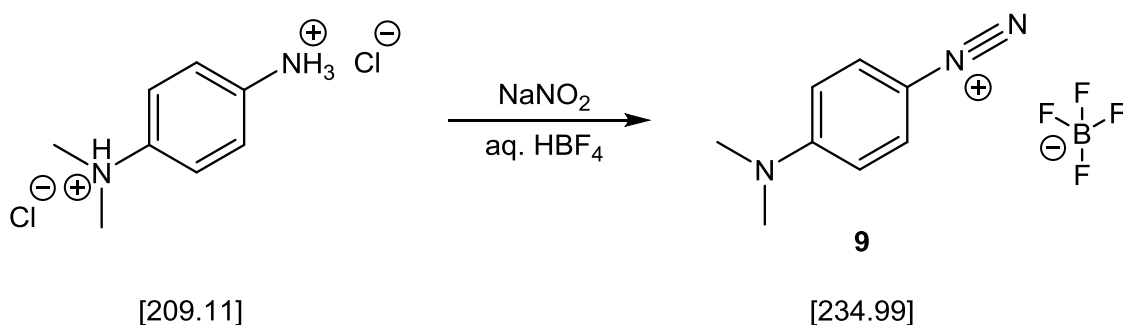
Analysis

TLC: $R_f = 0.36$ (toluene), 0.59 (Tol/Et₂O 20:1)
 mp: 73 - 75°C

^1H NMR (200 MHz, CDCl_3) δ (ppm) = 8.30 (1H, *d*, J = 15.7 Hz, $-\text{CH}=\text{CH}-\text{ar}$), 7.55 (2H, *d*, J = 8.8 Hz, $\text{Bu}_2\text{-N-ar-H}^{3,5}$), 6.94 (1H, *d*, J = 15.7 Hz, $-\text{CH}=\text{CH}-\text{ar}$), 6.65 (2H, *d*, J = 9.0 Hz, $\text{Bu}_2\text{-N-ar-H}^{2,6}$), 3.35 (4H, *t*, J = 7.5 Hz, $-\text{N}(\text{CH}_2\text{-CH}_2\text{-CH}_2\text{-CH}_3)_2$), 2.76 (3H, *s*, trz-CH_3), 1.52 - 1.74 (4H, *m*, $-\text{N}(\text{CH}_2\text{-CH}_2\text{-CH}_2\text{-CH}_3)_2$), 1.22 - 1.52 (4H, *m*, $-\text{N}(\text{CH}_2\text{-CH}_2\text{-CH}_2\text{-CH}_3)_2$), 1.00 (6H, *t*, J = 7.2 Hz, $-\text{N}(\text{CH}_2\text{-CH}_2\text{-CH}_2\text{-CH}_3)_2$)

^{13}C -NMR (50 MHz, CDCl_3) δ (ppm) = 177.5 (1C, trz-C^4), 173.2 (1C, trz-C^2), 172.5 (1C, trz-C^6), 150.1 (1C, $\text{Bu}_2\text{-N-ar-C}^1$), 145.4 (1C, $-\text{CH}=\text{CH}-\text{ar}$), 130.7 (2C, $\text{Bu}_2\text{-N-ar-C}^{3,5}$), 121.7 (1C, $\text{Bu}_2\text{-N-ar-C}^4$), 118.0 (1C, $-\text{CH}=\text{CH}-\text{ar}$), 111.3 (2C, $\text{Bu}_2\text{-N-ar-C}^{2,6}$), 94.1 (1C, trz-CCl_3), 50.7 (2C, $-\text{N}(\text{CH}_2\text{-CH}_2\text{-CH}_2\text{-CH}_3)_2$), 29.3 (2C, $-\text{N}(\text{CH}_2\text{-CH}_2\text{-CH}_2\text{-CH}_3)_2$), 25.8 (1C, trz-CH_3), 20.2 (2C, $-\text{N}(\text{CH}_2\text{-CH}_2\text{-CH}_2\text{-CH}_3)_2$), 13.9 (2C, $-\text{N}(\text{CH}_2\text{-CH}_2\text{-CH}_2\text{-CH}_3)_2$)

2.2.2.2.1. 4-(Dimethylamino)benzenediazonium tetrafluoroborate (9)



Reagents	MW [g/mol]	[g]	[mL]	[mmol]	[eq.]
<i>N,N</i> -dimethyl-1,4-phenylene-diammonium dichloride	209.11	3.01		14.3	1.0
NaNO_2	69.00	1.09		15.8	1.1
aq. HBF_4 20%			12		

Procedure

All steps were performed in an orange light room. *N,N*-dimethyl-1,4-phenylenediammonium dichloride (3.01 g, 14.3 mmol, 1.0 eq.) was dissolved in aq. HBF₄ (20%, 12 mL) and cooled to ~ 0°C. A solution of NaNO₂ (1.09 g, 15.8 mmol, 1.1 eq.) in deionized water (2 mL) was added dropwise under magnetic stirring, keeping the temperature between 0 - 5°C, eventually leading to formation of a thick, greenish-yellow precipitate. Stirring was continued for 1 h, then the precipitate was collected *via* suction filtration and washed consecutively with aq. HBF₄ (5%, 6 mL), MeOH (7 mL) and Et₂O (3 x 7 mL). Drying *in vacuo* at room temperature yielded diazonium salt **9** as yellow powder.

Yield

2.72 g of yellow powder **9** (81% of theory)

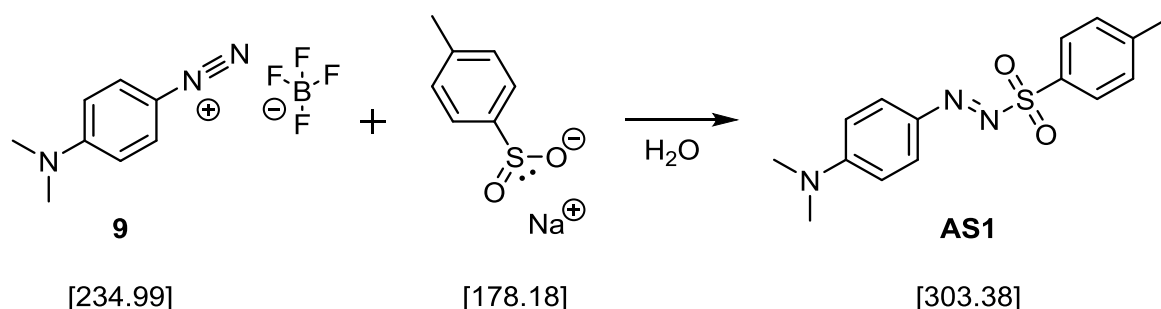
Analysis

mp: decomposition > 155°C

¹H NMR (200 MHz, DMSO-d₆) δ (ppm) = 8.21 (2H, *d*, *J* = 9.6 Hz, N₂⁺-ar-H^{2,6}), 7.06 (2H, *d*, *J* = 9.6 Hz, N₂⁺-ar-H^{3,5}), 3.25 (6H, *s*, (CH₃)₂-N-ar)

¹³C-NMR (50 MHz, DMSO-d₆) δ (ppm) = 156.2 (1C, N₂⁺-ar-C⁴), 134.0 (2C, N₂⁺-ar-C^{2,6}), 113.9 (2C, N₂⁺-ar-C^{3,5}), 88.9 (1C, N₂⁺-ar-C¹), 40.5 (2C, (CH₃)₂-N-ar)

2.2.2.2. (E)-N-[[4-(dimethylamino)phenyl]imino]-4-methylbenzenesulfonamide (AS1)



Reagents	MW [g/mol]	[mg]	[mL]	[mmol]	[eq.]
diazonium salt 9	234.99	750		3.19	1.0
NaTS	178.18	627		3.51	1.1
deionized water			6		

Procedure

All steps were performed in an orange light room. A solution of NaTS (627 mg, 3.51 mmol, 1.1 eq.) in deionized water (4 mL) was added dropwise to a magnetically stirred suspension of diazonium salt **9** (750 mg, 3.19 mmol, 1.0 eq.) in deionized water (2 mL). Stirring was continued for 18 h at room temperature. The dark orange precipitate is collected *via* suction filtration and dried *in vacuo*. Pure **AS1** was obtained by recrystallization from EA and drying *in vacuo* at room temperature.

Yield

710 mg of reddish-purple, shiny needles **AS1** (72% of theory)

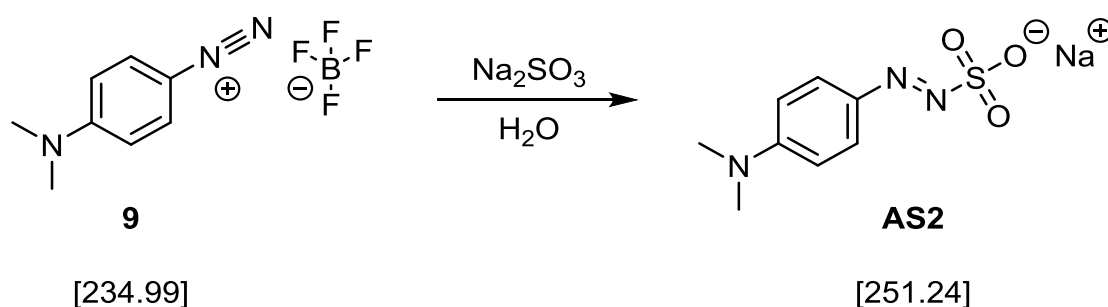
Analysis

mp: decomposition > 140°C

¹H NMR (200 MHz, CDCl₃) δ (ppm) = 7.76 (2H, *d*, *J* = 8.4 Hz, SO₂-ar-H^{2,6}), 7.64 (2H, *d*, *J* = 9.6 Hz, N₂-ar-H^{2,6}), 7.23 (2H, *d*, *J* = 8.2 Hz, SO₂-ar-H^{3,5}), 6.53 (2H, *d*, *J* = 9.6 Hz, N₂-ar-H^{3,5}), 3.02 (6H, *s*, (CH₃)₂-N-ar), 2.33 (3H, *s*, SO₂-ar-CH₃)

^{13}C -NMR (50 MHz, CDCl_3) δ (ppm) = 155.3 (1C, $\text{N}_2\text{-ar-C}^4$), 144.6 (1C, $\text{SO}_2\text{-ar-C}^1$), 139.8 (1C, $\text{SO}_2\text{-ar-C}^4$), 132.4 (1C, $\text{N}_2\text{-ar-C}^1$), 129.5 + 129.5 + 128.1 (6C, $\text{SO}_2\text{-ar-C}^{2,6}$, $\text{SO}_2\text{-ar-C}^{3,5}$, $\text{N}_2\text{-ar-C}^{2,6}$), 111.3 (2C, $\text{N}_2\text{-ar-C}^{3,5}$), 40.2 (2C, $(\text{CH}_3)_2\text{-N-ar}$), 21.6 (1C, $\text{SO}_2\text{-ar-CH}_3$)

2.2.2.2.3. Sodium (*E*)-[4-(dimethylamino)phenyl]diazenesulfonate (AS2)



Reagents	MW [g/mol]	[mg]	[mL]	[mmol]	[eq.]
diazonium salt 9	234.99	750		3.19	1.0
Na_2SO_3	126.04	442		3.51	1.1
deionized water			6		

Procedure

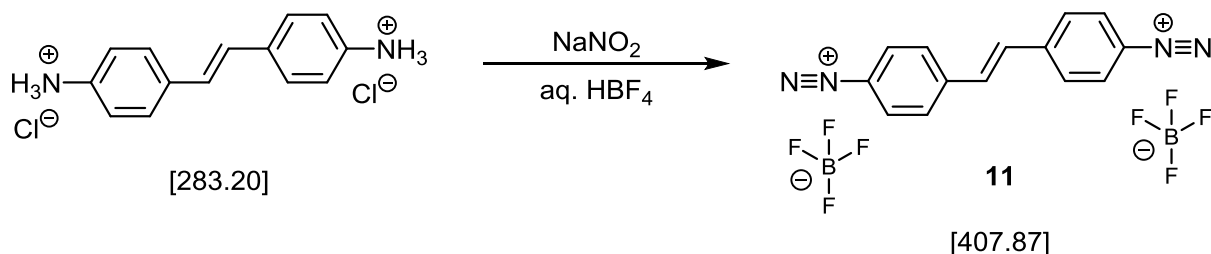
All steps were performed in an orange light room. A solution of Na_2SO_3 (442 mg, 3.51 mmol, 1.1 eq.) in deionized water (4 mL) was added dropwise to a magnetically stirred suspension of diazonium salt **9** (750 mg, 3.19 mmol, 1.0 eq.) in deionized water (2 mL). The suspension was heated to 70°C and stirring continued for 1 h at that temperature. Upon cooling, the product crystallizes and is collected *via* suction filtration. The crude product was recrystallized by dissolving in the minimal amount deionized water at 70°C , then cooling to 4°C . Pure **AS2** was collected *via* suction filtration and dried *in vacuo* at room temperature.

Yield

674 mg of orange needles **AS2** (84% of theory)

Analysis

mp: decomposition > 260°C

¹H NMR (200 MHz, D₂O) δ (ppm) = 7.58 (2H, *d*, *J* = 8.8 Hz, N₂-ar-H^{2,6}), 6.53 (2H, *d*, *J* = 9.0 Hz, N₂-ar- H^{3,5}), 2.91 (6H, *s*, (CH₃)₂-N-ar)¹³C-NMR (50 MHz, D₂O) δ (ppm) = 155.0 (1C, N₂-ar-C⁴), 138.7 (1C, N₂-ar-C¹), 126.8 (2C, N₂-ar-C^{2,6}), 111.7 (2C, N₂-ar-C^{3,5}), 39.5 (2C, (CH₃)₂-N-ar)**2.2.3.1.2.1. (E)-4,4'-(1,2-ethenediyl)bis[benzenediazonium] bis[tetrafluoroborate] (11)**

Reagents	MW [g/mol]	[mg]	[mL]	[mmol]	[eq.]
4,4'-diaminostilbene dihydrochloride	283.20	750		2.65	1.0
NaNO ₂	69.00	384		5.57	2.1
aq. HBF ₄ 20%			35		
deionized water			2		

Procedure

All steps were performed in an orange light room. 4,4'-Diaminostilbene dihydrochloride (750 mg, 2.65 mmol, 1.0 eq.) was dissolved in aq. HBF₄ (20%, 35 mL), resulting in a clear brown solution, which was cooled to ~ 0°C. A solution of NaNO₂ (384 mg, 5.57 mmol, 2.1 eq.) in deionized water (2 mL) was added dropwise under magnetic stirring, keeping the temperature between 0 - 5°C, eventually leading to formation of a brownish-orange precipitate as well as floating, dark particles. Stirring was continued for 3 h, then the precipitate was collected *via* centrifugation (3000 rpm, 5 min) and the floating particles discarded. The precipitate was washed

consecutively with deionized water (2 x 20 mL), MeOH (10 mL) and Et₂O (3 x 10 mL) always collecting the solids *via* centrifugation (3000 rpm, 10 min) and discarding the liquid phases. Drying *in vacuo* at room temperature yielded diazonium salt **11** as brownish-orange powder.

Yield

756 mg of brownish-orange powder **9** (70% of theory)

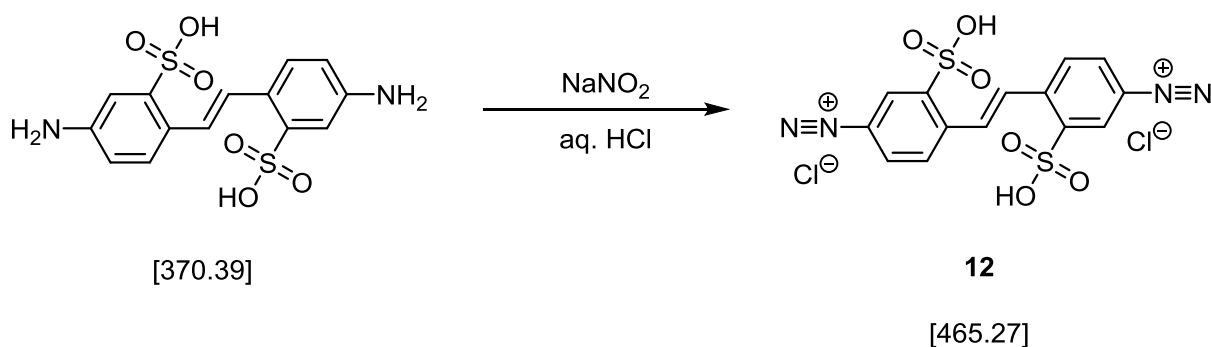
Analysis

mp: decomposition > 120°C

¹H NMR (200 MHz, DMSO-d₆) δ (ppm) = 8.92 - 8.59 (4H, *m*, N₂⁺-ar-H^{3,5}), 8.39 - 8.08 (4H, *m*, N₂⁺-ar-H^{2,6}), 8.02 (2H, *s*, -CH=CH-)

¹³C-NMR (50 MHz, DMSO-d₆) δ (ppm) = 147.3 (2C, N₂⁺-ar-C⁴), 134.2 (2C, -CH=CH-), 133.4 + 129.5 (8C, N₂⁺-ar-C^{2,6}, N₂⁺-ar-C^{3,5}), 114.1 (2C, N₂⁺-ar-C¹)

2.2.3.1.3.1. (*E*)-4,4'-(1,2-ethenediyl)bis[3-sulfobenzediazonium] dichloride (**12**)



Reagents	MW [g/mol]	[g]	[mL]	[mmol]	[eq.]
4,4'-diaminostilbene-2,2'-disulfonic acid	370.39	10.0		27.0	1.00
NaNO ₂	68.99	4.23		61.3	2.27
HCl 37% aq.			6.0		
deionized water			63		

Procedure

All steps were performed in an orange light room. Hydrochloric acid (6.0 mL, 37% aq.) is added dropwise to a magnetically stirred suspension of 4,4'-diaminostilbene-2,2'-disulfonic acid (10.0 g, 27.0 mmol, 1.0 eq.) in deionized water (54 mL). The stirred suspension is then cooled in an ice/water bath and a solution of NaNO₂ (4.23 g, 61.3 mmol, 2.27 eq.) in deionized water (9 mL) is slowly added so that the temperature always stays below 5°C. After addition of the NaNO₂ is completed, the suspension is stirred at room temperature for 30 min and then at 35°C for another 2.5 h. The suspension is then cooled to 4°C, the solids collected by centrifugation (3000 rpm, 10 min) and washed subsequently with deionized water (2 x 40 mL), MeOH (2 x 40 mL) and Et₂O (2 x 40 mL), always collecting the solids *via* centrifugation (3000 rpm, 10 min) and discarding the liquid phases. The resulting yellow paste is then carefully dried *in vacuo* at room temperature to obtain diazonium salt **12**.

Yield

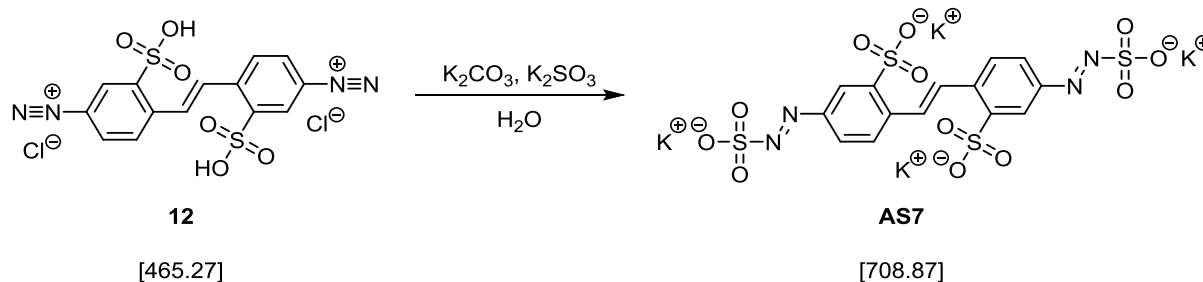
10.4 g of bright yellow powder **12** (83% of theory)

Analysis

mp: decomposition >90°C

¹H NMR (200 MHz, DMSO-d₆) δ (ppm) = 9.10 (2H, *d*, *J* = 2.2 Hz, N₂⁺-ar-H²), 8.70 (2H, *dd*, *J* = 2.2 and 8.7 Hz, N₂⁺-ar-H⁶), 8.52 (2H, *s*, -CH=CH-), 8.14 (2H, *d*, *J* = 8.7 Hz, N₂⁺-ar-H⁵)

2.2.3.1.3.2. Tetrapotassium (1*E*,1'*E*)-4,4'-[(*E*)-1,2-ethenediyl]bis[2-(3-sulphophenyl)diazenesulfonate] (AS7)



Reagents	MW [g/mol]	[g]	[mL]	[mmol]	[eq.]
diazonium salt 12	465.27	5.00		10.7	1.0
K_2CO_3	138.21	1.48		10.7	1.0
K_2SO_3 (90% purity)	158.26	3.78		21.5	2.0
deionized water			35		

Procedure

All steps were performed in an orange light room. Powdered K_2CO_3 (1.48 g, 10.7 mmol, 1.0 eq.) and K_2SO_3 (90% purity, 3.78 g, 21.5 mmol, 2.0 eq.) are mixed by shaking and the mixture of solids is added portionwise to a magnetically stirred suspension of diazonium salt **12** (5.0 g, 10.7 mmol, 1.0 eq.) in deionized water (35 mL). During the addition of solids the suspension first turns milky-orange and shortly before addition is completed changes to a very dark but clear solution. This solution is first stirred for 18 h at room temperature and then left over night to crystallize at 4°C. The precipitate is collected via centrifugation, recrystallized by dissolving in the minimal amount deionized water at 70°C then cooling to 4°C, and dried in vacuo over P_2O_5 to obtain a finely crystalline orange powder.

Yield

3.77 g of orange powder (50% of theory)

Analysis

mp: decomposition >300°C

^1H NMR (600 MHz, D_2O) δ (ppm) = 8.38 (2H, *d*, $J = 2.2$ Hz, $\text{N}_2\text{-ar-H}^2$), 8.12 (2H, *s*, -CH=CH-), 8.11 (2H, *d*, $J = 8.4$ Hz, $\text{N}_2\text{-ar-H}^5$), 8.06 (2H, *dd*, $J = 2.2$ and 8.4 Hz, $\text{N}_2\text{-ar-H}^6$)

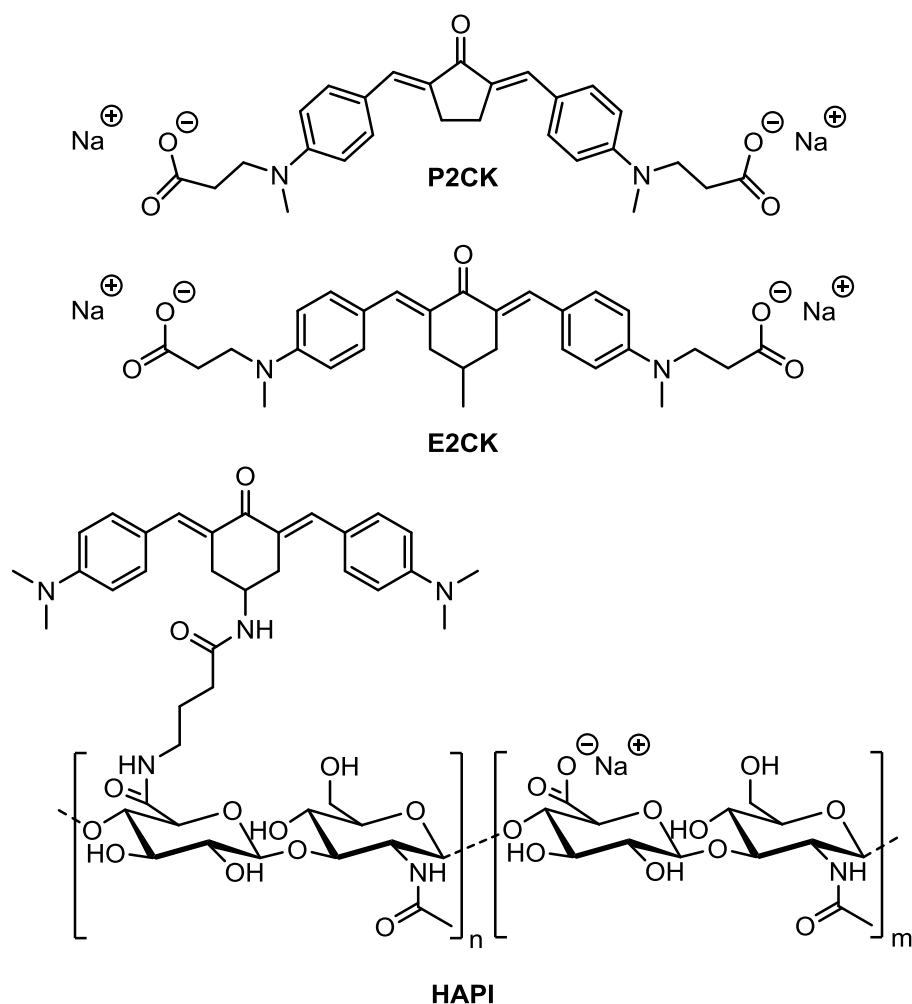
^{13}C NMR (100 MHz, D_2O) δ (ppm) = 148.8 (2C, $\text{N}_2\text{-ar-C}^3$), 142.0 (2C, $\text{N}_2\text{-ar-C}^4$), 139.9 (2C, $\text{N}_2\text{-ar-C}^1$), 130.3 (2C, -CH=CH-), 129.4 (2C, $\text{N}_2\text{-ar-C}^5$), 126.3 (2C, $\text{N}_2\text{-ar-C}^6$), 123.3 (2C, $\text{N}_2\text{-ar-C}^2$)

Elemental analysis: calculated for $\text{C}_{14}\text{H}_8\text{K}_4\text{N}_4\text{O}_{12}\text{S}_4$: C 23.72, H 1.14, K 22.06, N 7.90, O 27.08, S 18.09

found: C 23.35, H 1.37, K 22.40, N 7.01, O 28.18, S 17.18.

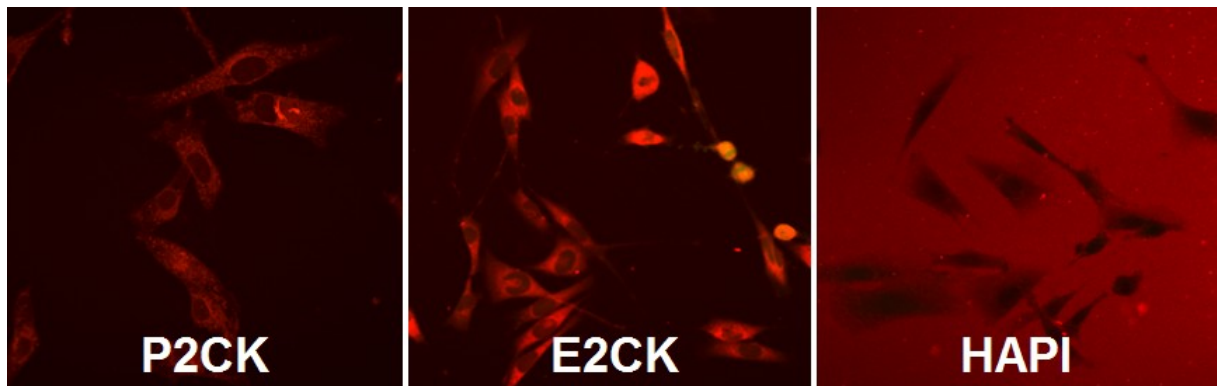
Conclusion

Two-photon absorption (2PA) enables the selective stimulation of chemical reactions with high spatial and temporal control in 3D. Within the scope of this thesis, novel initiators for two-photon initiated radical photopolymerization (2PP) were developed with the aim of enhancing the biocompatibility for tissue engineering applications. A novel macromolecular 2PI **HAPI** was designed based on the recently published, highly efficient dibenzylidene ketone (DBK) two-photon initiators (2PIs) **P2CK** and **E2CK**, which are water-soluble, but display problematic cyto- and phototoxicity in direct cell encapsulation applications.

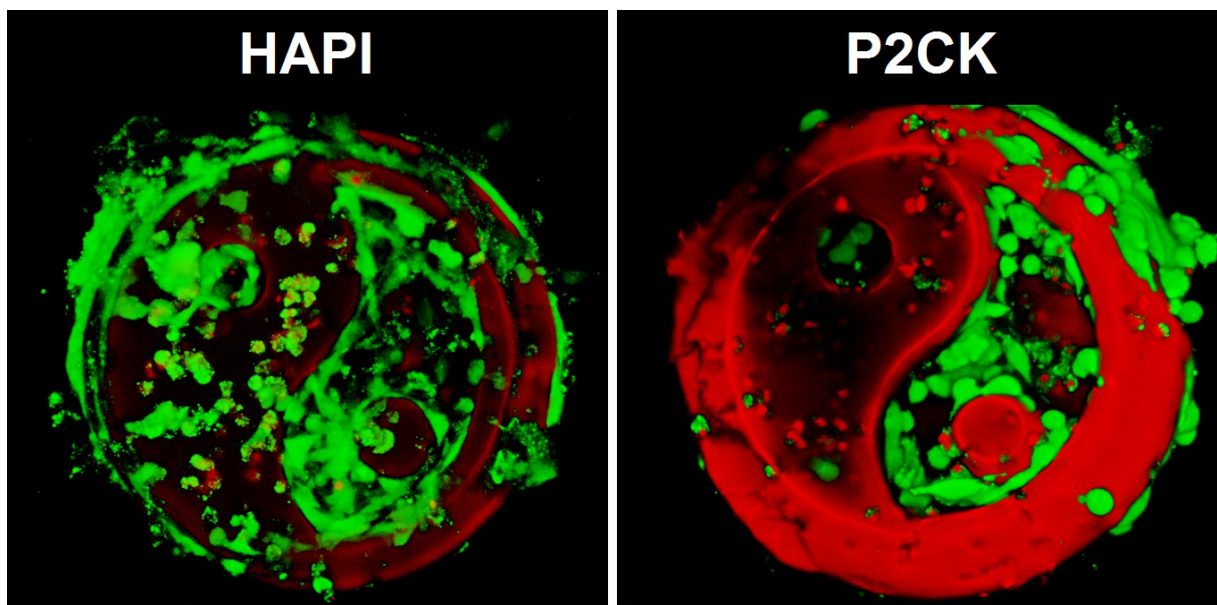


The strategy behind covalently linking a DBK 2PI to hyaluronan, creating **HAPI**, was to hinder the transmembrane migration of the 2PI, thus preventing it from freely entering cells and generating toxic radicals and reactive oxygen species (ROS) upon 2PA directly inside the cells.

The transmembrane migration hindrance was demonstrated by incubating murine pre-osteoblast cells (MC3T3) with solutions of macromolecular **HAPI** and the small molecule references **P2CK** and **E2CK**. Visualization of the red 2PI autofluorescence via laser scanning microscopy (LSM) showed that **P2CK** and **E2CK** accumulate inside cells while **HAPI** does not readily enter them.



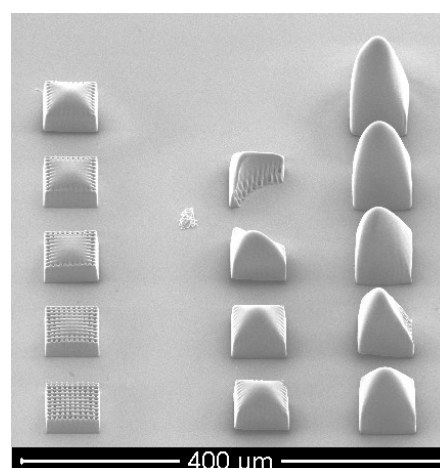
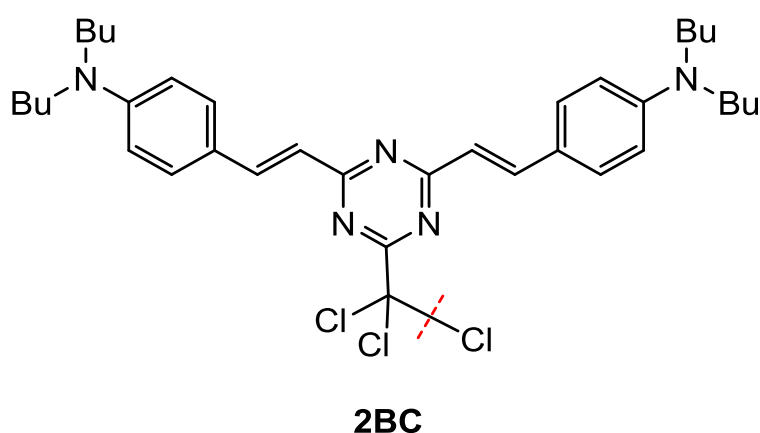
As a result, **HAPI** exhibits notably improved cytocompatibility in darkness and the phototoxicity during 2PP live cell encapsulation is also reduced compared to the established reference 2PI **P2CK**. MC3T3 directly encapsulated in methacrylated gelatin (gelMOD) hydrogel structures show less extensive damage after 2PP-printing, as indicated by their green coloration from "live"-stain calcein and a lesser uptake of the red "dead"-stain propidium iodide that can only pass through cell membranes of compromised integrity.



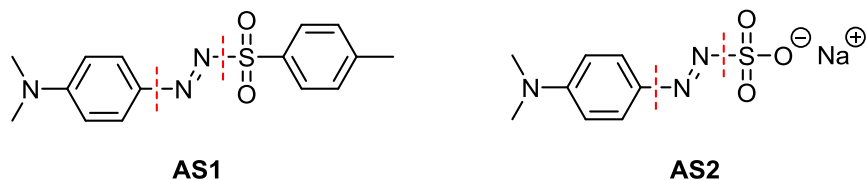
However, since some propidium iodide could enter the cells, there was still evidence of cellular damage during the 2PP printing process, that could be caused by reactive species damaging the outer cell membrane. Furthermore, when combined with gelMOD **HAPI** is prone to processability-impairing phase separation that can only be ameliorated with high concentrations of solvation stabilizer methyl- β -cyclodextrin.

Most of the biocompatible commercial one-photon initiators suitable for UV-cell encapsulation are based on photocleavable compounds, as opposed to DBK 2PIs for which a bimolecular electron transfer mechanism is assumed. This slow bimolecular radical generation process is prone to unwanted and potentially phototoxic side reactions such as a photosensitized formation of ROS. Thus, the next strategy was to develop cleavable 2PIs. Preliminary studies were performed on organosoluble compounds, due to generally simpler purification procedures, and water-soluble derivatives were developed when pre-studies were promising.

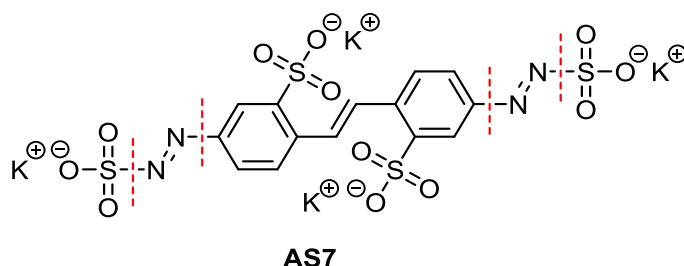
The system **2BC** was based on introducing a trichloromethyl-group to previously tested aminostyryl-triazine 2PIs, which enables efficient 2PA induced photocleavage of C-Cl-bonds (dotted red line). However, the compounds are extremely sensitive to visible light, and 2PP-printing tends to lead to significant over-polymerization so that defined structures can only be obtained within very narrow fabrication parameters, making their use impractical.



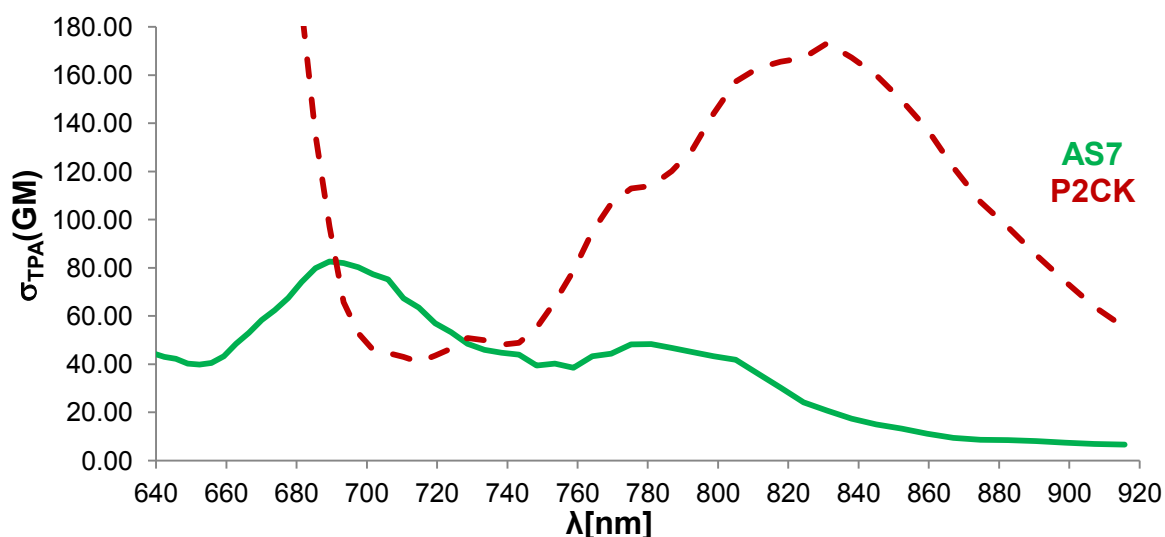
Another class of cleavable initiators was based on aryl diazosulfones (organo-soluble) and diazosulfonates (water-soluble), that dissociate into nitrogen gas as well as aryl- and sulfonyl-based radical. Two literature known compounds, the diazosulfone **AS1** and diazosulfonate **AS2** were tested regarding their performances 2PIs and yielded promising results in preliminary tests.



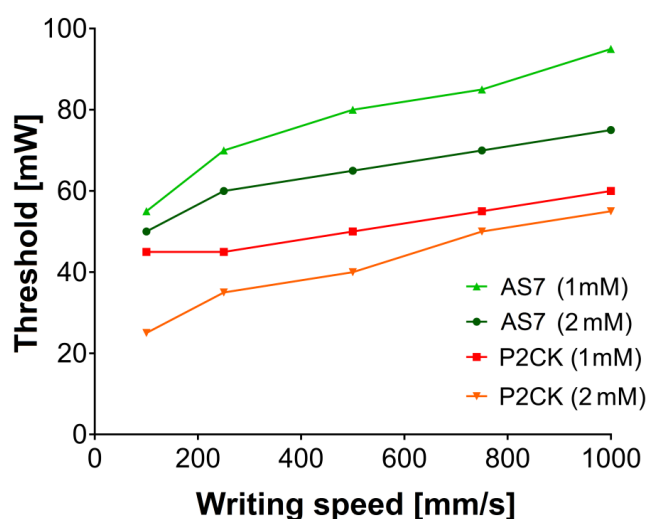
While **AS1** and its derivatives with an extended π -system (to increase two-photon cross section σ_{2PA}) suffer from solubility issues and limited thermal stability, several attempts to vary counter-ions, π -system length, and electron donor/acceptor structure of **AS2** resulted in **AS7**, which exhibits good thermal stability, excellent water-solubility and poses several other advantages over **P2CK** and **HAPI**, such as very simple preparation from inexpensive commercial starting materials.



P2CK	HAPI	AS7
<ul style="list-style-type: none"> • 3 step synthesis, medium cost 	<ul style="list-style-type: none"> • 5 step synthesis, high cost 	<ul style="list-style-type: none"> • 2 step synthesis, low cost
<ul style="list-style-type: none"> • significant cytotoxicity 	<ul style="list-style-type: none"> • low cytotoxicity 	<ul style="list-style-type: none"> • excellent biocompatibility
<ul style="list-style-type: none"> • solubility issues, tends to precipitate in presence of cells 	<ul style="list-style-type: none"> • precipitates with macromers, requires cyclodextrin for structuring 	<ul style="list-style-type: none"> • excellent solubility (purification difficult)

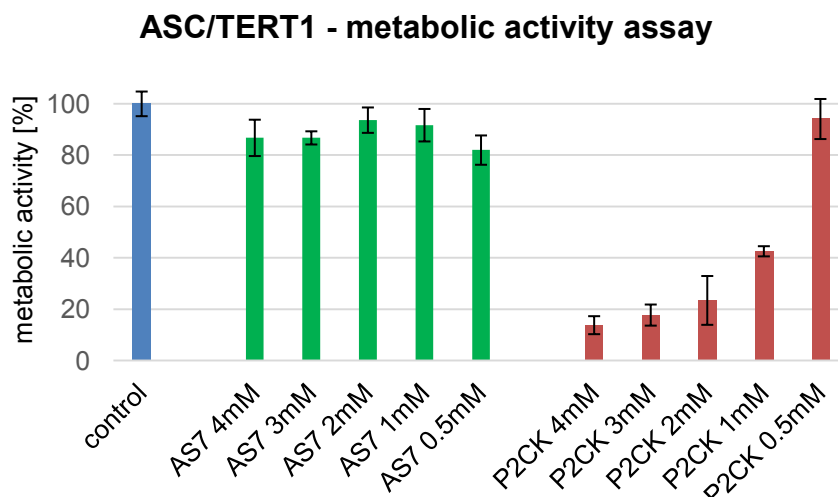


Due to its lack of electron donor groups and somewhat shorter π -system, the σ_{2PA} of **AS7** (43 GM) at 800 nm is lower than that of the DBK reference **P2CK** (145 GM). However, by using **AS7** at a concentration of 2 mM, it can achieve similar polymerization thresholds and 2PP performance as **P2CK**, which is used at 1 mM in cell encapsulation.

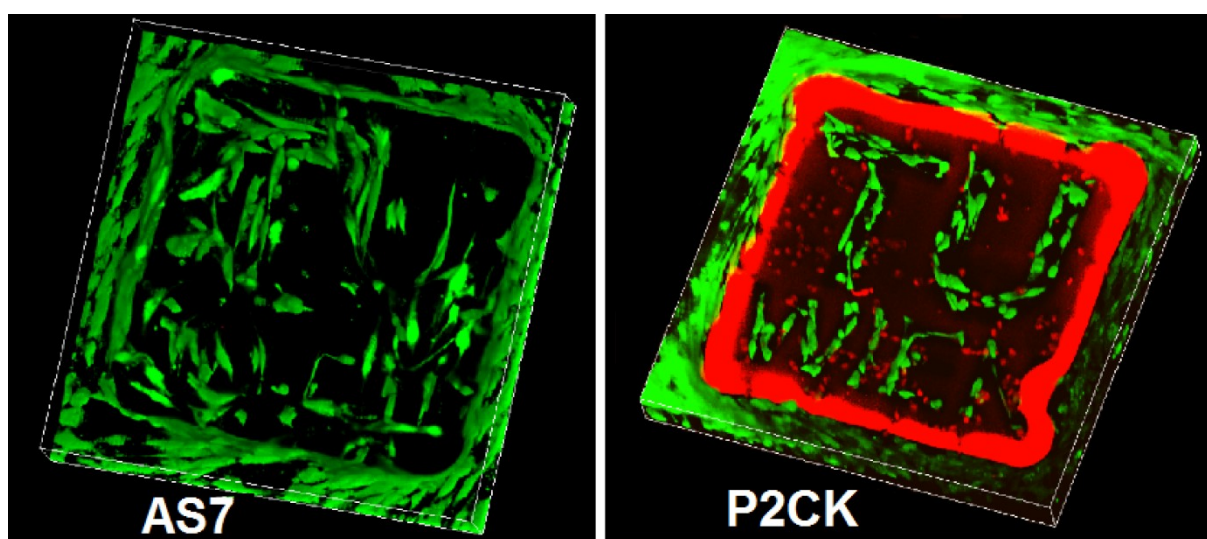


On the in-house built 2PP printing system, both **AS7** and **P2CK** perform well at impressive writing speeds of up to 1 m/s, which is 4 orders of magnitude higher than commercial systems.

Presto Blue[®] metabolic activity tests performed on MC3T3 as well as more sensitive human adipose-derived mesenchymal stem cells (ASC/TERT1) attest a far higher biocompatibility to **AS7** in comparison to **P2CK**.

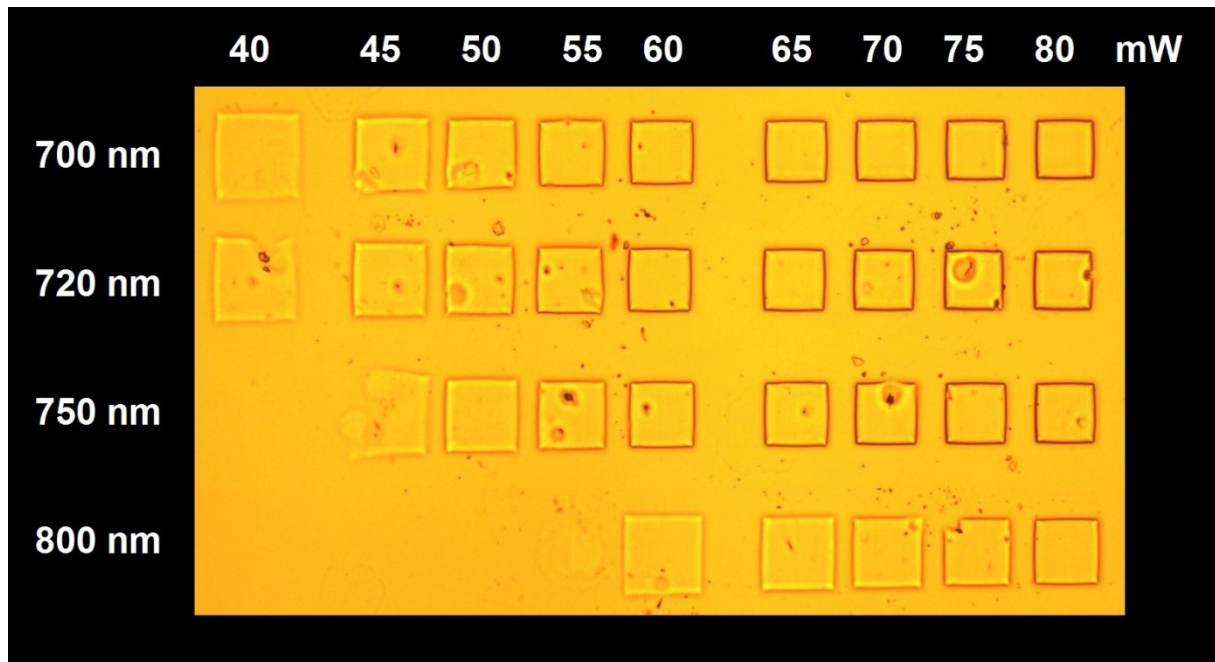


2PP cell encapsulation experiments with ASC/TERT1 showed that **AS7** also has excellent biocompatibility under laser excitation. Using **AS7**, cells embedded in the dense hydrogel as well as those trapped in the cavities stay viable (green stain), spread and proliferate, whereas with phototoxic **P2CK** only the cells in the cavities survive and almost all hydrogel embedded cells die (red stain).

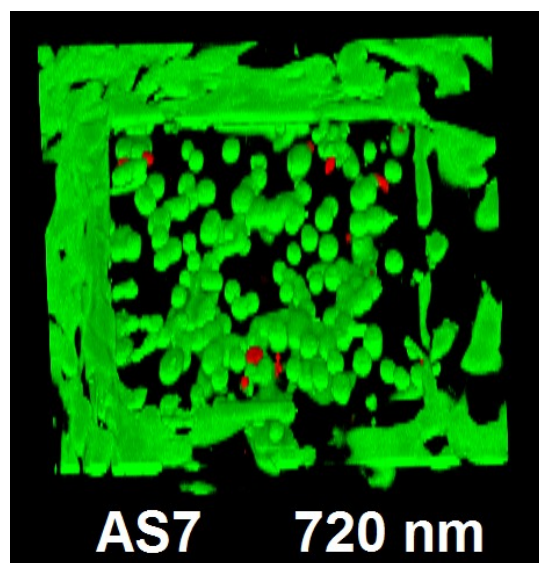


Comparative singlet oxygen luminescence measurements were inconclusive, resulting in very low oxygen photosensitization for **P2CK** and slightly higher values for **AS7** at 20 μM concentration, with both compounds exhibiting a quenching effect that is dominant over sensitization at concentrations of 1 mM. Thus, it is concluded that the phototoxicity may be mainly mediated by species other than singlet oxygen.

While the novel water-soluble, cleavable diazosulfonate 2PI **AS7** shows excellent cytocompatibility, transcending limitations of state-of-the-art materials, it is most efficient at laser wavelengths below 800 nm. Using a tunable Ti:sapphire femtosecond-pulsed laser, 2PP hydrogel structuring thresholds were also investigated at different wavelengths.



2PP encapsulation of ASC/TERT1 stem cells also works well at 720 nm. However, in light of the high cost of tunable lasers and the widespread commercial availability of Ti:sapphire lasers operating around 800 nm, future studies could aim at red-shifting the 2PA maximum of **AS7**, e.g. *via* extension of the conjugated π -system or introduction of electron donor groups.



Materials & Methods

Chemicals

All reagents were purchased from Sigma-Aldrich, Fluka, TCI or ABCR and were used without further purification. The solvents were dried and purified by standard laboratory methods.²²¹ Petroleum ether (PE) refers to the fraction boiling in the range 40-60 °C. (Flash) column chromatography was performed by either conventional techniques or preparative MPLC using a Buechi Sepacore Flash System (Buechi pump module C-605, Buechi control unit C-620, Buechi UV-Photometer C-635, Buechi fraction collector C-660). Glass and polyethylene columns were used, packed with Silicagel 60 on VWR silica gel 60 (0.040–0.063 mm particle size). Buechi Sepacore RP C18 Flash Cartridges were used for reversed phase chromatography. Trimethylolpropane triacrylate (**TTA**, Genomer 1330) and ethoxylated-(20/3)-trimethylolpropane triacrylate (**ETA**, Sartomer 415) were received as a gift from Rahn and Sartomer, respectively. Methacrylated gelatin (gelMOD) was provided by Prof. Sandra Van Vlierberghe and Prof. Peter Dubruel (Ghent University, Belgium). **P2CK** and **E2CK** free acid were prepared according to literature.¹⁰⁶ The sodium salts used in this work were obtained by dissolving **P2CK**- or **E2CK**-acid in aqueous NaOH at 50°C to a pH of 7.2 and freeze-drying the filtered solution. **M2CMK** was prepared in analogy to literature,⁹⁴ with a modified procedure that affords higher purity - the reaction was conducted in anhydrous EtOH, using KOH instead of NaOH. The product that precipitated upon stirring at room temperature was collected *via* suction filtration, washed with cold EtOH and recrystallized from EA.

Mode of practice for photosensitive compounds

The preparation and analysis of the photosensitive compounds and formulations was conducted in an orange light lab. The windows and fluorescent lamps were covered in adhesive foils or coated so that light with a wavelength <520nm was cut off. For compounds still too light-sensitive for these conditions, a red light lab (dark room with LEDs $\lambda_{\text{max}} = 620 \text{ nm}$ as the only light source) was used.

Thin layer chromatography (TLC) analysis

Thin layer chromatography analysis was performed on silica gel 60 F₂₅₄ aluminium sheets from Merck.

Melting points (mp) analysis

Melting points were measured with the aid of an automated melting point system (SRS OptiMelt MPA100).

Nuclear magnetic resonance (NMR) spectroscopy

¹H-, ¹³C- and HSQC-NMR spectra were measured with BRUKER Avance 200, BRUKER Avance 400 and BRUKER Ascend 600 FT-NMR-spectrometers. The chemical shift (s = singlet, bs = broad singlet, d = doublet, t = triplet, m = multiplet) is displayed in ppm using the non deuterated solvent as internal standard. Solvents with a grade of deuteration of at least 99.5 % were used and purchased from EURISOTOP.

HR-MS analysis

An Agilent 6230 LC TOFMS mass spectrometer equipped with an Agilent Dual AJS ESI-Source was used for HR-MS analysis

Gel permeation chromatography (GPC) analyses

Molecular weights (M_n) of hyaluronan before and after acidic degradation were determined by gel permeation chromatography using a Viscotek GPCmax VE 2001 with a VE 3580 RI detector calibrated with Shodex P-82 pullulan standards.

pH measurements

pH-values were determined with a WTW pH 340i pocket meter.

Ultrasonic bath

To accelerate dissolution of substances, the ultrasonic bath Sonorex Digitec from the company Bandelin was used.

UV/Vis-spectroscopy

Absorption spectra were recorded either on a Shimadzu UV-1800 or a Cary 50 absorption spectrometer at a controlled temperature of 25°C using quartz cuvettes with a beam path length of 1 cm. The spectra were obtained on samples with a maximal absorbance of approximately 1 (that was subsequently normalized) and baseline corrected using the pure solvent.

Two-photon excited fluorescence (2PEF) measurements¹⁵⁰

Two-photon cross sections σ_{2PA} were determined via two-photon excitation spectra using a set-up similar to the one described in ref.⁸⁰ and detailed in ref.²²²

The two-photon cross section at a given wavelength, $\sigma_{2PA}(\lambda)$, was calculated as follows:⁸⁰

$$\sigma_{2PA,s}(\lambda) = \frac{I_s(\lambda, \lambda_{obs}) \cdot c_r \cdot \phi_r(\lambda_{obs})}{I_r(\lambda, \lambda_{obs}) \cdot c_s \cdot \phi_s(\lambda_{obs})} \cdot \sigma_{2PA,r}(\lambda)$$

Here $I_x(\lambda, \lambda_{obs})$ is the (two-photon induced) fluorescence intensity at excitation wavelength λ and observation wavelength λ_{obs} for either sample or reference ($x \in \{s, r\}$). c_x and $\phi_x(\lambda_{obs})$ are the concentration and differential fluorescence quantum yield (at the observation wavelength) of sample and reference. Rhodamine 6G in methanol was used as reference for determining the absolute two-photon cross sections, while Coumarin 120 in ethanol, Coumarin 153 in methanol and LDS 698 in chloroform, were additionally used for assigning the bandshape.²²³

White light continuum z-scan (WLC) measurements²¹⁴

2PA spectra of weakly to non-fluorescent compounds were determined using white light continuum z-scan (WLC).⁷⁹ A Ti:sapphire laser system (FEMTOSOURCE COMPACT PRO, Femtolasers GmbH) producing 500 μJ , 30 fs, 800 nm pulses at 1 kHz repetition rate was used as source for WLC generation. The Ti:sapphire laser output beam is slightly focused using a 150 cm focal length plano-convex lens to a 200 μm diameter spot at the entrance of the 250 μm diameter 175 cm long hollow fiber (KALEIDOSCOPETM hollow fiber compressor) placed inside a chamber filled with argon gas at a pressure of 0.6 bar. This leads to a WLC beam spectrally broadened in the range of 550–1000 nm, which is first transmitted through a set of half-wave plate and polarizer in order to regulate the intensity and subsequently through an ultra-broadband dispersive mirror compressor consisting of 8 mirrors to produce sub-10 fs pulses.

The WLC beam emerging from the compressor was dispersed using an F2-glass prism-pair and then focused into the sample using a 150 mm focal length cylindrical lens. The sample was mounted on a translation stage moving step-wise in the laser beam propagation direction to facilitate Z-scans. The nonlinear transmittance was measured by a charge-coupled-device (CCD) line camera [CCDS3600-D from ALPHALAS (3648 pixels with pixel-width of 8 μm)] as a function of the sample position. Since different spectral components are spatially separated, any part of the sample in the beam cross section is irradiated with almost single wavelength pulses leading to only degenerate 2PA processes. The 2PA cross section at each wavelength can be extracted by fitting Equation (1) to the measured data and thus wavelength resolved degenerate 2PA spectra can be obtained by performing a single z-scan using dispersive WLC.

$$T(z) = \sum_{n=0}^{\infty} \frac{\left(-(\sigma_2 \lambda N_A \rho \times 10^{-3} / h c) L I_0\right)^n}{(n+1)^{3/2} \left(1 + \frac{z^2}{z_R^2}\right)^n}$$

where, T is the normalized transmittance, L is the sample thickness, z_R is the Rayleigh range, z is the sample position measured with respect to the focal plane, I_0 is the peak on-axis intensity at the focal plane, h is the Plank constant, c is the light

speed in free space, N_A is the Avogadro constant, ρ is the concentration of the examined solution in $\text{mol}\cdot\text{l}^{-1}$, λ is the wavelength and σ_2 is the 2PA cross section.

Cell culture

Mouse calvaria-derived preosteoblast cells (MC3T3-E1 Subclone 4) were obtained from ATCC-LGC Standards. MC3T3 were expanded in Alpha Minimum Essential Medium (α MEM) with ribonucleases, deoxyribonucleases, 2mM L-glutamine, without ascorbic acid (Gibco), supplemented with 10% fetal bovine serum (Sigma) and 1% of 10 000 U/mL Penicillin/Streptomycin (Lonza). Cells were cultivated in incubator in humid atmosphere with 5% CO_2 at 37°C. Medium was refreshed every second day.¹⁵⁰

ASC/TERT1 (Evercyte, Vienna, Austria) were cultured and maintained in EGM-2 media (Lonza, Basel, Switzerland) supplemented with 10% fetal calf serum (FCS) (Sigma-Aldrich, Saint Louis, MO, USA). Cells were incubated in a humidified atmosphere with 5% CO_2 at 37 °C. At 80% confluence the cells were detached using 0.5% trypsin-EDTA solution (Gibco, Waltham, MA, USA) and after the cells detached trypsin inhibitor was added (Gibco, Waltham, MA, USA), the cells were resuspended in media and centrifuged at 170g for 5 min before seeding onto T75 flasks.²¹⁴

Evaluation of 2PI transmembrane migration

MC3T3 cells were cultured in μ -dishes (35mm diameter with glass bottom, high version, Ibbidi GmbH, Martinsried, Germany) until the glass bottom was covered with a non-confluent monolayer of cells and then exposed to either **P2CK**, **E2CK** or **HAPI** (as 0.1 mM solutions in PBS). After 5 min incubation time, the autofluorescence of the 2PIs was visualized by laser scanning microscopy (Zeiss Axio Observer Z1 with a LSM 700 unit including an objective Zeiss EC Plan Neofluar 20x/0.5, ZEN11 software for evaluation) using the 488nm laser for excitation.¹⁵⁰

Evaluation of photoinitiator cytocompatibility^{150,214}

To evaluate the cytocompatibility of photoinitiators PrestoBlue Cell Viability Reagent (Life Technologies or Invitrogen) was used. For these tests 96-well plates were

seeded with 5 000 cells per well and incubated overnight for cells to attach. MC3T3 cells were incubated with 100 μ L of different dilutions of 2.0, 1.0 and 0.5 mM of **HAPI**, **P2CK** or **E2CK** dissolved in α MEM cell culture medium (either without or with 10 mM methyl- β -cyclodextrin added) for comparison. The procedure was performed under red light (620 nm LED) because of light sensitivity and potential additional phototoxicity of the 2PIs. After 5 h incubation with 2PIs, culture medium was exchanged twice to remove 2PI residues and cell viability was evaluated. Resazurin-based reagent PrestoBlue was diluted 1:10 with medium and 100 μ L were applied per well and incubated for 1 hour. Because of the reducing environment of viable cells, this reagent is transformed and turns red, becoming highly fluorescent. The fluorescence was measured with a plate reader (Synergy BioTek, excitation 560 nm, emission 590 nm). After correction for background fluorescence, the results of the cells exposed to different concentrations of photoinitiator were compared to each other and to the controls (non-stimulated cells). It was assumed that metabolic activity of the control not exposed to photoinitiators is 100%. Statistical evaluation of data was performed using software package IBM SPSS Statistic 22 (SPSS Inc., Chicago, IL) and Excel 2013 (Microsoft Office). Results are presented as average of repeated measurements \pm standard deviation (SD). After verifying normal distribution and homogeneity of variance, a one-way analysis of variance was used to compare means of the samples. If a significant difference was observed ($p < 0.05$), Bonferroni post hoc multiple comparison tests were performed to detect significant difference between the samples.

For cytocompatibility evaluation of **AS7**, MC3T3 and ASC/TERT1 cells were seeded in 96-well culture plates. 0.5 - 4.0 mM **AS7** and **P2CK** solution in cell culture media (α MEM for MC3T3 and EGM-2 (10% FCS) for ASC/TERT1) was added to the wells, followed by incubation for 3h at 37 °C. Afterwards the cells were washed with PBS twice before fresh media was added and the cells were left to recover overnight. After 24 h PrestoBlue assay was performed by diluting the reagent 1:10 with media and incubating the plates for 1h. The fluorescence was measured with a plate reader (Synergy BioTek, excitation 560 nm, emission 590 nm). Data were analyzed with GraphPad Prism software using one-way ANOVA with Kruskal–Wallis test followed by Dunn's multiple comparisons post-hoc.

Two-photon-polymerization (2PP) printing setup, assay of 2PIs and cell encapsulation^{150,214}

The details of the custom-built 2PP microfabrication setup were reported previously.⁶ For 2PP structuring, a femtosecond NIR-laser (MaiTai eHP DeepSee, Spectra-Physics) was used at 800 nm, with a minimum pulse duration of 70fs after the microscope objective (Plan-Apochromat 10x/0.3, Zeiss). To facilitate high-speed structuring, a combination of sample positioning via a motorized stage and a galvanometer scanner was used for laser beam positioning within the sample. The in-house developed software controls the complete setup. The structuring process was monitored real time with a CMOS-camera mounted behind the dichroic mirror in the beam path.²¹⁴

The polymerizable formulations were applied to μ -dishes (35mm diameter with glass bottom, high version, Ibidi GmbH, Martinsried, Germany) where the glass slide had been functionalized with methacrylate groups by cleaning and activation with a 4:1 mixture of conc. H₂SO₄ and H₂O₂ (30% in water), subsequently applying a freshly prepared ethanolic solution containing 1% 3-(trimethoxysilyl)propyl methacrylate (Sigma Aldrich), 3% water and 0.5% acetic acid for 15 min, and finally rinsing with EtOH and drying in an oven at 60°C.

For the cell encapsulation assays with **HAPI** and reference **P2CK**, methacrylamide-modified gelatin (gelMOD) with degree of substitution of 72% (provided by Ghent University) was used as hydrogel precursor and in accordance to a previously reported protocol.^{103,104} Yin-yang structures of 300 μ m diameter were 2PP-printed in a solution of 15% gelMOD in α MEM containing 1 mM **HAPI** and 10mM MBCD, or 1mM **P2CK**, and a cell density of 10 million cells per 1 mL. Fabrication was started slightly below the glass surface to ensure proper adhesion via covalent bonding between the methacrylated glass surface and the crosslinked hydrogel, operating the 2PP system at the following parameters: laser power after objective 60 mW, scanning speed 100 mm s⁻¹, hatch 0.5 μ m, layer spacing 0.5 μ m. Excess hydrogel precursor solution was removed after 2PP structuring by replacing supernatant solution above the structures three times with fresh α MEM, incubating 1h at 37°C in-between exchanges. Cells were stained by calcein-AM and propidium iodide (Life Technologies) as previously described,²⁹ 24 h and 5 days after 2PP structuring. Hydrogel constructs and encapsulated cells were visualized by laser scanning

microscopy using the 488nm and 555nm lasers for excitation (Zeiss LSM 700 and ZEN11 software for evaluation).

To evaluate the performance of the cleavable trichloromethyl-triazine 2PIs **2BC** and **BC**, they were tested under the same conditions as the non-cleavable reference compounds **2BTrz**, **BTrz**, and **M2CMK**. The 2PIs were dissolved at a concentration of 5 μmol per gram of a mixture of acrylate resins (ethoxylated-(20/3)-trimethylolpropane triacrylate (ETA) / trimethylolpropane triacrylate (TTA) molar ratio = 1:1). Arrays of defined woodpile structures (lateral dimensions: 50 x 50 μm , 5 μm hatch-distance, 0.5 μm layer-distance, 25 layers) were 2PP-printed at 800 nm, varying the laser power (10 - 100 mW) and writing speed (0.32 - 100 mm/s). The structures were carefully rinsed with iPrOH, dried and sputtered with gold. and images taken using a FEI Philips XL30 scanning electron microscope with EDX detection. The integrity and surface quality was investigated by means of scanning electron microscopy (FEI Quanta 200).

Organo-soluble diazosulfone **AS1** (10 $\mu\text{mol/g}$ ETA/TTA = 1:1) was compared to reference **M2CMK** (5 $\mu\text{mol/g}$ ETA/TTA = 1:1). Arrays of defined woodpile structures (lateral dimensions: 30 x 30 μm , 3 μm hatch-distance, 0.5 μm layer-distance, 25 layers) were 2PP-printed at 800 nm, varying the laser power (10 - 150 mW) and writing speed (20 - 200 mm/s). After printing, excess resin was carefully removed with iPrOH and structural integrity was assessed from laser scanning microscopy (LSM) images, using the 408nm and 488nm lasers for excitation of residual 2PI autofluorescence (Zeiss LSM 700 and ZEN11 software for evaluation). Water-soluble diazosulfonate **AS2** (8mM in 50 wt% PEGDA700 in PBS) was compared to reference **P2CK** (1mM in 50 wt% PEGDA700 in PBS). Arrays of dense hydrogel cubes (lateral dimensions: 30 x 30 μm , 0.5 μm hatch-distance, 0.5 μm layer-distance, 25 layers) were 2PP-printed at 800 nm, varying the laser power (10 - 150 mW) and writing speed (20 - 200 mm/s). After printing, excess hydrogel precursor was carefully removed with PBS and structural integrity was assessed from LSM images, using the 408nm and 488nm lasers for excitation of residual 2PI autofluorescence. Water-soluble diazosulfonate **AS7** (1mM in 50 wt% PEGDA700 in PBS) was compared to reference **P2CK** (1mM in 50 wt% PEGDA700 in PBS) in exactly the same manner as described above for **AS2**.

Further hydrogel structuring tests comparing **AS7** and **P2CK** were performed using either 2PI at 1 mM and 2 mM in a 10% gelMOD (95% substitution rate, provided by Ghent University) solution in EGM-2 media. Dense cubes with a side length of 100 μm were 2PP-printed at different writing speeds (100-1000 mm/s) and different powers (45-100 mW), with 0.5 μm line hatch and 0.5 μm layer spacing. Structuring threshold was defined as the minimal power needed for structuring. The swelling ratio of samples was addressed by measuring the changes in perimeter of the samples using ImageJ FIJI software. The printed structures were immersed in PBS for 48h until they reached the swelling equilibrium. The swelling ratio (Q) was calculated using the following equation:

$$Q = \frac{P_t - P_b}{P_b} * 100$$

where, P_t is the perimeter of the cubes on the top, P_b is the perimeter of the sample on the bottom.

Finally, ASC/TERT1 cells were suspended at a concentration of 2×10^6 cells/mL in 10% gelMOD (substitution rate of 95%, provided by Ghent University) solution in EGM-2 medium supplemented with either 1 mM P2CK or 2 mM AS7. 2PP encapsulation was performed in dense cubes (lateral dimensions: 300 x 300 μm , 0.5 μm line hatch, 0.5 μm layer-distance, 100 layers) fabricated at 1000 mm/s writing speed and laser powers ranging from 80- 110 mW. In order to assess the changes in cell numbers, calcein-AM/propidium iodide stain was applied at two time points (24 h and 5 days after 2PP printing) and the live cells were counted from 3D LSM images using ImageJ FIJI software. TU logos (dimensions 500 \times 500 \times 125 μm , , 0.5 μm line hatch, 0.5 μm layer-distance) were also printed at 80 mW laser power and a writing speed of 250 mm/s. The viability of cells was assessed with calcein-AM/propidium iodide staining 24 h and 5 days after 2PP printing and LSM visualization using the 488nm and 555nm lasers for excitation (Zeiss LSM 700 and ZEN11 software for evaluation).²¹⁴

Singlet Oxygen Measurements

The sensitized production of $^1\text{O}_2$ by the materials was studied by direct detection of near-infrared luminescence of $^1\text{O}_2$ around 1270 nm using a home-built set-up.²²⁴ The sample was irradiated by 5 ns long pulses at 420 nm with $\sim 5 \mu\text{J}$ in pulse provided by dye laser (FL1000, Lambda Physik) pumped by excimer laser (ATLEX 500i, ATL Lasertechnik). The luminescence signal was collected through two RG7 long-pass filters (Schott) and high-luminosity monochromator (H20IR, Jobin-Yvon) to the infrared sensitive photomultiplier (R5509, Hamamatsu) working in single photon counting mode. The photomultiplier output was detected by time-resolved multichannel photon counter (MSA-200, Becker-Hickl) with 5 ns per channel resolution. Increase of the signal after increasing the partial oxygen pressure as well as total quenching of the signal by specific $^1\text{O}_2$ quencher NaN_3 was used to verify that the obtained luminescence kinetics originates only in $^1\text{O}_2$. The kinetics obtained with the quencher was subtracted as a background before analysis of the $^1\text{O}_2$ kinetics. 300 000 sweeps were accumulated to obtain each kinetics. The lifetimes of $^1\text{O}_2$ were obtained by fitting a model based on single-exponential decays of both the sensitizer and the $^1\text{O}_2$.²¹⁴

Abbreviations

$^1\text{O}_2^*$	excited singlet oxygen	Et_2O	diethyl ether
1PA	one-photon absorption	ETA	ethoxylated-(20/3)-trimethylolpropane triacrylate
1PI	one-photon initiator	EtOH	ethanol
1PP	one-photon polymerization	FDM	fused deposition modeling
2PA	two-photon absorption	fs	femtosecond
2PEF	two-photon excited fluorescence	gelMOD	methacrylated gelatin
2PI	two-photon initiator	GM	1 Göppert-Mayer = $10^{-50} \text{ cm}^4 \text{ s photon}^{-1} \text{ molecule}^{-1}$
3D	three dimensional	h	hours
3DP	three-dimensional printing	\hbar	reduced Planck constant
A	electron acceptor group	HA	hyaluronan
ADS	4-amino-4'-(<i>N,N</i> -dimethylamino)stilbene	HO^\bullet	hydroxyl radical
AMT	additive manufacturing technology	h ν	light, photons
ASC	adipose-derived stem cell	I	light intensity
ASC/TERT1	hTERT immortalized human adipose-derived mesenchymal stem cell line	IC	internal conversion
Boc	tert-butoxycarbonyl	intra-CT	intramolecular charge transfer
Boc-CNK	4-(tert-butoxycarbonylamino)cyclohexanone	iPrOH	isopropanol
Boc-GABA-OH	4-(tert-butoxycarbonylamino)butyric acid	iPS cells	induced pluripotent stem cells
bp	boiling point	IR	infrared
BSA	bovine serum albumine	ISC	intersystem crossing
CAD	computer-aided design	KOt-Bu	potassium tert-butoxide
CAL-B	<i>Candida antarctica</i> lipase B	LDM	low-temperature deposition manufacturing
calcein-AM	calcein acetoxymethyl ester	LED	light emitting diode
CCD	charge-coupled-device	LFP	laser flash photolysis
CDCl_3	deuteriochloroform	LIFT	laser-induced forward transfer
CDI	1,1'-carbonyldiimidazole	LSM	laser scanning microscopy
CDMT	2-chloro-dimethoxy-1,3,5-triazine	MBCD	methyl- β -cyclodextrin
CHCl_3	chloroform	MBK	monobenzylidene ketone
CIDNP	chemically induced dynamic nuclear polarization	MC3T3	mouse osteoblast precursor cell line
CMPI	2-chloro-1-methylpyridinium iodide	MeCN	acetonitrile
CQ	camphorquinone	MeOH	methanol
CT	(trichloromethyl)-1,3,5-triazine	MG63	human osteosarcoma cell line
d	days	min	minutes
D	electron donor group	M_n	number average molecular weight
DBK	dibenzylidene ketone	mp	melting point
DCM	dichloromethane	MsOH	methanesulfonic acid
DIMCARB	dimethylammonium dimethylcarbamate	mW	milliwatts
DMF	dimethyl formamide	N_A	Avogadro's number
DMSO	dimethylsulfoxide	NaOMe	sodium methoxide
DS	degree of substitution	NaTS	sodium p-toluenesulfinate
EA	ethyl acetate	NIR	near infrared
ECM	extracellular matrix	nm	nanometer
EDC	1-ethyl-3-[3-(dimethylamino)-propyl]-carbodiimide	NMR	nuclear magnetic resonance
EGM-2	Endothelial Cell Growth Medium 2	$\text{O}_2^{\bullet-}$	superoxide

PAM	pressure-assisted microsyringe	THF	tetrahydrofuran
PAM2	piston-assisted microsyringe	Ti:S	titanium:sapphire
P _b	bottom perimeter	TLC	thin layer chromatography
PBS	phosphate buffered saline	TPPS4	tetraphenylporphine tetrasulfonate
PCL	polycaprolactone	Trz	2,4,6-trimethyl-1,3,5-triazine
PE	petrol ether	TTA	trimethylolpropane triacrylate
PEGDA700	poly(ethylene glycol) diacrylate (M _n ~ 700 g/mol)	UV	ultraviolet
PI	photoinitiator	Vis	visible light
PipAc	piperidinium acetate	voxel	volume element
PLLA	poly(L-lactide)	WLC	white light continuum
P _t	top perimeter	wt%	weight percent
p-TsOH	para-toluenesulfonic acid	α	linear absorption coefficient
Q	swelling ratio	α MEM	Minimum Essential Medium Eagle - alpha modification
R _f	retention factor	β	non-linear absorption coefficient
ROS	reactive oxygen species	ϵ_{max}	molar extinction coefficient at 1PA maximum
S ₁	lowest excited singlet state	ϕ	fluorescence quantum yield
SEM	scanning electron microscopy	λ_{2PA}	two photon absorption maximum
SLA	stereolithography	λ_{abs}	one photon absorption maximum
SLS	selective laser sintering	λ_{em}	fluorescence maximum
T ₁	lowest excited triplet state	λ_{z-scan}	wavelength used for z-scan
TBA-Cl	tetrabutylammonium chloride	μm	micrometer
TBA-HA	tetrabutylammonium salt of hyaluronan	σ_{2PA}	two-photon absorption cross section
TCP	β -tricalcium phosphate	ω	angular frequency
TEA	triethylamine		

Initiators

2BC	4,4'-[(6-trichloromethyl-1,3,5-triazine-2,4-diyl)di-(1E)-2,1-ethenediyl]bis[N,N-dibutylbenzenamine]
2BTrz	4,4'-[(6-methyl-1,3,5-triazine-2,4-diyl)di-(1E)-2,1-ethenediyl]bis[N,N-dibutylbenzenamine]
3BTrz	4,4',4''-[1,3,5-triazine-2,4,6-triyltri-(1E)-2,1-ethenediyl]tris[N,N-dibutylbenzenamine]
AHK	2-hydroxy-2-methyl-1-phenylpropan-1-one
AIBN	2,2'-azobis(isobutyronitrile)
AS	phenylazophenylsulfone
AS1	(E)-N-[[4-(dimethylamino)phenyl]imino]-4-methylbenzenesulfonamide
AS2	sodium (E)-[4-(dimethylamino)phenyl]diazenesulfonate
AS3	N,N-dimethyl-4-[(E)-4-((E)-tosyldiazenyl)styryl]aniline
AS4	sodium (E)-2-[4-(E)-4-(dimethylamino)styryl]phenyl]diazenesulfonate
AS5	(E)-1,2-bis[4-((E)-tosyldiazenyl)phenyl]ethene
AS6	disodium (1E,1'E)-2,2'-[(E)-1,2-ethenediyl]bis[(4,1-phenylene)diazenesulfonate]
AS7	tetrapotassium (1E,1'E)-4,4'-[(E)-1,2-ethenediyl]bis[2-(3-sulfophenyl)diazenesulfonate]
B3FL	2,7-bis[[4-(dibutylamino)phenyl]ethynyl]-9H-fluoren-9-one
BC	4-[(1E)-2-(4-methyl-6-trichloromethyl-1,3,5-triazin-2-yl)ethenyl]-N,N-dibutylbenzenamine
BTrz	4-[(1E)-2-(4,6-dimethyl-1,3,5-triazin-2-yl)ethenyl]-N,N-dibutylbenzenamine
E2CK	sodium 3,3'-[(((1E,1'E)-(5-methyl-2-oxocyclohexane-1,3-diyldene)bis(methanylylidene))bis(4,1-phenylene))bis(methylazanediy)]dipropanoate

HAPI	Hyaluronan-based photoinitiator
I2959	2-hydroxy-4'-(2-hydroxyethoxy)-2-methylpropiophenone
Irgacure 369	(2-benzyl-2-(dimethylamino)-1-[4-(morpholinyl) phenyl])-1-butanone
Irgacure 819	bis(2,4,6-trimethylbenzoyl)penylphosphine oxide
Irgacure OXE01	1-[4-(phenylthio) phenyl]-1,2-octanedione-2-(o-benzoyloxime)
ITX	isopropylthioxanthenes
Li-TPO	lithium phenyl-2,4,6-trimethylbenzoylphosphinate
M2CMK	(2E,6E)-2,6-bis[4-(dimethylamino) phenyl]methylene]-4-methylcyclohexanone
MCNK	(2E,6E)-4-amino-2,6-bis[[4-(dimethylamino)phenyl]methylene]cyclohexanone
MGABA	(3E,5E)-4-amino-N-[3,5-bis[[4-(dimethylamino)phenyl]methylene]-4-oxocyclohexyl]butanamide
N-AHK	1-(4-(dimethylamino)phenyl)-2-hydroxy-2-methylpropan-1-one
P2CK	sodium 3,3'-[(((1E,1'E)-(2-oxocyclopentane-1,3-diylidene) bis(methanylylidene))bis(4,1-phenylene))bis(methylazanediyl)]dipropanoate
PADE	1,5-bis(4-methoxyphenyl)-3-methyl-1,4-pentazadiene
R1	4,4'-((2,5-dimethoxy-1,4-phenylene)di-(1E)-2,1-ethenediyl)bis[N,N-dibutylbenzenamine]
Rose Bengal	4,5,6,7-tetrachloro-2',4',5',7'-tetraiodofluorescein
TA	2-(4-methoxyphenyl)-4,6-bis(trichloromethyl)-1,3,5-triazine
TB	2-(4-methoxystyryl)-4,6-bis(trichloromethyl)-1,3,5-triazine
TC	squarylium linked 2-(4-(oxycarbonyl)phenyl)-4,6-bis(trichloromethyl)-1,3,5-triazine
TCT	2,4,6-tris(trichloromethyl)-1,3,5-triazine
VA-086	2,2'-azobis[2-methyl-N-(2-hydroxyethyl)propionamide]
WSPI	1,4-bis[4'-(N,N-bis(6''-(N,N,N-trimethylammonium)hexyl)amino)-styryl]-2,5-dimethoxybenzene tetraiodide

References

- (1) Langer, R.; Vacanti, J. Tissue Engineering. *Science* (80-.). **1993**, *260* (5110), 920–926.
- (2) Berthiaume, F.; Maguire, T. J.; Yarmush, M. L. Tissue Engineering and Regenerative Medicine: History, Progress, and Challenges. *Annu. Rev. Chem. Biomol. Eng.* **2011**, *2* (1), 403–430.
- (3) Yang, F.; Neeley, W.; Moore, M.; Karp, J.; Shukla, A.; Langer, R. Tissue Engineering: The Therapeutic Strategy of the Twenty-First Century. In *Nanotechnology and Regenerative Engineering*; CRC Press, 2014; pp 3–38.
- (4) Ovsianikov, A.; Khademhosseini, A.; Mironov, V. The Synergy of Scaffold-Based and Scaffold-Free Tissue Engineering Strategies. *Trends Biotechnol.* **2018**, *36* (4), 348–357.
- (5) Nicodemus, G. D.; Bryant, S. J. Cell Encapsulation in Biodegradable Hydrogels for Tissue Engineering Applications. *Tissue Eng. Part B Rev.* **2008**, *14* (2), 149–165.
- (6) Ovsianikov, A.; Mühleder, S.; Torgersen, J.; Li, Z.; Qin, X. H.; Van Vlierberghe, S.; Dubruel, P.; Holthöner, W.; Redl, H.; Liska, R.; et al. Laser Photofabrication of Cell-Containing Hydrogel Constructs. *Langmuir* **2014**, *30* (13), 3787–3794.
- (7) Zorlutuna, P.; Jeong, J. H.; Kong, H.; Bashir, R. Stereolithography-Based Hydrogel Microenvironments to Examine Cellular Interactions. *Adv. Funct. Mater.* **2011**, *21* (19), 3642–3651.
- (8) Ahmed, E. M. Hydrogel: Preparation, Characterization, and Applications: A Review. *J. Adv. Res.* **2015**, *6* (2), 105–121.
- (9) Rahman, M. M.; Giol, E. D.; Cama, G.; Van Vlierberghe, S.; Dubruel, P. CHAPTER 4. Stimuli-Responsive Hydrogels for Tissue Engineering. In *Smart Materials for Tissue Engineering*; Royal Society of Chemistry: Cambridge; pp 62–99.
- (10) Tan, H.; Chu, C. R.; Payne, K. A.; Marra, K. G. Injectable in Situ Forming Biodegradable Chitosan–hyaluronic Acid Based Hydrogels for Cartilage Tissue Engineering. *Biomaterials* **2009**, *30* (13), 2499–2506.
- (11) Thanos, C.; Emerich, D. On the Use of Hydrogels in Cell Encapsulation and Tissue Engineering Systems. *Recent Pat. Drug Deliv. Formul.* **2008**, *2* (1), 19–24.
- (12) Kim, S. H.; Turnbull, J.; Guimond, S. Extracellular Matrix and Cell Signalling: The Dynamic Cooperation of Integrin, Proteoglycan and Growth Factor Receptor. *J. Endocrinol.* **2011**, *209* (2), 139–151.
- (13) Müller, U. Integrins and Extracellular Matrix in Animal Models. *Handb. Exp. Pharmacol.* **2004**, No. 165, 217–241.
- (14) Rozario, T.; DeSimone, D. W. The Extracellular Matrix in Development and Morphogenesis: A Dynamic View. *Dev. Biol.* **2010**, *341* (1), 126–140.

- (15) Frantz, C.; Stewart, K. M.; Weaver, V. M. The Extracellular Matrix at a Glance. *J. Cell Sci.* **2010**, *123*, 4195–4200.
- (16) Suri, S.; Schmidt, C. E. Photopatterned Collagen-Hyaluronic Acid Interpenetrating Polymer Network Hydrogels. *Acta Biomater.* **2009**, *5* (7), 2385–2397.
- (17) Freyman, T. M.; Yannas, I. V.; Gibson, L. J. Cellular Materials as Porous Scaffolds for Tissue Engineering. *Prog. Mater. Sci.* **2001**, *46* (3–4), 273–282.
- (18) Werner Brox. Gelatin Capsule. US4780316 A, 1986.
- (19) Hsu, W.-M.; Chen, K.-H.; Lai, J.-Y.; Hsiue, G.-H. Transplantation of Human Corneal Endothelial Cells Using Functional Biomaterials: Poly(N-Isopropylacrylamide) and Gelatin. *J. Exp. Clin. Med.* **2013**, *5* (2), 56–64.
- (20) Sakai, S.; Hirose, K.; Taguchi, K.; Ogushi, Y.; Kawakami, K. An Injectable, in Situ Enzymatically Gellable, Gelatin Derivative for Drug Delivery and Tissue Engineering. *Biomaterials* **2009**, *30* (20), 3371–3377.
- (21) Nikkhah, M.; Akbari, M.; Paul, A.; Memic, A.; Dolatshahi-Pirouz, A.; Khademhosseini, A. Gelatin-Based Biomaterials For Tissue Engineering And Stem Cell Bioengineering. In *Biomaterials from Nature for Advanced Devices and Therapies*; John Wiley & Sons, Inc.: Hoboken, New Jersey, 2016; pp 37–62.
- (22) Van Hoorick, J.; Gruber, P.; Markovic, M.; Tromayer, M.; Van Erps, J.; Thienpont, H.; Liska, R.; Ovsianikov, A.; Dubruel, P.; Van Vlierberghe, S. Cross-Linkable Gelatins with Superior Mechanical Properties Through Carboxylic Acid Modification: Increasing the Two-Photon Polymerization Potential. *Biomacromolecules* **2017**, *18* (10), 3260–3272.
- (23) Shu, X. Z.; Liu, Y.; Luo, Y.; Roberts, M. C.; Prestwich, G. D. Disulfide Cross-Linked Hyaluronan Hydrogels. *Biomacromolecules* **2002**, *3* (6), 1304–1311.
- (24) Zheng Shu, X.; Liu, Y.; Palumbo, F. S.; Luo, Y.; Prestwich, G. D. In Situ Crosslinkable Hyaluronan Hydrogels for Tissue Engineering. *Biomaterials* **2004**, *25* (7–8), 1339–1348.
- (25) Park, Y.; Lutolf, M. P.; Hubbell, J. A.; Hunziker, E. B.; Wong, M. Bovine Primary Chondrocyte Culture in Synthetic Matrix Metalloproteinase-Sensitive Poly(ethylene Glycol)-Based Hydrogels as a Scaffold for Cartilage Repair. *Tissue Eng.* **2004**, *10* (3–4), 515–522.
- (26) Temenoff, J. S.; Park, H.; Jabbari, E.; Conway, D. E.; Sheffield, T. L.; Ambrose, C. G.; Mikos, A. G. Thermally Cross-Linked Oligo(poly(ethylene Glycol) Fumarate) Hydrogels Support Osteogenic Differentiation of Encapsulated Marrow Stromal Cells In Vitro. *Biomacromolecules* **2004**, *5* (1), 5–10.
- (27) Hong, Y.; Song, H.; Gong, Y.; Mao, Z.; Gao, C.; Shen, J. Covalently Crosslinked Chitosan Hydrogel: Properties of in Vitro Degradation and Chondrocyte Encapsulation. *Acta Biomater.* **2007**, *3* (1), 23–31.
- (28) Temenoff, J. S.; Park, H.; Jabbari, E.; Sheffield, T. L.; LeBaron, R. G.; Ambrose, C. G.; Mikos, A. G. In Vitro Osteogenic Differentiation of Marrow Stromal Cells Encapsulated in Biodegradable Hydrogels. *J. Biomed. Mater. Res.* **2004**, *70A* (2), 235–244.

- (29) Markovic, M.; Van Hoorick, J.; Hölzl, K.; Tromayer, M.; Gruber, P.; Nürnberger, S.; Dubruel, P.; Van Vlierberghe, S.; Liska, R.; Ovsianikov, A. Hybrid Tissue Engineering Scaffolds by Combination of Three-Dimensional Printing and Cell Photoencapsulation. *J. Nanotechnol. Eng. Med.* **2015**, *6* (2), 21004.
- (30) Fedorovich, N. E.; Oudshoorn, M. H.; van Geemen, D.; Hennink, W. E.; Alblas, J.; Dhert, W. J. A. The Effect of Photopolymerization on Stem Cells Embedded in Hydrogels. *Biomaterials* **2009**, *30* (3), 344–353.
- (31) Occhetta, P.; Visone, R.; Russo, L.; Cipolla, L.; Moretti, M.; Rasponi, M. VA-086 Methacrylate Gelatine Photopolymerizable Hydrogels: A Parametric Study for Highly Biocompatible 3D Cell Embedding. *J. Biomed. Mater. Res. - Part A* **2015**, *103* (6), 2109–2117.
- (32) Fairbanks, B. D.; Schwartz, M. P.; Bowman, C. N.; Anseth, K. S. Photoinitiated Polymerization of PEG-Diacrylate with Lithium Phenyl-2,4,6-Trimethylbenzoylphosphinate: Polymerization Rate and Cytocompatibility. *Biomaterials* **2009**, *30* (35), 6702–6707.
- (33) Bryant, S. J.; Anseth, K. S. Controlling the Spatial Distribution of ECM Components in Degradable PEG Hydrogels for Tissue Engineering Cartilage. *J. Biomed. Mater. Res.* **2003**, *64A* (1), 70–79.
- (34) Williams, C. G.; Kim, T. K.; Taboas, A.; Malik, A.; Manson, P.; Elisseeff, J. In Vitro Chondrogenesis of Bone Marrow-Derived Mesenchymal Stem Cells in a Photopolymerizing Hydrogel. *Tissue Eng.* **2003**, *9* (4), 679–688.
- (35) Husár, B.; Hatzenbichler, M.; Mironov, V.; Liska, R.; Stampfl, J.; Ovsianikov, A. Photopolymerization-Based Additive Manufacturing for the Development of 3D Porous Scaffolds. In *Biomaterials for Bone Regeneration*; Elsevier, 2014; pp 149–201.
- (36) Bowman, C. N.; Kloxin, C. J. Toward an Enhanced Understanding and Implementation of Photopolymerization Reactions. *AIChE J.* **2008**, *54* (11), 2775–2795.
- (37) Bryant, S. J.; Nuttelman, C. R.; Anseth, K. S. Cytocompatibility of UV and Visible Light Photoinitiating Systems on Cultured NIH/3T3 Fibroblasts in Vitro. *J. Biomater. Sci. Polym. Ed.* **2000**, *11* (5), 439–457.
- (38) Williams, C. G.; Malik, A. N.; Kim, T. K.; Manson, P. N.; Elisseeff, J. H. Variable Cytocompatibility of Six Cell Lines with Photoinitiators Used for Polymerizing Hydrogels and Cell Encapsulation. *Biomaterials* **2005**, *26* (11), 1211–1218.
- (39) Sawhney, A. S.; Pathak, C. P.; Hubbell, J. A. Interfacial Photopolymerization of Poly(ethylene Glycol)-Based Hydrogels upon Alginate-Poly(L-Lysine) Microcapsules for Enhanced Biocompatibility. *Biomaterials* **1993**, *14* (13), 1008–1016.
- (40) Cruise, G. M.; Hegre, O. D.; Scharp, D. S.; Hubbell, J. A. A Sensitivity Study of the Key Parameters in the Interfacial Photopolymerization of Poly(ethylene Glycol) Diacrylate upon Porcine Islets. *Biotechnol. Bioeng.* **1998**, *57* (6), 655–665.
- (41) Chakraborty, M.; Panda, A. K. Spectral Behaviour of Eosin Y in Different Solvents and Aqueous Surfactant Media. *Spectrochim. Acta Part A Mol. Biomol. Spectrosc.*

- 2011**, *81* (1), 458–465.
- (42) Ullrich, G.; Burtscher, P.; Salz, U.; Moszner, N.; Liska, R. Phenylglycine Derivatives as Coinitiators for the Radical Photopolymerization of Acidic Aqueous Formulations. *J. Polym. Sci. Part A Polym. Chem.* **2006**, *44* (1), 115–125.
- (43) *3D Printing and Biofabrication*; Ovsianikov, A., Yoo, J., Mironov, V., Eds.; Springer International Publishing: Cham, 2018.
- (44) Qin, X.-H.; Ovsianikov, A.; Stampfl, J.; Liska, R. Additive Manufacturing of Photosensitive Hydrogels for Tissue Engineering Applications. *BioNanoMaterials* **2014**, *15* (3–4).
- (45) Mota, C.; Puppi, D.; Chiellini, F.; Chiellini, E. Additive Manufacturing Techniques for the Production of Tissue Engineering Constructs. *J. Tissue Eng. Regen. Med.* **2015**, *9* (3), 174–190.
- (46) Levy, R. A.; Chu, T. M.; Halloran, J. W.; Feinberg, S. E.; Hollister, S. CT-Generated Porous Hydroxyapatite Orbital Floor Prosthesis as a Prototype Bioimplant. *AJNR. Am. J. Neuroradiol.* **1997**, *18* (8), 1522–1525.
- (47) Jansen, J.; Melchels, F. P. W.; Grijpma, D. W.; Feijen, J. Fumaric Acid Monoethyl Ester-Functionalized poly(D,L-Lactide)/N-Vinyl-2-Pyrrolidone Resins for the Preparation of Tissue Engineering Scaffolds by Stereolithography. *Biomacromolecules* **2009**, *10* (2), 214–220.
- (48) Eosoly, S.; Brabazon, D.; Lohfeld, S.; Looney, L. Selective Laser Sintering of Hydroxyapatite/poly- ϵ -Caprolactone Scaffolds. *Acta Biomater.* **2010**, *6* (7), 2511–2517.
- (49) Kolan, K. C. R.; Leu, M. C.; Hilmas, G. E.; Brown, R. F.; Velez, M. Fabrication of 13-93 Bioactive Glass Scaffolds for Bone Tissue Engineering Using Indirect Selective Laser Sintering. *Biofabrication* **2011**, *3* (2), 25004.
- (50) Yeong, W. Y.; Sudarmadji, N.; Yu, H. Y.; Chua, C. K.; Leong, K. F.; Venkatraman, S. S.; Boey, Y. C. F.; Tan, L. P. Porous Polycaprolactone Scaffold for Cardiac Tissue Engineering Fabricated by Selective Laser Sintering. *Acta Biomater.* **2010**, *6* (6), 2028–2034.
- (51) You, W.; Wang, M.; Lam, W.; Yuk, W. Selective Laser Sintering of Poly(L-Lactide)/Carbonated Hydroxyapatite Nanocomposite Porous Scaffolds for Bone Tissue Engineering. In *Tissue Engineering*; InTech, 2010.
- (52) Butscher, A.; Bohner, M.; Hofmann, S.; Gauckler, L.; Müller, R. Structural and Material Approaches to Bone Tissue Engineering in Powder-Based Three-Dimensional Printing. *Acta Biomater.* **2011**, *7* (3), 907–920.
- (53) Kim, S. S.; Utsunomiya, H.; Koski, J. A.; Wu, B. M.; Cima, M. J.; Sohn, J.; Mukai, K.; Griffith, L. G.; Vacanti, J. P. Survival and Function of Hepatocytes on a Novel Three-Dimensional Synthetic Biodegradable Polymer Scaffold with an Intrinsic Network of Channels. *Ann. Surg.* **1998**, *228* (1), 8–13.
- (54) Rowe, C. W.; Wang, C.-C.; Monkhouse, D. C. TheriForm Technology. In *Modified-Release Drug Delivery Technology*; Rathbone, M., Hadgraft, J., Roberts, M., Eds.; Drugs and the Pharmaceutical Sciences; Informa Healthcare, 2002; Vol.

- 183, pp 77–87.
- (55) Hutmacher, D. W.; Schantz, T.; Zein, I.; Ng, K. W.; Teoh, S. H.; Tan, K. C. Mechanical Properties and Cell Cultural Response of Polycaprolactone Scaffolds Designed and Fabricated via Fused Deposition Modeling. *J. Biomed. Mater. Res.* **2001**, *55* (2), 203–216.
- (56) Rohner, D.; Hutmacher, D. W.; Cheng, T. K.; Oberholzer, M.; Hammer, B. In Vivo Efficacy of Bone-Marrow-Coated Polycaprolactone Scaffolds for the Reconstruction of Orbital Defects in the Pig. *J. Biomed. Mater. Res.* **2003**, *66B* (2), 574–580.
- (57) Osteopore™ www.osteopore.com (accessed Jul 19, 2018).
- (58) Low, S. W.; Ng, Y. J.; Yeo, T. T.; Chou, N. Use of Osteoplug Polycaprolactone Implants as Novel Burr-Hole Covers. *Singapore Med. J.* **2009**, *50* (8), 777–780.
- (59) Vozzi, G.; Previti, A.; De Rossi, D.; Ahluwalia, A. Microsyringe-Based Deposition of Two-Dimensional and Three-Dimensional Polymer Scaffolds with a Well-Defined Geometry for Application to Tissue Engineering. *Tissue Eng.* **2002**, *8* (6), 1089–1098.
- (60) Tirella, A.; Vozzi, F.; Vozzi, G.; Ahluwalia, A. PAM2 (Piston Assisted Microsyringe): A New Rapid Prototyping Technique for Biofabrication of Cell Incorporated Scaffolds. *Tissue Eng. Part C Methods* **2011**, *17* (2), 229–237.
- (61) Xiong, Z. Fabrication of Porous Scaffolds for Bone Tissue Engineering via Low-Temperature Deposition. *Scr. Mater.* **2002**, *46* (11), 771–776.
- (62) Miranda, P.; Saiz, E.; Gryn, K.; Tomsia, A. P. Sintering and Robocasting of β -Tricalcium Phosphate Scaffolds for Orthopaedic Applications. *Acta Biomater.* **2006**, *2* (4), 457–466.
- (63) Fu, Q.; Saiz, E.; Tomsia, A. P. Direct Ink Writing of Highly Porous and Strong Glass Scaffolds for Load-Bearing Bone Defects Repair and Regeneration. *Acta Biomater.* **2011**, *7* (10), 3547–3554.
- (64) Abarrategi, A.; Moreno-Vicente, C.; Martínez-Vázquez, F. J.; Civantos, A.; Ramos, V.; Sanz-Casado, J. V.; Martínez-Corriá, R.; Perera, F. H.; Mulero, F.; Miranda, P.; et al. Biological Properties of Solid Free Form Designed Ceramic Scaffolds with BMP-2: In Vitro and In Vivo Evaluation. *PLoS One* **2012**, *7* (3), e34117.
- (65) Mironov, V.; Kasyanov, V.; Markwald, R. R. Organ Printing: From Bioprinter to Organ Biofabrication Line. *Curr. Opin. Biotechnol.* **2011**, *22* (5), 667–673.
- (66) Boland, T.; Xu, T.; Damon, B.; Cui, X. Application of Inkjet Printing to Tissue Engineering. *Biotechnol. J.* **2006**, *1* (9), 910–917.
- (67) Saunders, R. E.; Gough, J. E.; Derby, B. Delivery of Human Fibroblast Cells by Piezoelectric Drop-on-Demand Inkjet Printing. *Biomaterials* **2008**, *29* (2), 193–203.
- (68) Devillard, R.; Pagès, E.; Correa, M. M.; Kériquel, V.; Rémy, M.; Kalisky, J.; Ali, M.; Guillotin, B.; Guillemot, F. Cell Patterning by Laser-Assisted Bioprinting; 2014; pp 159–174.

- (69) Guillotin, B.; Ali, M.; Ducom, A.; Catros, S.; Keriquel, V.; Souquet, A.; Remy, M.; Fricain, J.-C.; Guillemot, F. Laser-Assisted Bioprinting for Tissue Engineering. In *Biofabrication*; Elsevier, 2013; pp 95–118.
- (70) Göppert-Mayer, M. Über Elementarakte Mit Zwei Quantensprüngen. *Ann. Phys.* **1931**, *401* (3), 273–294.
- (71) Kaiser, W.; Garrett, C. G. B. Two-Photon Excitation in CaF₂: Eu²⁺. *Phys. Rev. Lett.* **1961**, *7* (6), 229–231.
- (72) Sibbett, W.; Lagatsky, A. A.; Brown, C. T. A. The Development and Application of Femtosecond Laser Systems. *Opt. Express* **2012**, *20* (7), 6989.
- (73) Andrade, C. D.; Yanez, C. O.; Rodriguez, L.; Belfield, K. D. A Series of Fluorene-Based Two-Photon Absorbing Molecules: Synthesis, Linear and Nonlinear Characterization, and Bioimaging. *J. Org. Chem.* **2010**, *75* (12), 3975–3982.
- (74) Reinhardt, B. A. Two-Photon Technology. New Materials and Evolving Applications. *Photonics Sci. News* **1999**, *4* (2), 21–34.
- (75) Pawlicki, M.; Collins, H. A.; Denning, R. G.; Anderson, H. L. Two-Photon Absorption and the Design of Two-Photon Dyes. *Angew. Chemie - Int. Ed.* **2009**, *48* (18), 3244–3266.
- (76) Katan, C.; Terenziani, F.; Mongin, O.; Werts, M. H. V.; Porrès, L.; Pons, T.; Mertz, J.; Tretiak, S.; Blanchard-Desce, M. Effects of (Multi)branching of Dipolar Chromophores on Photophysical Properties and Two-Photon Absorption. *J. Phys. Chem. A* **2005**, *109* (13), 3024–3037.
- (77) Tromayer, M. Thesis: Novel Multipolar Initiators for Two-Photon Induced Photopolymerization. **2014**.
- (78) Ajami, A.; Husinsky, W.; Liska, R.; Pucher, N. Two-Photon Absorption Cross Section Measurements of Various Two-Photon Initiators for Ultrashort Laser Radiation Applying the Z-Scan Technique. *J. Opt. Soc. Am. B* **2010**, *27* (11), 2290.
- (79) Ajami, A.; Husinsky, W.; Tromayer, M.; Gruber, P.; Liska, R.; Ovsianikov, A. Measurement of Degenerate Two-Photon Absorption Spectra of a Series of Developed Two-Photon Initiators Using a Dispersive White Light Continuum Z-Scan. *Appl. Phys. Lett.* **2017**, *111* (7), 71901.
- (80) Makarov, N. S.; Drobizhev, M.; Rebane, A. Two-Photon Absorption Standards in the 550-1600 Nm Excitation Wavelength Range. *Opt. Express* **2008**, *16* (6), 4029.
- (81) Wu, S.; Serbin, J.; Gu, M. Two-Photon Polymerisation for Three-Dimensional Micro-Fabrication. *J. Photochem. Photobiol. A Chem.* **2006**, *181* (1), 1–11.
- (82) Sun, H. B.; Kawata, S. Two-Photon Photopolymerization and 3D Lithographic Microfabrication. *Adv. Polym. Sci.* **2004**, *170*, 169–273.
- (83) Rumi, M.; Barlow, S.; Wang, J.; Perry, J. W.; Marder, S. R. Two-Photon Absorbing Materials and Two-Photon-Induced Chemistry. In *Photoresponsive Polymers I*; Springer Berlin Heidelberg: Berlin, Heidelberg, 2008; pp 1–95.
- (84) Digaum, J. L.; Pazos, J. J.; Chiles, J.; D'Archangel, J.; Padilla, G.; Tatulian, A.;

- Rumpf, R. C.; Fathpour, S.; Boreman, G. D.; Kuebler, S. M. Tight Control of Light Beams in Photonic Crystals with Spatially-Variant Lattice Orientation. *Opt. Express* **2014**, *22* (21), 25788.
- (85) Duc Nguyen, H. H.; Hollenbach, U.; Ostrzinski, U.; Pfeiffer, K.; Hengsbach, S.; Mohr, J. Freeform Three-Dimensional Embedded Polymer Waveguides Enabled by External-Diffusion Assisted Two-Photon Lithography. *Appl. Opt.* **2016**, *55* (8), 1906.
- (86) Wu, E.-S.; Strickler, J. H.; Harrell, W. R.; Webb, W. W. Two-Photon Lithography for Microelectronic Application; Cuthbert, J. D., Ed.; 1992; p 776.
- (87) Farrer, R. A.; LaFratta, C. N.; Li, L.; Praino, J.; Naughton, M. J.; Saleh, B. E. A.; Teich, M. C.; Fourkas, J. T. Selective Functionalization of 3-D Polymer Microstructures. *J. Am. Chem. Soc.* **2006**, *128* (6), 1796–1797.
- (88) Maruo, S.; Inoue, H. Optically Driven Micropump Produced by Three-Dimensional Two-Photon Microfabrication. *Appl. Phys. Lett.* **2006**, *89* (14), 144101.
- (89) Silva, K. R.; Rezende, R. A.; Pereira, F. D. A. S.; Gruber, P.; Stuart, M. P.; Ovsianikov, A.; Brakke, K.; Kasyanov, V.; da Silva, J. V. L.; Granjeiro, J. M.; et al. Delivery of Human Adipose Stem Cells Spheroids into Lockyballs. *PLoS One* **2016**, *11* (11), e0166073.
- (90) Shpichka, A.; Koroleva, A.; Kuznetsova, D.; Burdukovskii, V.; Chichkov, B.; Bagratashvili, V.; Timashev, P. Two-Photon Polymerization in Tissue Engineering. *Polym. Photonic Mater. Towar. Biomed. Break.* **2018**, 71–98.
- (91) Belfield, K. D.; Ren, X.; Van Stryland, E. W.; Hagan, D. J.; Dubikovskiy, V.; Miesak, E. J. Near-IR Two-Photon Photoinitiated Polymerization Using a Fluorone/Amine Initiating System. *J. Am. Chem. Soc.* **2000**, *122* (6), 1217–1218.
- (92) Belfield, K. D.; Schafer, K. J.; Liu, Y.; Liu, J.; Ren, X.; Stryland, E. Van. Multiphoton-Absorbing Organic Materials for Microfabrication, Emerging Optical Applications and Non-Destructive Three-Dimensional Imaging. *J. Phys. Org. Chem.* **2000**, *13* (12), 837–849.
- (93) Schafer, K. J.; Hales, J. M.; Balu, M.; Belfield, K. D.; Van Stryland, E. W.; Hagan, D. J. Two-Photon Absorption Cross-Sections of Common Photoinitiators. *J. Photochem. Photobiol. A Chem.* **2004**, *162* (2–3), 497–502.
- (94) Li, Z.; Pucher, N.; Cicha, K.; Torgersen, J.; Ligon, S. C.; Ajami, A.; Husinsky, W.; Rosspeintner, A.; Vauthey, E.; Naumov, S.; et al. A Straightforward Synthesis and Structure – Activity Relationship of Highly Efficient Initiators for Two-Photon Polymerization. *Macromolecules* **2012**, *46* (2), 352–361.
- (95) Li, Z.; Siklos, M.; Pucher, N.; Cicha, K.; Ajami, A.; Husinsky, W.; Rosspeintner, A.; Vauthey, E.; Gescheidt, G.; Stampfl, J.; et al. Synthesis and Structure-Activity Relationship of Several Aromatic Ketone-Based Two-Photon Initiators. *J. Polym. Sci. Part A Polym. Chem.* **2011**, *49* (17), 3688–3699.
- (96) Cumpston, B. H.; Ananthavel, S. P.; Barlow, S.; Dyer, D. L.; Ehrlich, J. E.; Erskine, L. L.; Heikal, A. A.; Kuebler, S. M.; Lee, I.-Y. S.; McCord-Maughon, D.; et al. Two-Photon Polymerization Initiators for Three-Dimensional Optical Data Storage and Microfabrication. *Nature* **1999**, *398* (6722), 51–54.

- (97) He, G. S.; Tan, L. S.; Zheng, Q.; Prasad, P. N. Multiphoton Absorbing Materials: Molecular Designs, Characterizations, and Applications. *Chem. Rev.* **2008**, *108* (4), 1245–1330.
- (98) Mongin, O.; Porrès, L.; Charlot, M.; Katan, C.; Blanchard-Desce, M. Synthesis, Fluorescence, and Two-Photon Absorption of a Series of Elongated Rodlike and Banana-Shaped Quadrupolar Fluorophores: A Comprehensive Study of Structure–Property Relationships. *Chem. - A Eur. J.* **2007**, *13* (5), 1481–1498.
- (99) Cukierman, E.; Pankov, R.; Stevens, D. R.; Yamada, K. M. Taking Cell-Matrix Adhesions to the Third Dimension. *Science* **2001**, *294* (November), 1708–1712.
- (100) Ciuciu, A. I.; Cywiński, P. J. Two-Photon Polymerization of Hydrogels – Versatile Solutions to Fabricate Well-Defined 3D Structures. *RSC Adv.* **2014**, *4* (85), 45504–45516.
- (101) Cunningham, L. P.; Veilleux, M. P.; Campagnola, P. J. Freeform Multiphoton Excited Microfabrication for Biological Applications Using a Rapid Prototyping CAD-Based Approach. *Opt. Express* **2006**, *14* (19), 8613.
- (102) Basu, S.; Cunningham, L. P.; Pins, G. D.; Bush, K. A.; Taboada, R.; Howell, A. R.; Wang, J.; Campagnola, P. J. Multiphoton Excited Fabrication of Collagen Matrixes Cross-Linked by a Modified Benzophenone Dimer: Bioactivity and Enzymatic Degradation. *Biomacromolecules* **2005**, *6* (3), 1465–1474.
- (103) Ovsianikov, A.; Deiwick, A.; Van Vlierberghe, S.; Dubruel, P.; Möller, L.; Dräger, G.; Chichkov, B. Laser Fabrication of Three-Dimensional CAD Scaffolds from Photosensitive Gelatin for Applications in Tissue Engineering. *Biomacromolecules* **2011**, *12* (4), 851–858.
- (104) Ovsianikov, A.; Deiwick, A.; Van Vlierberghe, S.; Pflaum, M.; Wilhelmi, M.; Dubruel, P.; Chichkov, B. Laser Fabrication of 3D Gelatin Scaffolds for the Generation of Bioartificial Tissues. *Materials (Basel)*. **2011**, *4* (1), 288–299.
- (105) Torgersen, J.; Ovsianikov, A.; Mironov, V.; Pucher, N.; Qin, X.; Li, Z.; Cicha, K.; Machacek, T.; Liska, R.; Jantsch, V.; et al. Photo-Sensitive Hydrogels for Three-Dimensional Laser Microfabrication in the Presence of Whole Organisms. *J. Biomed. Opt.* **2012**, *17* (10), 105008.
- (106) Li, Z.; Torgersen, J.; Ajami, A.; Mühleder, S.; Qin, X.; Husinsky, W.; Holthoner, W.; Ovsianikov, A.; Stampfl, J.; Liska, R. Initiation Efficiency and Cytotoxicity of Novel Water-Soluble Two-Photon Photoinitiators for Direct 3D Microfabrication of Hydrogels. *RSC Adv.* **2013**, *3* (36), 15939.
- (107) Pins, G. D.; Bush, K. A.; Cunningham, L. P.; Campagnola, P. J. Multiphoton Excited Fabricated Nano and Micro Patterned Extracellular Matrix Proteins Direct Cellular Morphology. *J. Biomed. Mater. Res. Part A* **2006**, *78A* (1), 194–204.
- (108) Tong, M. H.; Huang, N.; Zhang, W.; Zhou, Z. L.; Ngan, A. H. W.; Du, Y.; Chan, B. P. Multiphoton Photochemical Crosslinking-Based Fabrication of Protein Micropatterns with Controllable Mechanical Properties for Single Cell Traction Force Measurements. *Sci. Rep.* **2016**, *6* (December 2015), 20063.
- (109) Ovsianikov, A.; Gruene, M.; Pflaum, M.; Koch, L.; Maiorana, F.; Wilhelmi, M.; Haverich, A.; Chichkov, B. Laser Printing of Cells into 3D Scaffolds. *Biofabrication*

- 2010**, 2 (1), 14104.
- (110) Connell, J. L.; Ritschdorff, E. T.; Whiteley, M.; Shear, J. B. 3D Printing of Microscopic Bacterial Communities. *Proc. Natl. Acad. Sci.* **2013**, 110 (46), 18380–18385.
- (111) Basu, S.; Rodionov, V.; Terasaki, M.; Campagnola, P. J. Multiphoton-Excited Microfabrication in Live Cells via Rose Bengal Cross-Linking of Cytoplasmic Proteins. *Opt. Lett.* **2005**, 30 (2), 159–161.
- (112) nanoscribe Photonic Professional data sheet http://www.nanoscribe.de/files/4414/7393/1095/DataSheet_PP_V05_2016_Web.pdf (accessed Jul 28, 2018).
- (113) Giustina, G. Della; Giulitti, S.; Brigo, L.; Zanatta, M.; Tromayer, M.; Liska, R.; Elvassore, N.; Brusatin, G. Hydrogel with Orthogonal Reactive Units: 2D and 3D Cross-Linking Modulation. *Macromol. Rapid Commun.* **2017**, 38 (1).
- (114) Gruber, P.; Van Hoorick, J.; Tromayer, M.; Dubruel, P.; Van Vlierberghe, S.; Ovsianikov, A. Laser Photofabrication of Gelatin Hydrogel Constructs with High Degree of Functionalization. *Front. Bioeng. Biotechnol.* **2016**, 4.
- (115) Qin, X.-H.; Gruber, P.; Markovic, M.; Plochberger, B.; Klotzsch, E.; Stampfl, J.; Ovsianikov, A.; Liska, R. Enzymatic Synthesis of Hyaluronic Acid Vinyl Esters for Two-Photon Microfabrication of Biocompatible and Biodegradable Hydrogel Constructs. *Polym. Chem.* **2014**, 5 (22), 6523–6533.
- (116) Nichol, J. W.; Koshy, S. T.; Bae, H.; Hwang, C. M.; Yamanlar, S.; Khademhosseini, A. Cell-Laden Microengineered Gelatin Methacrylate Hydrogels. *Biomaterials* **2010**, 31 (21), 5536–5544.
- (117) Boyd, V.; Cholewa, O. M.; Papas, K. K. Limitations in the Use of Fluorescein Diacetate/Propidium Iodide (FDA/PI) and Cell Permeable Nucleic Acid Stains for Viability Measurements of Isolated Islets of Langerhans. *Curr. Trends Biotechnol. Pharm.* **2008**, 2 (2), 66–84.
- (118) Chacon, E.; Acosta, D.; Lemasters, J. J. Primary Cultures of Cardiac Myocytes as In Vitro Models for Pharmacological and Toxicological Assessments. In *In Vitro Methods in Pharmaceutical Research*; Elsevier, 1997; pp 209–223.
- (119) Smith, A. M.; Mancini, M. C.; Nie, S. Second Window for in Vivo Imaging. *Nat. Nanotechnol.* **2009**, 4 (11), 710–711.
- (120) Vigetti, D.; Karousou, E.; Viola, M.; Deleonibus, S.; De Luca, G.; Passi, A. Hyaluronan: Biosynthesis and Signaling. *Biochim. Biophys. Acta - Gen. Subj.* **2014**, 1840 (8), 2452–2459.
- (121) Van Vlierberghe, S.; Dubruel, P.; Schacht, E. Biopolymer-Based Hydrogels As Scaffolds for Tissue Engineering Applications: A Review. *Biomacromolecules* **2011**, 12 (5), 1387–1408.
- (122) Burdick, J. A.; Prestwich, G. D. Hyaluronic Acid Hydrogels for Biomedical Applications. *Adv. Mater.* **2011**, 23 (12), 41–56.
- (123) Collins, M. N.; Birkinshaw, C. Hyaluronic Acid Based Scaffolds for Tissue engineering—A Review. *Carbohydr. Polym.* **2013**, 92 (2), 1262–1279.

- (124) Highley, C. B.; Prestwich, G. D.; Burdick, J. A. Recent Advances in Hyaluronic Acid Hydrogels for Biomedical Applications. *Curr. Opin. Biotechnol.* **2016**, *40*, 35–40.
- (125) Mehrishi, J. N.; Bauer, J. Electrophoresis of Cells and the Biological Relevance of Surface Charge. *Electrophoresis* **2002**, *23* (13), 1984–1994.
- (126) Schanté, C. E.; Zuber, G.; Herlin, C.; Vandamme, T. F. Chemical Modifications of Hyaluronic Acid for the Synthesis of Derivatives for a Broad Range of Biomedical Applications. *Carbohydr. Polym.* **2011**, *85* (3), 469–489.
- (127) Zou, Q.; Zhao, Y.; Makarov, N. S.; Campo, J.; Yuan, H.; Fang, D.-C.; Perry, J. W.; Wu, F. Effect of Alicyclic Ring Size on the Photophysical and Photochemical Properties of Bis(arylidene)cycloalkanone Compounds. *Phys. Chem. Chem. Phys.* **2012**, *14* (33), 11743.
- (128) Pinal, R. Effect of Molecular Symmetry on Melting Temperature and Solubility. *Org. Biomol. Chem.* **2004**, *2* (18), 2692.
- (129) Kreher, U. P.; Rosamilia, A. E.; Raston, C. L.; Scott, J. L.; Strauss, C. R. Direct Preparation of Monoarylidene Derivatives of Aldehydes and Enolizable Ketones with DIMCARB. *Org. Lett.* **2003**, *5* (17), 3107–3110.
- (130) Zheng, Q.; He, G. S.; Lin, T.-C.; Prasad, P. N. Synthesis and Properties of Substituted (P-Aminostyryl)-1-(3-Sulfooxypropyl)pyridinium Inner Salts as a New Class of Two-Photon Pumped Lasing dyes Electronic Supplementary Information (ESI) Available: Synthesis Details for Compounds 7b, 7c, 8b and 8c. See. *J. Mater. Chem.* **2003**, *13* (10), 2499.
- (131) Meth-Cohn, O.; Stanforth, S. P. The Vilsmeier–Haack Reaction. In *Comprehensive Organic Synthesis*; Elsevier, 1991; pp 777–794.
- (132) Li, Z. Novel Organic Materials for Multi-Photon Photopolymerization and Photografting: Powerful Tools for Precise Microfabrication and Functionalization in 3D, TU Wien, 2013.
- (133) Armarego, W. L. F.; Chai, C. L. L. Purification of Organic Chemicals — Aromatic Compounds. In *Purification of Laboratory Chemicals*; Elsevier, 2009; pp 223–353.
- (134) Ohshima, T.; Hayashi, Y.; Agura, K.; Fujii, Y.; Yoshiyama, A.; Mashima, K. Sodium Methoxide: A Simple but Highly Efficient Catalyst for the Direct Amidation of Esters. *Chem. Commun.* **2012**, *48* (44), 5434.
- (135) Kim, B. R.; Lee, H. G.; Kang, S. B.; Sung, G. H.; Kim, J. J.; Park, J. K.; Lee, S. G.; Yoon, Y. J. Tert-Butoxide-Assisted Amidation of Esters under Green Conditions. *Synthesis (Stuttg.)* **2012**, *44* (1), 42–50.
- (136) Goswami, A.; Guo, Z.; Parker, W. L.; Patel, R. N. Enzymatic Resolution of Sec-Butylamine. *Tetrahedron: Asymmetry* **2005**, *16* (9), 1715–1719.
- (137) Priego, J.; Ortíz-Nava, C.; Carrillo-Morales, M.; López-Munguía, A.; Escalante, J.; Castillo, E. Solvent Engineering: An Effective Tool to Direct Chemoselectivity in a Lipase-Catalyzed Michael Addition. *Tetrahedron* **2009**, *65* (2), 536–539.
- (138) Wuts, P. G. M.; Greene, T. W. Protection for the Amino Group. In *Greene's Protective Groups in Organic Synthesis*; John Wiley & Sons, Inc.: Hoboken, NJ,

- USA; pp 696–926.
- (139) Li, B.; Berliner, M.; Buzon, R.; Chiu, C. K. F.; Colgan, S. T.; Kaneko, T.; Keene, N.; Kissel, W.; Le, T.; Leeman, K. R.; et al. Aqueous Phosphoric Acid as a Mild Reagent for Deprotection of Tert-Butyl Carbamates, Esters, and Ethers. *J. Org. Chem.* **2006**, *71* (24), 9045–9050.
- (140) Nakajima, N.; Ikada, Y. Mechanism of Amide Formation by Carbodiimide for Bioconjugation in Aqueous Media. *Bioconjug. Chem.* **1995**, *6* (1), 123–130.
- (141) Bergman, K.; Elvingson, C.; Hilborn, J.; Svensk, G.; Bowden, T. Hyaluronic Acid Derivatives Prepared in Aqueous Media by Triazine-Activated Amidation. *Biomacromolecules* **2007**, *8* (7), 2190–2195.
- (142) Magnani, A.; Rappuoli, R.; Lamponi, S.; Barbucci, R. Novel Polysaccharide Hydrogels: Characterization and Properties. *Polym. Adv. Technol.* **2000**, *11* (8–12), 488–495.
- (143) Bellini, D.; Topai, A. Amides of Hyaluronic Acid and the Derivatives Thereof and a Process for Their Preparation. WO2000001733A1, 2000.
- (144) Armstrong, A.; Li, W. N,N'-Carbonyldiimidazole. In *Encyclopedia of Reagents for Organic Synthesis*; John Wiley & Sons, Ltd: Chichester, UK, 2007.
- (145) Khetan, S.; Katz, J. S.; Burdick, J. A. Sequential Crosslinking to Control Cellular Spreading in 3-Dimensional Hydrogels. *Soft Matter* **2009**, *5* (8), 1601.
- (146) Pavan, M.; Galesso, D.; Menon, G.; Renier, D.; Guarise, C. Hyaluronan Derivatives: Alkyl Chain Length Boosts Viscoelastic Behavior to Depolymerization. *Carbohydr. Polym.* **2013**, *97* (2), 321–326.
- (147) Farwick, M.; Lersch, P.; Strutz, G. Low Molecular Weight Hyaluronic Acid: Its Effects on Epidermal Gene Expression & Skin Ageing. *SOFW J.* **2008**, *134* (11–2008).
- (148) Campo, G. M.; Avenoso, A.; Nastasi, G.; Micali, A.; Prestipino, V.; Vaccaro, M.; D'Ascola, A.; Calatroni, A.; Campo, S. Hyaluronan Reduces Inflammation in Experimental Arthritis by Modulating TLR-2 and TLR-4 Cartilage Expression. *Biochim. Biophys. Acta - Mol. Basis Dis.* **2011**, *1812* (9), 1170–1181.
- (149) Rayahin, J. E.; Buhrman, J. S.; Zhang, Y.; Koh, T. J.; Gemeinhart, R. A. High and Low Molecular Weight Hyaluronic Acid Differentially Influence Macrophage Activation. *ACS Biomater. Sci. Eng.* **2015**, *1* (7), 481–493.
- (150) Tromayer, M.; Gruber, P.; Markovic, M.; Rosspeintner, A.; Vauthey, E.; Redl, H.; Ovsianikov, A.; Liska, R.; Rumi, M.; Barlow, S.; et al. A Biocompatible Macromolecular Two-Photon Initiator Based on Hyaluronan. *Polym. Chem.* **2017**, *8* (2), 451–460.
- (151) Farwick, M.; Gauglitz, G.; Pavicic, T.; Köhler, T.; Wegmann, M.; Schwach-Abdellaoui, K.; Malle, B.; Tarabin, V.; Schmitz, G.; Korting, H. C. Fifty-kDa Hyaluronic Acid Upregulates Some Epidermal Genes without Changing TNF- α Expression in Reconstituted Epidermis. *Skin Pharmacol. Physiol.* **2011**, *24* (4), 210–217.
- (152) Loftsson, T.; Brewster, M. E. Pharmaceutical Applications of Cyclodextrins. 1.

- Drug Solubilization and Stabilization. *J. Pharm. Sci.* **1996**, *85* (10), 1017–1025.
- (153) Kiss, T.; Fenyvesi, F.; Bácskay, I.; Váradi, J.; Fenyvesi, É.; Iványi, R.; Szente, L.; Tósaki, Á.; Vecsernyés, M. Evaluation of the Cytotoxicity of β -Cyclodextrin Derivatives: Evidence for the Role of Cholesterol Extraction. *Eur. J. Pharm. Sci.* **2010**, *40* (4), 376–380.
- (154) Fouassier, J. P.; Lalevée, J. *Photoinitiators for Polymer Synthesis*; Wiley-VCH Verlag GmbH & Co. KGaA: Weinheim, Germany, 2012.
- (155) Kolczak, U.; Rist, G.; Dietliker, K.; Wirz, J. Reaction Mechanism of Monoacyl- and Bisacylphosphine Oxide Photoinitiators Studied by ^{31}P -, ^{13}C -, and ^1H -CIDNP and ESR. *J. Am. Chem. Soc.* **1996**, *118* (27), 6477–6489.
- (156) Ikemura, K.; Endo, T. A Review of the Development of Radical Photopolymerization Initiators Used for Designing Light-Curing Dental Adhesives and Resin Composites. *Dent. Mater. J.* **2010**, *29* (5), 481–501.
- (157) Fouassier, J. .; Allonas, X.; Burget, D. Photopolymerization Reactions under Visible Lights: Principle, Mechanisms and Examples of Applications. *Prog. Org. Coatings* **2003**, *47* (1), 16–36.
- (158) Lu, Y.; Hasegawa, F.; Kawazu, Y.; Totani, K.; Yamashita, T.; Toshiyuki, W. Investigation of Mechanism of Photo Induced Polymerization Excited by Two-Photon Absorption. *Sen'i Gakkaishi* **2004**, *60* (6), 165–172.
- (159) Lu, Y.; Hasegawa, F.; Goto, T.; Ohkuma, S.; Fukuhara, S.; Kawazu, Y.; Totani, K.; Yamashita, T.; Watanabe, T. Highly Sensitive Measurement in Two-Photon Absorption Cross Section and Investigation of the Mechanism of Two-Photon-Induced Polymerization. *J. Lumin.* **2004**, *110* (1–2), 1–10.
- (160) Wang, C.-K.; Zhao, K.; Su, Y.; Ren, Y.; Zhao, X.; Luo, Y. Solvent Effects on the Electronic Structure of a Newly Synthesized Two-Photon Polymerization Initiator. *J. Chem. Phys.* **2003**, *119* (2), 1208–1213.
- (161) Baskaran, D.; Mller, A. H. E. Anionic Vinyl Polymerization. In *Controlled and Living Polymerizations*; Wiley-VCH Verlag GmbH & Co. KGaA: Weinheim, Germany; pp 1–56.
- (162) Winterbourn, C. C. Reconciling the Chemistry and Biology of Reactive Oxygen Species. *Nat. Chem. Biol.* **2008**, *4* (5), 278–286.
- (163) Bonham, J. A.; Rossman, M. A.; Grant, R. J. Halomethyl-1,3,5-Triazines Containing a Monomeric Moiety. US5496504A, 1996.
- (164) Vesley, G. Photoactive Mixture of Acrylic Monomers and Chromophore-Substituted Halomethyl-2-Triazine. US4330590A, 1982.
- (165) Vesley, G. Pressure-Sensitive Adhesive. WO1993013149A1, 1993.
- (166) Bonham, J. A.; Petrellis, P. Chromophore-Substituted Vinyl-Halomethyl-S-Triazines. US3987037A, 1976.
- (167) Bonham, J. A.; Rossman, M.; Grant, R. J. Halomethyl-1,3,5-Triazines Containing a Photoinitiator Moiety. EP0361682A1, 1989.

- (168) Grotzinger, C.; Burget, D.; Fouassier, Patrice Jacques, J. P. Photopolymerization Reactions Initiated by a Visible Light Photoinitiating System: Dye/Amine/Bis(trichloromethyl)-Substituted-1,3,5-Triazine. *Macromol. Chem. Phys.* **2001**, *202* (18), 3513–3522.
- (169) Tarzi, O. I.; Allonas, X.; Ley, C.; Fouassier, J.-P. Pyrromethene Derivatives in Three-Component Photoinitiating Systems for Free Radical Photopolymerization. *J. Polym. Sci. Part A Polym. Chem.* **2010**, *48* (12), 2594–2603.
- (170) Monroe, B. M.; Weed, G. C. Photoinitiators for Free-Radical-Initiated Photoimaging Systems. *Chem. Rev.* **1993**, *93* (1), 435–448.
- (171) Karatsu, T.; Yanai, M.; Yagai, S.; Mizukami, J.; Urano, T.; Kitamura, A. Evaluation of Sensitizing Ability of Barbiturate-Functionalized Non-Ionic Cyanine Dyes; Application for Photoinduced Radical Generation System Initiated by near IR Light. *J. Photochem. Photobiol. A Chem.* **2005**, *170* (2), 123–129.
- (172) Michalski, R.; Marcinek, A. Benzothiazine Dyes/2,4,6-Tris(trichloromethyl)-1,3,5-Triazine as a New Visible Two-Component Photoinitiator System. *Int. J. Photoenergy* **2012**, *2012*, 1–8.
- (173) Kabatc, J.; Zasada, M.; Pączkowski, J. Photopolymerization Reactions Initiated by a Visible Light Photoinitiating System: Cyanine Dye/borate salt/1,3,5-Triazine. *J. Polym. Sci. Part A Polym. Chem.* **2007**, *45* (16), 3626–3636.
- (174) Christmann, J.; Allonas, X.; Ley, C.; Ibrahim, A.; Croutxé-Barghorn, C. Triazine-Based Type-II Photoinitiating System for Free Radical Photopolymerization: Mechanism, Efficiency, and Modeling. *Macromol. Chem. Phys.* **2017**, *218* (18), 1600597.
- (175) Zhang, J.; Xiao, P.; Morlet-Savary, F.; Graff, B.; Fouassier, J. P.; Lalevée, J. A Known Photoinitiator for a Novel Technology: 2-(4-Methoxystyryl)-4,6-Bis(trichloromethyl)-1,3,5-Triazine for near UV or Visible LED. *Polym. Chem.* **2014**, *5* (20), 6019–6026.
- (176) Kawamura, K.; Ley, C.; Schmitt, J.; Barnet, M.; Allonas, X. Relevance of Linked Dye-Coinitiator in Visible Three-Component Photoinitiating Systems: Application to Red Light Photopolymerization. *J. Polym. Sci. Part A Polym. Chem.* **2013**, *51* (20), 4325–4330.
- (177) Jockusch, S.; Landis, M. S.; Freiermuth, B.; Turro, N. J. Photochemistry and Photophysics of α -Hydroxy Ketones. *Macromolecules* **2001**, *34* (6), 1619–1626.
- (178) Kim, D. A Theoretical Understanding of the Energy Difference between Singlet and Triplet States of Oligoacene Molecules. *Int. J. Quantum Chem.* **2016**, *116* (8), 651–655.
- (179) Kuimova, M. K.; Hoffmann, M.; Winters, M. U.; Eng, M.; Balaz, M.; Clark, I. P.; Collins, H. A.; Tavender, S. M.; Wilson, C. J.; Albinsson, B.; et al. Determination of the Triplet State Energies of a Series of Conjugated Porphyrin Oligomers. *Photochem. Photobiol. Sci.* **2007**, *6* (6), 675.
- (180) Schaefer, F. C.; Peters, G. A. Synthesis of the S-Triazine System. III. Trimerization of Imidates. *J. Org. Chem.* **1961**, *26* (5), 2778–2784.

- (181) Herrera, A.; Martínez-Alvarez, R.; Ramiro, P.; Chioua, M.; Chioua, R. A Practical and Easy Synthesis of 2,4,6-Trisubstituted-S-Triazines. *Synthesis (Stuttg)*. **2004**, 2004 (4), 503–505.
- (182) Wakabayashi, K.; Tsunoda, M.; Suzuki, Y. Studies on S-Triazines. I. Cotrimerization of Trichloroacetonitrile with Other Nitriles. *Bull. Chem. Soc. Jpn.* **1969**, 42 (10), 2924–2930.
- (183) Peters, G.; Schaefer, F. 2, 4, 6-Trisubstituted-S-Triazines and Process for Preparing Same. US3169963A, 1965.
- (184) Staško, A.; Erentová, K.; Rapta, P.; Nuyken, O.; Voit, B. Investigation of the Decomposition of Compounds Containing Azo Groups by EPR Spectroscopy. *Magn. Reson. Chem.* **1998**, 36 (1), 13–34.
- (185) Novikova, O.; Syromyatnikov, V.; Avramenko, L.; Kondratenko, N.; Kolisnichenko, T.; Abadie, M. Photoinitiation Ability of Some Pentaaza-1,4-Dienes. *Mater. Sci.* **2002**, 20 (4), 19–28.
- (186) Magedov, I. V.; Maklakov, S. A.; Smushkevich, Y. I. New Procedure for Obtaining Indomethacin. *Chem. Heterocycl. Compd.* **2005**, 41 (4), 449–451.
- (187) Kamigata, N.; Kobayashi, M. Azosulfones: Versatile Precursors for Aryl Radicals, Aryl Cations, Aryl Anions, Carbenes, and Benzynes. *Sulfur reports* **1982**, 2 (3), 87–128.
- (188) Sapountzis, I.; Knochel, P. A General Animation Method Based on the Addition of Polyfunctional Arylmagnesium Reagents to Functionalized Arylazo Tosylates. *Angew. Chemie - Int. Ed.* **2004**, 43 (7), 897–900.
- (189) Kreher, R.; Halpaap, R. Arylierungsreaktionen Mit Aryldiazosulfonen / Arylation Reactions of Aryldiazosulfones. *Zeitschrift für Naturforsch. B* **1977**, 32 (11).
- (190) Nuyken, O.; Knepe, T.; Voit, B. Sulfur-Containing Azoinitiators and Their Properties. *Macromol. Chem. Phys.* **1989**, 190 (5), 1015–1024.
- (191) Laridon, U.; Delzenne, G.; Peeters, H. Photopolymerisation of Ethylenically Unsaturated Organic Compounds. US3847610A, 1974.
- (192) Staško, A.; Nuyken, O.; Volt, B.; Biskupič, S. Azo Compounds as Spin Traps in Their Photochemical Decomposition. *Tetrahedron Lett.* **1990**, 31 (40), 5737–5740.
- (193) Levinos, S. Photopolymerization Utilizing Diazosulfonate and Aromatic Hydroxy Compounds. US3909273A, 1975.
- (194) Desjarlais, R. C. Background Coloration Inhibition in Diazosulfonate Photoreproduction. US3623875A, 1971.
- (195) Urbschat, E.; Frohberger, P. Fungicides. US2911336A, November 3, 1959.
- (196) Kojima, M.; Minato, H.; Kobayashi, M. Kinetic Study on Homolysis of Aryl Arylazo Sulfones. *Bulletin of the Chemical Society of Japan*. 1972, pp 2032–2035.
- (197) Stollé, R.; Gunzert, K. T. Über P-Dimethylamino- Und P-Diäthylamino-Phenylhydrazin. *J. für Prakt. Chemie* **1934**, 139 (5–6), 141–161.

- (198) Merino, E. Synthesis of Azobenzenes: The Coloured Pieces of Molecular Materials. *Chem. Soc. Rev.* **2011**, *40* (7), 3835.
- (199) Roe, A. Preparation of Aromatic Fluorine Compounds from Diazonium Fluoroborates. In *Organic Reactions*; John Wiley & Sons, Inc.: Hoboken, NJ, USA, 2011; pp 193–228.
- (200) Becker, H.; Grossmann, K. Spectral Sensitization of Dediazonation by the 2-Electron-Transfer System Meso-tetraphenylporphinatodichlorostannate(IV)/10-Methyl-9-Phenyl-9,10-Dihydro-Acridine. *J. f. Prakt. Chemie* **1990**, *332* (2), 241–250.
- (201) van Beek, L. K. H.; Boven, J.; Helfferich, J. Properties of Diazosulfonates: Part V. The Effect of Substituents on Spectra and Dissociation of 4-Dimethylaminobenzenediazosulfonate. *Recl. des Trav. Chim. des Pays-Bas* **1968**, *87* (7), 737–745.
- (202) Barbero, M.; Crisma, M.; Degani, I.; Fochi, R.; Perracino, P. New Dry Arenediazonium Salts, Stabilized to an Exceptionally High Degree by the Anion of O-Benzenedisulfonimide. *Synthesis (Stuttg.)* **1998**, *1998* (8), 1171–1175.
- (203) Colas, C.; Goeldner, M. An Efficient Procedure for the Synthesis of Crystalline Aryldiazonium Trifluoroacetates – Synthetic Applications. *European J. Org. Chem.* **1999**, *1999* (6), 1357–1366.
- (204) Zarei, A.; Hajipour, A. R.; Khazdooz, L.; Mirjalili, B. F.; Najafi Chermahini, A. Rapid and Efficient Diazotization and Diazo Coupling Reactions on Silica Sulfuric Acid under Solvent-Free Conditions. *Dye. Pigment.* **2009**, *81* (3), 240–244.
- (205) Zarei, A.; Hajipour, A. R.; Khazdooz, L.; Aghaei, H. Fast, Efficient, and Convenient Method for the Preparation of Arylazo Aryl Sulfones Using Stable Aryldiazonium Silica Sulfates under Mild Conditions. *Synlett* **2010**, No. 8, 1201–1204.
- (206) Zolfigol, M. A. Silica Sulfuric acid/NaNO₂ as a Novel Heterogeneous System for Production of Thionitrites and Disulfides under Mild Conditions. *Tetrahedron* **2001**, *57* (46), 9509–9511.
- (207) Harder, T.; Wessig, P.; Bendig, J.; Stösser, R. Photochemical Reactions of Nitroso Oxides at Low Temperatures: The First Experimental Evidence for Dioxaziridines. *J. Am. Chem. Soc.* **1999**, *121* (28), 6580–6588.
- (208) Walkow, F.; Epperlein, J.; Mustroph, H. Lichtabsorption Und Substituenteneffekte Bei Stilben-4-Diazoniumionen. *J. für Prakt. Chemie* **1985**, *327* (5), 799–807.
- (209) *Biodegradation of Azo Dyes*; Atacag Erkurt, H., Ed.; The Handbook of Environmental Chemistry; Springer Berlin Heidelberg: Berlin, Heidelberg, 2010; Vol. 9.
- (210) Vogt, P. F.; Gerulis, J. J. Amines, Aromatic. In *Ullmann's Encyclopedia of Industrial Chemistry*; Wiley-VCH Verlag GmbH & Co. KGaA: Weinheim, Germany, 2000.
- (211) Smith, S. B. Farbstoff Und Verfahren Zur Herstellung Desselben. DE2405855, 1974.

- (212) Müller, P.; Müller-Dolezal, H.; Padeken, H. G.; Stoltz, R.; Söll, H. R. Pütter: Sonstige Arylazoverbindungen. In *Houben-Weyl Methods of Organic Chemistry Vol. X/3, 4th Edition: Diazonium Salts; Azo-, Azoxy-Compounds II; Diazenes II; Azides; Nitrile Oxides*; Thieme, 2014; pp 570–585.
- (213) Moret, S.; Dyson, P. J.; Laurency, G. Direct, in Situ Determination of pH and Solute Concentrations in Formic Acid Dehydrogenation and CO₂ Hydrogenation in Pressurised Aqueous Solutions Using ¹H and ¹³C NMR Spectroscopy. *Dalt. Trans.* **2013**, 42 (13), 4353.
- (214) Tromayer, M.; Dobos, A.; Gruber, P.; Ajami, A.; Dedic, R.; Ovsianikov, A.; Liska, R. A Biocompatible Diazosulfonate Initiator for Direct Encapsulation of Human Stem Cells via Two-Photon Polymerization. *Polym. Chem.* **2018**, 9 (22), 3108–3117.
- (215) Wilkinson, F.; Helman, W. P.; Ross, A. B. Rate Constants for the Decay and Reactions of the Lowest Electronically Excited Singlet State of Molecular Oxygen in Solution. An Expanded and Revised Compilation. *J. Phys. Chem. Ref. Data* **1995**, 24 (2), 663–677.
- (216) Skovsen, E.; Snyder, J. W.; Lambert, J. D. C.; Ogilby, P. R. Lifetime and Diffusion of Singlet Oxygen in a Cell. *J. Phys. Chem. B* **2005**, 109 (18), 8570–8573.
- (217) Dröse, S.; Brandt, U. The Mechanism of Mitochondrial Superoxide Production by the Cytochrome Bc 1 Complex. *J. Biol. Chem.* **2008**, 283 (31), 21649–21654.
- (218) Ward, H. R. Chemically Induced Dynamic Nuclear Polarization (CIDNP). I. Phenomenon, Examples, and Applications. *Acc. Chem. Res.* **1972**, 5 (1), 18–24.
- (219) Smith, P. J.; Dimmock, J. R.; Turner, W. A. Mass Spectrometry of Some Substituted 2-Benzylidenecyclohexanones and 2,6-Bis-Benzylidenecyclohexanones. *Can. J. Chem.* **1973**, 51 (9), 1458–1470.
- (220) Liu, Y.; Lee, Y. H.; Zhang, Q.; Cui, Y.; Ling, X. Y. Plasmonic Nanopillar Arrays Encoded with Multiplex Molecular Information for Anti-Counterfeiting Applications. *J. Mater. Chem. C* **2016**, 4 (19), 4312–4319.
- (221) Armarego, W. L. F.; Chai, C. *Purification of Laboratory Chemicals*; Elsevier, 2013.
- (222) Ceymann, H.; Rosspeintner, A.; Schreck, M. H.; Mützel, C.; Stoy, A.; Vauthey, E.; Lambert, C. Cooperative Enhancement versus Additivity of Two-Photon-Absorption Cross Sections in Linear and Branched Squaraine Superchromophores. *Phys. Chem. Chem. Phys.* **2016**, 18 (24), 16404–16413.
- (223) de Reguardati, S.; Pahapill, J.; Mikhailov, A.; Stepanenko, Y.; Rebane, A. High-Accuracy Reference Standards for Two-Photon Absorption in the 680–1050 Nm Wavelength Range. *Opt. Express* **2016**, 24 (8), 9053.
- (224) Dedic, R.; Svoboda, A.; Pšenčík, J.; Hála, J. Phosphorescence of Singlet Oxygen and Meso-tetra(4-Sulfonatophenyl)porphyrin: Time and Spectral Resolved Study. *J. Mol. Struct.* **2003**, 651–653, 301–304.